

Up-down asymmetric tokamaks



Justin Ball
Worcester College
University of Oxford

Submitted for the degree of
Doctor of Philosophy
Trinity Term 2016

Up-down asymmetric tokamaks

Justin Ball

Worcester College, University of Oxford

Submitted for the degree of Doctor of Philosophy

Trinity Term 2016

Bulk toroidal rotation has proven capable of stabilising both dangerous MHD modes and turbulence. This has allowed existing tokamaks to generate extra fusion power at a fixed size and magnetic field. However, most methods of inducing the plasma to spin do not appear to scale well to larger devices such as ITER or a future power plant. In this thesis, we explore a notable exception: up-down asymmetry in the tokamak magnetic equilibrium. When tokamak flux surfaces are not mirror symmetric about the midplane, turbulence can transport momentum from one surface to the next, creating spontaneous rotation that is “intrinsic” to the geometry. We seek to maximise this intrinsic rotation by finding optimal up-down asymmetric flux surface shapes.

First, we use the ideal MHD model to show that low order external shaping (e.g. elongation) is best for creating up-down asymmetric flux surfaces throughout the device. Then, we calculate realistic up-down asymmetric equilibria for input into nonlinear gyrokinetic turbulence analysis. Analytic gyrokinetics shows that, in the limit of fast shaping effects, a poloidal tilt of the flux surface shaping has little effect on turbulent transport. Since up-down symmetric surfaces do not transport momentum, this invariance to tilt implies that devices with mirror symmetry about any line in the poloidal plane will drive minimal rotation. Accordingly, further analytic investigation suggests that non-mirror symmetric flux surfaces with envelopes created by the beating of fast shaping effects may create significantly stronger momentum transport.

Guided by these analytic results, we carry out local nonlinear gyrokinetic simulations of non-mirror symmetric flux surfaces created with the lowest possible shaping effects. First, we consider tilted elliptical flux surfaces with a Shafranov shift and find little increase in the momentum transport when the effect of the pressure profile on the equilibrium is included. We then simulate flux surfaces with independently-tilted elongation and triangularity. These two-mode configurations show a 60% increase over configurations with just elongation or triangularity. A rough analytic estimate indicates that the optimal two-mode configuration can drive rotation with an on-axis Alfvén Mach number of 1.5% in an ITER-like machine.

Acknowledgements

First and foremost, I would like to thank Professor Felix Parra for being a great advisor and a great person. Five years is a long time, yet without his steady guidance it would have been (and felt) so much longer. I am deeply grateful to Felix for his patience and kindness.

On countless occasions during the course of my degree I depended on help from the leaders of our extended research group. Whether it be a practice talk, a last minute recommendation, or a conference bar crawl they were there. Thank you Michael Barnes, Peter Catto, Paul Dellar, Bill Dorland, and Alex Schekochihin!

I would also like to salute my fellow plasma theory students: Ferdinand van Wyk, Alessandro Geraldini, Michael Fox, Michael Hardman, and Greg Colyer. Through countless discussions they have made my lunch, my research, and my life more interesting. I think it is safe to say that we will forever be “on tour”?

The biggest surprise of my time at Oxford was how quickly I felt at ease at Worcester College. No matter where I moved, the MCR still felt like home. For this I owe Steve Server, Rachel Kan, Helena Rodriguez, Belinda Lo, Stephanie Tam, Flo Benn, Geoff Pascoe, Sarah Barber, and Katie Light among others. I am especially indebted to Kim Fuellenbach for her company and encouragement during those final long evenings of writing.

Lastly, I thank my family for being a constant and continual source of support throughout my life. Mom, Dad, Elyse, Aunt Jill, Uncle Lex, and Aunt Margie: I believe this thesis is more a result of your efforts than my own.

Contents

1	Introduction	7
1.1	Terrestrial nuclear fusion	8
1.2	Toroidal plasma rotation	10
1.3	Up-down asymmetric plasma shaping	11
I	Ideal MHD Equilibrium	14
2	Global equilibria for arbitrary flux surface shaping	15
2.1	Solutions to the $O(B_0)$ Grad-Shafranov equation	18
2.2	Solutions to the $O(\epsilon B_0)$ Grad-Shafranov equation	19
3	Radial penetration of flux surface shaping	22
3.1	Quantifying shaping penetration	23
3.2	Effect of flux surface shape	24
3.3	Effect of the toroidal current profile	26
4	Global equilibria with a Shafranov shift and tilted elliptical boundary	32
4.1	Solution to the $O(B_0)$ Grad-Shafranov equation for a tilted elliptical boundary condition	33
4.2	Solution to the $O(\epsilon B_0)$ Grad-Shafranov equation for a tilted elliptical boundary condition	34
4.3	Location of the magnetic axis	38
5	Derivation of local Miller equilibria	41
5.1	Specification of arbitrary flux surface shaping	41
5.1.1	Expanded flux surface specification	42
5.1.2	Exact flux surface specification	44
5.2	Shafranov shift in tilted elliptical tokamaks	45

5.3	Summary	47
II	Turbulent transport	48
6	Overview of gyrokinetics	49
6.1	Estimating intrinsic momentum transport	54
6.2	Momentum flux from up-down symmetric flux surface shaping	55
7	Mirror symmetry: Scaling of momentum flux with shaping mode number	57
7.1	Poloidal tilting symmetry of high order flux surface shaping	59
7.1.1	Geometric coefficients	59
7.1.2	Asymptotic expansion	61
7.1.3	Gyrokinetic tilting symmetry	62
7.1.4	Accuracy of the local equilibrium approximation	67
7.2	Numerical results	69
7.2.1	Poloidal structure of fluxes	70
7.2.2	Change in total fluxes with tilt	76
7.3	Consequences for momentum flux in mirror symmetric tokamaks . . .	76
8	Envelopes: Scaling of momentum flux with shaping mode number	79
8.1	Analytic gyrokinetic analysis	79
8.1.1	Asymptotic expansion ordering	82
8.1.2	Two mode shaping in the large aspect ratio gyrokinetic model	82
8.1.3	General shaping in the gyrokinetic model	92
8.2	Numerical results	96
8.3	Interpretation	99
9	Non-mirror symmetry: Shafranov shift and tilted elongation	101
9.1	Input Parameters	102
9.2	Parameter scan results	103
9.2.1	Elliptical boundary tilt scans	104
9.2.2	Minor radial scans	105
9.2.3	Circular flux surface scan	106
9.3	Effect of the value of β'	109
9.4	Effect of the β profile	111

10 Non-mirror symmetry: Tilted elongation and tilted triangularity	113
10.1 Exact shaping geometry scan	114
11 Conclusions	117
 III Appendices	 120
A Maximum achievable flux surface shaping	121
B Location of the magnetic axis for a tilted elliptical boundary and constant current profile	122
C Electromagnetic turbulent fluxes and energy exchange	126
D Calculation of the geometric coefficients within Miller local equilib- rium	130
E Non-mirror symmetric geometric coefficients	134
F Dependence of the geometric coefficients on β'	140
References	144

Chapter 1

Introduction

Nuclear fusion is a fundamental and universal source of energy. Following the Big Bang nucleosynthesis, the universe was effectively a large cloud of hydrogen with small density fluctuations. In such a cloud there are two dominant sources of free energy: particle rest energy and gravitational potential energy. Through the action of gravity, the density perturbations have been gradually amplified into stars, which possess the conditions necessary to release particle rest energy via the process of nuclear fusion.

While gravity enables stellar fusion, it does not appear to be as attractive of an energy source. The sun, which dominates the energy budget of our solar system, has a capacity to produce $E_{\text{fusion}} \approx M_{\odot}c^2 \approx 10^{47}J$ of fusion energy, while it only released $E_{\text{gravity}} \approx GM_{\odot}^2/R_{\odot} \approx 10^{41}J$ of gravitational potential energy during its entire formation. Here G is the gravitational constant, M_{\odot} is the solar mass, R_{\odot} is the solar radius, and c is the speed of light. On our own planet, the oceans [1] alone contain approximately $10^{30}J$ of fusion energy directly accessible through deuterium-deuterium fusion. This is roughly the entire gravitational potential energy in the Earth-moon system. Unfortunately, fully extracting this through tidal power involves the destruction of earth by lunar impact.

From figure 1.1, we see that stellar fusion (i.e. solar) is the ultimate drive for nearly all sources of energy on earth. Unfortunately, though the solar energy incident on earth is on average $\sim 10^5$ times the current world energy consumption, the local value varies dramatically and unpredictably. Furthermore, the by-products of solar shown in figure 1.1 do not seem promising as we have the intuition that they will contain little energy. This turns out to be true for geothermal, biomass, fossil, wind, and hydro. For example, the total geothermal energy flux arriving at the surface of the earth is only $\sim 0.01\%$ of the solar energy flux and is barely above the current world energy consumption [2, 3]. However, the nuclear fission of uranium and thorium in breeder reactors is an exception to this intuition, with an energy content that

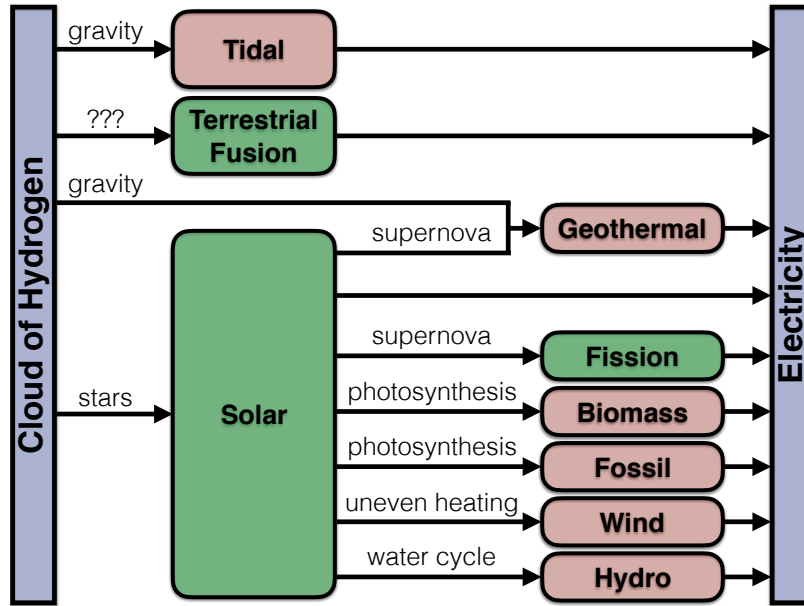


Figure 1.1: Techniques to generate electricity from an astronomically large cloud of hydrogen.

rivals deuterium-deuterium fusion. This is because much of the hydrogen escaped the atmosphere early in the formation of the earth, dramatically increasing the relative abundance of heavy elements compared to most places in the solar system.

Considering the above facts, it appears that here on earth we ultimately have three options:

- solar power with energy storage,
- nuclear fission using breeder reactors, and/or
- terrestrial nuclear fusion.

The fact that none of these options are currently competitive with short-term energy solutions motivates this thesis, which will focus exclusively on the last.

1.1 Terrestrial nuclear fusion

Achieving fusion on earth has proven substantially more difficult than originally imagined. No terrestrial fusion device has ever produced more power than it has consumed, a basic requirement for a power plant. The device with the best experimental performance has consistently been the tokamak, a donut-shaped magnetic bottle capable of creating the stellar conditions necessary for fusion. Since the fuel must be astronomically hot, the thermal energy is sufficient to ionise the atoms making plasma, an

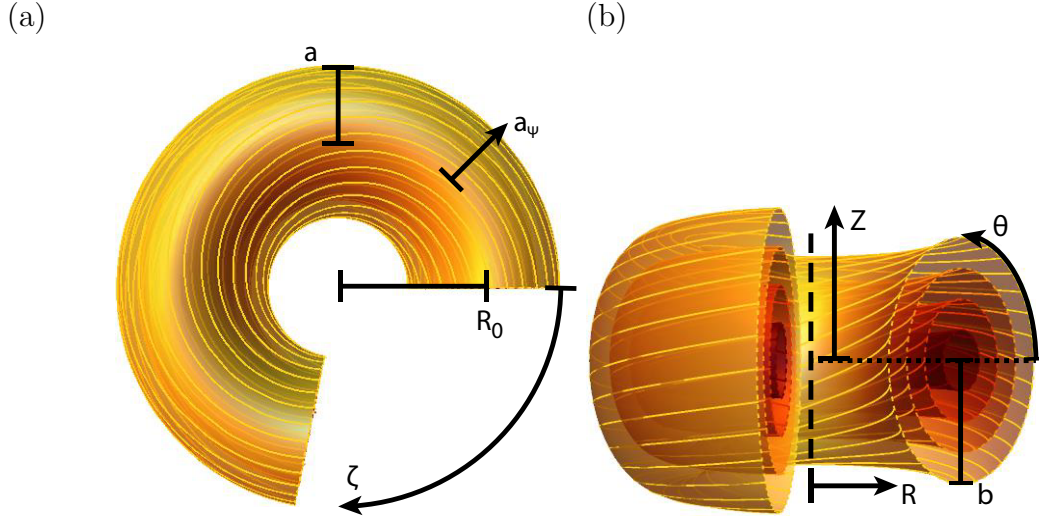


Figure 1.2: The (a) top and (b) side views of the magnetic field lines that form four elliptical flux surfaces in an example tokamak (with a toroidal section removed for illustrative purposes) showing the axis of symmetry (black, dashed) and the midplane (black, dotted), where R is the major radial coordinate, Z is the axial coordinate, ζ is the toroidal angle, a_ψ is the minor radius flux surface label, θ is the poloidal angle, a is the device minor radius, R_0 is the major radial location of the magnetic axis, and $\kappa \equiv b/a$ is the elongation.

electrically-charged gas of ions and free electrons. Because the fuel is charged, it is constrained to follow the magnetic field lines in the device (see figure 1.2) according to the laws of electromagnetism. Currents in both external magnets and the plasma itself are used to create these magnetic field lines in such a way that they wrap around and close on themselves, forming nested magnetic surfaces known as flux surfaces (see figure 1.2).

This would seem to work very well in principle. The energetic charged particles would spiral around the field lines and stream around the device, but never touch a solid surface. Thus, the magnetic field would provide the immense thermal insulation necessary to permit the stellar conditions for fusion to exist only a few metres from the solid material surface of the surrounding vacuum vessel.

However, in practice the enormous temperature gradients give rise to plasma turbulence, which degrades the thermal insulation and determines the performance of the device. If the plasma has stronger turbulence, energy leaks out faster and the plasma must be heated more in order to maintain the same temperature and fusion power. This necessitates more external heating power, which is what causes devices to consume more power than they generate. The fusion power record, achieved in the JET tokamak in 1997, is 16 MW, 70% of the power needed to heat the device [4].

Additionally, there is a constraint on how much plasma pressure a given magnetic field can contain. Even though the plasma may be forced to follow magnetic field lines, if the plasma pressure is large enough it can escape confinement by simply dragging the magnetic field with it. This notion is governed by magnetohydrodynamics (MHD) and is formalised through a limit on the plasma β called the Troyon limit [5],

$$\beta_N \equiv \frac{(a/\text{m})(B_0/\text{T})}{(I_p/\text{MA})}\beta \lesssim 0.03, \quad (1.1)$$

where B_0 is the on-axis magnetic field, I_p is the plasma current, $\beta \equiv 2\mu_0 p/B_0^2$ is the plasma beta, μ_0 is the vacuum permeability, and p is the plasma pressure. Exceeding this limit typically causes the whole plasma to go unstable, kinking until it makes contact with the vacuum vessel and rapidly cools. The Troyon limit is especially important not just because it constrains the safe operating space, but because it is related to the economics of a power plant. The reactor size and the magnetic field strength are the two most significant factors that determine the capital cost of a device. The plasma pressure is directly related to fusion power density and by that the total amount of power produced. The final quantity appearing is the plasma current, which must be driven externally and often dominates the external power needed to run the device. Hence, the Troyon limit can be thought of as a rough, but direct constraint on the cost of electricity.

1.2 Toroidal plasma rotation

In this context, it is understandable that there has been much work on strategies to exceed the Troyon limit without inducing instability [6, 7, 8]. One method, which also has the potential to directly reduce turbulence [9, 10, 11, 12], is to use toroidal rotation. When the plasma has an average toroidal flow, interactions with the surrounding vacuum vessel are able to damp bulk plasma instabilities [13]. Experiments have used toroidal rotation to sustain discharges that violate the Troyon limit by a factor of two [14]. If only for this purpose, it is clear that control of toroidal rotation is beneficial for plasma performance. Unfortunately, the mechanisms that generate toroidal rotation in current experiments do not appear to scale well to future high-performance devices, which will likely be larger and have stronger magnetic fields. One such device that is currently under construction is ITER [15]. Current projections indicate that ITER will not be able to generate sufficiently fast toroidal rotation

to allow violation of the Troyon limit. The necessary rotation is difficult to determine, but is estimated [6] to be in the range of

$$M_A \equiv \frac{V_\zeta}{v_{\text{Alfvén}}} \approx 0.5\% - 5\%, \quad (1.2)$$

where M_A is the Alfvén Mach number of the rotation, V_ζ is the bulk plasma toroidal velocity, and $v_{\text{Alfvén}}$ is the Alfvén speed. For ITER, one can multiply these values by 10 to estimate the necessary Mach number, $M_S \equiv V_\zeta/c_S \approx 5\% - 50\%$, where c_S is the plasma sound speed.

Tokamak plasmas start off at rest, but will start to spin if pushed using external injection of momentum. This is commonly done with beams of neutral particles, which enable current experiments to achieve toroidal rotation with $M_A \approx 3\%$ [14]. However, since ITER has a much larger plasma, it has significantly more inertia and requires higher velocity neutral beams in order to penetrate to the plasma centre. Since energy is quadratic with velocity and momentum is linear, it can be shown that the ratio of the momentum to energy carried by a neutral beam varies inversely with the beam velocity [16]. Hence, the neutral beams on ITER will be less efficient at driving rotation. Therefore, we should not be surprised that detailed modelling predicts external injection will only be capable of driving rotation with $M_A \approx 0.3\%$ [6], significantly less than what is required for violation of the Troyon limit.

1.3 Up-down asymmetric plasma shaping

Alternatively, experiments observe “intrinsic” rotation, or rotation spontaneously generated in the absence of external injection. This rotation arises from plasma turbulence moving momentum between flux surfaces and is especially attractive because it does not require any external power. In current experiments the speed of this intrinsic rotation is roughly $M_A \approx 1\%$, but (as we will see in chapter 6) it is limited by a poloidal symmetry of tokamak turbulence to be small in $\rho_* \equiv \rho_i/a \ll 1$, the ratio of the ion gyroradius to the tokamak minor radius. Unfortunately, we expect that ρ_* will get progressively smaller in future devices like ITER or a power plant.

However, there is one mechanism capable of breaking the symmetry of the turbulence to generate lowest order rotation in a stationary plasma: up-down asymmetric plasma shaping. When the tokamak flux surfaces do not have mirror symmetry about the midplane, the momentum transport at the top of the device is no longer guaranteed to cancel the momentum transport at the bottom. Hence large toroidal flows can

spontaneously develop. In fact, reference [17] presents results from the TCV tokamak that have provided the first experimental evidence of intrinsic rotation generated by up-down asymmetry. Consequently, reference [18] performed nonlinear gyrokinetic simulations that are consistent with the TCV results and suggest that up-down asymmetry is a feasible method to generate the current, experimentally-measured rotation levels in reactor-sized devices.

This thesis will seek the up-down asymmetric flux surface shapes that maximise intrinsic rotation and overall plasma performance. It is separated into two fairly independent lines of inquiry. In part I, we will use the ideal MHD model to calculate practical tokamak equilibria that maximise up-down asymmetric shaping throughout the plasma. In part II, we will perform nonlinear gyrokinetic analysis of these realistic equilibria to identify the configurations that maximise turbulent momentum transport and minimise turbulent energy transport.

First, in chapter 2, we will find solutions for up-down asymmetric MHD equilibria using an expansion in large aspect ratio, given simple radial profiles of the toroidal current and pressure. In chapter 3, we will study how the flux surface shaping in these solutions penetrates from the plasma edge to the magnetic axis in order to identify poloidally-tilted elongation as optimal for maximising up-down asymmetry throughout the device. Next, in chapter 4, we will extend our MHD calculation to find the strength and direction of the Shafranov shift in tokamaks with tilted elliptical poloidal cross-sections. In chapter 5, we will derive local equilibria from the global equilibria of chapters 2 and 4 to use as input to turbulence simulations.

Chapter 6 introduces the theoretical model of gyrokinetics, which is thought to govern turbulence in the core of tokamaks. Then the results of references [19, 20, 21] are summarised, which demonstrates a symmetry of the gyrokinetic equation that constrains rotation to be small in up-down symmetric devices. This provides background for chapter 7, which presents a new symmetry of the gyrokinetic model. The new symmetry establishes the invariance of turbulent transport to a poloidal tilt of “fast” flux surface shaping, where “fast” refers to shaping with a small spatial scale. By the up-down symmetry argument, this invariance to poloidal tilt constrains the momentum transport generated by mirror symmetric fast shaping (i.e. has reflectional symmetry about at least one line in the poloidal plane) to be exponentially small in the Fourier mode number of the fast shaping. In chapter 8, we show that beating fast shaping effects together to produce slowly varying envelopes can generate momentum flux that is only polynomially small in the Fourier mode number of the fast shaping. This, together with an argument showing that mirror symmetric screw

pinches have no momentum transport, motivates non-mirror symmetric flux surfaces (i.e. surfaces that do not have mirror symmetry about any line in the poloidal plane) with up-down asymmetric envelopes. Accordingly, chapter 9 studies turbulent transport in tilted elliptical flux surfaces that have a Shafranov shift (which breaks the flux surface mirror symmetry) and finds mixed results. As expected, the Shafranov shift can enhance the amount of rotation, but the effect is entirely cancelled when the influence of the pressure gradient on the equilibrium is consistently included. Then, chapter 10 examines non-mirror symmetric configurations created using elongation and triangularity with separate poloidal tilt angles. We identify specific tilt angles that can enhance the momentum transport by $\sim 60\%$ compared to purely elongated configurations and also tend to minimise the energy transport.

Chapter 11 identifies the optimal flux surface geometry for driving intrinsic rotation and uses it to illustrate the most significant results of this thesis.

Part I

Ideal MHD Equilibrium

Chapter 2

Global equilibria for arbitrary flux surface shaping

Much of this chapter appears in reference [22].

Ideal magnetohydrodynamics (MHD) [23] is a simple, single fluid model that describes the macroscopic behaviour of plasma in a magnetic field. It is valid when the plasma has sufficiently high collisionality, small gyroradius, and small electrical resistivity. Strictly speaking fusion plasmas are not collisional enough for the model to be valid, but for subtle reasons it is empirically accurate for some calculations. In particular, it can be used to calculate the equilibrium magnetic field.

We start by writing the general form for the magnetic field in a tokamak,

$$\vec{B} = I(\psi) \vec{\nabla}\zeta + \vec{\nabla}\zeta \times \vec{\nabla}\psi, \quad (2.1)$$

where ψ is the poloidal magnetic flux divided by 2π , $I(\psi) \equiv RB_\zeta$ is the toroidal magnetic field flux function, and B_ζ is the toroidal magnetic field. Noting that $\vec{B} \cdot \vec{\nabla}\psi = 0$ we see that the magnetic field lines (and hence the plasma) are confined to nested surfaces of constant ψ , which are called flux surfaces. The ideal MHD equilibria of the flux surfaces is governed by the Grad-Shafranov equation [24],

$$R^2 \vec{\nabla} \cdot \left(\frac{\vec{\nabla}\psi}{R^2} \right) = -\mu_0 R^2 \left. \frac{\partial p}{\partial \psi} \right|_R - I \frac{dI}{d\psi}, \quad (2.2)$$

where the derivative of the pressure is performed holding the major radius constant. We note that with the exception of chapters 6 and 7 we will assume the plasma flow is subsonic, meaning that the pressure becomes a flux function and $\partial p / \partial \psi|_R = dp / d\psi$. Using Ampere's law and (2.1) we see that the entire right-hand side of the Grad-Shafranov equation is closely related to j_ζ , the toroidal current density in the plasma,

according to

$$-\mu_0 R^2 \frac{dp}{d\psi} - I \frac{dI}{d\psi} = \mu_0 j_\zeta R. \quad (2.3)$$

In order to find flux surface shapes that generate high levels of intrinsic rotation in real experiments, we must first identify practical up-down asymmetric equilibria. There has been significant work on general solutions to the Grad-Shafranov equation [25], but here we will restrict our attention to several simple, approximate solutions. These solutions will allow us to identify feasible up-down asymmetric geometries as well as determine which features of the equilibria are robust and which are sensitive to the details of the configuration. We will expand the Grad-Shafranov equation in the large aspect ratio limit, i.e. $\epsilon \equiv a/R_{0b} \ll 1$, where R_{0b} is the major radial location of the centre of the boundary flux surface. Note that we are expanding in the aspect ratio of the boundary flux surface as it will be more convenient than using the usual aspect ratio, which is based on the major radial location of the magnetic axis (i.e. R_0). We will also take the typical orderings for a low β , ohmically heated tokamak [26] of

$$\frac{B_p}{B_{0b}} \sim \epsilon, \quad \frac{2\mu_0 p}{B_{0b}^2} \sim \epsilon^2, \quad (2.4)$$

where $B_p = |\vec{\nabla}\psi|/R$ is the poloidal magnetic field and B_{0b} is the strength of the toroidal magnetic field at the centre of the boundary flux surface. Since we will need to know how the Shafranov shift (i.e. the shift in the magnetic axis due to toroidicity) behaves in up-down asymmetric geometries we must solve the Grad-Shafranov equation both to lowest and next order in ϵ . In order to see the effect of the shapes of the toroidal current and pressure profiles we will look at three simple cases: constant, linear (in poloidal flux) peaked, and linear hollow.

First we must expand (2.2) in $\epsilon \ll 1$ using $\psi = \psi_0 + \psi_1 + \dots$, $I = I_0 + I_1 + I_2$, and $p = p_2$, where the subscripts indicate the order of the quantity in ϵ . To $O(\epsilon^{-1}B_0)$ we find that the Grad-Shafranov equation is

$$-I_0 \frac{dI_1}{d\psi_0} - I_1 \frac{dI_0}{d\psi_0} = 0. \quad (2.5)$$

Since $I_0 = R_{0b}B_{0b}$ is a constant, this requires that I_1 also be a constant. We are free to absorb I_1 into I_0 and set $I_1 = 0$. Hence, to $O(B_0)$ the Grad-Shafranov equation is

$$\frac{1}{r} \frac{\partial}{\partial r} \left(r \frac{\partial \psi_0}{\partial r} \right) + \frac{1}{r^2} \frac{\partial^2 \psi_0}{\partial \theta^2} = -\mu_0 R_{0b}^2 \frac{dp_2}{d\psi_0} - I_0 \frac{dI_2}{d\psi_0} \quad (2.6)$$

and to $O(\epsilon B_0)$ we find

$$\begin{aligned} \frac{1}{r} \frac{\partial}{\partial r} \left(r \frac{\partial \psi_1}{\partial r} \right) + \frac{1}{r^2} \frac{\partial^2 \psi_1}{\partial \theta^2} - \psi_1 \frac{d}{d\psi_0} \left(-\mu_0 R_{0b}^2 \frac{dp_2}{d\psi_0} - I_0 \frac{dI_2}{d\psi_0} \right) \\ = -2\mu_0 r R_{0b} \frac{dp_2}{d\psi_0} \cos(\theta) + \frac{\cos(\theta)}{R_{0b}} \frac{\partial \psi_0}{\partial r} - \frac{\sin(\theta)}{r R_{0b}} \frac{\partial \psi_0}{\partial \theta}, \end{aligned} \quad (2.7)$$

where $r \equiv \sqrt{(R - R_{0b})^2 + (Z - Z_{0b})^2}$ is the distance from the centre of the boundary flux surface, $\theta \equiv \arctan((Z - Z_{0b}) / (R - R_{0b}))$ is the usual cylindrical poloidal angle (see figure 1.2), and Z_{0b} is the axial location of the centre of the boundary flux surface. We note that the $O(B_0)$ Grad-Shafranov equation has cylindrical symmetry (i.e. translational symmetry in θ), unlike the $O(\epsilon B_0)$ equation.

Next, we will parameterize all three current profiles (i.e. constant, peaked, and hollow) by

$$-\mu_0 R_{0b}^2 \frac{dp_2}{d\psi_0} - I_0 \frac{dI_2}{d\psi_0} = \mu_0 j_{\zeta 0} R_{0b} = \hat{j}_0 \left(1 - \hat{f}_0 \psi_0 \right), \quad (2.8)$$

where $j_{\zeta 0}$ is the lowest order current density in the aspect ratio expansion, \hat{j}_0 is a positive constant, $\hat{f}_0 \in [-\psi_{0b}^{-1}, \psi_{0b}^{-1}]$ determines the slope of the current profile, and ψ_{0b} is the lowest order value of the poloidal flux on the boundary flux surface (where ψ is taken to vanish at the magnetic axis). The constant current case is achieved by setting $\hat{f}_0 = 0$, while the hollow current case arises from allowing \hat{f}_0 to be negative.

Additionally, from (2.7) we see that it will be necessary to distinguish the contributions to the current from the pressure and magnetic field terms in (2.3). Like the toroidal current, we will assume the pressure gradient has the form of

$$-\mu_0 R_{0b}^2 \frac{dp_2}{d\psi_0} = \hat{j}_{0p} \left(1 - \hat{f}_{0p} \psi_0 \right), \quad (2.9)$$

where \hat{j}_{0p} and $\hat{f}_{0p} \in [-\psi_{0b}^{-1}, \psi_{0b}^{-1}]$ are constants. By (2.8), this pressure profile implies that the toroidal magnetic field flux function term must be

$$-I_0 \frac{dI_2}{d\psi_0} = \hat{j}_{0I} \left(1 - \hat{f}_{0I} \psi_0 \right), \quad (2.10)$$

where

$$\hat{j}_{0I} \equiv \hat{j}_0 - \hat{j}_{0p} \quad (2.11)$$

$$\hat{f}_{0I} \equiv \frac{1}{\hat{j}_{0I}} \left(\hat{j}_0 \hat{f}_0 - \hat{j}_{0p} \hat{f}_{0p} \right) \quad (2.12)$$

are constants.

2.1 Solutions to the $O(B_0)$ Grad-Shafranov equation

In order to solve the $O(B_0)$ Grad-Shafranov equation we will Fourier analyse the magnetic flux in poloidal angle as

$$\psi_0(r, \theta) = \psi_{0,0}^C(r) + \sum_{m=1}^{\infty} [\psi_{0,m}^C(r) \cos(m\theta) + \psi_{0,m}^S(r) \sin(m\theta)], \quad (2.13)$$

where m is the poloidal flux surface shaping mode number. Using (2.13) we can rewrite (2.6) as

$$\frac{1}{r} \frac{d}{dr} \left(r \frac{d\psi_{0,m}^T}{dr} \right) + \left(\hat{f}_0 \hat{j}_0 - \frac{m^2}{r^2} \right) \psi_{0,m}^T(r) = \hat{j}_0 \delta_{m,0}, \quad (2.14)$$

where $\delta_{i,j}$ is the Kronecker delta and $T = C, S$ is a superscript that indicates the sine or cosine mode. The solutions to this equation with zero poloidal flux at the magnetic axis are

$$\psi_{0,0}^C(r) = -\frac{1}{\hat{f}_0} \left(J_0 \left(\sqrt{\hat{f}_0 \hat{j}_0} r \right) - 1 \right) \quad (2.15)$$

$$\psi_{0,m}^C(r) = C_{0,m} \frac{m! 2^m}{(\hat{f}_0 \hat{j}_0)^{m/2}} J_m \left(\sqrt{\hat{f}_0 \hat{j}_0} r \right) \quad (2.16)$$

$$\psi_{0,m}^S(r) = S_{0,m} \frac{m! 2^m}{(\hat{f}_0 \hat{j}_0)^{m/2}} J_m \left(\sqrt{\hat{f}_0 \hat{j}_0} r \right), \quad (2.17)$$

where J_m is the m^{th} order Bessel function of the first kind. The Fourier coefficients $C_{0,m}$ and $S_{0,m}$ are determined by the boundary conditions at the plasma edge, which is physically controlled by the locations and currents of external plasma shaping coils. Using trigonometric identities, (2.13) and (2.15) through (2.17) can be rewritten as

$$\begin{aligned} \psi_0(r, \theta) = & -\frac{1}{\hat{f}_0} \left(J_0 \left(\sqrt{\hat{f}_0 \hat{j}_0} r \right) - 1 \right) \\ & + \sum_{m=2}^{\infty} N_{0,m} \frac{m! 2^m}{(\hat{f}_0 \hat{j}_0)^{m/2}} J_m \left(\sqrt{\hat{f}_0 \hat{j}_0} r \right) \cos(m(\theta + \theta_{t0,m})), \end{aligned} \quad (2.18)$$

where

$$N_{0,m} \equiv \sqrt{C_{0,m}^2 + S_{0,m}^2} \quad (2.19)$$

is the magnitude of the Fourier mode and

$$\theta_{t0,m} \equiv -\frac{1}{m} \arctan \left(\frac{S_{0,m}}{C_{0,m}} \right) \quad (2.20)$$

is the Fourier mode tilt angle.

Note that for the constant current case (i.e. $\hat{f}_0 = 0$), (2.18) reduces to

$$\psi_0(r, \theta) = \frac{\hat{j}_0}{4} r^2 + \sum_{m=2}^{\infty} N_{0,m} r^m \cos(m(\theta + \theta_{t0,m})). \quad (2.21)$$

To understand the hollow current case, it is helpful to make use of the identity

$$J_m(ix) = i^m I_m(x), \quad (2.22)$$

where I_m is the m^{th} order modified Bessel function of the first kind. From this we can demonstrate that (2.18) is equivalent to

$$\begin{aligned} \psi_0(r, \theta) = & \frac{1}{-\hat{f}_0} \left(I_0 \left(\sqrt{-\hat{f}_0 \hat{j}_0} r \right) - 1 \right) \\ & + \sum_{m=2}^{\infty} N_{0,m} \frac{m! 2^m}{(-\hat{f}_0 \hat{j}_0)^{m/2}} I_m \left(\sqrt{-\hat{f}_0 \hat{j}_0} r \right) \cos(m(\theta + \theta_{t0,m})), \end{aligned} \quad (2.23)$$

which can be more easily applied to hollow toroidal current profiles (i.e. $\hat{f}_0 < 0$).

2.2 Solutions to the $O(\epsilon B_0)$ Grad-Shafranov equation

In order to solve the $O(\epsilon B_0)$ equation we again must Fourier analyse the magnetic flux in poloidal angle. The lowest order Fourier-analysed flux is given by (2.13) and (2.15) through (2.17). To next order, we can write

$$\psi_1(r, \theta) = \psi_{1,0}^C(r) + \sum_{m=1}^{\infty} [\psi_{1,m}^C(r) \cos(m\theta) + \psi_{1,m}^S(r) \sin(m\theta)], \quad (2.24)$$

but we still must solve for $\psi_{1,m}^C(r)$ and $\psi_{1,m}^S(r)$ by substituting (2.13) and (2.24) into (2.7). Since $\psi_{1,m}^C(r)$ and $\psi_{1,m}^S(r)$ do not depend on θ , we can take each Fourier component of (2.7) as a separate equation. This gives

$$\frac{1}{r} \frac{d}{dr} \left(r \frac{d\psi_{1,m}^T}{dr} \right) + \left(\hat{f}_0 \hat{j}_0 - \frac{m^2}{r^2} \right) \psi_{1,m}^T(r) = \Lambda_m^T(r) \quad (2.25)$$

for each Fourier mode m , where the inhomogeneous terms are given by $\Lambda_m^T(r)$. For $m = 0$ and $T = C$

$$\Lambda_0^C(r) \equiv \frac{1}{R_0} \left[\frac{1}{2} \frac{d\psi_{0,1}^C}{dr} + \left(\frac{1}{2r} - r\hat{f}_{0p}\hat{j}_{0p} \right) \psi_{0,1}^C(r) \right], \quad (2.26)$$

for $m = 1$ and $T = C$

$$\begin{aligned} \Lambda_1^C(r) \equiv & \frac{1}{R_0} \left[\frac{1}{2} \frac{d\psi_{0,2}^C}{dr} + \left(\frac{1}{r} - r\hat{f}_{0p}\hat{j}_{0p} \right) \psi_{0,2}^C(r) \right. \\ & \left. + \frac{d\psi_{0,0}^C}{dr} + 2r\hat{j}_{0p} \left(1 - \hat{f}_{0p}\psi_{0,0}^C(r) \right) \right], \end{aligned} \quad (2.27)$$

for $m = 1$ and $T = S$

$$\Lambda_1^S(r) \equiv \frac{1}{R_0} \left[\frac{1}{2} \frac{d\psi_{0,2}^S}{dr} + \left(\frac{1}{r} - r\hat{f}_{0p}\hat{j}_{0p} \right) \psi_{0,2}^S(r) \right], \quad (2.28)$$

and for all other m and $T = C, S$

$$\begin{aligned} \Lambda_m^T(r) \equiv & \frac{1}{R_0} \left[\frac{1}{2} \frac{d\psi_{0,m+1}^T}{dr} + \left(\frac{m+1}{2r} - r\hat{f}_{0p}\hat{j}_{0p} \right) \psi_{0,m+1}^T(r) \right. \\ & \left. + \frac{1}{2} \frac{d\psi_{0,m-1}^T}{dr} - \left(\frac{m-1}{2r} + r\hat{f}_{0p}\hat{j}_{0p} \right) \psi_{0,m-1}^T(r) \right]. \end{aligned} \quad (2.29)$$

Equation (2.25) can be solved using the method of variation of parameters, yielding

$$\begin{aligned} \psi_{1,m}^T(r) = & -\frac{\pi}{2} J_m \left(\sqrt{\hat{f}_0 \hat{j}_0} r \right) \int_0^r dr' r' Y_m \left(\sqrt{\hat{f}_0 \hat{j}_0} r' \right) \Lambda_m^T(r') \\ & + \frac{\pi}{2} Y_m \left(\sqrt{\hat{f}_0 \hat{j}_0} r \right) \int_0^r dr' r' J_m \left(\sqrt{\hat{f}_0 \hat{j}_0} r' \right) \Lambda_m^T(r') \\ & + T_{1,m} \frac{m! 2^m}{(\hat{f}_0 \hat{j}_0)^{m/2}} J_m \left(\sqrt{\hat{f}_0 \hat{j}_0} r \right), \end{aligned} \quad (2.30)$$

where we have imposed regularity at the origin, Y_m is the m^{th} order Bessel function of the second kind, and $T_{1,m} = C_{1,m}, S_{1,m}$ are Fourier coefficients determined by the boundary conditions at the plasma edge. Combining (2.24), (2.26) through (2.29), and (2.30) gives the complete solution to the $O(\epsilon B_0)$ Grad-Shafranov equation for an arbitrary boundary condition.

To understand the hollow current case (i.e. $\hat{f}_0 < 0$), we will use (2.22) and the identity

$$Y_m(ix) = i^{m+1}I_m(x) - \frac{2}{\pi}i^{-m}K_m(x), \quad (2.31)$$

where K_m is the m^{th} order modified Bessel function of the second kind. This enables (2.30) to be reformulated as

$$\begin{aligned} \psi_{1,m}^T(r) = & I_m\left(\sqrt{-\hat{f}_0\hat{j}_0}r\right) \int_0^r dr' r' K_m\left(\sqrt{-\hat{f}_0\hat{j}_0}r'\right) \Lambda_m^T(r') \\ & - K_m\left(\sqrt{-\hat{f}_0\hat{j}_0}r\right) \int_0^r dr' r' I_m\left(\sqrt{-\hat{f}_0\hat{j}_0}r'\right) \Lambda_m^T(r') \\ & + T_{1,m} \frac{m! 2^m}{(-\hat{f}_0\hat{j}_0)^{m/2}} I_m\left(\sqrt{-\hat{f}_0\hat{j}_0}r\right). \end{aligned} \quad (2.32)$$

For a constant current profile (i.e. $\hat{f}_0 = 0$), we can take the limit of (2.24), (2.26) through (2.29), and (2.30) as $\hat{f}_0\hat{j}_0 \rightarrow 0$ to find

$$\begin{aligned} \psi_1(r, \theta) = & \frac{1}{4R_{0b}} \left[\left(\frac{\hat{j}_0 + 4\hat{j}_{0p}}{4} r^3 - \frac{\hat{j}_0\hat{f}_{0p}\hat{j}_{0p}}{12} r^5 \right) \cos(\theta) \right. \\ & + \sum_{m=2}^{\infty} \left(r^{m+1} - \frac{\hat{f}_{0p}\hat{j}_{0p}}{2(m+1)} r^{m+3} \right) N_{0,m} \cos((m-1)\theta + m\theta_{t0,m}) \\ & - \sum_{m=2}^{\infty} \frac{\hat{f}_{0p}\hat{j}_{0p}}{m+2} r^{m+3} N_{0,m} \cos((m+1)\theta + m\theta_{t0,m}) \Big] \\ & + \sum_{m=0}^{\infty} r^m N_{1,m} \cos(m(\theta + \theta_{t1,m})), \end{aligned} \quad (2.33)$$

where $N_{1,m} \equiv \sqrt{C_{1,m}^2 + S_{1,m}^2}$ is the magnitude of the next order Fourier mode, $\theta_{t1,m} \equiv -\arctan(S_{1,m}/C_{1,m})/m$ is the next order Fourier mode tilt angle, and we have used (2.21) with

$$\lim_{\hat{f}_0\hat{j}_0 \rightarrow 0} \frac{m! 2^m}{(\hat{f}_0\hat{j}_0)^{m/2}} J_m\left(\sqrt{\hat{f}_0\hat{j}_0}r\right) = r^m \quad (2.34)$$

$$\lim_{\hat{f}_0\hat{j}_0 \rightarrow 0} Y_m\left(\sqrt{\hat{f}_0\hat{j}_0}r\right) = -\frac{1}{m\pi} \frac{m! 2^m}{(\hat{f}_0\hat{j}_0)^{m/2}} r^{-m} \quad (2.35)$$

for $m \neq 0$. The first line of (2.33) contains the direct effect of toroidicity on the equilibrium, i.e. the Shafranov shift. The second and third lines show that a zeroth order shaping mode m splits into two modes, $m-1$ and $m+1$, at first order. The last line contains the homogeneous solution, which enables an arbitrary boundary condition to be satisfied.

Chapter 3

Radial penetration of flux surface shaping

Much of this chapter appears in reference [27].

This chapter uses a series of independent arguments to show that tokamaks with lower order shaping modes and a more hollow current profile will better allow shaping to penetrate to the magnetic axis. This provides intuition for existing analytic [28, 29, 30] and numerical [31, 32] results concerning how flux surface shaping penetrates in the ideal MHD model.

Here we will use the large aspect ratio solutions found in chapter 2 to investigate the effects of both free parameters in the lowest order Grad-Shafranov equation: the boundary condition and the toroidal current profile (see (2.2) and (2.3)). Although the motivation is to create up-down asymmetric flux surfaces near the magnetic axis, the main results of this chapter also apply to the penetration of traditional up-down symmetric plasma shaping. Additionally, the following derivations are appropriate to treat the Shafranov shift, but it will not be investigated specifically. This is because it is formally small in aspect ratio and, in isolation, does not create up-down asymmetry. As we will explore in chapter 4, the Shafranov shift becomes up-down asymmetric when the flux surfaces already have an up-down asymmetric shape. Hence it can enhance existing up-down asymmetry, but cannot create asymmetry by itself.

The traditional argument concerning shaping penetration [28, 33, 34] uses a Taylor expansion of the poloidal flux about the magnetic axis to find

$$\begin{aligned} \psi(R, Z) \approx & \frac{1}{2} \left. \frac{\partial^2 \psi}{\partial R^2} \right|_{R_0, Z_0} (R - R_0)^2 + \left. \frac{\partial^2 \psi}{\partial R \partial Z} \right|_{R_0, Z_0} (R - R_0) (Z - Z_0) \\ & + \frac{1}{2} \left. \frac{\partial^2 \psi}{\partial Z^2} \right|_{R_0, Z_0} (Z - Z_0)^2, \end{aligned} \quad (3.1)$$

where Z_0 is the axial location of the magnetic axis. Here we have imposed that at the magnetic axis the poloidal flux vanishes and is at a minimum. This implies that the constant and linear terms in the Taylor expansion are zero. Hence, no matter what external fields shape the plasma, close enough to the magnetic axis the flux surface ellipticity will dominate over higher order shaping effects. This argument fails if all the second order Taylor coefficients are zero. However, very close to the magnetic axis the plasma current can be assumed to be constant (since the slope of the current must be zero on axis), so (2.21) must be a valid equilibrium in the region. Therefore, we see that, in order for the second order Taylor coefficients to vanish, the on-axis toroidal current density must be zero. This prevents closed, nested flux surfaces [35]. Thus, the case in which the second order Taylor coefficients vanish is uninteresting.

While the argument based on the Taylor expansion around the magnetic axis is compelling, it says nothing about how shaping behaves away from the magnetic axis or how triangularity penetrates in the absence of elongation. A more sophisticated version of this argument is presented in references [18, 33], which includes effects from having a linear toroidal current profile.

In section 3.1, we show that the shaping of a given flux surface depends on the magnitude of the poloidal variation of the poloidal magnetic field on the flux surface. Then, in section 3.2, we use this dependence to study why different flux surface shapes penetrate better than others. In section 3.3, we explore a limit of the Grad-Shafranov equation that separates the effects of magnetic pressure and tension. In this limit we clearly see how the current profile affects shaping penetration.

3.1 Quantifying shaping penetration

First, we will define the parameter

$$\Delta(a_\psi) \equiv \frac{b_\psi(a_\psi)}{a_\psi}, \quad (3.2)$$

where a_ψ is the minimum distance of the flux surface from the magnetic axis and b_ψ is the maximum distance of the flux surface from the magnetic axis. For circular flux surfaces without a Shafranov shift $\Delta = 1$. Since the definitions of a_ψ and b_ψ are based on the magnetic axis, $\Delta \neq 1$ for circular flux surfaces with a Shafranov shift. We note that Δ reduces to the typical definition of elongation (usually denoted by κ) when the flux surfaces are purely elliptical without a Shafranov shift.

Taking a derivative of (3.2) we find the change in Δ across a flux surface is given by

$$\frac{d\Delta}{da_\psi} = \frac{1}{a_\psi} \frac{db_\psi}{da_\psi} - \frac{b_\psi(a_\psi)}{a_\psi^2}. \quad (3.3)$$

The derivative db_ψ/da_ψ can be calculated from the poloidal magnetic flux,

$$\psi = \frac{1}{2\pi} \oint_{-\pi}^{\pi} d\zeta \int_0^r dr' R B_p. \quad (3.4)$$

We note that (3.4) is only valid along the integration path connecting the radial minimum on each flux surface, a_ψ , and the path connecting the radial maximum on each flux surface, b_ψ . This is because, at the flux surface radial extrema, the poloidal field is necessarily perpendicular to the usual cylindrical radial direction. Using implicit differentiation and evaluating on both of these integration paths, (3.4) gives

$$\frac{da_\psi}{d\psi} = \frac{1}{RB_p|_a} \quad (3.5)$$

$$\frac{db_\psi}{d\psi} = \frac{1}{RB_p|_b}. \quad (3.6)$$

Here $|_a$ and $|_b$ indicate the quantity should be evaluated at the poloidal locations of the minimum and maximum radial positions on a given flux surface. Therefore, we find that (3.3) becomes

$$\frac{a_\psi}{\Delta} \frac{d\Delta}{da_\psi} = \frac{1}{\Delta} \frac{RB_p|_a}{RB_p|_b} - 1, \quad (3.7)$$

which is only a consequence of geometry and the definition of the poloidal flux. In current experiments [32, 36, 37, 38] this quantity is generally between 0 and 0.3, but, as additional shaping is generally advantageous, the goal would be to make it as negative as possible. We will use (3.7) to understand why different flux surface shapes (elongated, triangular, etc.) penetrate better from the edge to the core and how the toroidal current profile affects this penetration.

3.2 Effect of flux surface shape

In this section we will compare different flux surface shapes and show that lower order shaping effects penetrate from the plasma boundary to the magnetic axis more effectively. First, we must determine which shapes to consider and argue that comparisons between them are fair. We will use large aspect ratio equilibria produced

with a constant toroidal current profile because it is a reasonable approximation of experimental profiles and the solutions are simple cylindrical harmonics given by (2.21). From these equilibria we will investigate each cylindrical harmonic shaping effect in isolation by creating strongly shaped flux surfaces, specifically those that approach having magnetic field nulls (see figure 3.1). These configurations are created by including only a single shaping mode m in (2.21) with the maximum possible value of Δ as calculated in appendix A. This Δ is given by the numerical solution of (A.2) and can be converted to the Fourier shaping coefficient using

$$N_{0,m} = \frac{\hat{j}_0}{4} \frac{\Delta^2 - 1}{\Delta^m + 1} a_\psi^{2-m}. \quad (3.8)$$

Equation (3.8) is a consequence of the definitions of a_ψ as well as Δ and can be derived from $\psi_0(a_\psi, -\theta_{tm}) = \psi_0(\Delta a_\psi, (\pi/m) - \theta_{tm})$ and (2.21). We also need to solve for the relationship between the poloidal flux and the minor radius, which can be found to be

$$\psi_0(a_\psi) = \frac{\hat{j}_0}{4} a_\psi^2 + N_{0,m} a_\psi^m \quad (3.9)$$

from (2.21) and the definition of a_ψ . These configurations will be analytically tractable and exaggerate the effects we mean to investigate. It should be noted that we expect flux surfaces with higher order shaping to be more difficult to create experimentally. This is because they have more magnetic field nulls, so they require more poloidal shaping magnets and more total external current to create.

From Ampere's law we find that $RB_p|_a \approx (S_p/L_p) \mu_0 j_\zeta R$ is a finite quantity, where S_p is the poloidal area enclosed by the flux surface and L_p is the poloidal perimeter. Additionally, we note that $RB_p|_b$ approaches zero because we have chosen configurations that nearly have magnetic nulls. This reveals that, as the flux surface shaping is increased, the ratio of poloidal fields in (3.7) diverges to positive infinity. This implies that $d\Delta/da_\psi$ is positive and large, i.e. it will be impossible to maintain strong shaping from the boundary to the magnetic axis. While this is true for nearly all configurations, there is one caveat: when the shaping parameter Δ also diverges to infinity. Then, $d\Delta/da_\psi$ can be finite and negative. This makes the $m = 2$ cylindrical harmonic shaping effect special because flux surfaces with arbitrarily large elongation are possible. Additionally, the $m = 1$ mode is an exception as it is impossible to create magnetic field nulls with a pure Shafranov shift. However, all pure shaping effects above $m = 2$ cannot make flux surfaces that are both closed and have arbitrarily large shaping.

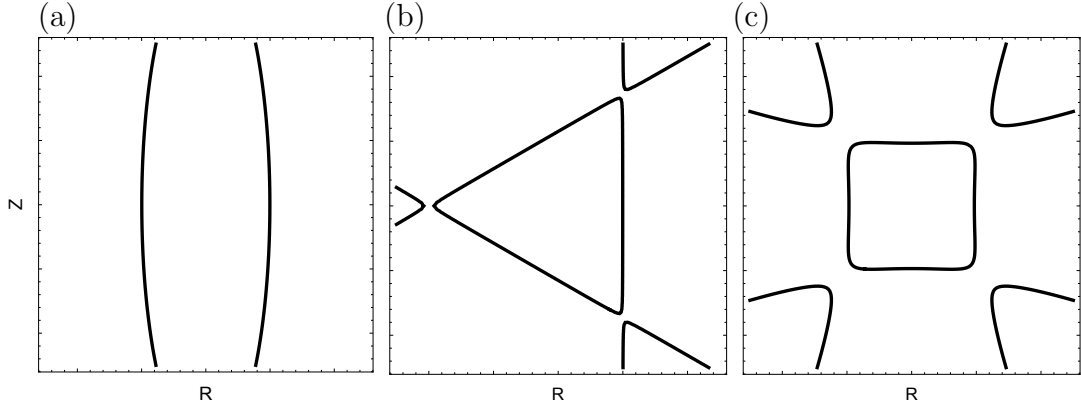


Figure 3.1: The (a) $m = 2$, (b) $m = 3$, and (c) $m = 4$ strongly shaped flux surface shapes.

Lastly, we note that (3.8) directly determines how different flux surface shaping effects penetrate radially (given a constant current profile). In general, solving (3.8) for $\Delta(a_\psi)$ cannot be done analytically, but after expanding to lowest order in $\Delta - 1 \ll 1$ we find that

$$\Delta - 1 = (\Delta_b - 1) \rho^{m-2}, \quad (3.10)$$

where Δ_b is the shaping parameter of the outermost flux surface, $\rho \equiv a_\psi/a$ is the usual normalised minor radial coordinate, and a is the tokamak minor radius (i.e. a_ψ of the outermost flux surface). From this we see that, to lowest order in aspect ratio, a constant current profile does not alter the externally applied elongation [18, 33, 39] (meaning that $d\Delta/da_\psi = 0$). Furthermore, we see that all higher order shaping effects have exponentially poor radial penetration in m . Therefore, elongation will penetrate throughout the plasma better than all higher order shaping modes.

3.3 Effect of the toroidal current profile

As we compare configurations with different toroidal current profiles, we will choose to keep the external flux surface shape fixed. Therefore, from (3.7) we conclude that changing the current profile, while maintaining a constant boundary flux surface shape, only affects the shaping penetration by altering $RB_p|_a / RB_p|_b$.

In order to calculate the ratio of the poloidal fields we will start with the toroidal component of Ampere's law,

$$(\vec{\nabla} \times \vec{B}) \cdot \hat{e}_\zeta = \mu_0 j_\zeta. \quad (3.11)$$

Noting that $\vec{B} = I\vec{\nabla}\zeta + \vec{B}_p$, we see that

$$\left(\vec{\nabla} \times \vec{B}_p\right) \cdot R\vec{\nabla}\zeta = \mu_0 j_\zeta. \quad (3.12)$$

Since $\vec{B}_p = \vec{\nabla}\zeta \times \vec{\nabla}\psi$, we know that $\vec{\nabla}\zeta = \vec{\nabla}\psi \times \vec{B}_p / \left|\vec{\nabla}\psi\right|^2$. Making this substitution and using a number of vector identities on the quantity $\vec{B}_p \times \left(\vec{\nabla} \times \vec{B}_p\right)$ we find that

$$R \frac{\vec{\nabla}\psi}{\left|\vec{\nabla}\psi\right|^2} \cdot \left(\vec{\nabla} \vec{B}_p\right) \cdot \vec{B}_p - \frac{RB_p^2}{\left|\vec{\nabla}\psi\right|^2} \hat{b}_p \cdot \left(\vec{\nabla} \hat{b}_p\right) \cdot \vec{\nabla}\psi = \mu_0 j_\zeta, \quad (3.13)$$

where $\hat{b}_p \equiv \vec{B}_p/B_p$ is the poloidal field unit vector. Using the definition of the poloidal field curvature,

$$\kappa_p \equiv -\left(\hat{b}_p \cdot \vec{\nabla} \hat{b}_p\right) \cdot \frac{\vec{\nabla}\psi}{\left|\vec{\nabla}\psi\right|}, \quad (3.14)$$

together with $\vec{\nabla}\psi = RB_p \hat{e}_\psi$ gives

$$\frac{R}{2} \frac{\vec{\nabla}\psi}{\left|\vec{\nabla}\psi\right|^2} \cdot \vec{\nabla} (B_p^2) + B_p \kappa_p = \mu_0 j_\zeta, \quad (3.15)$$

a rearranged form of (2.2), the Grad-Shafranov equation. We choose this form because it clearly separates the effects of poloidal magnetic pressure in the first term and field line tension in the second, while the right hand side is constant on a flux surface to lowest order in aspect ratio. Equation (3.15) is a different way to express the conclusion reached in reference [39]: in non-circular flux surfaces, the current profile determines the gradient of the shaping. We can determine the poloidal magnetic field from the current profile using (3.15), which can then be related to the gradient of the shaping through (3.7).

We apply (3.15) to strongly shaped flux surfaces, which causes the first and second terms to vary dramatically with the poloidal location. We will assume that, at the poloidal location of the minimum radial position, the field lines become straight and the curvature term vanishes. Additionally, since the poloidal derivative necessarily vanishes at this location, the gradient can be converted according to the chain rule as

$$\vec{\nabla} (B_p^2) \Big|_a = \vec{\nabla}\psi \Big|_a \frac{da_\psi}{d\psi} \frac{d}{da_\psi} \left(B_p^2 \Big|_a \right). \quad (3.16)$$

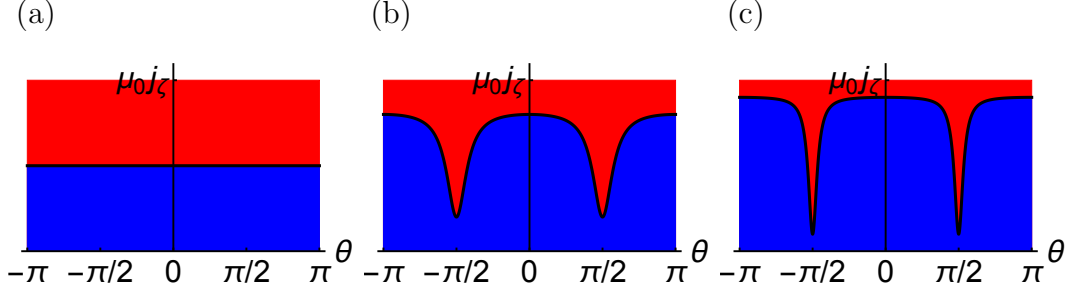


Figure 3.2: A stacked area graph showing, to lowest order in aspect ratio, the contributions of the magnetic pressure (blue, below the curve) and tension (red, above the curve) terms from (3.15) on an elongated flux surface with (a) $\Delta = 1$, (b) $\Delta = 2$, and (c) $\Delta = 3$.

Then (3.5) and (3.15) can be used to find

$$B_p|_a = \mu_0 \int_0^{a_\psi} da'_\psi j_\zeta|_a(a'_\psi). \quad (3.17)$$

Furthermore, we assume that, at the poloidal location of the maximum radial position, the magnetic pressure term is small, giving

$$B_p|_b = \frac{\mu_0 j_\zeta}{\kappa_p} \Big|_b \quad (3.18)$$

from (3.15). The integral in (3.17) assumes that the separation between magnetic pressure and tension must be valid over the entire radial profile, not just on the flux surface of interest. If the flux surfaces are circular over a substantial region near the axis, (3.17) is no longer accurate. For the $m = 2$ mode with a constant current profile, (3.17) and (3.18) are exact in the limits of $\Delta \rightarrow \infty$ and $\epsilon \rightarrow 0$ (see figure 3.2). This is because, in these conditions, the flux surface exactly maintains its shape as it penetrates the plasma [18, 33, 39]. One can use an exact solution (given by (2.18)) to estimate that (3.17) and (3.18) are only accurate to about 20% for a linear peaked current profile with $\hat{f}_0 \psi_{0b} = 0.2$ and an elongation of $\Delta = 2$. These equations are not exact for other shaping modes, but we will keep the derivation completely general because approximate results may still be useful and other exact limits may exist for different current profiles.

Substituting (3.17) and (3.18) into (3.7) we find that

$$\frac{a_\psi}{\Delta} \frac{d\Delta}{da_\psi} = \frac{\kappa_p|_b}{\Delta} \frac{R|_a \int_0^{a_\psi} da' j_\zeta|_a(a'_\psi)}{R|_b j_\zeta|_b} - 1. \quad (3.19)$$

Since we are considering a fixed flux surface shape, we can solve for the required current profile properties to locally permit the shape to penetrate (i.e. $d\Delta/da_\psi = 0$) and find

$$\frac{\kappa_p|_b}{\Delta} = \frac{R|_b j_{\zeta c}|_b}{R|_a \int_0^a da'_\psi j_{\zeta c}|_a(a'_\psi)}. \quad (3.20)$$

Here $j_{\zeta c}$ is any toroidal current density profile that ensures $d\Delta/da_\psi = 0$ locally. We are guaranteed that a solution to (3.20) exists for every boundary flux surface shape because, by different choices of $j_{\zeta c}$, we can make the right-hand side span the full range of $[0, \infty)$. Furthermore, due to the integral, this requirement can be satisfied by many different profiles.

Solving for this constant shape penetration case is useful because we are comparing configurations holding the flux surface shape constant, so both $\kappa_p|_b$ and Δ will stay fixed. Substituting (3.20) into (3.19), we find that

$$\frac{a_\psi}{\Delta} \frac{d\Delta}{da_\psi} = \frac{j_{\zeta c}|_b}{j_\zeta|_b} \frac{\int_0^{a_\psi} da'_\psi j_\zeta|_a(a'_\psi)}{\int_0^{a_\psi} da'_\psi j_{\zeta c}|_a(a'_\psi)} - 1. \quad (3.21)$$

By normalising this equation, we see that the total plasma current can be scaled without changing the flux surface shapes (by scaling the external currents accordingly). In other words, we can multiply $j_{\zeta c}$ or j_ζ by any numerical factor without changing any flux surface shapes. Equation (3.21) is a differential equation for $\Delta(a_\psi)$, which can be solved giving

$$\frac{\Delta(a_\psi)}{\Delta_b} = \exp \left(- \int_{a_\psi}^a da'_\psi \frac{1}{a'_\psi} \left(\frac{j_{\zeta c}|_b(a'_\psi)}{j_\zeta|_b(a'_\psi)} \frac{\int_0^{a'_\psi} da''_\psi j_\zeta|_a(a''_\psi)}{\int_0^{a'_\psi} da''_\psi j_{\zeta c}|_a(a''_\psi)} - 1 \right) \right). \quad (3.22)$$

This equation gives the radial profile of the flux surface shaping, but it is only exact when the separation of the two terms in (3.15) is valid over the entire radial profile. For example, elongated flux surfaces with a linear current profile defined by (2.8) have an exact solution in the limits that $\hat{f}_0 \ll 1$, $\epsilon \rightarrow 0$, and $\Delta_b \gg 1$. Using these limits, we can simplify (3.22) to

$$\frac{\Delta(\rho)}{\Delta_b} = 1 + \frac{a^2}{6} \hat{f}_0 \hat{j}_0 (1 - \rho^2). \quad (3.23)$$

Figure 3.3 shows good agreement between this simple quadratic profile, (3.22), and the exact numerical solution calculated from (2.18).

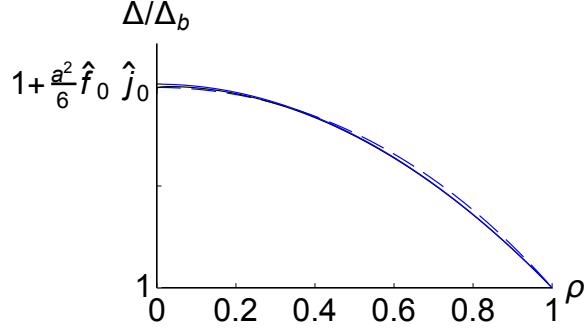


Figure 3.3: The exact radial shaping profile (black, solid) along with (3.22) (blue, dashed) and (3.23) (blue, solid), which are nearly indistinguishable, for elongated flux surfaces in the limit that $\hat{f}_0 \ll 1$, $\epsilon \rightarrow 0$, and $\Delta_b \gg 1$.

Since $j_{\zeta c}$ can be scaled arbitrarily, (3.21) can be further simplified by choosing $j_{\zeta c}|_b$ to be $j_{\zeta}|_b$, the toroidal current on the flux surface of interest, giving

$$\frac{\rho}{\Delta} \frac{d\Delta}{d\rho} = \frac{\int_0^\rho d\rho' j_{\zeta}|_a(\rho')}{\int_0^\rho d\rho' j_{\zeta c}|_a(\rho')} - 1 \quad (3.24)$$

at a specific radial location. This shows that the shaping penetration only depends on the amount of toroidal current within the flux surface compared with the constant shape penetration case. Profiles that are more hollow will help shaping penetrate into the plasma. What happens is, as the on-axis current is lowered, the shaping and $RB_p|_b$ stay constant (maintained by the external magnets), while $RB_p|_a$ decreases because of the drop in the total plasma current. From (3.7) we see that a change in the ratio of these magnetic fields allows the shaping to penetrate radially. Analogously, peaked current profiles will tend to limit the shaping to the edge. In figure 3.4, we plot (2.18) for different boundary conditions and values of \hat{f}_0 . From figure 3.4(a,b,c), we see that achieving an on-axis elongation of 2 with a peaked current profile requires a 25% greater edge elongation than it would with a hollow profile. Figure 3.4(d,e,f) shows that triangular flux surface shaping is only large near the boundary, as would be expected from the arguments in both the introduction to this chapter and section 3.2. However, we still observe that the shaping penetrates more effectively with a hollow current profile, relative to a peaked profile. This, along with (3.24), suggests that the beneficial effect of hollow current profiles for shaping penetration is general to all flux surface shapes (see references [18, 33] for a different approach to the same problem). Numerical evidence of this using EFIT equilibrium reconstruction on simulated experimental data can be seen in figure 5(b) of reference [32].

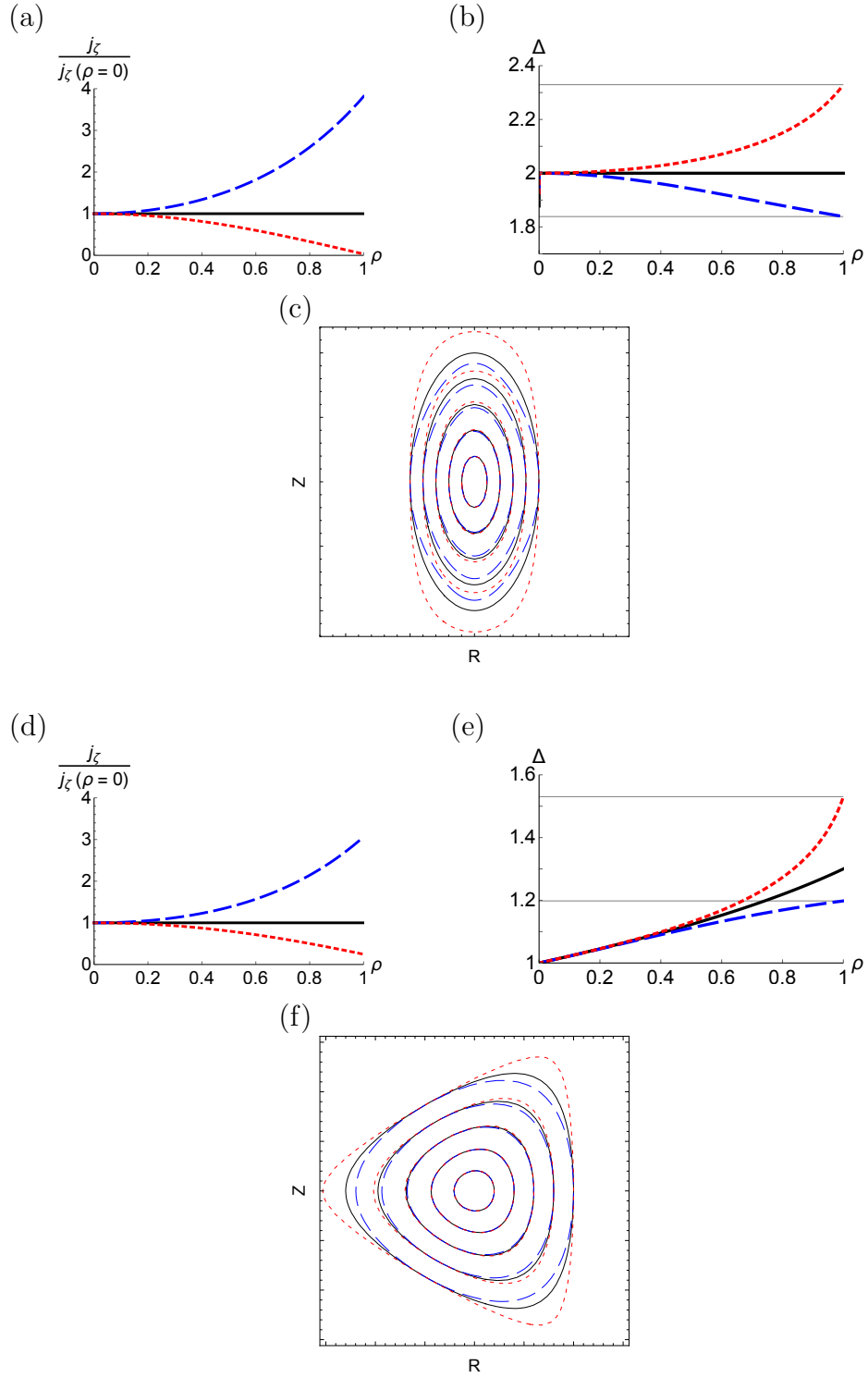


Figure 3.4: The (a,d) normalised radial current profile, (b,e) flux surface shapes, and (c,f) shaping profile for solutions to the Grad-Shafranov equation to lowest order in aspect ratio with constant (black, solid), hollow (blue, dashed), and peaked (red, dotted) toroidal current profiles with (a,b,c) elongated or (d,e,f) triangular boundary conditions.

Chapter 4

Global equilibria with a Shafranov shift and tilted elliptical boundary

Much of this chapter appears in reference [22].

In order to model a realistic Shafranov shift we must know how it depends on the free parameters that appear in the next order (in large aspect ratio) Grad-Shafranov equation: the boundary flux surface, the current profile, and the pressure profile. We will restrict our investigation to using a tilted elliptical boundary because the MHD analysis in chapter 3 suggests that low modes penetrate most effectively. We will explicitly calculate how the Shafranov shift depends on the tilt angle of the elliptical boundary flux surface (parameterized by $\theta_{\kappa b}$). We will argue that the Shafranov shift is insensitive to the shape of the current and pressure profiles (parameterized by \hat{f}_0 and \hat{f}_{0p} respectively) when the geometry, plasma current, and average $dp/d\psi$ is kept fixed. Doing so makes the gyrokinetic simulations presented in chapter 9 more widely applicable, as they use equilibria derived assuming constant current and pressure gradient profiles. In order to accomplish this, we require a general solution for the magnitude and direction of the Shafranov shift in tokamaks with a tilted elliptical boundary as well as linear current and pressure gradient profiles.

Together (2.18), (2.24), (2.26) through (2.29), and (2.30) give this general solution to $O(\epsilon B_0)$, which is sufficient to capture the behaviour of the Shafranov shift. However, we still must determine the Fourier coefficients $N_{0,m}$, $\theta_{t0,m}$, $C_{1,m}$, and $S_{1,m}$ in order to create a tilted elliptical boundary flux surface. To do so we require the poloidal flux to be constant on the boundary, parameterized in polar form by

$$r_b(\theta) = \frac{\sqrt{2}\kappa_b a}{\sqrt{\kappa_b^2 + 1 + (\kappa_b^2 - 1) \cos(2(\theta + \theta_{\kappa b}))}}, \quad (4.1)$$

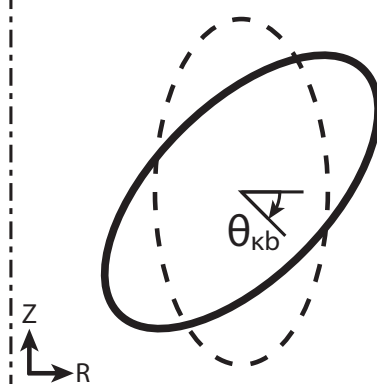


Figure 4.1: The boundary flux surface specified by (4.1) for two values of the boundary elongation tilt angle, $\theta_{\kappa b} = \pi/4$ (solid) and $\theta_{\kappa b} = 0$ (dotted), where the axis of axisymmetry is indicated by a dash-dotted line.

where κ_b is the elongation of the boundary flux surface, $\theta_{\kappa b}$ is the boundary tilt angle, and a is the tokamak minor radius (i.e. the minor radial position of the boundary flux surface at $\theta = -\theta_{\kappa b}$).

4.1 Solution to the $O(B_0)$ Grad-Shafranov equation for a tilted elliptical boundary condition

To calculate $N_{0,m}$ and $\theta_{t0,m}$ we substitute (4.1) into (2.18) to give

$$\psi_0(r_b(\theta), \theta) = \psi_{0b}, \quad (4.2)$$

where ψ_{0b} is the value of the poloidal flux on the plasma boundary. Since ψ_{0b} is a constant we know that $\psi_0(r_b(\theta), \theta)$ does not depend on θ . In theory, ensuring that this is true for all values of θ determines all of the lowest order Fourier coefficients. However, the exact solution for these coefficients is not analytic, so we will resort to a numerical solution. Before we do so we will note that, because the lowest order Grad-Shafranov equation has cylindrical symmetry, the only angle intrinsic to the problem is $\theta_{\kappa b}$, which is introduced by the boundary condition. This implies that

$$\theta_{t0,m} = \theta_{\kappa b} \quad (4.3)$$

for all m , which suggests that it will be useful to define a new poloidal angle

$$\theta_s \equiv \theta + \theta_{\kappa b}. \quad (4.4)$$

Furthermore, since an ellipse has mirror symmetry about exactly two axes, we know that $N_{0,m} = 0$ for odd m .

To determine $N_{0,m}$ for even m we will take the Fourier series of $\psi_0(r_b(\theta_s), \theta_s) - \psi_{0b}$. Truncating the series at a large mode number m_{\max} gives a long series of cosine terms. Requiring that the coefficient of each term must individually vanish gives a numerical approximation for all $N_{0,m}$ with $m \leq m_{\max}$. In the limit that $m_{\max} \rightarrow \infty$ this approximation approaches the exact solution, though in practice $m_{\max} \approx 10$ was found to achieve sufficient precision for our purposes. This was determined by visually assessing how well the solution matched the boundary condition at the plasma edge.

4.2 Solution to the $O(\epsilon B_0)$ Grad-Shafranov equation for a tilted elliptical boundary condition

To next order we must determine $C_{1,m}$ and $S_{1,m}$ such that

$$\psi_1(r_b(\theta), \theta) = \psi_{1b} \quad (4.5)$$

is true, where ψ_{1b} is the next order value of the poloidal flux on the boundary flux surface. This is done in a similar manner to the lowest order equations, except the Grad-Shafranov equation no longer has cylindrical symmetry and we must evaluate the integral in (2.30). The lack of symmetry means that we do not automatically know the tilt angle of the modes. However, since ψ_0 only has even Fourier mode numbers, it can be shown that (2.7) only has odd Fourier modes. Hence, $C_{1,m} = S_{1,m} = 0$ for even m .

To calculate $C_{1,m}$ and $S_{1,m}$ for odd m we take $\psi_1(r, \theta)$ from (2.24) and Taylor expand in $\hat{f}_0 \hat{j}_0 a^2 \ll 1$ to $O\left(\left(\hat{f}_0 \hat{j}_0 a^2\right)^{f_{\max}}\right)$. This allows us to analytically calculate the integrals appearing in (2.30) because the Bessel functions become summations of polynomials. We can now substitute (4.1) and find the Fourier series of $\psi_1(r_b(\theta), \theta) - \psi_{1b}$ to mode number m_{\max} . Again, we require that all of the Fourier coefficients must individually vanish, which produces a numerical approximation for each $C_{1,m}$ and $S_{1,m}$ with $m \leq m_{\max}$. A value of $f_{\max} \approx 10$ was found to give a sufficiently accurate solution.

For a hollow current profile, we repeat the entire above process except for using (2.23) instead of (2.18) and (2.32) instead of (2.30). While the above process also works for the case of a constant toroidal current profile, it has an analytic solution, which we derive in appendix B.

In order to understand the effect of changing the current and pressure profiles in a single experimental device, we will choose to keep the major radial location of the centre of the boundary flux surface (R_{0b}), the minor radius (a), the edge elongation (κ_b), the total plasma current (I_p), and an estimate of the average pressure gradient ($p_{\text{axis}}/\psi_{0b}$, i.e. the on-axis pressure divided by the lowest order edge poloidal flux) fixed. In order to keep these parameters fixed as we change the current and pressure profiles we must calculate how they enter into both \hat{j}_0 and \hat{j}_{0p} . Calculating \hat{j}_{0p} is straightforward, as we can directly integrate (2.9) over poloidal flux to find

$$\hat{j}_{0p} = \mu_0 R_{0b}^2 \frac{p_{\text{axis}}}{\psi_{0b}} \left(1 - \frac{\hat{f}_{0p} \psi_{0b}}{2} \right)^{-1}. \quad (4.6)$$

To calculate \hat{j}_0 we start with the definition of the plasma current,

$$I_p \equiv \int dS j_\zeta = \int_0^{2\pi} d\theta_s \int_0^{r_b(\theta_s)} dr j_\zeta r, \quad (4.7)$$

where S is the poloidal cross-sectional surface. Since we are only searching for a simple estimate, we will use (2.8) to rewrite (4.7) as

$$I_p = \int_0^{2\pi} d\theta_s \int_0^{r_b(\theta_s)} dr \frac{\hat{j}_0}{\mu_0 R_{0b}} \left(1 - \hat{f}_0 \psi_0 \right) r, \quad (4.8)$$

which is accurate to lowest order in aspect ratio. Substituting the boundary shape (i.e. (4.1)) and the constant current solution for $\psi_0(r, \theta_s)$ (i.e. (2.21), (4.3), (B.1), and (B.2)) allows us to directly take the integral to find

$$\hat{j}_0 = \mu_0 \frac{I_p}{\pi a^2 \kappa_b} R_{0b} \left(1 - \frac{\hat{f}_0 \psi_{0b}}{2} \right)^{-1} + O\left(\hat{f}_0^2 \hat{j}_0^2 a^4\right). \quad (4.9)$$

The $O\left(\hat{f}_0^2 \hat{j}_0^2 a^4\right)$ error arises from the fact that we used the constant current solution for $\psi_0(r, \theta_s)$, which is only accurate to lowest order in $\hat{f}_0 \hat{j}_0 a^2 \ll 1$. This means that as we change \hat{f}_{0p} and \hat{f}_0 we must change \hat{j}_{0p} and \hat{j}_0 according to (4.6) and (4.9) respectively.

In figure 4.2 we plot the calculated flux surfaces resulting from three different current profiles, setting $\hat{f}_{0p} = \hat{f}_0$. We use inputs of

$$R_{0b} = 3, \quad a = 1, \quad \kappa_b = 2, \quad (4.10)$$

(we have normalised all lengths to the minor radius), and

$$\frac{\hat{j}_{0p}}{\hat{j}_0} \approx \frac{\pi a^2 \kappa_b R_{0b}}{I_p} \frac{p_{\text{axis}}}{\psi_{0b}} \approx 0.7 \quad (4.11)$$

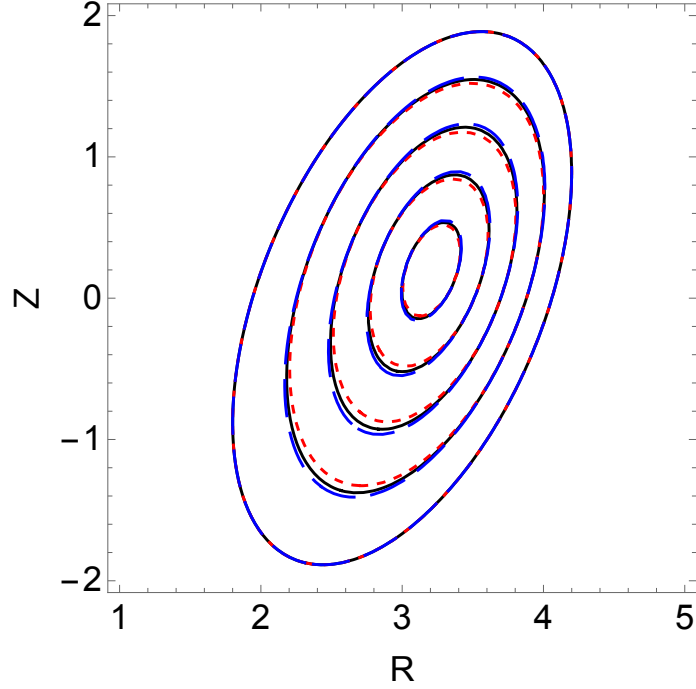


Figure 4.2: Calculated flux surfaces for $\hat{f}_0\psi_{0b} = \hat{f}_{0p}\psi_{0b} = 0$ (black, solid), $\hat{f}_0\psi_{0b} = \hat{f}_{0p}\psi_{0b} = 0.4$ (red, dotted), and $\hat{f}_0\psi_{0b} = \hat{f}_{0p}\psi_{0b} = -0.4$ (blue, dashed).

(from projections for ITER [15]). Additionally, we choose to plot the case of $\theta_{\kappa b} = \pi/8$ because nonlinear gyrokinetic simulations have shown this value to be optimal for generating rotation (see figure 9.2 and reference [18]). Note that the ψ_{0b} appearing in (4.11) is part of $p_{\text{axis}}/\psi_{0b}$, so it is fixed for all three profiles and can be calculated for a constant current profile from (B.1). In figure 4.2 we see that the current profile has an effect on the penetration of elongation from the boundary to the magnetic axis. This indicates that hollower current profiles better support elongation throughout the plasma, which is consistent with the results of chapter 3 as well as previous work [18, 33]. However, given these parameters, the Shafranov shift is not visibly altered, even with the significant changes to the current profile.

In order to verify our calculation, we compared our results with the ECOM code [40], a fixed boundary equilibrium solver capable of modelling up-down asymmetric configurations. In figure 4.3 we see a direct graphical comparison between ECOM and the results of our calculation that were shown in figure 4.2. The two sets of results agree well, especially for the constant and hollow current profile cases. We believe that the most significant source of error is finite aspect ratio effects in our analytic calculation, which arise from the assumption that $\epsilon = 1/3 \ll 1$. Hence, formally we would only expect the analytic calculation to be accurate to about $\epsilon^2 \sim 10\%$.

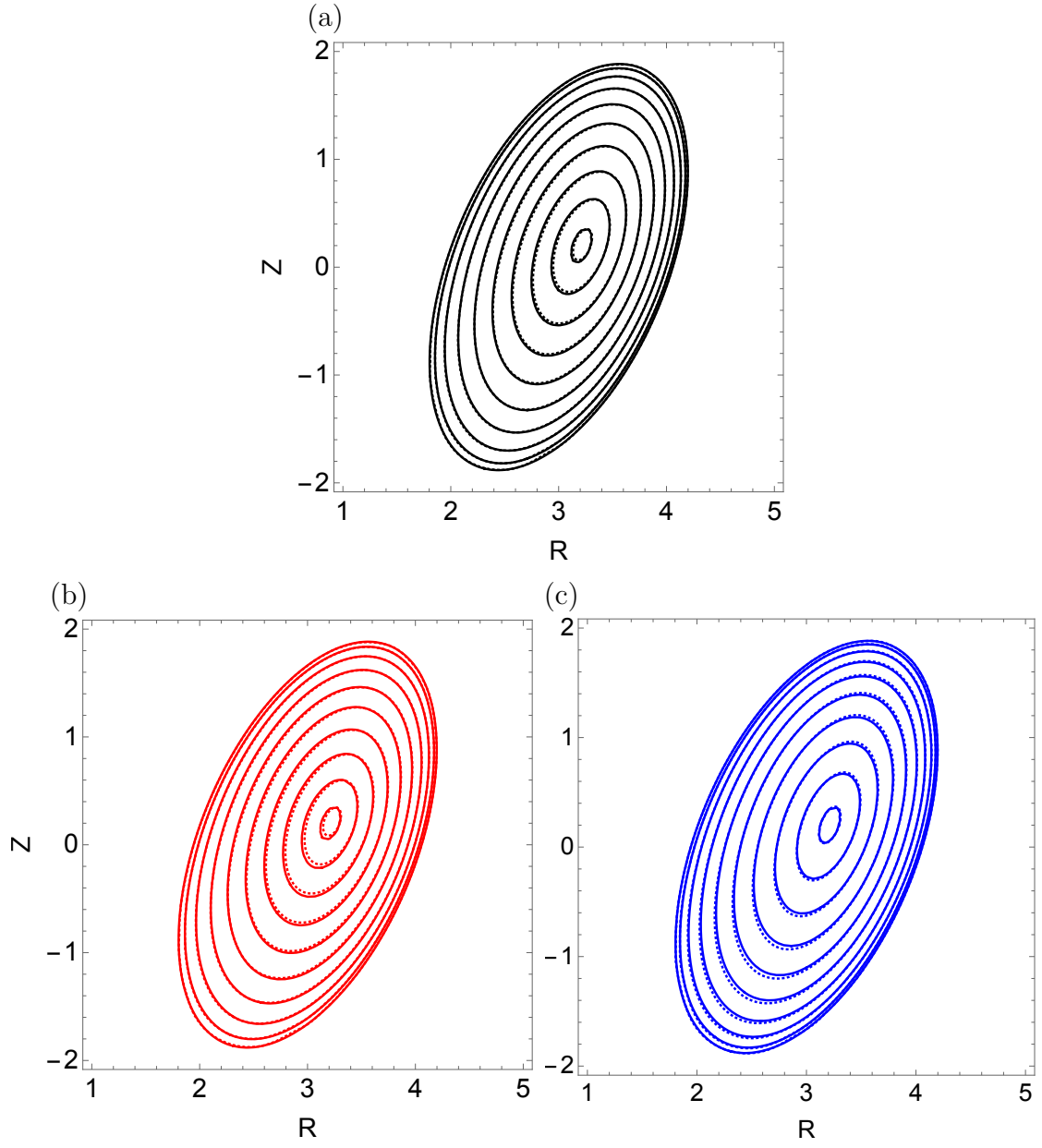


Figure 4.3: Flux surfaces calculated by both ECOM (dotted) and analytically (solid) for (a) $\hat{f}_0\psi_{0b} = \hat{f}_{0p}\psi_{0b} = 0$ (black), (b) $\hat{f}_0\psi_{0b} = \hat{f}_{0p}\psi_{0b} = 0.4$ (red), and (c) $\hat{f}_0\psi_{0b} = \hat{f}_{0p}\psi_{0b} = -0.4$ (blue).

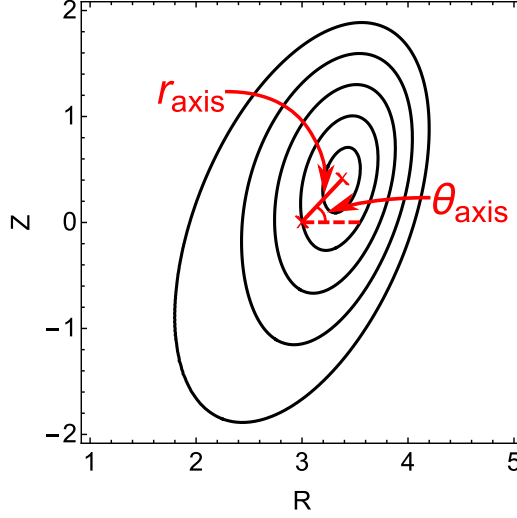


Figure 4.4: Example flux surfaces showing the geometric meaning of the parameters r_{axis} and θ_{axis} , the minor radial and poloidal locations of the magnetic axis respectively.

4.3 Location of the magnetic axis

We can obtain the Shafranov shift from our calculation by numerically solving the equation

$$\vec{\nabla}(\psi_0(r, \theta) + \psi_1(r, \theta)) \Big|_{r=r_{\text{axis}}, \theta=\theta_{\text{axis}}} = 0 \quad (4.12)$$

using (2.18), (2.24), (2.26) through (2.29), (2.30), and (4.3) as well as our numerical solutions for $N_{0,m}$, $C_{1,m}$, and $S_{1,m}$. Here r_{axis} and θ_{axis} are the minor radial and poloidal location of the magnetic axis respectively, as indicated in figure 4.4. For the special case of a tilted elliptical boundary with a constant toroidal current profile (i.e. $\hat{f}_0 = 0$) we can exactly solve (4.12) as shown in appendix B. Equations (B.15) and (B.16) give the exact location of the magnetic axis when considering the poloidal flux to lowest order and next order in $\epsilon \ll 1$.

In figure 4.5 we show the location of the magnetic axis for different boundary tilt angles as we vary the shape of the current/pressure profile (by changing \hat{f}_0 and keeping $\hat{f}_{0p} = \hat{f}_0$). In this scan we hold the geometry, I_p , and $p_{\text{axis}}/\psi_{0b}$ fixed at the values determined by (4.10) and (4.11). For the most part, we see reasonable quantitative agreement between our theoretical results and ECOM. However, the trend of r_{axis} with $\hat{f}_0\psi_{0b}$ at large tilt angles is inconsistent between the two calculations. This appears to be a breakdown in our inverse aspect ratio expansion as the analytical calculation and ECOM become consistent at smaller tilt angles (where the effective aspect ratio is larger) and if the aspect ratio is directly increased. An important property of

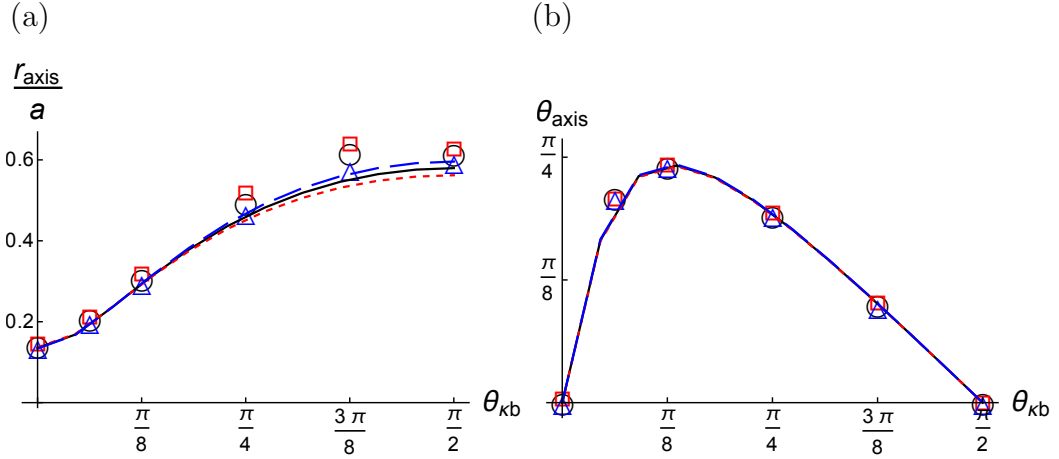


Figure 4.5: The (a) minor radial and (b) poloidal location of the magnetic axis for constant ($\hat{f}_0\psi_{0b} = \hat{f}_{0p}\psi_{0b} = 0$) (black, solid, circles), linear peaked ($\hat{f}_0\psi_{0b} = \hat{f}_{0p}\psi_{0b} = 0.4$) (red, dotted, squares), and linear hollow ($\hat{f}_0\psi_{0b} = \hat{f}_{0p}\psi_{0b} = -0.4$) (blue, dashed, triangles) current/pressure gradient profiles, calculated analytically (lines) and by ECOM (points).

figure 4.5, which is supported by both the analytic and ECOM calculations, is the insensitivity of the Shafranov shift to significant changes in the shape of the current profile. Both the magnitude and the direction of the Shafranov shift change very little between the different current profiles. This is especially true in the domain of $\theta_{\text{kb}} \in [0, \pi/4]$, which is the range of tilt angles that seem most promising for implementing in an experiment [17, 18]. This means that, even though we will only run gyrokinetic simulations of equilibria with constant current and pressure gradient profiles, we expect the Shafranov shift to have a similar effect in equilibria with other profiles.

Conversely, we see that the boundary elongation tilt angle has a large effect, not just on the direction of the Shafranov shift, but also its magnitude. This is intuitive because we know that, for an ellipse with $\kappa = 2$, the midplane chord length is twice as long in the $\theta_{\text{kb}} = \pi/2$ geometry as it is in the $\theta_{\text{kb}} = 0$ geometry. Lastly, we see that the direction of the Shafranov shift varies considerably, but it is purely outwards for the 0 and $\pi/2$ tilt angles as expected. We note that (except at $\theta_{\text{kb}} = 0$ and $\theta_{\text{kb}} = \pi/2$) it does not align with the lines of symmetry of the ellipse, so it breaks the mirror symmetry of the configuration.

In figure 4.6 we show the location of the magnetic axis as we vary the shape of the pressure profile (by changing \hat{f}_{0p}) with a constant current profile (i.e. $\hat{f}_0 = 0$), while holding the geometry, I_p , and $p_{\text{axis}}/\psi_{0b}$ fixed. We see good quantitative agreement

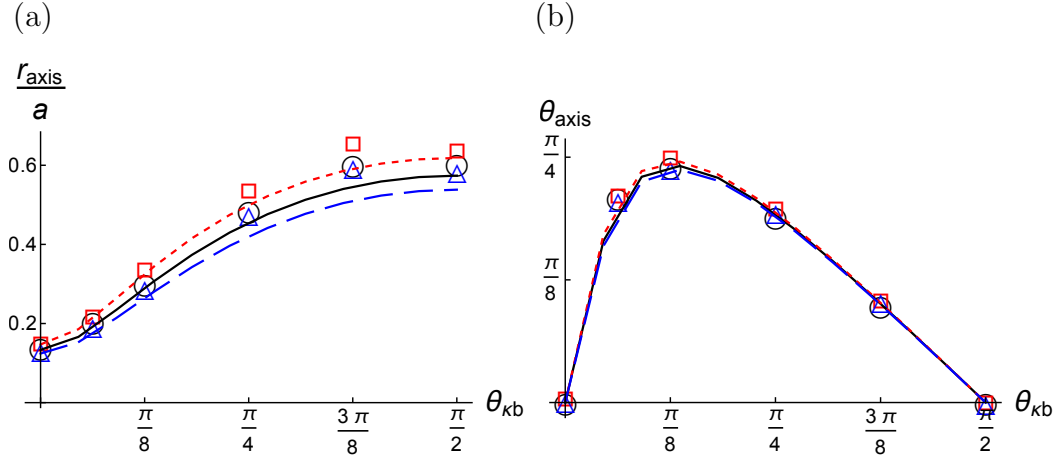


Figure 4.6: The (a) minor radial and (b) poloidal location of the magnetic axis for constant ($\hat{f}_{0p}\psi_{0b} = 0$) (black, solid, circles), linear peaked ($\hat{f}_{0p}\psi_{0b} = 0.4$) (red, dotted, squares), and linear hollow ($\hat{f}_{0p}\psi_{0b} = -0.4$) (blue, dashed, triangles) pressure gradient profiles, calculated analytically (lines) and by ECOM (points) for a constant current profile.

between the results of appendix B and ECOM. Additionally, it appears that varying the profile of the pressure gradient while holding its average fixed has little effect on the Shafranov shift. We note that, in general, varying the pressure gradient has a large effect on the magnitude of the Shafranov shift, but not when I_p and $p_{\text{axis}}/\psi_{0b}$ are held constant. This is important as it justifies using our MHD results for the Shafranov shift with a constant $dp/d\psi$ profile as input for gyrokinetic simulations that are based on ITER, which we will take to have a constant dp/dr_ψ profile [15]. Even though this is formally inconsistent, our analysis suggests the Shafranov shift in a configuration with constant $dp/d\psi$ will be a reasonable estimate of the Shafranov shift in a configuration with constant dp/dr_ψ (as long as the geometry, I_p , and $p_{\text{axis}}/\psi_{0b}$ are the same).

Chapter 5

Derivation of local Miller equilibria

Much of this chapter appears in references [22] and [41].

In this chapter we will take the simple, but physical large aspect ratio global MHD equilibria found in chapters 2 and 4 and derive the corresponding Miller local equilibria [42] for use in gyrokinetic simulations. The Miller local equilibrium model includes the shape of the flux surface of interest as an input and also requires the radial derivative of the flux surface shape in order to calculate the local poloidal field. We will derive two distinct local equilibrium specifications from the lowest order constant current global equilibrium. The first, the “Expanded” specification, is a simple Fourier series useful for analytic calculations. The second, the “Exact” specification, is more appropriate for creating realistic flux surface shapes for use in gyrokinetic simulations. These specifications can produce arbitrary flux surface shaping, which is specified by an infinite series of modes with independent tilt angles θ_{tm} . Then, we will calculate the local Shafranov shift from the constant current global equilibrium assuming a constant $dp/d\psi$ profile and a tilted elliptical boundary flux surface.

5.1 Specification of arbitrary flux surface shaping

To calculate the lowest order Miller local equilibrium, we will start with

$$\psi_0(r, \theta) = \frac{\hat{j}_0}{4} r^2 + N_{0,m} r^m \cos(m(\theta + \theta_{t0,m})), \quad (5.1)$$

which is just the constant current global equilibrium (i.e. (2.21)) when considering only one shaping mode m . We will define a new parameter

$$\Delta_m(a_{\psi,m}) \equiv \frac{b_{\psi,m}(a_{\psi,m})}{a_{\psi,m}}, \quad (5.2)$$

which is similar to (3.2), but quantifies the magnitude of flux surface shaping from each poloidal shaping effect m in isolation. Here $a_{\psi,m}$ is the minimum distance of the flux surface from the magnetic axis if all other shaping modes are ignored in (2.13). Similarly, $b_{\psi,m}$ is the maximum distance of the flux surface from the magnetic axis if all other shaping modes are ignored. For circular flux surfaces without a Shafranov shift $\Delta_m = 1$ for all m . Since the definitions of $a_{\psi,m}$ and $b_{\psi,m}$ are based on the magnetic axis, $\Delta_1 \neq 1$ for circular flux surfaces with a Shafranov shift. We note that Δ_2 is the typical definition of the elongation usually denoted by κ . The parameter Δ_m can be related to the Fourier coefficients used in chapter 2 by substituting (5.1) into $\psi_0(a_{\psi,m}, -\theta_{t0,m}) = \psi_0(\Delta_m a_{\psi,m}, (\pi/m) - \theta_{t0,m})$. For a constant current profile this gives the relation

$$N_{0,m} = \frac{\hat{j}_0}{4} \frac{\Delta_m^2 - 1}{\Delta_m^m + 1} a_{\psi,m}^{2-m}, \quad (5.3)$$

which is analogous to (3.8). On a given flux surface, we can use (3.9), (5.1), and (5.3) to find

$$\left(\frac{r}{a_{\psi,m}}\right)^2 + \frac{\Delta_m^2 - 1}{\Delta_m^m + 1} \left(\frac{r}{a_{\psi,m}}\right)^m \cos(m(\theta + \theta_{tm})) = \frac{\Delta_m^m + \Delta_m^2}{\Delta_m^m + 1}, \quad (5.4)$$

where we have let $\theta_{t0,m} = \theta_{tm}$ for notational simplicity. We would like to exactly solve this equation for r to get a polar expression for each flux surface shape, but it is not analytic in general. Our method of dealing with this will distinguish two different geometry specifications.

5.1.1 Expanded flux surface specification

To derive the “Expanded” flux surface specification we will expand (5.4) in $\Delta_m - 1 \ll 1$ (i.e. weak shaping) and assume the flux surface is circular to lowest order to find the solution of

$$r(a_{\psi,m}, \theta) = a_{\psi,m} \left(1 + \frac{\Delta_m - 1}{2} (1 - \cos(m(\theta + \theta_{tm}))) \right). \quad (5.5)$$

However, in this work we will want to study geometries with shaping from more than one mode number. In order to parameterize these configurations we will simply superimpose the different effects, in keeping with (5.5), as

$$r(r_{\psi}, \theta) = r_{\psi} \left(1 - \sum_m \frac{\Delta_m - 1}{2} \cos(m(\theta + \theta_{tm})) \right), \quad (5.6)$$

where we have defined a new flux surface label

$$r_\psi \equiv a_\psi \left(1 + \sum_m \frac{\Delta_m - 1}{2} \right) \quad (5.7)$$

to make the specification as simple as possible. Then, by choosing $r_\psi = r_{\psi 0}$ we pick a particular flux surface of interest with the shape

$$r_0(\theta) = r_{\psi 0} \left(1 - \sum_m \frac{\Delta_m - 1}{2} \cos(m(\theta + \theta_{tm})) \right) \quad (5.8)$$

to be the centre of the local equilibrium. Note that we are free to prescribe this shape however we wish as external coils can be used to arbitrarily shape any single flux surface in the global MHD equilibrium.

In fact, the change in the flux surface shape with minor radius is the important quantity determined by the global equilibrium. To calculate it we will directly differentiate (5.6) to find

$$\begin{aligned} \left. \frac{\partial r}{\partial r_\psi} \right|_{r_{\psi 0}, \theta} &= 1 - \sum_m \left[\left(\frac{\Delta_m - 1}{2} + \frac{r_{\psi 0}}{2} \frac{d\Delta_m}{dr_\psi} \right) \cos(m(\theta + \theta_{tm})) \right. \\ &\quad \left. - m(\Delta_m - 1) \frac{r_{\psi 0}}{2} \frac{d\theta_{tm}}{dr_\psi} \sin(m(\theta + \theta_{tm})) \right] \end{aligned} \quad (5.9)$$

to lowest order in $\Delta_m - 1 \ll 1$, where all quantities are evaluated on the flux surface of interest. The values of $d\Delta_m/dr_\psi$ and $d\theta_{tm}/dr_\psi$ are unknown, but can be calculated from the constant current global equilibrium.

To estimate $d\Delta_m/dr_\psi$ from the global equilibrium, we will also expand (5.3) to lowest order in the weak shaping limit to get

$$N_{0,m} = \frac{\hat{j}_0}{4} (\Delta_m - 1) r_\psi^{2-m}. \quad (5.10)$$

Remembering that $N_{0,m}$ and \hat{j}_0 are constants of the equilibrium, we can differentiate this implicitly to find

$$\frac{d\Delta_m}{dr_\psi} = (m - 2) \frac{\Delta_m - 1}{r_{\psi 0}} \quad (5.11)$$

to lowest order in $\Delta_m - 1 \ll 1$ on the flux surface of interest. Lastly, since $\theta_{tm} = \theta_{t0,m}$ is a constant defined by (2.20) we know that

$$\frac{d\theta_{tm}}{dr_\psi} = 0. \quad (5.12)$$

5.1.2 Exact flux surface specification

While the Expanded flux surface specification is simple, the $m = 2$ mode does not exactly correspond to elongation and single-mode flux surfaces become unrealistic at large shaping. This motivates the “Exact” flux surface specification, which is found by exactly solving (5.4) for the $m = 2$ case to get

$$r(a_{\psi,2}, \theta) = \frac{a_{\psi,2}\Delta_2}{\sqrt{1 + (\Delta_2^2 - 1) \cos^2(\theta + \theta_{t2})}}. \quad (5.13)$$

This is the polar equation for an ellipse and matches (4.1). From this we will extrapolate a simple generalisation for arbitrary m of

$$r(a_{\psi,m}, \theta) = \frac{a_{\psi,m}\Delta_m}{\sqrt{1 + (\Delta_m^2 - 1) \cos^2(m(\theta + \theta_{tm})/2)}}. \quad (5.14)$$

This particular generalisation is acceptable because it is consistent with (5.4) and (5.5) to $O(\Delta_m - 1)$ in the weak shaping limit (i.e. the error is $O((\Delta_m - 1)^2)$) and satisfies

$$r(a_{\psi,m}, -\theta_{tm}) = a_{\psi,m} \quad (5.15)$$

$$\frac{r(a_{\psi,m}, \pi/m - \theta_{tm})}{r(a_{\psi,m}, -\theta_{tm})} = \Delta_m. \quad (5.16)$$

Repeating the method used for the Expanded specification, we will superimpose the different shaping effects from (5.14) to find

$$r(a_{\psi}, \theta) = a_{\psi} \left[1 + \sum_m \left(\frac{\Delta_m}{\sqrt{1 + (\Delta_m^2 - 1) \cos^2(m(\theta + \theta_{tm})/2)}} - 1 \right) \right]. \quad (5.17)$$

The plus and minus 1 terms were added to ensure that $r(a_{\psi}, \theta) = a_{\psi}$ when $\Delta_m = 1$ for all m . Note that strictly speaking in writing (5.17) (and (5.7)) we have somewhat modified our definition of the flux surface label a_{ψ} . In section 3.1 we had defined it as the minimum radial location on a given flux surface, but from (5.17) we see that this is not true for geometries with multiple shaping modes that are not aligned. Instead it is defined by (5.17) from the definitions of r and θ . Evaluating (5.17) at $a_{\psi} = a_{\psi 0}$ we find

$$r_0(\theta) = a_{\psi 0} \left[1 + \sum_m \left(\frac{\Delta_m}{\sqrt{1 + (\Delta_m^2 - 1) \cos^2(m(\theta + \theta_{tm})/2)}} - 1 \right) \right], \quad (5.18)$$

the shape of the flux surface of interest.

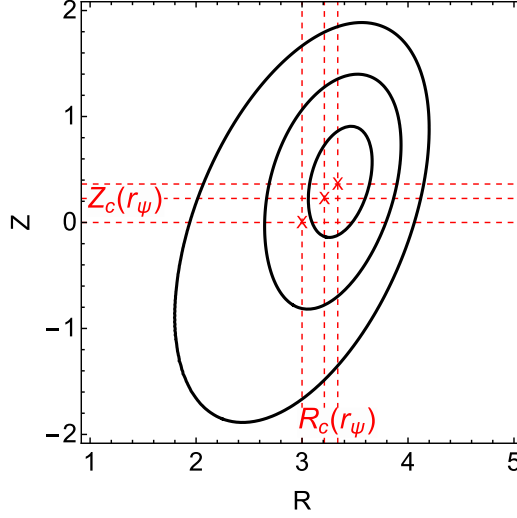


Figure 5.1: Example flux surfaces showing the geometric meaning of the parameters $R_c(a_\psi)$ and $Z_c(a_\psi)$, the major radial and axial locations of the centre of each flux surface respectively.

Directly differentiating (5.17) gives

$$\begin{aligned} \left. \frac{\partial r}{\partial a_\psi} \right|_{a_{\psi 0}, \theta} &= 1 + \sum_m \left[-1 + \frac{\Delta_m}{\sqrt{1 + (\Delta_m^2 - 1) \cos^2(m(\theta + \theta_{tm})/2)}} \right. \\ &\quad \times \left(1 + \frac{a_{\psi 0}}{\Delta_m} \frac{d\Delta_m}{da_\psi} - \frac{a_{\psi 0} \cos^2(m(\theta + \theta_{tm})/2)}{1 + (\Delta_m^2 - 1) \cos^2(m(\theta + \theta_{tm})/2)} \right. \\ &\quad \left. \left. \times \left(\Delta_m \frac{d\Delta_m}{da_\psi} - m \frac{\Delta_m^2 - 1}{2} \frac{d\theta_{tm}}{da_\psi} \tan(m(\theta + \theta_{tm})/2) \right) \right) \right], \end{aligned} \quad (5.19)$$

where we have evaluated all quantities on the flux surface of interest. We can estimate that $d\Delta_m/da_\psi = (m - 2)(\Delta_m - 1)/a_{\psi 0}$ and $d\theta_{tm}/da_\psi = 0$ to lowest order in weak shaping from (5.7), (5.11), (5.12), and the chain rule.

5.2 Shafranov shift in tilted elliptical tokamaks

The Miller geometry specification captures the Shafranov shift through local values of dR_c/da_ψ and dZ_c/da_ψ , where $R_c(a_\psi)$ and $Z_c(a_\psi)$ indicate the location of the centre of each flux surface as shown in figure 5.1. In order to model a realistic geometry, we will include its effect in the Exact specification by calculating local values of dR_c/da_ψ and dZ_c/da_ψ for arbitrary tilt angle from our global MHD results. Specifically, we will use the dependence of the global Shafranov shift on tilt angle calculated for constant current and $dp/d\psi$ profiles (i.e. the solid black line shown in figure 4.5).

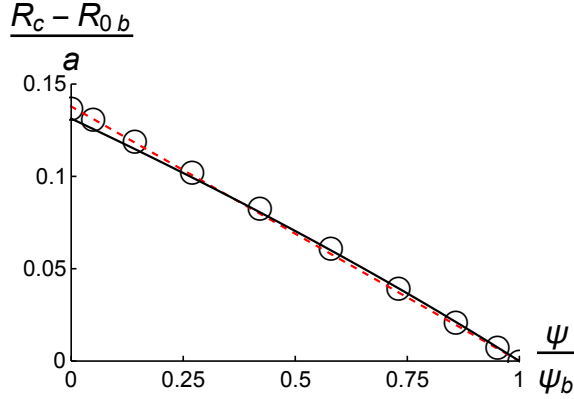


Figure 5.2: The shift in the centre of flux surfaces (relative to the centre of the boundary flux surface R_{0b}) as a function of normalised poloidal flux for a constant current profile and $\theta_{\kappa b} = 0$, according to ECOM (black, circles) and our analytic calculation (black, solid) with a linear best fit (red, dotted).

First we will assume that $dR_c/d\psi$ and $dZ_c/d\psi$ are constant from the boundary flux surface to the magnetic axis. In figure 5.2, we plot our analytic solution (using the coefficients calculated in appendix B) and ECOM results to show that this assumption is satisfied for the case of a vertically-elongated boundary. Additionally, using (2.21) and (B.2) we see that

$$\psi \propto a_\psi^2 \quad (5.20)$$

for a constant current profile and an exactly elliptical boundary. Therefore, using that $\psi = \psi_b$ at $a_\psi = a$, one can calculate the constant of proportionality to show that

$$\frac{d\psi}{da_\psi} = 2\frac{\psi_b}{a}\rho, \quad (5.21)$$

where $\rho \equiv a_\psi/a$ is the usual normalised minor radial flux surface label. Hence, the local Shafranov shift can be written as

$$\left. \frac{dR_c}{da_\psi} \right|_{a_{\psi 0}} = \left. \frac{d\psi}{da_\psi} \right|_{a_{\psi 0}} \frac{dR_c}{d\psi} = \left(2\frac{\psi_b}{a}\rho_0 \right) \frac{R_{0b} - R_0}{\psi_b - 0} = -2\rho_0 \frac{r_{\text{axis}}}{a} \cos(\theta_{\text{axis}}) \quad (5.22)$$

$$\left. \frac{dZ_c}{da_\psi} \right|_{a_{\psi 0}} = \left. \frac{d\psi}{da_\psi} \right|_{a_{\psi 0}} \frac{dZ_c}{d\psi} = \left(2\frac{\psi_b}{a}\rho_0 \right) \frac{Z_{0b} - Z_0}{\psi_b - 0} = -2\rho_0 \frac{r_{\text{axis}}}{a} \sin(\theta_{\text{axis}}), \quad (5.23)$$

where $\rho_0 \equiv a_{\psi 0}/a$, $a_{\psi 0}$ is the value of a_ψ on the flux surface of interest and the coordinate system is defined such that the boundary flux surface is centred at $(R = R_{0b}, Z = Z_{0b})$.

5.3 Summary

In summary, we have defined two different sets of expressions for the flux surface shape and its derivative. The first, which we call the “Expanded” parameterization, is a simple Fourier parameterization given by (5.8), (5.9), and

$$r(r_\psi, \theta) = r_0(\theta) + \left. \frac{\partial r}{\partial r_\psi} \right|_{r_{\psi 0}, \theta} (r_\psi - r_{\psi 0}) \quad (5.24)$$

$$R(r_\psi, \theta) = R_{c0} + r(r_\psi, \theta) \cos(\theta) \quad (5.25)$$

$$Z(r_\psi, \theta) = Z_{c0} + r(r_\psi, \theta) \sin(\theta), \quad (5.26)$$

where the flux surface of interest is centred at $(R = R_{c0}, Z = Z_{c0})$. This shaping parameterization will be useful for theoretical scaling calculations (see chapters 7 and 8).

The second set, which we call the “Exact” parameterization, is consistent with the Expanded parameterization to next order in the weak shaping expansion. It is given by (5.18), (5.19), and

$$r(a_\psi, \theta) = r_0(\theta) + \left. \frac{\partial r}{\partial a_\psi} \right|_{a_{\psi 0}, \theta} (a_\psi - a_{\psi 0}) \quad (5.27)$$

$$R_c(a_\psi) = R_{c0} + \left. \frac{dR_c}{da_\psi} \right|_{a_{\psi 0}} (a_\psi - a_{\psi 0}) \quad (5.28)$$

$$Z_c(a_\psi) = Z_{c0} + \left. \frac{dZ_c}{da_\psi} \right|_{a_{\psi 0}} (a_\psi - a_{\psi 0}) \quad (5.29)$$

$$R(a_\psi, \theta) = R_c(a_\psi) + r(a_\psi, \theta) \cos(\theta) \quad (5.30)$$

$$Z(a_\psi, \theta) = Z_c(a_\psi) + r(a_\psi, \theta) \sin(\theta). \quad (5.31)$$

In this parameterization the $m = 2$ mode exactly corresponds to elliptical flux surfaces, which will be useful for realistic numerical simulations (see chapters 9 and 10). We note that to treat the Shafranov shift we calculate $dR_c/da_\psi|_{a_{\psi 0}}$ and $dZ_c/da_\psi|_{a_{\psi 0}}$ for an ITER-like pressure profile using (5.22) and (5.23) as well as the constant current results shown in figure 4.5 (and given in appendix B).

Both of these prescriptions require either $d\Delta_m/da_\psi$ or $d\Delta_m/dr_\psi$, which were estimated from the global equilibrium.

Part II

Turbulent transport

Chapter 6

Overview of gyrokinetics

Much of this chapter appears in reference [43].

Gyrokinetics has many variations [44, 45, 46, 47, 48, 49, 50, 51, 52, 53]. It is based on the expansion of the Fokker-Planck and Maxwell's equations in $\rho_* \equiv \rho_i/a \ll 1$, where ρ_i is the ion gyroradius and a is the tokamak minor radius. This model investigates plasma behaviour with timescales much slower than the ion gyrofrequency Ω_i and the electron gyrofrequency Ω_e (i.e. $\omega \ll \Omega_i \ll \Omega_e$), but retains the finite size of the gyroradius by assuming that the perpendicular wavenumber of the turbulence is comparable to the ion gyroradius (i.e. $k_\perp \rho_i \sim 1$ where k_\perp is the characteristic wavenumber of the turbulence perpendicular to the magnetic field). In this limit, the six dimensions of velocity space reduce to five because the particle gyrophase can be ignored. As such, gyrokinetics evolves rings of charge as they generate and respond to electric and magnetic fields. In this thesis we will use δf gyrokinetics, which assumes that the turbulence arises from perturbations to the distribution function that are small compared to the background (i.e. $f_{s1} \ll f_{s0}$, where f_{s0} is the background distribution function for species s and f_{s1} is the lowest order perturbation). These particular choices have been shown experimentally to be appropriate for modelling core turbulence [54]. Furthermore, we will assume the plasma is sufficiently collisional so that the background distribution function is Maxwellian,

$$f_{s0} = F_{Ms} \equiv n_s \left(\frac{m_s}{2\pi T_s} \right)^{3/2} \exp \left(-\frac{m_s w^2}{2T_s} \right). \quad (6.1)$$

Here n_s is the density of species s , m_s is the particle mass, T_s is the temperature, $\vec{w} \equiv \vec{v} - R\Omega_\zeta \hat{e}_\zeta$ is the velocity shifted into the rotating frame, and $\Omega_\zeta(\psi) = V_\zeta/R$ is the toroidal rotation frequency. We note that Ω_ζ is a flux function and $R\Omega_\zeta \sim v_{thi}$ in the high flow regime, where $v_{thi} \equiv \sqrt{2T_i/m_i}$ is the ion thermal speed. To

lowest order in $\rho_* \ll 1$, it can be shown that all species rotate at $\Omega_\zeta = -d\Phi_{-1}/d\psi$, where $\Phi_{-1} \sim \rho_*^{-1}T_e/e$ is the lowest order electrostatic potential and a flux function [55, 56, 57] while e is the proton electric charge. Though T_s and Ω_ζ are flux functions, the centrifugal force can cause the density to vary on a flux surface according to [58]

$$n_s(\psi, \theta) = \eta_s(\psi) \exp\left(\frac{m_s R^2 \Omega_\zeta^2}{2T_s} - \frac{Z_s e \Phi_0}{T_s}\right), \quad (6.2)$$

where $\eta_s(\psi)$ is the pseudo-density flux function, Z_s is the electric charge number, and Φ_0 is the next order electrostatic potential. We can find Φ_0 by imposing quasineutrality,

$$\sum_s Z_s e n_s = \sum_s Z_s e \eta_s(\psi) \exp\left(\frac{m_s R^2 \Omega_\zeta^2}{2T_s} - \frac{Z_s e \Phi_0}{T_s}\right) = 0. \quad (6.3)$$

From the assumption that $k_\perp \rho_i \sim 1$ (remembering our expansion in $\rho_i/a \ll 1$), we know that the background plasma quantities vary little on the scale of the turbulence in the directions perpendicular to the background magnetic field. Neglecting this small variation is called the local approximation and it motivates periodic boundary conditions in the perpendicular directions. Ballooning coordinates [59] are generally used in local gyrokinetics to model turbulence in a flux tube, a long narrow domain that follows a single field line. These boundary conditions allow us to Fourier analyse in the poloidal flux ψ (which parameterizes the radial direction) and in

$$\alpha \equiv \zeta - I(\psi) \int_{\theta_\alpha(\psi)}^\theta \left| d\theta' \left(R^2 \vec{B} \cdot \vec{\nabla} \theta' \right)^{-1} - \Omega_\zeta t \right. \quad (6.4)$$

(which parameterizes the direction perpendicular to the field lines, but within the flux surface). Note the free parameter $\theta_\alpha(\psi)$, which determines the field line selected by $\alpha = 0$ on each flux surface and will be important in chapter 7.

The high-flow, Fourier analysed gyrokinetic equation can be written as [20]

$$\begin{aligned} \frac{\partial h_s}{\partial t} + w_{||} \hat{b} \cdot \vec{\nabla} \theta \frac{\partial h_s}{\partial \theta} \Big|_{w_{||}, \mu} + i(k_\psi v_{ds\psi} + k_\alpha v_{ds\alpha}) h_s + a_{s||} \frac{\partial h_s}{\partial w_{||}} \Big|_{\theta, \mu} - \sum_{s'} \langle C_{ss'}^{(l)} \rangle_\varphi \\ + \{ \langle \chi \rangle_\varphi, h_s \} = \frac{Z_s e F_{Ms}}{T_s} \frac{\partial \langle \chi \rangle_\varphi}{\partial t} - v_{\chi s \psi} F_{Ms} \left[\frac{1}{n_s} \frac{\partial n_s}{\partial \psi} \Big|_\theta \right. \\ \left. + \frac{m_s I w_{||}}{B T_s} \frac{d\Omega_\zeta}{d\psi} + \frac{Z_s e}{T_s} \frac{\partial \Phi_0}{\partial \psi} \Big|_\theta - \frac{m_s R \Omega_\zeta^2}{T_s} \frac{\partial R}{\partial \psi} \Big|_\theta + \left(\frac{m_s w^2}{2T_s} - \frac{3}{2} \right) \frac{1}{T_s} \frac{dT_s}{d\psi} \right], \end{aligned} \quad (6.5)$$

where the coordinates are t (the time), θ (the poloidal angle), k_ψ (the radial wavenumber), k_α (the poloidal wavenumber), $w_{||}$ (the parallel velocity in the rotating frame),

$\mu \equiv m_s w_\perp^2 / 2B$ (the magnetic moment), and we have already eliminated φ (the gyrophase) by gyroaveraging. The unknowns are

$$h_s \equiv \left\langle \left\langle \left(f_{s1} + \frac{Z_s e \phi}{T_s} F_{Ms} \right) \exp(-ik_\psi \psi - ik_\alpha \alpha) \right\rangle_{\Delta\psi} \right\rangle_{\Delta\alpha} \quad (6.6)$$

(the Fourier-analysed nonadiabatic portion of the distribution function) and the fields contained in

$$\langle \chi \rangle_\varphi \equiv J_0(k_\perp \rho_s) (\phi - w_\parallel A_\parallel) + \frac{1}{\Omega_s} \frac{\mu B}{m_s} \frac{2J_1(k_\perp \rho_s)}{k_\perp \rho_s} B_\parallel \quad (6.7)$$

(the Fourier analysed gyroaveraged generalised potential). We note that $\langle \dots \rangle_{\Delta\psi} \equiv \Delta\psi^{-1} \int_{\Delta\psi} d\psi (\dots)$ is a coarse-grain average over the radial distance $\Delta\psi$ (which is larger than the scale of the turbulence, but smaller than the scale of the device), $\langle \dots \rangle_{\Delta\alpha} \equiv \Delta\alpha^{-1} \int_{\Delta\alpha} d\alpha (\dots)$ is a coarse-grain average over the poloidal distance $\Delta\alpha$ (which is larger than the scale of the turbulence, but smaller than the scale of the device), $\langle \dots \rangle_\varphi$ is the gyroaverage at fixed guiding centre, $J_n(\dots)$ is the n th order Bessel function of the first kind, ϕ is the Fourier analysed perturbed electrostatic potential, A_\parallel is the Fourier analysed perturbed magnetic vector potential, B_\parallel is the component of the Fourier analysed perturbed magnetic field parallel to the background magnetic field,

$$k_\perp = \sqrt{k_\psi^2 |\vec{\nabla}\psi|^2 + 2k_\psi k_\alpha \vec{\nabla}\psi \cdot \vec{\nabla}\alpha + k_\alpha^2 |\vec{\nabla}\alpha|^2} \quad (6.8)$$

is the perpendicular wavevector, $\rho_s \equiv \sqrt{2\mu B / m_s} / \Omega_s$ is the gyroradius, $\Omega_s \equiv Z_s e B / m_s$ is the gyrofrequency, and Z_s is the species charge number.

The drift coefficients are given by

$$\begin{aligned} v_{ds\psi} &\equiv \vec{v}_{ds} \cdot \vec{\nabla}\psi \\ &= \left(-\frac{I}{B} \frac{\partial \Phi_0}{\partial \theta} - \frac{I (m_s w_\parallel^2 + \mu B)}{m_s \Omega_s B} \frac{\partial B}{\partial \theta} + \frac{2BR\Omega_\zeta w_\parallel}{\Omega_s} \frac{\partial R}{\partial \theta} + \frac{IR\Omega_\zeta^2}{\Omega_s} \frac{\partial R}{\partial \theta} \right) \hat{b} \cdot \vec{\nabla}\theta \end{aligned} \quad (6.9)$$

and

$$\begin{aligned} v_{ds\alpha} &\equiv \vec{v}_{ds} \cdot \vec{\nabla}\alpha = -\frac{\partial \Phi_0}{\partial \psi} + \frac{\partial \Phi_0}{\partial \theta} \frac{\hat{b} \cdot (\vec{\nabla}\theta \times \vec{\nabla}\alpha)}{B} \\ &\quad - \frac{m_s w_\parallel^2 + \mu B}{m_s \Omega_s} \left(\frac{\partial B}{\partial \psi} - \frac{\partial B}{\partial \theta} \frac{\hat{b} \cdot (\vec{\nabla}\theta \times \vec{\nabla}\alpha)}{B} \right) - \frac{\mu_0 w_\parallel^2}{B \Omega_s} \frac{\partial p}{\partial \psi} \Big|_R \\ &\quad + \frac{2\Omega_\zeta w_\parallel}{\Omega_s} \hat{e}_\zeta \cdot (\vec{\nabla}\alpha \times \vec{\nabla}R) + \frac{m_s R \Omega_\zeta^2}{Z_s e} \left(\frac{\partial R}{\partial \psi} - \frac{\partial R}{\partial \theta} \frac{\hat{b} \cdot (\vec{\nabla}\theta \times \vec{\nabla}\alpha)}{B} \right), \end{aligned} \quad (6.10)$$

where $p \equiv \sum_s n_s T_s$ is the plasma pressure and

$$\left. \frac{\partial p}{\partial \psi} \right|_R = \left. \frac{\partial p}{\partial \psi} \right|_\theta - \sum_s n_s m_s R \Omega_\zeta^2 \left. \frac{\partial R}{\partial \psi} \right|_\theta. \quad (6.11)$$

The parallel acceleration is given by

$$a_{s||} = \left(-\frac{\mu}{m_s} \frac{\partial B}{\partial \theta} - \frac{Z_s e}{m_s} \frac{\partial \Phi_0}{\partial \theta} + R \Omega_\zeta^2 \frac{\partial R}{\partial \theta} \right) \hat{b} \cdot \vec{\nabla} \theta, \quad (6.12)$$

$C_{ss'}^{(l)}$ is the linearized collision operator, the nonlinear term is

$$\{\langle \chi \rangle_\varphi, h_s\} = \sum_{k'_\psi, k'_\alpha} (k'_\psi k_\alpha - k_\psi k'_\alpha) \langle \chi \rangle_\varphi (k'_\psi, k'_\alpha) h_s (k_\psi - k'_\psi, k_\alpha - k'_\alpha), \quad (6.13)$$

and

$$v_{\chi s \psi} \equiv i k_\alpha \langle \chi \rangle_\varphi. \quad (6.14)$$

In order to solve for ϕ , $A_{||}$, and $B_{||}$ we also need the Fourier analysed quasineutrality equation [20]

$$\phi = 2\pi \left(\sum_s \frac{Z_s^2 e^2 n_s}{T_s} \right)^{-1} \sum_s \frac{Z_s e B}{m_s} \int dw_{||} \int d\mu J_0(k_\perp \rho_s) h_s, \quad (6.15)$$

parallel current equation [20]

$$A_{||} = \frac{2\pi\mu_0}{k_\perp^2} \sum_s \frac{Z_s e B}{m_s} \int dw_{||} \int d\mu J_0(k_\perp \rho_s) w_{||} h_s, \quad (6.16)$$

and perpendicular current equation [20]

$$B_{||} = -2\pi\mu_0 \sum_s \frac{B}{m_s} \int dw_{||} \int d\mu \frac{2J_1(k_\perp \rho_s)}{k_\perp \rho_s} \mu h_s. \quad (6.17)$$

Equations (6.5), (6.15), (6.16), and (6.17) comprise the nonlinear electromagnetic gyrokinetic model, in the presence of rotation, which we will use in chapter 7. These equations simplify considerably when the plasma is assumed to be electrostatic (i.e. $A_{||} = B_{||} = 0$) and stationary (i.e. $\Omega_\zeta = 0$) as is done in chapters 8, 9, and 10.

Solving the gyrokinetic model for h_s , ϕ , $A_{||}$, and $B_{||}$ allows us to calculate the turbulent radial fluxes of particles, momentum, and energy as well as the turbulent energy exchange between species. These are the only turbulent quantities needed to evolve the transport equations for particles, momentum, and energy [20, 49, 53].

The full expressions are written in appendix C. Here we give only the electrostatic contribution to the particle flux

$$\Gamma_s^\phi \equiv - \left\langle R \left\langle \left\langle \int d^3w \underline{h}_s \hat{e}_\zeta \cdot \delta \vec{E} \right\rangle_{\Delta\psi} \right\rangle_{\Delta t} \right\rangle_\psi \quad (6.18)$$

$$= \frac{4\pi^2 i}{m_s V'} \left\langle \sum_{k_\psi, k_\alpha} k_\alpha \oint d\theta J B \phi(k_\psi, k_\alpha) \int dw_{||} d\mu h_s(-k_\psi, -k_\alpha) J_0(k_\perp \rho_s) \right\rangle_{\Delta t}, \quad (6.19)$$

the momentum flux

$$\Pi_{\zeta s}^\phi \equiv - \left\langle R \left\langle \left\langle \int d^3w \underline{h}_s m_s R (\vec{w} \cdot \hat{e}_\zeta + R \Omega_\zeta) \hat{e}_\zeta \cdot \delta \vec{E} \right\rangle_{\Delta\psi} \right\rangle_{\Delta t} \right\rangle_\psi \quad (6.20)$$

$$= \frac{4\pi^2 i}{V'} \left\langle \sum_{k_\psi, k_\alpha} k_\alpha \oint d\theta J B \phi(k_\psi, k_\alpha) \int dw_{||} d\mu h_s(-k_\psi, -k_\alpha) \right. \\ \left. \times \left[\left(\frac{I}{B} w_{||} + R^2 \Omega_\zeta \right) J_0(k_\perp \rho_s) + \frac{i}{\Omega_s} \frac{k^\psi}{B} \frac{\mu B}{m_s} \frac{2J_1(k_\perp \rho_s)}{k_\perp \rho_s} \right] \right\rangle_{\Delta t}, \quad (6.21)$$

the energy flux

$$Q_s^\phi \equiv - \left\langle R \left\langle \left\langle \int d^3w \underline{h}_s \left(\frac{m_s}{2} w^2 + Z_s e \Phi_0 - \frac{m_s}{2} R^2 \Omega_\zeta^2 \right) \hat{e}_\zeta \cdot \delta \vec{E} \right\rangle_{\Delta\psi} \right\rangle_{\Delta t} \right\rangle_\psi \quad (6.22)$$

$$= \frac{4\pi^2 i}{V'} \left\langle \sum_{k_\psi, k_\alpha} k_\alpha \oint d\theta J B \phi(k_\psi, k_\alpha) \int dw_{||} d\mu h_s(-k_\psi, -k_\alpha) \right. \\ \left. \times \left(\frac{w^2}{2} + \frac{Z_s e \Phi_0}{m_s} - \frac{1}{2} R^2 \Omega_\zeta^2 \right) J_0(k_\perp \rho_s) \right\rangle_{\Delta t}, \quad (6.23)$$

and the turbulent energy exchange between species

$$P_{Qs}^\phi \equiv \left\langle \left\langle \left\langle \int d^3w Z_s e \underline{h}_s \frac{\partial \phi}{\partial t} \right\rangle_{\Delta\psi} \right\rangle_{\Delta t} \right\rangle_\psi \quad (6.24)$$

$$= \frac{4\pi^2}{V'} \left\langle \sum_{k_\psi, k_\alpha} \oint d\theta J \Omega_s \frac{\partial}{\partial t} (\phi(k_\psi, k_\alpha)) \int dw_{||} d\mu h_s(-k_\psi, -k_\alpha) J_0(k_\perp \rho_s) \right\rangle_{\Delta t}. \quad (6.25)$$

Here $\underline{h}_s \equiv f_{s1} + Z_s e \underline{\phi} F_{Ms}/T_s$ is the nonadiabatic portion of the distribution function, (\dots) indicates the quantity has not been Fourier analysed, $\delta \vec{E} = -\vec{\nabla}_\perp \underline{\phi}$ is the turbulent electric field, $\langle \dots \rangle_\psi \equiv (2\pi/V') \oint_0^{2\pi} d\theta J(\dots)$ is the flux surface average, $\langle \dots \rangle_{\Delta t} \equiv \Delta t^{-1} \int_{\Delta t} dt (\dots)$ is a coarse-grain average over a time Δt (which is longer than the turbulent decorrelation time, but shorter than the transport time), $V' \equiv 2\pi \oint d\theta J$, $J \equiv \left| \vec{B} \cdot \vec{\nabla} \theta \right|^{-1}$ is the Jacobian, and $k^\psi \equiv \vec{k}_\perp \cdot \vec{\nabla} \psi = k_\psi \left| \vec{\nabla} \psi \right|^2 + k_\alpha \vec{\nabla} \psi \cdot \vec{\nabla} \alpha$.

6.1 Estimating intrinsic momentum transport

Equations (6.20) and (6.22) allow us to calculate the local momentum flux and energy flux respectively. The energy flux signifies how much power must be injected to maintain the temperature gradient specified in (6.5). A lower energy flux is desirable as it means that less external heating power is needed to maintain a fixed temperature profile. Similarly, the momentum flux tells how much external momentum must be injected to maintain the specified rotation shear (at a given value of rotation). However, in this work we will use GS2 [60], a local δf gyrokinetic code, to self-consistently calculate the nonlinear turbulent fluxes of momentum and energy generated at zero rotation and rotation shear. From this information we can estimate the intrinsic ability of a given geometry to drive rotation by following the analysis of reference [18].

First, we will Taylor expand the momentum flux around zero rotation and rotation shear to get the usual momentum transport equation [61],

$$\langle \Pi_{\zeta i} \rangle_t - P_{\Pi i} n_i m_i R_c^2 \Omega_\zeta - D_{\Pi i} n_i m_i R_c^2 \frac{d\Omega_\zeta}{da_\psi} \approx 0, \quad (6.26)$$

where $\langle \Pi_{\zeta i} \rangle_t$ is the time-averaged intrinsic ion momentum flux (i.e. the momentum flux calculated for $\Omega_\zeta = d\Omega_\zeta/da_\psi = 0$), $P_{\Pi i}$ is the momentum pinch, $D_{\Pi i}$ is the momentum diffusivity (i.e. the kinematic viscosity), and R_c is the major radial location of the centre of a given flux surface. By neglecting the momentum pinch we find

$$\langle \Pi_{\zeta i} \rangle_t \approx D_{\Pi i} n_i m_i R_c^2 \frac{d\Omega_\zeta}{da_\psi}, \quad (6.27)$$

a balance between rotation diffusion and the intrinsic momentum flux. Doing so is conservative as the momentum pinch can only ever enhance the level of rotation, maybe by as much as a factor of three [62]. We will also write the energy flux as a diffusive term [63] according to

$$\langle Q_i \rangle_t \approx -D_{Q_i} n_i \frac{dT_i}{da_\psi}, \quad (6.28)$$

where $\langle Q_i \rangle_t$ is the time-averaged energy flux. Combining these two equations through the turbulent ion Prandtl number $Pr_i \equiv D_{\Pi i}/D_{Q_i}$ gives

$$\frac{1}{v_{thi}} \frac{d(R_c \Omega_\zeta)}{da_\psi} \approx \frac{-1}{2Pr_i} \left(\frac{v_{thi}}{R_c} \frac{\langle \Pi_{\zeta i} \rangle_t}{\langle Q_i \rangle_t} \right) \frac{d}{da_\psi} \ln(T_i), \quad (6.29)$$

where we used that $T_i = m_i v_{thi}^2/2$. Doing this is useful because the Prandtl number is expected to be both $O(1)$ and unaffected by changes in tokamak parameters. We

now substitute the Alfvén Mach number, $M_A \equiv |R_c \Omega_\zeta| \sqrt{\mu_0 n_i m_i} / B_0$, as it is the relevant quantity for stabilising MHD modes. Assuming that $n_e = n_i$, $T_e = T_i$, and $\eta_i \equiv (d \ln(T_i) / da_\psi) / (d \ln(n_i) / da_\psi) \gg 1$ allows us to use (6.29) to estimate the Alfvén Mach number profile as

$$M_A(\rho) \approx \left| \int_1^\rho d\rho' \frac{1}{2\sqrt{2}Pr_i(\rho')} \left(\frac{v_{thi}(\rho') \langle \Pi_{\zeta i}(\rho') \rangle_t}{R_c(\rho') \langle Q_i(\rho') \rangle_t} \right) \frac{\beta'(\rho')}{\sqrt{\beta(\rho')}} \right|. \quad (6.30)$$

Notice that this expression is in terms of $(v_{thi}/R_c) \langle \Pi_{\zeta i} \rangle_t / \langle Q_i \rangle_t$, a normalised parameter that indicates how strongly a given geometry drives rotation from the turbulent fluxes of momentum and energy. The remainder of this thesis will be focused on finding the geometries that maximise this momentum transport figure of merit as well as minimise the energy flux.

First, in this chapter we will briefly outline the argument for why the intrinsic rotation in up-down symmetric tokamaks must be small in $\rho_* \ll 1$. Then, in chapter 7 we will present a similar argument demonstrating that the momentum flux from fast mirror symmetric flux surface shaping (i.e. shaping with poloidal variation on a small spatial scale) must be exponentially small in the Fourier mode numbers of the fast shaping. This motivates the calculation in chapter 8, which shows that flux surfaces with slowly varying envelopes created by the beating of fast shaping can generate momentum flux that is only polynomially small. We also argue that a mirror symmetric tokamak has no momentum transport in the screw pinch limit. Accordingly, in chapters 9 and 10 we search for the optimal configurations in the space of non-mirror symmetric geometries created by the beating of low order shaping modes. Chapter 9 reveals that introducing the Shafranov shift into tilted elliptical flux surfaces breaks mirror symmetry and enhances the rotation. Unfortunately, this enhancement is entirely cancelled by including the effect of the pressure profile on the equilibrium, which is needed to be consistent. However, in chapter 10 we use independently tilted elongation and triangularity to directly break mirror symmetry and significantly increase the momentum transport. Lastly, in chapter 11 we present the optimal geometry, as indicated by the analysis of this thesis, and comment on some overarching conclusions.

6.2 Momentum flux from up-down symmetric flux surface shaping

In this thesis we are concerned with the effect of geometry on the turbulent fluxes. All of the information concerning the tokamak geometry enters the gyrokinetic model

via ten geometric coefficients: B , $\hat{b} \cdot \vec{\nabla}\theta$, $v_{ds\psi}$, $v_{ds\alpha}$, $a_{s||}$, $|\vec{\nabla}\psi|^2$, $\vec{\nabla}\psi \cdot \vec{\nabla}\alpha$, $|\vec{\nabla}\alpha|^2$, R , and $\partial R/\partial\psi|_\theta$. We note that, when the plasma is stationary (i.e. $\Omega_\zeta = 0$), only eight coefficients appear as the terms containing R and $\partial R/\partial\psi|_\theta$ vanish. In appendix D we show the full, explicit calculation of these geometric coefficients in the context of the Miller local equilibrium model introduced in chapter 5.

As shown by references [19, 20, 21], in an up-down symmetric tokamak all of the geometric coefficients have a well defined parity, which has important consequences for the overall symmetry properties of the gyrokinetic model. In an up-down symmetric tokamak, the coefficients $v_{ds\psi}$, $a_{s||}$, and $\vec{\nabla}\psi \cdot \vec{\nabla}\alpha$ are necessarily odd in θ , while $\hat{b} \cdot \vec{\nabla}\theta$, B , $v_{ds\alpha}$, $|\vec{\nabla}\psi|^2$, $|\vec{\nabla}\alpha|^2$, R , and $\partial R/\partial\psi|_\theta$ are even. This means that, when the rotation and rotation shear are zero, the equations become invariant to the $(k_\psi, k_\alpha, \theta, w_{||}, \mu, t) \rightarrow (-k_\psi, k_\alpha, -\theta, -w_{||}, \mu, t)$ coordinate system transformation, which is not true in up-down asymmetric devices. This symmetry means that, given any solution $h_s(k_\psi, k_\alpha, \theta, w_{||}, \mu, t)$, we can construct a second solution $-h_s(-k_\psi, k_\alpha, -\theta, -w_{||}, \mu, t)$ that will also satisfy the gyrokinetic equations. From (6.21) (or (C.3), (C.8), and (C.9)) we see that this second solution will have a momentum flux that cancels that of the first. These two solutions are each valid for different initial conditions, but since the turbulence is presumed to be chaotic, both solutions will arise within a turbulent decorrelation time (statistically speaking). This demonstrates that, in the gyrokinetic limit, the time-averaged momentum flux must be zero in a stationary, up-down symmetric tokamak.

Chapter 7

Mirror symmetry: Scaling of momentum flux with shaping mode number

Much of this chapter appears in reference [43].

In this chapter, we demonstrate a new symmetry of the local, high-flow, electromagnetic δf gyrokinetic equations. This symmetry means that poloidally rotating all “fast” flux surface shaping (i.e. poloidal variation with a spatial scale much smaller than the connection length) by a single tilt angle (as shown in figure 7.1) has little effect on the transport properties of a tokamak. More broadly, it indicates that turbulence is insensitive to the interactions between flux surface variation on different poloidal scales.

To establish this tilting symmetry we expand the high-flow gyrokinetic equations in the limit of large flux surface shaping Fourier mode number. Here we distinguish between fast flux surface shaping and shaping with a large mode number because different large mode number shaping effects can beat together to create rapid variation with an envelope that varies on the slow connection length scale. We will see that gyrokinetics is symmetric to a tilt in the rapid variation, but not a tilt in the slowly varying envelope. This is intuitive as we expect turbulent eddies to extend along the field line and average over rapid poloidal variation, but still respond to large-scale flux surface shaping. Therefore, we would expect the effect of tilting flux surface shaping should diminish as poloidal flux surface variation becomes faster. However, what is surprising is that this symmetry proves that the effect diminishes exponentially, rather than polynomially. Hence we find that tilting fast flux surface shaping to create up-down asymmetry has an exponentially small effect on the turbulent momentum flux.

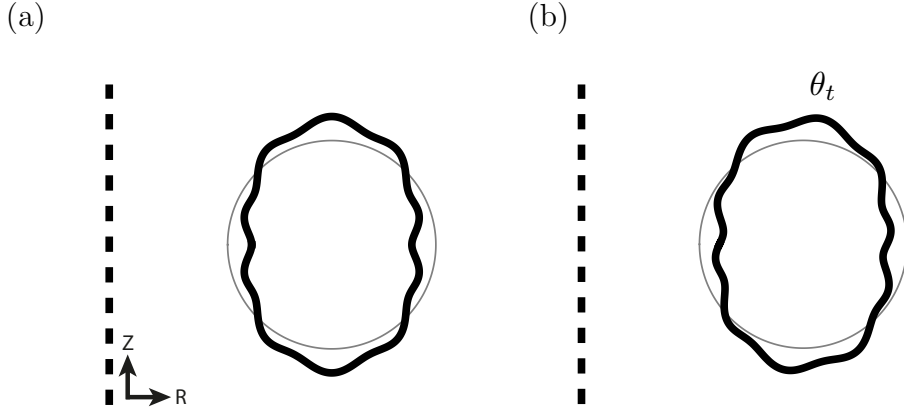


Figure 7.1: Example poloidal cross-section of a tokamak (a) without any tilt and (b) with the fast flux surface shaping effects tilted by an angle θ_t , noting that slow shaping effects like the elongation and envelopes (not shown) are not rotated. Circular flux surfaces are shown in grey for comparison and the axis of axisymmetry is indicated by a dashed line.

In section 6.2 we presented an argument showing that up-down symmetric devices generate no momentum transport in the usual lowest order gyrokinetics. This argument, together with the tilting symmetry presented in this chapter, will show that flux surfaces with mirror symmetry across some line in the poloidal plane can only generate exponentially small momentum transport, in the limit of fast shaping effects. This is because mirror symmetric flux surfaces can be transformed into up-down symmetric flux surfaces by poloidally tilting of all the shaping effects by a single global tilt angle. Consequently, this establishes a distinction between devices with mirror symmetric flux surfaces and devices without mirror symmetry, which may have important consequences for flux surface shaping of any mode number. Additionally, the exponential scaling suggests that generating rotation using up-down asymmetric triangularity or squareness will be significantly less effective than up-down asymmetric elongation, which is consistent with previous work [18]. The tilting symmetry also indicates that the geometry used in the TCV up-down asymmetry experiments [17] is close to the optimal mirror symmetric shape for generating large rotation [18], but this has not been tested experimentally. Regardless, a significant enhancement over the TCV results may still be found in the space of non-mirror symmetric shapes.

While the practical implications of the tilting symmetry are most relevant to momentum transport, it also applies to energy and particle transport. For example, references [64, 65] look at the effect of elongation and triangularity on the energy confinement time in TCV. From the scaling presented in this chapter, we would

expect that tilting triangularity or higher order shaping would have a smaller effect on energy confinement compared with tilting elongation. This can have significance for purely up-down symmetric configurations. For example, horizontal elongation can be thought of as vertical elongation with a 90° tilt just as changing the sign of triangularity is equivalent to tilting the triangularity by 180° . Therefore, we would expect switching from vertical to horizontal elongation would have a larger effect on the energy confinement time than changing the sign of the triangularity.

Section 7.1 of this chapter contains the analytic analysis demonstrating the poloidal tilting symmetry of fast flux surface shaping, while section 7.2 presents the results of nonlinear local gyrokinetic simulations. These simulations are aimed at providing numerical verification of the analytic work.

7.1 Poloidal tilting symmetry of high order flux surface shaping

In this section we will show the tilting symmetry of fast flux surface shaping in the nonlinear local δf gyrokinetic model. First, we will start with results from appendix D, which gives a detailed calculation of the geometric coefficients from the Miller local equilibrium specification. Then, we will use the Expanded local flux surface specification derived in chapter 5 to prescribe arbitrarily-shaped flux surfaces using Fourier analysis. This reveals how arbitrary high order shaping enters into the gyrokinetic equations. Finally we will expand the gyrokinetic equations in the limit of large flux surface shaping Fourier mode number and show that tilting fast shaping does not affect particle, momentum, or energy transport.

7.1.1 Geometric coefficients

To specify the background tokamak equilibrium for our local gyrokinetic model we will use the generalisation of the Miller local equilibrium model derived in chapter 5. The Miller prescription approximates the equilibrium around a single flux surface of interest when given: R_{c0} (the major radial location of the centre of the flux surface of interest), $r_0(\theta)$ (the shape of the flux surface of interest), $\partial r / \partial r_\psi|_{r_{\psi 0}, \theta}$ (how the shape of the flux surface of interest changes with minor radius), and several additional scalar quantities. We note that a local equilibrium is exactly mirror symmetric if $r_0(\theta) = r_0(-\theta + \theta_0)$ and $\partial r / \partial r_\psi|_{\psi_0, \theta} = \partial r / \partial r_\psi|_{\psi_0, -\theta + \theta_0}$ for some θ_0 , otherwise it is non-mirror symmetric. Similarly, if $r_0(\theta) = r_0(-\theta)$ and $\partial r / \partial r_\psi|_{\psi_0, \theta} = \partial r / \partial r_\psi|_{\psi_0, -\theta}$,

then the local equilibrium is exactly up-down symmetric (as well as mirror symmetric), otherwise it is up-down asymmetric. We will completely specify the geometry of the equilibrium using the Expanded prescription, given by (5.8), (5.9), and (5.24) through (5.26) while assuming $Z_{c0} = 0$ without loss of generality.

The four scalar quantities needed for the Miller equilibrium are commonly taken to be $I \equiv RB_\zeta$ (the toroidal field flux function),

$$q \equiv \frac{I}{2\pi} \oint_0^{2\pi} \left|_{\psi} d\theta \left(R^2 \vec{B}_p \cdot \vec{\nabla} \theta \right)^{-1} \quad (7.1)$$

(the safety factor), dq/dr_ψ (the magnetic shear), and dp/dr_ψ (the pressure gradient) of the flux surface of interest. However, when the plasma is rotating quickly the pressure ceases to be a flux function because the density varies poloidally. Therefore, we replace dp/dr_ψ with $\partial p/\partial r_\psi|_R$, which requires four additional, species-dependent parameters: $\eta_s T_s$ (the pseudo-pressure), $d(\eta_s T_s)/dr_\psi$ (the derivative of the pseudo-pressure), $m_s \Omega_\zeta^2/2T_s$ (a rotational frequency parameter), and $d(m_s \Omega_\zeta^2/2T_s)/dr_\psi$ (the derivative of the rotational frequency parameter). These four species-dependent parameters specify the pressure (and its radial gradient) on the flux surface of interest by using (6.2).

The functions $r_0(\theta)$ and $\partial r/\partial r_\psi|_{r_{\psi 0}, \theta}$ allow us to calculate poloidal derivatives of any order as well as the first order radial derivatives: $\partial R/\partial r_\psi|_\theta$ and $\partial Z/\partial r_\psi|_\theta$ (but not higher order radial derivatives). As shown in appendix D this is enough information to calculate seven of the ten geometric coefficients, specifically $\hat{b} \cdot \vec{\nabla} \theta$, B , $v_{ds\psi}$, a_s , $|\vec{\nabla} \psi|^2$, R , and $\partial R/\partial \psi|_\theta$. However, calculating $\vec{\nabla} \alpha$, which appears in the other three coefficients, is more complex as it involves second order radial derivatives of the flux surface shape and an integral. In the Miller local equilibrium, second order radial derivatives must be calculated by ensuring that the Grad-Shafranov equation is satisfied. Referring to (D.8) and (D.15), we see that doing so produces

$$\begin{aligned} \vec{\nabla} \alpha = & - \left(I \int_{\theta_\alpha}^{\theta} \left|_{\psi} d\theta' \left\{ \frac{1}{R^2 B_p} \frac{\partial l_p}{\partial \theta'} \left|_{\psi} \left[\frac{1}{I} \frac{dI}{d\psi} + \frac{I}{R^2 B_p^2} \frac{dI}{d\psi} + \frac{\mu_0}{B_p^2} \frac{\partial p}{\partial \psi} \right|_R \right. \right. \right. \\ & - \left. \frac{2}{R^2 B_p} \left(\frac{\partial l_p}{\partial \theta'} \right)^{-1} \frac{\partial Z}{\partial \theta'} + \frac{2\kappa_p}{R B_p} \right\} - \left[\frac{I}{R^4 B_p^3} \frac{\partial l_p}{\partial \theta'} \left|_{\psi} \vec{\nabla} \psi \cdot \vec{\nabla} \theta' \right|_{\theta'=\theta_\alpha}^{\theta'=\theta} \right. \\ & \left. \left. - \left[\frac{I}{R^2 B_p} \frac{\partial l_p}{\partial \theta} \left|_{\psi} \right]_{\theta=\theta_\alpha} \frac{d\theta_\alpha}{d\psi} + \frac{d\Omega_\zeta}{d\psi} t \right) \vec{\nabla} \psi - \frac{I}{R^2 B_p} \frac{\partial l_p}{\partial \theta} \left|_{\psi} \vec{\nabla} \theta + \vec{\nabla} \zeta, \right. \right. \end{aligned} \quad (7.2)$$

where

$$\kappa_p = \left(\frac{\partial l_p}{\partial \theta} \right)^{-3} \left(\frac{\partial R}{\partial \theta} \frac{\partial^2 Z}{\partial \theta^2} - \frac{\partial^2 R}{\partial \theta^2} \frac{\partial Z}{\partial \theta} \right) \quad (7.3)$$

is the poloidal magnetic field curvature (defined by (3.14) such that the inwards normal direction is positive), l_p is the poloidal arc length defined such that

$$\left. \frac{\partial l_p}{\partial \theta} \right|_\psi = \sqrt{\left. \frac{\partial \vec{r}}{\partial \theta} \right|_\psi \cdot \left. \frac{\partial \vec{r}}{\partial \theta} \right|_\psi} = \sqrt{\left(\left. \frac{\partial R}{\partial \theta} \right|_\psi \right)^2 + \left(\left. \frac{\partial Z}{\partial \theta} \right|_\psi \right)^2}, \quad (7.4)$$

and all quantities are evaluated on the flux surface of interest. Note that $dI/d\psi$ can be found from dq/dr_ψ using (D.17).

7.1.2 Asymptotic expansion

Now we will investigate the effect of high order flux surface shaping, first on the geometric coefficients and then on the fluxes of particles, momentum, and energy. We can always Fourier analyse the flux surface shape and its derivative (without loss of generality) to write (5.8) and (5.9). Next, using trigonometric identities we can convert (5.8) and (5.9) to

$$r_0(\theta, z) = r_{\psi 0} \left(1 - \sum_{l=0}^{\infty} \sum_{k=k_{\min}}^{k_{\max}} \frac{\Delta_{k+lm_c} - 1}{2} [\cos(l(z + m_c \theta_{tm})) \cos(k(\theta + \theta_{tm})) - \sin(l(z + m_c \theta_{tm})) \sin(k(\theta + \theta_{tm}))] \right) \quad (7.5)$$

$$\begin{aligned} \left. \frac{\partial r}{\partial r_\psi} \right|_{r_{\psi 0}, \theta, z} &= 1 - \sum_{l=0}^{\infty} \sum_{k=k_{\min}}^{k_{\max}} \left[\left(\frac{\Delta_{k+lm_c} - 1}{2} + \frac{r_{\psi 0}}{2} \frac{d\Delta_{k+lm_c}}{dr_\psi} \right) \right. \\ &\quad \times [\cos(l(z + m_c \theta_{tm})) \cos(k(\theta + \theta_{tm})) - \sin(l(z + m_c \theta_{tm})) \sin(k(\theta + \theta_{tm}))] \\ &\quad - (k + lm_c) (\Delta_{k+lm_c} - 1) \frac{r_{\psi 0}}{2} \frac{d\theta_{t(k+lm_c)}}{dr_\psi} \\ &\quad \left. \times [\sin(l(z + m_c \theta_{tm})) \cos(k(\theta + \theta_{tm})) + \cos(l(z + m_c \theta_{tm})) \sin(k(\theta + \theta_{tm}))] \right] \end{aligned} \quad (7.6)$$

respectively, where m_c is the characteristic Fourier mode number of the fast shaping,

$$z \equiv m_c \theta \quad (7.7)$$

is a fast spatial scale poloidal coordinate, $k \equiv m - lm_c$, and m_c is in the range $[k_{\min}, k_{\max}]$. Additionally, we require $k_{\max} - k_{\min} = m_c - 1$ to ensure that the summation is over all possible modes. This is the form of a two dimensional Fourier decomposition in the slow spatial scale coordinate θ and the fast spatial scale coordinate z . The definition of l contains the physics of the scale separation as it divides the poloidal variation into fast and slow components. Later, using numerical results we

will motivate $l \equiv \lfloor (m+2)/m_c \rfloor$, where $\lfloor x \rfloor$ is the floor function that gives the integer value n such that $n \leq x < n+1$ for any real number x . This definition of l means that variation at least as rapid as the $m_c - 2$ Fourier mode is considered fast, while any lower modes are considered slow. However, analytically we will expand in $m_c \gg 1$ to investigate the effect of high order flux surface shaping on a traditionally shaped equilibrium. This means that the precise definition of l does not matter because the scales are sufficiently distinct by construction of the expansion.

The separation of scales in (7.5) and (7.6), e.g. $r_0(\theta, z)$, means that

$$\left. \frac{\partial}{\partial \theta} \right|_{w_{||}, \mu} = \left. \frac{\partial}{\partial \theta} \right|_{z, w_{||}, \mu} + m_c \left. \frac{\partial}{\partial z} \right|_{\theta, w_{||}, \mu}. \quad (7.8)$$

Additionally, because we are only interested in bulk behaviour, we will eventually average quantities in z using

$$\overline{(\dots)} \equiv \frac{1}{2\pi} \oint_{-\pi}^{\pi} \Big|_{\theta} dz (\dots). \quad (7.9)$$

7.1.3 Gyrokinetic tilting symmetry

This section contains an analytic calculation that demonstrates a symmetry of the gyrokinetic model, when expanding in $m_c \gg 1$. Since turbulent eddies are generally quite extended along the field line, we expect them to effectively average over the small scale magnetic variations created by fast flux surface shaping. Therefore, we would anticipate that tilting such shaping should have a minimal effect on the turbulence. However, the unexpected result of this calculation is that tilting fast flux surface shaping has an exponentially small effect on the turbulent fluxes in $m_c \gg 1$, rather than a polynomial effect. This argument only relies on $m_c \gg 1$ and does *not* presume that the flux surface shaping is weak.

We will start with a completely general local equilibrium, with flux surfaces specified by $r_0(\theta, z(\theta))$ and $\partial r / \partial r_{\psi}|_{r_{\psi 0}, \theta, z(\theta)}$ (see (7.5) and (7.6)). Using this specification we will compare two different geometries that are identical except for the form of $z(\theta)$. In the untilted case $z(\theta) = z_u(\theta) \equiv m_c \theta$, while in the tilted case $z(\theta) = z_t(\theta) \equiv m_c(\theta + \theta_t)$. We see that the tilted case translates all the fast poloidal variation by a single global tilt angle. Note that this is different than simply translating all of the shaping effects with large Fourier mode numbers. Due to the form of (7.5), the fast variation is tilted, while any slowly varying envelopes that might have been created by high mode number shaping effects are not. Introducing the

tilt into the form of $z(\theta)$ alters the equilibrium and in principle changes the transport properties, but we will show its effect is exponentially small when expanding in $m_c \gg 1$.

Although we just presented two specific examples of $z(\theta)$, we are free to calculate the geometric coefficients for a completely general $z(\theta)$. From the form of the ten geometric coefficients (see appendix D) we see that $z(\theta)$ only enters as z , derivatives of z , and in the integral over poloidal angle contained in $\vec{\nabla}\alpha$ (see (7.2)). This means that we can indicate the poloidal dependence of any geometric coefficient, $Q_{\text{geo}} \in \left\{ B, \hat{b} \cdot \vec{\nabla}\theta, v_{ds\psi}, v_{ds\alpha}, a_{s||}, \left| \vec{\nabla}\psi \right|^2, \vec{\nabla}\psi \cdot \vec{\nabla}\alpha, \left| \vec{\nabla}\alpha \right|^2, R, \partial R / \partial \psi|_{\theta} \right\}$, by writing it as

$$Q_{\text{geo}} \left(\theta, z, \frac{\partial z}{\partial \theta}, \frac{\partial^2 z}{\partial \theta^2}, \int_{\theta_\alpha}^{\theta} \left|_{\psi} d\theta' F_\alpha \left(\theta', z(\theta'), \frac{\partial z}{\partial \theta'}, \frac{\partial^2 z}{\partial \theta'^2} \right) - \left[\frac{1}{R^2 B_p^2} \frac{\partial l_p}{\partial \theta} \right]_{\psi} \right|_{\theta=\theta_\alpha} \frac{d\theta_\alpha}{d\psi} \right), \quad (7.10)$$

where

$$F_\alpha \left(\theta, z(\theta), \frac{\partial z}{\partial \theta}, \frac{\partial^2 z}{\partial \theta^2} \right) \equiv \frac{1}{R^2 B_p} \frac{\partial l_p}{\partial \theta} \left|_{\psi} \left[\frac{1}{I} \frac{dI}{d\psi} - \frac{1}{B_p} \frac{\partial B_p}{\partial \psi} \right]_{\theta} - \frac{2}{R} \frac{\partial R}{\partial \psi} \right|_{\theta} + \left(\frac{\partial l_p}{\partial \theta} \right|_{\psi} \right)^{-1} \frac{\partial}{\partial \psi} \left|_{\theta} \left(\frac{\partial l_p}{\partial \theta} \right|_{\psi} \right) \quad (7.11)$$

is a periodic function of both θ and z .

Now we will compare the untilted equilibrium ($z(\theta) = z_u(\theta) \equiv m_c \theta$) and the equilibrium with tilted fast shaping effects ($z(\theta) = z_t(\theta) \equiv m_c(\theta + \theta_t)$). Since the only difference between the two cases is contained in the form of $z(\theta)$, we only need to look for differences in the arguments of (7.10). We immediately see that $\partial z_u / \partial \theta = \partial z_t / \partial \theta = m_c$ and all higher order poloidal derivatives are zero. Hence, we can eliminate the derivatives to write the geometric coefficients as

$$Q_{\text{geo}}(\theta, z, G_\alpha(\theta, z(\theta)) + H_\alpha) \quad (7.12)$$

for both cases, where we choose to define

$$G_\alpha(\theta, z(\theta)) \equiv \int_{\theta_\alpha}^{\theta} \left|_{\psi} d\theta' F_\alpha(\theta', z(\theta')) \quad (7.13)$$

$$H_\alpha \equiv - \left[\frac{1}{R^2 B_p^2} \frac{\partial l_p}{\partial \theta} \right]_{\psi} \bigg|_{\theta=\theta_\alpha} \frac{d\theta_\alpha}{d\psi}. \quad (7.14)$$

As we will now show, we can also eliminate the integral $\int_{\theta_\alpha}^\theta \Big|_\psi d\theta' F_\alpha(\theta', z(\theta'))$, in addition to the derivatives. To do so, we start by defining the operator

$$\Lambda[g](\theta, z) \equiv \int_{z_0}^z \Big|_\theta dz' \left(g(\theta, z') - \overline{g(\theta, z)} \right), \quad (7.15)$$

where the integral over z is done holding θ constant, $g(\theta, z)$ is a yet unspecified function that is periodic in both θ and z , and z_0 is chosen such that

$$\overline{\Lambda[g](\theta, z)} = 0 \quad (7.16)$$

(which can always be found when g is periodic in z). Taking the total derivative in θ we find

$$\frac{d}{d\theta} \Lambda[g](\theta, z(\theta)) = \frac{\partial}{\partial \theta} \Big|_z \Lambda[g] + m_c \frac{\partial}{\partial z} \Big|_\theta \Lambda[g] \quad (7.17)$$

from (7.8), where we have taken $dz/d\theta = m_c$. Substituting in (7.15) and rearranging gives

$$g(\theta, z) - \overline{g(\theta, z)} = \frac{1}{m_c} \frac{d}{d\theta} \Lambda[g] - \frac{1}{m_c} \frac{\partial}{\partial \theta} \Big|_z \Lambda[g]. \quad (7.18)$$

Integrating (7.18) with respect to θ and then using

$$\frac{\partial}{\partial \theta} \Big|_z \Lambda[g] = \Lambda \left[\frac{\partial g}{\partial \theta} \Big|_z \right] \quad (7.19)$$

gives

$$\begin{aligned} \int_{\theta_\alpha}^\theta \Big|_\psi d\theta' \left(g(\theta', z(\theta')) - \overline{g(\theta', z)} \right) &= \frac{1}{m_c} \left(\Lambda[g](\theta, z) - \Lambda[g](\theta_\alpha, z(\theta_\alpha)) \right) \\ &\quad - \frac{1}{m_c} \int_{\theta_\alpha}^\theta \Big|_\psi d\theta' \Lambda \left[\frac{\partial g}{\partial \theta'} \Big|_z \right]. \end{aligned} \quad (7.20)$$

Now since $g(\theta, z)$ is an unspecified periodic function, we can always make the substitution $g(\theta, z) \rightarrow \Lambda[\partial g / \partial \theta|_z]$ because $\Lambda[\partial g / \partial \theta|_z]$ is also a periodic function. Doing so in (7.20) gives

$$\begin{aligned} \int_{\theta_\alpha}^\theta \Big|_\psi d\theta' \Lambda \left[\frac{\partial g}{\partial \theta'} \Big|_z \right] &= \frac{1}{m_c} \left(\Lambda^2 \left[\frac{\partial g}{\partial \theta} \Big|_z \right](\theta, z(\theta)) - \Lambda^2 \left[\frac{\partial g}{\partial \theta} \Big|_z \right](\theta_\alpha, z(\theta_\alpha)) \right) \\ &\quad - \frac{1}{m_c} \int_{\theta_\alpha}^\theta \Big|_\psi d\theta' \Lambda^2 \left[\frac{\partial^2 g}{\partial \theta'^2} \Big|_z \right]. \end{aligned} \quad (7.21)$$

The second term on the left-hand side vanished because the definition of z_0 requires (7.16), so we know $\partial \overline{\Lambda[g]}/\partial \theta \Big|_z = \overline{\Lambda[\partial g/\partial \theta|_z]} = 0$ from (7.19). Here $\Lambda^i[\dots]$ indicates that the operator $\Lambda[\dots]$ is applied i times. Substituting (7.21) into the last term of (7.20), we see that (7.20) is a recursion relation that can be put in the form of an infinite series,

$$\int_{\theta_\alpha}^\theta \Big|_\psi d\theta' \left(g(\theta', z(\theta')) - \overline{g(\theta', z)} \right) = \sum_{p=1}^{\infty} \frac{(-1)^{p-1}}{m_c^p} \left(\Lambda^p \left[\frac{\partial^{p-1} g}{\partial \theta^{p-1}} \Big|_z \right] (\theta, z(\theta)) - \Lambda^p \left[\frac{\partial^{p-1} g}{\partial \theta^{p-1}} \Big|_z \right] (\theta_\alpha, z(\theta_\alpha)) \right). \quad (7.22)$$

Finally choosing the form $g(\theta, z) = F_\alpha(\theta, z)$ and rearranging we can calculate the integral appearing in the geometric coefficients (see (7.13)) to be

$$G_\alpha(\theta, z(\theta)) = \int_{\theta_\alpha}^\theta \Big|_\psi d\theta' \overline{F_\alpha(\theta', z)} + \sum_{p=1}^{\infty} \frac{(-1)^{p-1}}{m_c^p} \left(\Lambda^p \left[\frac{\partial^{p-1} F_\alpha}{\partial \theta^{p-1}} \Big|_z \right] (\theta, z(\theta)) - \Lambda^p \left[\frac{\partial^{p-1} F_\alpha}{\partial \theta^{p-1}} \Big|_z \right] (\theta_\alpha, z(\theta_\alpha)) \right). \quad (7.23)$$

For the untilted case we can set $\theta_\alpha = d\theta_\alpha/d\psi = 0$ and use (7.23) to prove that the quantity appearing in the geometric coefficients (see (7.12)) is

$$G_\alpha(\theta, z_u(\theta)) + H_\alpha = \int_0^\theta \Big|_\psi d\theta' \overline{F_\alpha(\theta', z)} + \sum_{p=1}^{\infty} \frac{(-1)^{p-1}}{m_c^p} \left(\Lambda^p \left[\frac{\partial^{p-1} F_\alpha}{\partial \theta^{p-1}} \Big|_z \right] (\theta, z_u(\theta)) - \Lambda^p \left[\frac{\partial^{p-1} F_\alpha}{\partial \theta^{p-1}} \Big|_z \right] (0, 0) \right). \quad (7.24)$$

In the tilted case ($z = z_t = m_c(\theta + \theta_t)$) we can carefully choose

$$\frac{d\theta_\alpha}{d\psi} = \left[\frac{1}{R^2 B_p^2} \frac{\partial l_p}{\partial \theta} \Big|_\psi \right]_{\theta=\theta_\alpha}^{-1} \left\{ \int_{\theta_\alpha}^0 \Big|_\psi d\theta' \overline{F_\alpha(\theta', z)} + \sum_{p=1}^{\infty} \frac{(-1)^{p-1}}{m_c^p} \left(\Lambda^p \left[\frac{\partial^{p-1} F_\alpha}{\partial \theta^{p-1}} \Big|_z \right] (0, 0) - \Lambda^p \left[\frac{\partial^{p-1} F_\alpha}{\partial \theta^{p-1}} \Big|_z \right] (\theta_\alpha, z_t(\theta_\alpha)) \right) \right\} \quad (7.25)$$

to substitute into (7.14), giving

$$G_\alpha(\theta, z_t(\theta)) + H_\alpha = \int_0^\theta \Big|_\psi d\theta' \overline{F_\alpha(\theta', z)} + \sum_{p=1}^{\infty} \frac{(-1)^{p-1}}{m_c^p} \left(\Lambda^p \left[\frac{\partial^{p-1} F_\alpha}{\partial \theta^{p-1}} \Big|_z \right] (\theta, z_t(\theta)) - \Lambda^p \left[\frac{\partial^{p-1} F_\alpha}{\partial \theta^{p-1}} \Big|_z \right] (0, 0) \right). \quad (7.26)$$

This exactly matches (7.24) (except for replacing z_u with z_t) and means the entire effect of the tilt can be contained in the functional form of z . To make things as simple as possible we also choose

$$\theta_\alpha = 0 \quad (7.27)$$

for the tilted case.

The choice of $d\theta_\alpha/d\psi$ in (7.25) means that the geometric coefficients for both the untilted and tilted cases can be written in the form

$$Q_{\text{geo}}(\theta, z), \quad (7.28)$$

where $z = z_u$ for the untilted case and $z = z_t$ for the tilted case. Therefore, we know that

$$Q_{\text{geo}}^t(\theta, z_u) = Q_{\text{geo}}^u(\theta, z_u + m_c \theta_t) \quad (7.29)$$

for each of the geometric coefficients, where the superscript u indicates the quantity in the untilted configuration and the superscript t indicates the tilted configuration.

Since all of the geometric coefficients depend separately on both θ and z we know that h_s , ϕ , $A_{||}$, and $B_{||}$ must also. Apart from the geometric coefficients, the only way the poloidal coordinate enters the gyrokinetic equations is through the poloidal derivative in the streaming term (i.e. the second term of (6.5)). However, (7.8) is appropriate for both $z = z_u$ and $z = z_t$. Hence, using any solution to the gyrokinetic equation for the untilted case, $\{h_s^u(\theta, z_u), \phi^u(\theta, z_u), A_{||}^u(\theta, z_u), B_{||}^u(\theta, z_u)\}$, we can construct a solution for the tilted case,

$$\begin{aligned} & \{h_s^t(\theta, z_u), \phi^t(\theta, z_u), A_{||}^t(\theta, z_u), B_{||}^t(\theta, z_u)\} \\ &= \{h_s^u(\theta, z_u + m_c \theta_t), \phi^u(\theta, z_u + m_c \theta_t), A_{||}^u(\theta, z_u + m_c \theta_t), B_{||}^u(\theta, z_u + m_c \theta_t)\}, \end{aligned} \quad (7.30)$$

given our choices for the free parameter $\theta_\alpha(\psi)$ in the definition of α (i.e. (7.25) and (7.27)). Because the average over z (see (7.9)) can always be shifted by $m_c \theta_t$ without affecting the result these two solution sets give the same large scale turbulent fluxes and turbulent energy exchange between species, e.g. in the electrostatic limit they

are

$$\Gamma_s^\phi = \frac{4\pi^2 i}{m_s V'} \left\langle \sum_{k_\psi, k_\alpha} k_\alpha \oint d\theta J B \phi(k_\psi, k_\alpha) \int dw_\parallel d\mu h_s(-k_\psi, -k_\alpha) J_0(k_\perp \rho_s) \right\rangle_{\Delta t} \quad (7.31)$$

$$\begin{aligned} \Pi_{\zeta s}^\phi &= \frac{4\pi^2 i}{V'} \left\langle \sum_{k_\psi, k_\alpha} k_\alpha \oint d\theta J B \phi(k_\psi, k_\alpha) \int dw_\parallel d\mu h_s(-k_\psi, -k_\alpha) \right. \\ &\quad \times \left. \left[\left(\frac{I}{B} w_\parallel + R^2 \Omega_\zeta \right) J_0(k_\perp \rho_s) + \frac{i}{\Omega_s} \frac{k^\psi}{B} \frac{\mu B}{m_s} \frac{2J_1(k_\perp \rho_s)}{k_\perp \rho_s} \right] \right\rangle_{\Delta t} \end{aligned} \quad (7.32)$$

$$\begin{aligned} Q_s^\phi &= \frac{4\pi^2 i}{V'} \left\langle \sum_{k_\psi, k_\alpha} k_\alpha \oint d\theta J B \phi(k_\psi, k_\alpha) \int dw_\parallel d\mu h_s(-k_\psi, -k_\alpha) \right. \\ &\quad \times \left. \left(\frac{w^2}{2} + \frac{Z_s e \Phi_0}{m_s} - \frac{1}{2} R^2 \Omega_\zeta^2 \right) J_0(k_\perp \rho_s) \right\rangle_{\Delta t} \end{aligned} \quad (7.33)$$

$$P_{Qs}^\phi = \frac{4\pi^2}{V'} \left\langle \sum_{k_\psi, k_\alpha} \oint d\theta J \Omega_s \frac{\partial}{\partial t} (\phi(k_\psi, k_\alpha)) \int dw_\parallel d\mu h_s(-k_\psi, -k_\alpha) J_0(k_\perp \rho_s) \right\rangle_{\Delta t} . \quad (7.34)$$

Looking at the full electromagnetic fluxes and the turbulent energy exchange between species (see appendix C) we see that they also remain unchanged by the tilt.

Since we relied on expanding in $m_c \gg 1$ to separate scales in (7.31) through (7.34), this argument can only give the fluxes as an expansion in powers of $1/m_c$, not the unexpanded quantity. We already know that, since the two configuration are not *exactly* identical, they will in general produce different fluxes. However, the above argument proves the two configurations must have the same fluxes to all orders in $1/m_c$. This demonstrates that, while the fluxes from the two configurations can be different, the difference does not scale polynomially and so cannot scale more strongly than $\sim \exp(-\beta m_c^\gamma)$, where β and γ are both positive and do not depend on m_c .

7.1.4 Accuracy of the local equilibrium approximation

We finish with an important remark concerning our use of an approximate local MHD equilibrium, as opposed to the full global MHD equilibria. Although there was no problem in the Miller local equilibrium, it may not be possible to exactly tilt the fast flux surface shaping poloidally in a real global equilibrium. We can always Fourier analyse a flux surface shape and its radial derivative (see (5.8) and (5.9)). We can also use the external shaping coils to arbitrarily tilt the fast shaping of the flux surface of

interest. However, the way that the radial derivative of the flux surface shape changes with tilt is set by the global MHD equilibrium and is not under our control (as it is in the Miller local equilibrium approximation). The global equilibrium in a screw pinch has cylindrical symmetry, but in a tokamak toroidal effects may preclude tilting the radial derivative of the flux surface shape in exactly the same manner we tilted the flux surface shape itself.

This means that, strictly speaking, when we introduce $z_t(\theta) = m_c(\theta + \theta_t)$ into the derivative of the flux surface shape we may no longer be modelling a physically possible tokamak. However, we can construct a proof by induction to show that the effect of toroidicity on mode m_c must be exponentially small in $m_c \gg 1$. We start by rearranging the Grad-Shafranov equation (i.e. (2.2)) as

$$R\vec{\nabla} \cdot \left(\frac{\vec{\nabla}\psi}{R} \right) + I \frac{dI}{d\psi} = \frac{1}{R} \vec{\nabla} R \cdot \vec{\nabla} \psi - \mu_0 R^2 \left. \frac{\partial p}{\partial \psi} \right|_R. \quad (7.35)$$

The left side of this equation is completely cylindrically symmetric, while the right side contains all of the toroidal effects. To $O(B_0)$ in the large aspect ratio limit the Grad-Shafranov equation does not include toroidicity (see (2.6)). This is the base case of the inductive argument and demonstrates that ψ_0 has tilting symmetry, i.e. $\psi_0^t(\theta, z) = \psi_0^u(\theta, z + m_c \theta_t)$. To $O(\epsilon^i B_0)$ the Grad-Shafranov equation only depends on R , derivatives of R , and $\psi_j(\theta, z)$ (where i and j are integers and $0 \leq j < i$). During the proof of the gyrokinetic tilting symmetry (see section 7.1.3), we showed that R and the derivatives of R have the appropriate tilting symmetry. Furthermore, by the complete induction hypothesis we know that $\psi_j(\theta, z)$ is tilting symmetric for all $0 \leq j < i$. Therefore, ψ follows the same tilting symmetry as gyrokinetics to all orders. Hence, tilting the radial derivative of the flux surface shape in the same manner as the flux surface shape produces a local Miller equilibrium that only differs from the actual equilibrium by an exponentially small error in $m_c \gg 1$.

As an illustration of this, reference [66] uses an equilibrium that is circular to lowest order in aspect ratio to show that at $O(B_0)$ the Grad-Shafranov equation is entirely cylindrically symmetric, at $O(\epsilon B_0)$ toroidicity introduces a natural shift (i.e. the Shafranov shift), at $O(\epsilon^2 B_0)$ toroidicity introduces a natural elongation, and at $O(\epsilon^3 B_0)$ toroidicity introduces a natural triangularity. This indicates that, in a global equilibrium, toroidicity introduces an $O(\epsilon^m)$ modification to the m^{th} Fourier mode of a flux surface. Therefore, the error introduced into the geometric coefficients by ignoring this effect in the local equilibrium approximation is $O(\epsilon^{m_{\min}})$, where m_{\min} is the smallest mode number that is tilted. This error is exponentially small in $m_c \gg 1$,

hence it does not change our result that tilting the equilibrium has an exponentially small effect on the turbulent fluxes.

7.2 Numerical results

In this section we will give numerical results to test the analytic conclusions of the previous section. We use GS2 to calculate the nonlinear turbulent fluxes of momentum and energy generated by a given geometry. We investigate the influence of the shape of the flux surface of interest by scanning m_c , the characteristic mode number of the fast poloidal shaping. The geometry is specified using the generalisation of the Miller local equilibrium model presented in chapter 5. The flux surface shapes (shown in figure 7.2) are parameterized by (7.5) through (7.7) as well as (5.7), with only one high order mode, $m = m_c$ (which corresponds to $l = 1$ and $k = 0$). We will choose

$$\Delta_m - 1 = \frac{3}{2}m_c^{-2} \quad (7.36)$$

because it has a physical scaling (see appendix A) and seems reasonably similar to the typical magnitude of flux surface shaping effects in experiments. For example, regular polygons have $\Delta_m - 1 = \sec(\pi/m) - 1 \sim m^{-2}$, so we see that exceeding this scaling necessarily leads to flux surfaces with convex regions. With the exception of “bean-shaped” tokamaks [67], practically all proposed experimental configurations have purely concave flux surfaces, so we know they respect this scaling. We will also take $d\Delta_m/dr_\psi = (m_c - 2)(\Delta_m - 1)/r_{\psi 0}$ (appropriate for a constant current profile according to (5.11)) and $d\theta_{tm}/dr_\psi = 0$ (appropriate for a constant current profile according to (5.12)) in the scan to give the neighbouring flux surfaces a reasonable shape. Up-down asymmetric geometries are created by fixing the tilt angle at $\theta_{tm} = \pi/(2m_c)$, the angle halfway between neighbouring up-down symmetric configurations (at $\theta_{tm} = 0$ and $\theta_{tm} = \pi/m_c$), while the up-down symmetric configurations have $\theta_{tm} = 0$.

Except for the shape, all parameters of the flux surface of interest are fixed at Cyclone base case values [68] of

$$\begin{aligned} \rho_0 \equiv a_{\psi 0}/a &= 0.54, & R_{c0}/a &= 3, & q &= 1.4, \\ \hat{s} &= 0.8, & a/L_{Ts} &= 2.3, & a/L_{ns} &= 0.733 \end{aligned} \quad (7.37)$$

for the minor radius, major radius, safety factor, magnetic shear, temperature gradient, and density gradient respectively. All simulations are electrostatic and collisionless. The fluxes calculated by GS2 are normalised to their gyroBohm values

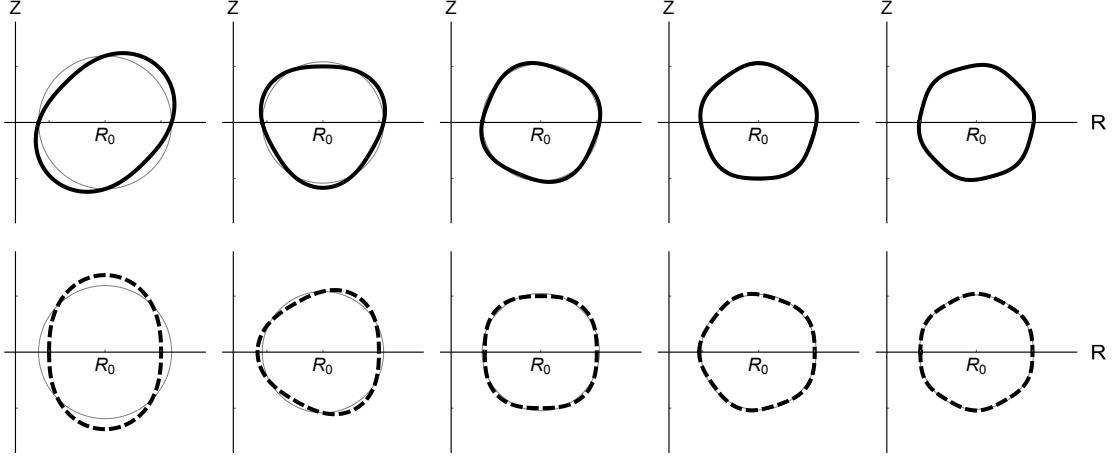


Figure 7.2: The $m_c = 2$ through $m_c = 6$ flux surface geometries in the tilted (solid) and up-down symmetric (dashed) configurations, with circular flux surfaces shown for comparison (grey).

of

$$\Pi_{gB} \equiv \rho_*^2 n_i a m_i v_{thi}^2 \quad (7.38)$$

$$Q_{gB} \equiv \rho_*^2 n_i T_i v_{thi}, \quad (7.39)$$

where n_i is the ion density, m_i is the ion mass, T_i is the local ion temperature, and $v_{thi} \equiv \sqrt{2T_i/m_i}$ is the local ion thermal speed.

We will compare the numerical scans in m_c (shown in figure 7.2) to the analytic theory in two different manners. From (7.30) we expect that, using the poloidal distribution of any flux from a given geometry, it should be possible to predict the flux from any geometry that is identical except for a poloidal tilt of the fast variation. First, we will directly investigate this by comparing the poloidal dependence of the fluxes of particles, momentum, and energy in just such geometries. Then, we will show that the change in the total fluxes due to tilting fast shaping disappears in the limit of $m_c \gg 1$.

7.2.1 Poloidal structure of fluxes

In section 7.1.3, we presented an analytic argument showing that (when expanding in $m_c \gg 1$) the solution to the gyrokinetic equation for a given geometry can be used to generate the solution to any geometry that is identical, except for a global tilt of the fast poloidal variation. This relationship, given by (7.30), makes predictions about the poloidal distributions of fluxes. In appendix C we define the poloidal distribution

of the different quantities that appear in the gyrokinetic model. In the electrostatic limit they are given by

$$\gamma_s^\phi \equiv -R \left\langle \left\langle \int d^3w \underline{h}_s \hat{e}_\zeta \cdot \delta \vec{E} \right\rangle_{\Delta\psi} \right\rangle_{\Delta t} \quad (7.40)$$

$$\pi_{\zeta s}^\phi \equiv -R \left\langle \left\langle \int d^3w \underline{h}_s m_s R (\vec{w} \cdot \hat{e}_\zeta + R \Omega_\zeta) \hat{e}_\zeta \cdot \delta \vec{E} \right\rangle_{\Delta\psi} \right\rangle_{\Delta t} \quad (7.41)$$

$$q_s^\phi \equiv -R \left\langle \left\langle \int d^3w \underline{h}_s \left(\frac{m_s}{2} w^2 + Z_s e \Phi_0 - \frac{m_s}{2} R^2 \Omega_\zeta^2 \right) \hat{e}_\zeta \cdot \delta \vec{E} \right\rangle_{\Delta\psi} \right\rangle_{\Delta t} \quad (7.42)$$

$$p_{Qs}^\phi \equiv \left\langle \left\langle \int d^3w Z_s e \underline{h}_s \frac{\partial \phi}{\partial t} \right\rangle_{\Delta\psi} \right\rangle_{\Delta t}, \quad (7.43)$$

which are just (6.18), (6.20), (6.22), and (6.24) without the flux surface average (e.g. $Q_s = \langle q_s \rangle_\psi$). Specifically, using (7.30) the analytic theory predicts that we should find

$$\gamma_s^t(\theta, z) = \gamma_s^u(\theta, z + m_c \theta_t) \quad (7.44)$$

$$\pi_{\zeta s}^t(\theta, z) = \pi_{\zeta s}^u(\theta, z + m_c \theta_t) \quad (7.45)$$

$$q_s^t(\theta, z) = q_s^u(\theta, z + m_c \theta_t) \quad (7.46)$$

$$p_{Qs}^t(\theta, z) = p_{Qs}^u(\theta, z + m_c \theta_t), \quad (7.47)$$

where the superscript u indicates the geometry is up-down symmetric (i.e. untilted), t indicates the geometry is tilted, and for our chosen geometries $\theta_t = \theta_{tm}$. By simulating several up-down symmetric geometries (see the bottom row of figure 7.2) and their corresponding tilted geometries (see the top row of figure 7.2) we can numerically verify (7.44) through (7.47). We will focus on the ion momentum flux because the symmetry has particularly profound consequences for it, but the analysis in this section can be applied to any of the fluxes.

We should note that GS2 automatically takes $\theta_\alpha(\psi) = 0$ in its definition of α (see (6.4)), so we have to be careful about making numerical predictions from our analytic results. In general, converting between our definition of α and the GS2 definition, α_{GS2} , involves accounting for a shift in α and $\vec{\nabla} \alpha$ of

$$\delta(\alpha) = -I \int_{\theta_\alpha}^0 \left|_{\psi} d\theta' \left(R^2 \vec{B} \cdot \vec{\nabla} \theta' \right)^{-1} \right. \quad (7.48)$$

$$\delta(\vec{\nabla} \alpha) = -I \left(\int_{\theta_\alpha}^0 \left|_{\psi} d\theta' F_\alpha(\theta') - \left[\frac{1}{R^2 B_p} \frac{\partial l_p}{\partial \theta} \right]_{\psi} \right)_{\theta=\theta_\alpha} \frac{d\theta_\alpha}{d\psi} \right) \vec{\nabla} \psi \quad (7.49)$$

respectively. However, given our specific choices in (7.25) and (7.27) we see that

$$\delta(\alpha) = 0 \quad (7.50)$$

$$\begin{aligned} \delta(\vec{\nabla}\alpha) = I \sum_{p=1}^{\infty} \frac{(-1)^{p-1}}{m_c^p} \left(\Lambda^p \left[\frac{\partial^{p-1} F_\alpha}{\partial \theta^{p-1}} \right]_z (0, 0) \right. \\ \left. - \Lambda^p \left[\frac{\partial^{p-1} F_\alpha}{\partial \theta^{p-1}} \right]_z (0, m_c \theta_t) \right) \vec{\nabla}\psi. \end{aligned} \quad (7.51)$$

The only effect of the shift in α is to introduce a phase factor of $\exp(-ik_\alpha \delta(\alpha))$ in the Fourier analysed turbulent quantities h_s , ϕ , A_\parallel , and B_\parallel (e.g. (6.6)). The shift in $\vec{\nabla}\alpha$ only enters the gyrokinetic model through the quantity

$$\vec{k}_\perp = k_\psi \vec{\nabla}\psi + k_\alpha \vec{\nabla}\alpha = \left[k_\psi + k_\alpha \frac{\partial \vec{r}}{\partial \psi} \cdot \delta(\vec{\nabla}\alpha) \right] \vec{\nabla}\psi + k_\alpha \vec{\nabla}\alpha_{\text{GS2}}. \quad (7.52)$$

Fortunately, neither of these changes has an effect on (7.44) through (7.47). The phase factor cancels because all transport is driven by the beating of two turbulent quantities (see appendix C): one with the complex conjugate taken, the other without. As seen in (7.52), the tilt of $\vec{\nabla}\alpha$ can be taken into account by shifting k_ψ . Since the fluxes we are looking at involve the sum over all of wavenumber space, shifting flux from one wavenumber to another does not alter the total value.

Because GS2 is not constructed to separate the two spatial scales represented by θ and z , our simulations give $\pi_{\zeta s}(\theta) = \pi_{\zeta s}(\theta, z(\theta))$ rather than $\pi_{\zeta s}(\theta, z)$. Therefore, we have to take the data produced by GS2, separate the dependences on the fast and slow poloidal coordinate, and tilt only the fast spatial variation. Repeating the analysis from section 7.1.2, we start by Fourier analysing the poloidal distribution of momentum flux from GS2,

$$\pi_{\zeta s}^u(\theta) = \sum_{m=1}^{\infty} P_m \sin(m\theta), \quad (7.53)$$

in the untilted case. Figure 7.3(a) shows a typical Fourier spectrum for the momentum flux calculated by GS2. Since the untilted case is up-down symmetric, we know from section 6.2 that the momentum flux distribution must be odd in θ , so we have neglected the even terms in (7.53). These even terms must be retained when considering the particle or energy fluxes. As in section 7.1.2, we want to transform (7.53) into the form of a two dimensional Fourier series in the two separate spatial scales, e.g.

$$\pi_{\zeta s}^u(\theta, z) = \sum_{l=0}^{\infty} \sum_{k=k_{\min}}^{k_{\max}} P_{k+lm_c} \left(\sin(lz) \cos(k\theta) + \cos(lz) \sin(k\theta) \right). \quad (7.54)$$

Using some trigonometric identities and (7.7) it can be shown that if we choose to define k as

$$k \equiv m - lm_c, \quad (7.55)$$

then we can transform (7.53) into (7.54) as long as $k_{max} - k_{min} = m_c - 1$.

The definition of l contains the physics of the scale separation and consequently will strongly affect how well we match GS2 results. The definition of l controls which Fourier harmonics (enumerated by m) are mapped to $l = 0$ (and remain untilted), as opposed to $l = 1$ (which are tilted by $m_c\theta_t$), $l = 2$ (which are tilted by $2m_c\theta_t$), etc. Intuitively we expect modes with $m \approx 1$ should remain untilted (i.e. map to $l = 0$), modes with $m \approx m_c$ should map to $l = 1$, and modes with $m \approx 2m_c$ should map to $l = 2$. This general intuition motivates some sort of rounding to integers. The specific form of

$$l \equiv \left\lfloor \frac{m+2}{m_c} \right\rfloor \quad (7.56)$$

(where $\lfloor x \rfloor$ is the floor function) was chosen in accordance with figure 7.3(b). We see that, as the shaping effect mode number m_c is increased, the $m_c - 2$ and $m_c - 1$ Fourier terms of the momentum flux track with it, while all lower modes stay roughly constant. Unsurprisingly, this definition of l was also found to produce the best agreement between theory and GS2 data. Our choice for k and l requires that $k_{min} = -2$ and $k_{max} = m_c - 3$ in order to include all modes in the summation, meaning (7.54) becomes

$$\pi_{\zeta s}^u(\theta, z) = \sum_{l=0}^{\infty} \sum_{k=-2}^{m_c-3} P_{k+lm_c} \left(\sin(lz) \cos(k\theta) + \cos(lz) \sin(k\theta) \right). \quad (7.57)$$

Now we can use (7.45) to construct

$$\pi_{\zeta s}^t(\theta, z) = \sum_{l=0}^{\infty} \sum_{k=-2}^{m_c-3} P_{k+lm_c} \left(\sin(lz + lm_c\theta_t) \cos(k\theta) + \cos(lz + lm_c\theta_t) \sin(k\theta) \right), \quad (7.58)$$

a prediction for the distribution of momentum flux in the tilted geometry.

Fundamentally, in this comparison we are testing the truth of (7.30) and (7.45), which we used in deriving (7.58). In figure 7.4, we use the numerical results from the untilted configuration and (7.58) to generate what we expect the momentum flux to be in the corresponding tilted configuration. Visually we see good agreement between

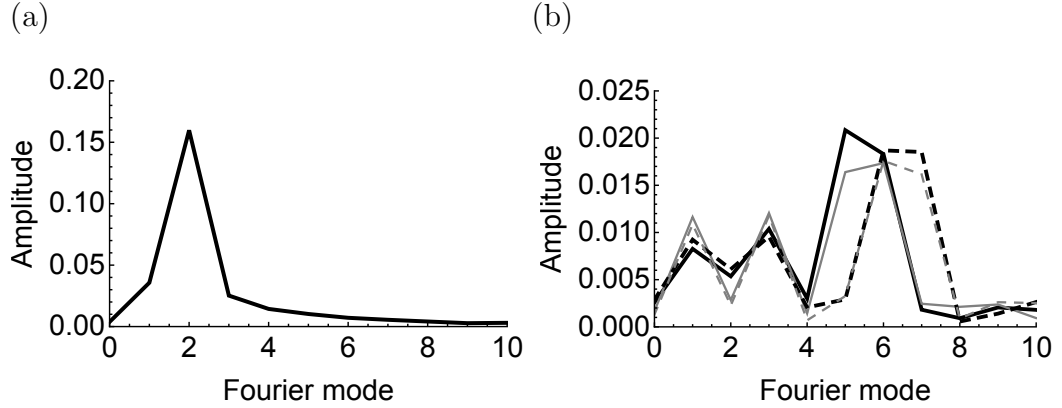


Figure 7.3: (a) The Fourier spectrum of the poloidal distribution of the ion momentum flux generated in circular flux surfaces.
(b) The Fourier spectrum of the poloidal distribution of ion momentum flux after subtracting the flux generated by circular flux surfaces (shown in (a)) for up-down symmetric (grey) and tilted (black) configurations in the $m_c = 7$ (solid) and $m_c = 8$ (dashed) geometries.

the analytic expectation and the actual GS2 results. In figure 7.5 we quantify the agreement by calculating the fractional error according to

$$\Delta_\pi \equiv \frac{\oint_{-\pi}^{\pi} d\theta |\pi_{\zeta s}^{\text{act}}(\theta) - \pi_{\zeta s}^{\text{calc}}(\theta)|}{\oint_{-\pi}^{\pi} d\theta |\pi_{\zeta s}^{\text{act}}(\theta)|}, \quad (7.59)$$

where $\pi_{\zeta s}^{\text{act}}(\theta)$ is the GS2 momentum flux distribution from the tilted geometry (the thick black lines in figure 7.4) and $\pi_{\zeta s}^{\text{calc}}(\theta)$ is either the predicted distribution calculated analytically from the GS2 untilted result (the dashed black lines in figure 7.4) or the raw GS2 untilted result (the thin grey lines in figure 7.4) to serve as a control. As is also apparent from figure 7.4, when we look at geometries with larger values of m_c we find better agreement between the titled geometry and the analytic prediction from the up-down symmetric geometry. The agreement breaks down significantly below $m_c = 5$ and we have enough information to understand why. Extrapolating from figure 7.3(b), we would expect $m_c = 4$ shaping to be problematic because it generates an ion momentum flux distribution with a strong $m = 2$ Fourier mode. This would be indistinguishable from the dominant $m = 2$ Fourier mode, which is from toroidicity (see figure 7.3(a)). Since we cannot separate these two contributions (the one from the $m_c = 4$ shaping and the one from toroidicity), it is not possible to translate the contribution from the $m_c = 4$ shaping as is appropriate.

These numerical results verify (7.30) and the analytic derivation of section 7.1.3. Additionally, though not shown here, the poloidal distributions of particle, momen-

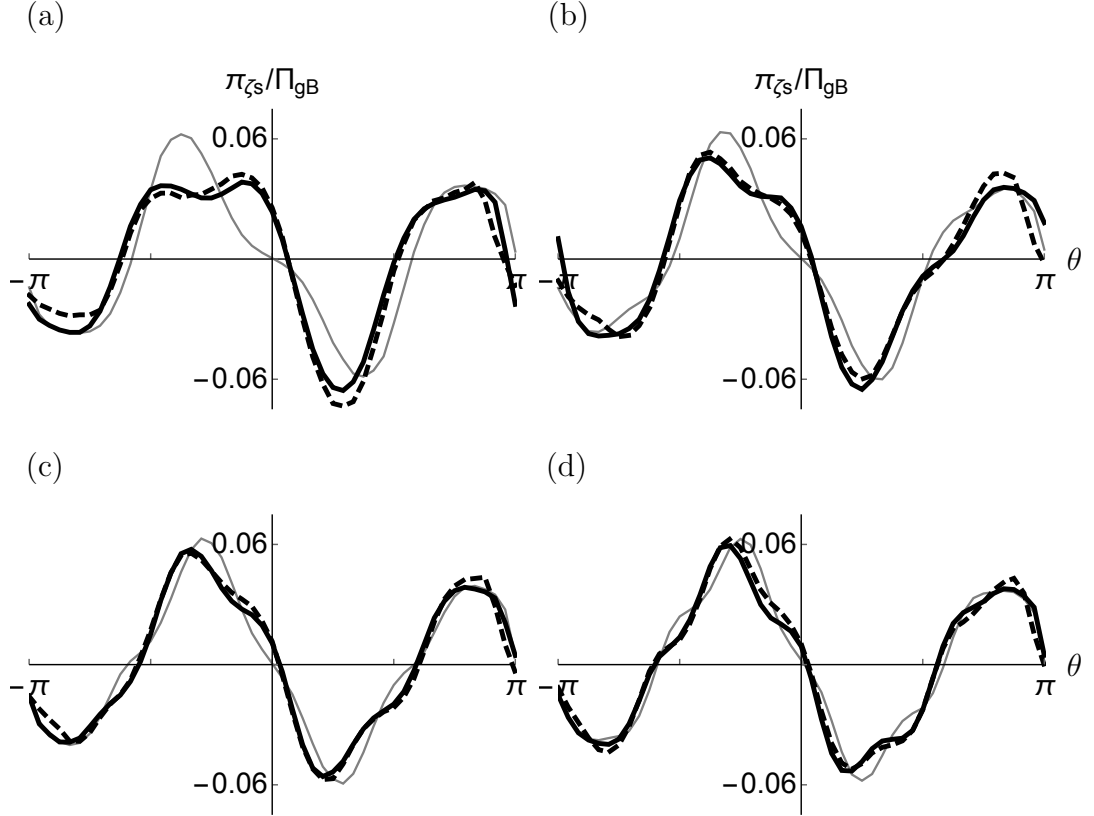


Figure 7.4: The full poloidal distribution of the ion momentum flux (see (7.41)) for the tilted geometry (black, thick), up-down symmetric geometry transformed according to the analytic argument (dashed, thick), and up-down symmetric geometry without any transformation (grey, thin), using (a) $m_c = 5$, (b) $m_c = 6$, (c) $m_c = 7$, and (d) $m_c = 8$ geometries (see figure 7.2). The momentum flux is normalised to the gyroBohm value.

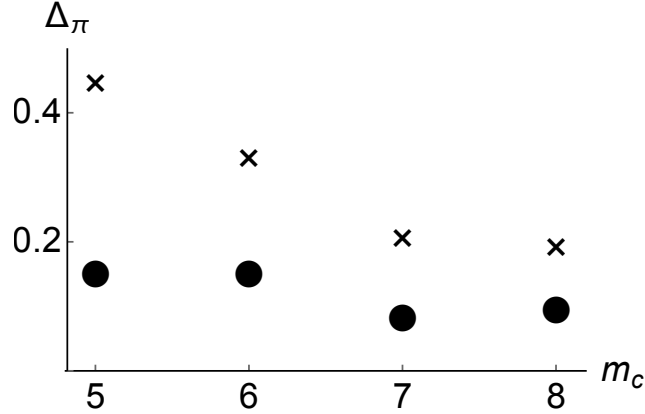


Figure 7.5: The fractional error (i.e. (7.59)) between the poloidal distribution of the momentum flux in the tilted geometry and the distribution predicted from the untilted geometry (circles), with the fractional error between the tilted and untilted (without any adjustment) shown as a control (crosses).

tum, and energy flux (for both ions and electrons) all agree with theory in a similar manner to what is seen in figure 7.4.

7.2.2 Change in total fluxes with tilt

From section 7.1.3 we expect the change in the turbulent fluxes (i.e. (7.31) through (7.33)) due to the tilt of fast shaping effects to be exponentially small in $m_c \gg 1$. In figure 7.6, we show the fractional difference between the ion energy flux from an up-down symmetric configuration and the corresponding tilted configuration, for the geometries of figure 7.2. We see that the difference is consistent with an exponential as expected. It is most pronounced for the $m_c = 2$ case and rapidly diminishes at higher m_c .

7.3 Consequences for momentum flux in mirror symmetric tokamaks

The gyrokinetic symmetry presented in this chapter demonstrates that a poloidal translation of all fast poloidal variation (i.e. that of order m_c) by a single tilt angle has an exponentially small effect in $m_c \gg 1$ on the turbulent transport. Additionally, we know from the argument reviewed in section 6.2 that up-down symmetric flux surfaces generate no momentum flux in the gyrokinetic model. Since, by definition, mirror symmetric tokamaks must have mirror symmetry about some line in

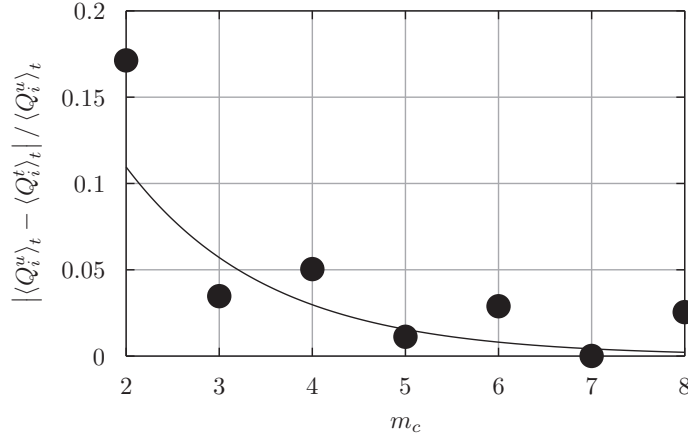


Figure 7.6: The fractional difference in the ion energy flux between up-down symmetric and tilted geometries (see figure 7.2) as a function of m_c (points), with an exponential fit of the form $K \exp(-\beta m_c)$ (line).

the poloidal plane, we can rotate all of the shaping effects by a single tilt angle until the line of mirror symmetry is coincident with the midplane. Hence, because all mirror symmetric flux surfaces can be generated by tilting up-down symmetric surfaces, we know that the momentum flux in mirror symmetric tokamaks cannot scale more strongly than $\Pi_{\zeta s} \sim \exp(-\beta m_c^\gamma)$, where β and γ are both positive and do not depend on m_c . This exponential scaling is true for all flux surfaces that have mirror symmetry about any line in the poloidal plane, not just those with mirror symmetry about the midplane (i.e. up-down symmetry). This argument only relies on the conditions needed for the symmetry, namely $m_c \gg 1$. It does *not* presume that the flux surface shaping is weak.

However, there is a subtlety concerning flux surfaces that possess slowly varying envelopes as well as fast variation. In figure 7.7(a) we show a cartoon up-down symmetric flux surface specified by (5.8) with just two shaping modes, $m = 10$ and $m = 11$, which beat to create an $m = 1$ envelope. We are free to consider all flux surface variation “fast” and tilt the entire flux surface. This produces figure 7.7(b) which is a mirror symmetric flux surface. However, since we rotated the $m = 1$ variation of the envelope, we have considered $m = 1$ variation to be fast. This means that the difference in the fluxes produced by figures 7.7(a) and 7.7(b) is exponentially small in an expansion in $m_c = 1 \gg 1$, which is not particularly meaningful.

This example illustrates that if a flux surface is mirror symmetric it produces momentum transport that is exponentially small in the Fourier mode number of the mirror symmetric variation. However, the validity of this expansion may be

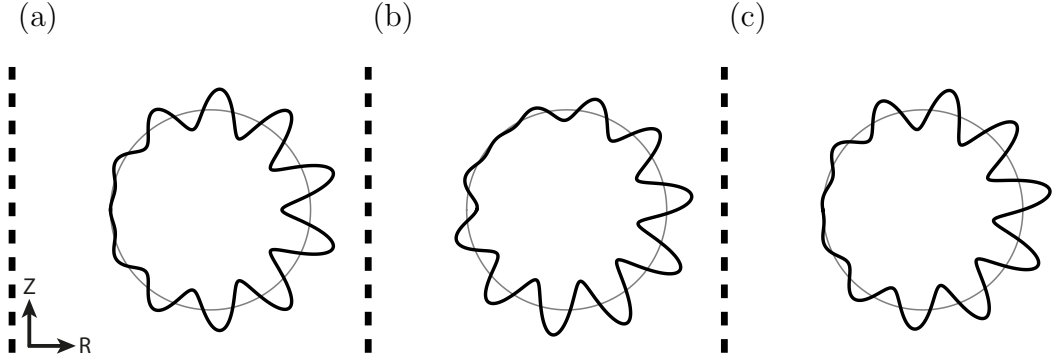


Figure 7.7: Exaggerated flux surface geometries (black) with $m = 10$ and $m = 11$ Fourier shaping modes and (a) no tilt, (b) a $\pi/4$ tilt of the entire flux surface, and (c) a $\pi/4$ tilt of the fast poloidal variation, where circular flux surfaces (grey) are shown for comparison.

questionable for certain cases such as geometries with low shaping effects or a slowly varying envelope created by the beating of several high mode number effects.

Conversely, we can choose to consider the $m = 1$ envelope as slow and refrain from tilting it. To do so, we convert the flux surface specification into (7.5) and introduce the global tilt through the form of $z(\theta)$. This produces figure 7.7(c), which is not mirror symmetric. However, it has a mirror symmetric fast shaping and up-down symmetric slow shaping (because the envelope remains unchanged). Hence, the difference in the fluxes produced by figures 7.7(a) and 7.7(c) is exponentially small in an expansion in $m_c = 10 \gg 1$.

This example shows that formally non-mirror symmetric configurations can still have exponentially small momentum flux if the slow variation is up-down symmetric and the fast variation is mirror symmetric. This becomes intuitive if we consider toroidicity as a second type of $m = 1$ mode (in addition to the Shafranov shift). From this perspective up-down symmetry is just mirror symmetry with respect to the inherent, untilted mode from toroidicity. Hence we can add any slow shaping mode as long as it is aligned with the mode from toroidicity, keeping the slow shaping mirror symmetric.

Interpreted broadly, this symmetry demonstrates that variation on two spatial scales interact to generate momentum transport that is exponentially small in the scale separation. Hence, using neighbouring shaping modes to drive rotation is optimal.

Chapter 8

Envelopes: Scaling of momentum flux with shaping mode number

Much of this chapter appears in reference [41].

This chapter investigates slowly varying envelopes created by the beating of different fast flux surface shaping effects. We will prove that fast shaping effects can create slowly varying envelopes that generate momentum transport that is polynomially small in the fast shaping mode number. This contrasts with the exponential scaling found for mirror symmetric surfaces in chapter 7 and suggests that up-down asymmetric envelopes created using low shaping effects could increase rotation. In this chapter we restrict our attention to momentum transport generated in stationary plasmas (i.e. $\Omega_\zeta = d\Omega_\zeta/dr_\psi = 0$) and will assume the turbulence is electrostatic for simplicity.

In section 8.1, we expand the gyrokinetic equation order-by-order in large shaping mode number to compare the momentum flux generated by different types of flux surface shaping. In section 8.1.2 we calculate how the momentum flux scales with the shaping effect mode number, given a specific set of simple geometries with two independently-tilted shaping modes. This is designed to give a concrete illustration of the more abstract and general scaling argument for geometries with up-down asymmetric envelopes presented in section 8.1.3. Then, in section 8.2 we use nonlinear local gyrokinetic simulations to contrast the analytic results of section 8.1 with chapter 7. Lastly, section 8.3 gives a broad interpretation of these analytic scalings.

8.1 Analytic gyrokinetic analysis

First, we must calculate the local value of the eight geometric coefficients that appear in the stationary gyrokinetic equation from the local Miller equilibrium model in

chapter 5. The full calculation is shown in appendix D, but here we will only calculate them to lowest order in large aspect ratio for use in section 8.1.2. We will specify the flux surface geometry by the Expanded prescription (i.e. (5.8), (5.9), and (5.24) through (5.26)). These equations represent a completely general Fourier decomposition of the flux surface shape. Note that the change in the strength, $d\Delta_m/dr_\psi$, and tilt, $d\theta_{tm}/dr_\psi$, of each mode is determined by the global MHD equilibrium. In chapter 5 we derive these quantities using a constant toroidal current profile in the limits of large aspect ratio and weak shaping. We will keep these parameters free and only use the constant current profile solutions to provide scalings for these quantities.

Additionally, the Miller model requires four scalar quantities, usually I (the toroidal field flux function), q (the safety factor), dq/dr_ψ (the magnetic shear), and dp/dr_ψ (the pressure gradient) of the flux surface of interest. However, for ease of notation, we will choose to replace I by $B_{c0} = I/R_{c0}$ (the toroidal magnetic field at $R = R_{c0}$ on the flux surface of interest) and q by $d\psi/dr_\psi$ (see (D.3)). Also, when we expand to lowest order in aspect ratio, we will find that we can replace both dp/dr_ψ and dq/dr_ψ (related to $dI/d\psi$ by (D.17)) with

$$\begin{aligned}\hat{s}' &\equiv 2 + r_{\psi 0} \left(\frac{d\psi}{dr_\psi} \right)^{-1} \left(\mu_0 R_{c0}^2 \left(\frac{d\psi}{dr_\psi} \right)^{-1} \frac{dp}{dr_\psi} + R_{c0} B_{c0} \frac{dI}{d\psi} \right) \\ &= 2 - r_{\psi 0} \left(\frac{d\psi}{dr_\psi} \right)^{-1} \mu_0 j_\zeta R_{c0}.\end{aligned}\tag{8.1}$$

We can make this replacement because the toroidal current, which appears on the right side of the Grad-Shafranov equation, is a flux function to lowest order in aspect ratio (see (2.2)). We note that if the flux surfaces are exactly circular and $dp/dr_\psi = 0$, then $\hat{s}' = \hat{s} \equiv (r_{\psi 0}/q) dq/dr_\psi$.

To lowest order in aspect ratio we immediately see that $B \rightarrow B_{c0}$ and $a_{||s} \rightarrow 0$, so we can focus on the other six (i.e. $\hat{b} \cdot \vec{\nabla}\theta$, $v_{ds\psi}$, $v_{ds\alpha}$, $|\vec{\nabla}\psi|^2$, $\vec{\nabla}\psi \cdot \vec{\nabla}\alpha$, and $|\vec{\nabla}\alpha|^2$). In this limit the momentum flux, given by (6.21), becomes

$$\begin{aligned}\Pi_{\zeta s} &= \frac{2\pi i R_{c0} B_{c0}}{\oint d\theta (\hat{b} \cdot \vec{\nabla}\theta)^{-1}} \sum_{k_\psi, k_\alpha} k_\alpha \oint d\theta (\hat{b} \cdot \vec{\nabla}\theta)^{-1} \\ &\times \int dw_{||} d\mu w_{||} J_0(k_\perp \rho_s) \phi(k_\psi, k_\alpha) h_s(-k_\psi, -k_\alpha).\end{aligned}\tag{8.2}$$

In order to calculate the poloidal field we must use

$$\vec{B}_p = \vec{\nabla}\zeta \times \vec{\nabla}r_\psi \frac{d\psi}{dr_\psi},\tag{8.3}$$

our geometry specification (given by (5.8), (5.9), and (5.24) through (5.26)), and the vector identity

$$\vec{\nabla}_{u_1} = \frac{\partial \vec{r} / \partial u_2 \times \partial \vec{r} / \partial u_3}{\partial \vec{r} / \partial u_1 \cdot (\partial \vec{r} / \partial u_2 \times \partial \vec{r} / \partial u_3)} \quad (8.4)$$

for (u_1, u_2, u_3) , a cyclic permutation of (r_ψ, θ, ζ) . Having calculated the poloidal field we can find $\hat{b} \cdot \vec{\nabla} \theta$,

$$v_{ds\psi} = \frac{m_s}{Z_s e} \hat{b} \cdot \vec{\nabla} \theta \frac{\partial R}{\partial \theta}, \quad (8.5)$$

and $|\vec{\nabla} \psi|^2 = R^2 B_p^2$ to lowest order in aspect ratio.

However, $\vec{\nabla} \alpha$ contains second-order radial derivatives, which are not specified as input. The Miller model determines them by ensuring that the Grad-Shafranov equation is satisfied. With considerable work (shown in appendix D), we can use the Grad-Shafranov equation to calculate that

$$\vec{\nabla} \alpha = \frac{\partial \alpha}{\partial \psi} \vec{\nabla} \psi + \frac{\partial \alpha}{\partial \theta} \vec{\nabla} \theta, \quad (8.6)$$

where

$$\frac{\partial \alpha}{\partial \psi} = - \int_{\theta_\alpha}^{\theta} \left|_{\psi} d\theta' \frac{\partial A_\alpha}{\partial \psi} + A_\alpha(\psi, \theta_\alpha) \frac{d\theta_\alpha}{d\psi} \quad (8.7)$$

$$\begin{aligned} &= - \int_{\theta_\alpha}^{\theta} \left|_{\psi} d\theta' \left(\frac{\partial A_\alpha}{\partial \psi} \right)_{\text{orthog}} + \left[\frac{B_{c0}}{R_{c0}^3 B_p^3} \frac{\partial l_p}{\partial \theta'} \vec{\nabla} \psi \cdot \vec{\nabla} \theta' \right]_{\theta'=\theta_\alpha}^{\theta'=\theta} \\ &+ \left(\frac{B_{c0}}{R_{c0} B_p} \frac{\partial l_p}{\partial \theta} \right)_{\theta=\theta_\alpha} \frac{d\theta_\alpha}{d\psi}. \end{aligned} \quad (8.8)$$

and

$$\frac{\partial \alpha}{\partial \theta} = -A_\alpha(\psi, \theta) = -\frac{B_{c0}}{R_{c0} B_p} \frac{\partial l_p}{\partial \theta} \quad (8.9)$$

to lowest order in aspect ratio. Here

$$\left(\frac{\partial A_\alpha}{\partial \psi} \right)_{\text{orthog}} = \frac{B_{c0}}{R_{c0}^2 B_p^2} \frac{\partial l_p}{\partial \theta'} \left(\frac{d\psi}{dr_\psi} \frac{\hat{s}' - 2}{r_{\psi 0} R_{c0} B_p} + 2\kappa_p \right) \quad (8.10)$$

is the part of $\partial A_\alpha / \partial \psi$ that remains if the (r_ψ, θ, ζ) coordinate system is orthogonal, κ_p is the poloidal magnetic field curvature given by (7.3), and l_p is the poloidal arc length (defined such that (7.4) is true). The form of (8.10) is useful because it does not contain any radial derivatives (except $d\psi/dr_\psi$ which is an input to the calculation)

and distinguishes the important term: the poloidal curvature. This allows us to find $\vec{\nabla}\psi \cdot \vec{\nabla}\alpha$, $|\vec{\nabla}\alpha|^2$, and

$$v_{ds\alpha} = \frac{1}{\Omega_s} \left(\frac{B_{c0}}{R_{c0}} \frac{\partial R}{\partial \psi} + \frac{\partial R}{\partial \theta} \frac{\partial \alpha}{\partial \psi} \vec{\nabla}\psi \cdot (\vec{\nabla}\theta \times \vec{\nabla}\zeta) \right) \quad (8.11)$$

to lowest order in aspect ratio.

8.1.1 Asymptotic expansion ordering

We know from section 6.2 that, unless the up-down symmetry of the geometric coefficients is broken, the time-averaged momentum flux will always be zero to lowest order in $\rho_* \equiv \rho_i/a \ll 1$. We will investigate the consequences of breaking the up-down symmetry using different shaping effects. To do this we will expand (6.5), (6.15), and (8.2) in large Fourier shaping mode number, i.e. $m_c \gg 1$ where m_c is a characteristic mode number of the fast shaping effects. We will expand

$$h_s = h_{s0} + h_{s1} + h_{s2} + h_{s3} + \dots \quad (8.12)$$

$$\phi = \phi_0 + \phi_1 + \phi_2 + \phi_3 + \dots, \quad (8.13)$$

where the subscript indicates the order of the quantity in $m_c^{-1} \ll 1$. This expansion separates the long spatial scale coordinate θ , from a short spatial scale coordinate, z , defined by (7.7). Distinguishing the variation on each scale, e.g. $h_s(\theta, z)$ and $\phi(\theta, z)$, means that we can rewrite poloidal derivatives according to (7.8). Ultimately we will only be interested in large scale phenomena, so we will need to average quantities in z using (7.9), but we must still manipulate the z -dependent portion, given by

$$(\widetilde{\dots}) \equiv (\dots) - \overline{(\dots)}. \quad (8.14)$$

8.1.2 Two mode shaping in the large aspect ratio gyrokinetic model

In this section we will prescribe a specific geometry and expand the large aspect ratio gyrokinetic, quasineutrality, and momentum flux equations order-by-order to determine the scaling of the momentum flux with $m_c \gg 1$. Hence formally we require that $\epsilon \ll 1$ for the aspect ratio expansion and also that $\epsilon \ll m_c^{-1} \ll 1$ for the subsidiary expansion in shaping mode number. We perform a more general calculation for $\epsilon \sim 1$ in section 8.1.3.

We completely specify the shape of the flux surface of interest (and how it changes with radius) by (5.8), (5.9), and (5.24) through (5.26). We will choose the ordering

$$\Delta_m - 1 \sim m_c^{-2} \quad (8.15)$$

for the magnitude of the large mode number shaping effects to be consistent with (7.36). We can determine that

$$\frac{d\Delta_m}{dr_\psi} \sim \frac{m_c (\Delta_m - 1)}{r_\psi}. \quad (8.16)$$

from (5.11) and $d\theta_{tm}/dr_\psi = 0$ from (5.12), which were derived for a constant current profile.

In this calculation, we will use flux surfaces with simple fast shaping that beats together to form slowly varying envelopes. To create these flux surfaces, we include only two high-order shaping effects, m and n , in (5.8) and (5.9). We will order both $m \sim m_c$ and $n \sim m_c$, which are free to have different strengths, Δ_m and Δ_n , and tilt angles, θ_{tm} and θ_{tn} . However, we order $n - m \sim 1$, $\Delta_n - 1 \sim \Delta_m - 1 \sim m_c^{-2}$, and $d\Delta_n/dr_\psi \sim d\Delta_m/dr_\psi \sim m_c (\Delta_m - 1) / r_\psi$. Given these orderings (5.8) and (5.9) become

$$r_0(\theta) = r_{\psi 0} \left(1 - \frac{\Delta_m - 1}{2} \cos(z_{ms}) - \frac{\Delta_n - 1}{2} \cos(z_{ns}) \right) + O(m_c^{-4} r_\psi) \quad (8.17)$$

$$\left. \frac{\partial r}{\partial r_\psi} \right|_{\psi_0} = 1 - \frac{r_{\psi 0}}{2} \frac{d\Delta_m}{dr_\psi} \cos(z_{ms}) - \frac{r_{\psi 0}}{2} \frac{d\Delta_n}{dr_\psi} \cos(z_{ns}) + O(m_c^{-2}), \quad (8.18)$$

where

$$z_{ms} \equiv m(\theta + \theta_{tm}) \quad (8.19)$$

$$z_{ns} \equiv n(\theta + \theta_{tn}). \quad (8.20)$$

Note that we are not using the form of (7.5), instead we have the sum of two arbitrary fast modes. By doing so we will explicitly see how the mode numbers and tilt angles combine, sometimes generating a slowly varying envelope.

8.1.2.1 Geometric coefficients

To lowest order, $O(1)$, the geometric coefficients are those of a circular tokamak and are entirely independent of the short spatial scale coordinate, z . To next order the coefficients depend on z , but are algebraically intensive to find. The full expressions for all six coefficients (and several intermediate quantities that are useful in the

derivation) are given in appendix E, but here we will only derive $v_{ds\alpha}$ to serve as an illustrative example. This coefficient signifies the magnetic drifts in the direction perpendicular to the magnetic field, but still within the flux surface. We will start with (5.24) through (5.26), (8.17), and (8.18) and use them to construct all of the quantities appearing in (8.11), the expression for $v_{ds\alpha}$ to lowest order in aspect ratio.

It will be sufficient to calculate all quantities to $O(m_c^{-1})$ with the exception of $\partial R/\partial\theta$ and $\partial Z/\partial\theta$, because they appear in the poloidal curvature with an extra poloidal derivative (see (7.3)). This extra derivative creates an additional factor of m_c , which boosts $O(m_c^{-2})$ effects to $O(m_c^{-1})$. Directly differentiating (5.25) and (5.26) we find

$$\frac{\partial R}{\partial\theta} = \frac{dr_0}{d\theta} \cos(\theta) - r_0 \sin(\theta) \quad (8.21)$$

$$\frac{\partial Z}{\partial\theta} = \frac{dr_0}{d\theta} \sin(\theta) + r_0 \cos(\theta) \quad (8.22)$$

$$\frac{\partial^2 R}{\partial\theta^2} = \frac{d^2 r_0}{d\theta^2} \cos(\theta) - 2 \frac{dr_0}{d\theta} \sin(\theta) - r_0 \cos(\theta) \quad (8.23)$$

$$\frac{\partial^2 Z}{\partial\theta^2} = \frac{d^2 r_0}{d\theta^2} \sin(\theta) + 2 \frac{dr_0}{d\theta} \cos(\theta) - r_0 \sin(\theta), \quad (8.24)$$

where

$$\frac{dr_0}{d\theta} = \frac{r_{\psi 0}}{2} \left(m(\Delta_m - 1) \sin(z_{ms}) + n(\Delta_n - 1) \sin(z_{ns}) \right) + O(m_c^{-3} r_\psi) \quad (8.25)$$

$$\frac{d^2 r_0}{d\theta^2} = \frac{r_{\psi 0}}{2} \left(m^2(\Delta_m - 1) \cos(z_{ms}) + n^2(\Delta_n - 1) \cos(z_{ns}) \right) + O(m_c^{-2} r_\psi). \quad (8.26)$$

From this point forward we will only need quantities to $O(m_c^{-1})$ to accurately capture the up-down symmetry breaking. Substituting (8.21) and (8.22) into (7.4) gives

$$\frac{\partial l_p}{\partial\theta} = r_{\psi 0} + O(m_c^{-2} r_\psi). \quad (8.27)$$

We can now substitute (8.21) through (8.27) into (7.3) to find

$$\kappa_p = \frac{1}{r_{\psi 0}} \left(1 - \frac{1}{r_{\psi 0}} \frac{d^2 r_0}{d\theta^2} \right) + O\left(\frac{m_c^{-2}}{r_\psi}\right) \quad (8.28)$$

$$= \frac{1}{r_{\psi 0}} \left(1 - \frac{1}{2} \left[m^2(\Delta_m - 1) \cos(z_{ms}) + n^2(\Delta_n - 1) \cos(z_{ns}) \right] \right) + O\left(\frac{m_c^{-2}}{r_\psi}\right). \quad (8.29)$$

Next we will calculate

$$\frac{\partial R}{\partial r_\psi} = \left. \frac{\partial r}{\partial r_\psi} \right|_{\psi_0} \cos(\theta) \quad (8.30)$$

$$\frac{\partial Z}{\partial r_\psi} = \left. \frac{\partial r}{\partial r_\psi} \right|_{\psi_0} \sin(\theta) \quad (8.31)$$

straightforwardly from (5.25) and (5.26). We can determine $\vec{\nabla} r_\psi$ through (8.4) and immediately find

$$\vec{\nabla} \theta = \frac{\hat{e}_\theta}{r_0(\theta)} \quad (8.32)$$

$$\vec{\nabla} \zeta = \frac{\hat{e}_\zeta}{R} = \frac{\hat{e}_\zeta}{R_{c0}} + O\left(\frac{\epsilon}{R_0}\right), \quad (8.33)$$

where \hat{e}_θ and \hat{e}_ζ are the poloidal and toroidal angle unit vectors respectively. From this we know that the coordinate scalar triple product is

$$\vec{\nabla} \psi \cdot (\vec{\nabla} \theta \times \vec{\nabla} \zeta) = \frac{1}{J} = \frac{1}{r_{\psi 0} R_{c0}} \frac{d\psi}{dr_\psi} \left(\frac{\partial r}{\partial r_\psi} \Big|_{\psi_0} \right)^{-1} + O\left(m_c^{-2} \frac{B_0}{R_0}\right), \quad (8.34)$$

which is needed to calculate the second term of (8.11). Since we are using $d\psi/dr_\psi$ as an input instead of q , it is simple to find $\partial R/\partial \psi$ from (8.30) in order to calculate the first term of (8.11).

At this point we see that we have calculated all of the quantities appearing in (8.11), except for $\partial \alpha/\partial \psi$. This is specified by (8.8) and is made up of three terms. All of the terms require that we know

$$B_p = \frac{1}{J} \frac{\partial l_p}{\partial \theta} = \frac{1}{R_{c0}} \frac{d\psi}{dr_\psi} \left(\frac{\partial r}{\partial r_\psi} \Big|_{\psi_0} \right)^{-1} + O\left(m_c^{-2} B_p\right), \quad (8.35)$$

which is found using (7.4), (8.3), (8.4), (8.33), and (8.34). Using (8.27), (8.28), and (8.35), we can determine the integrand (i.e. (8.10)) that appears in the first term to be

$$\begin{aligned} \left(\frac{\partial A_\alpha}{\partial \psi} \right)_{\text{orthog}} &= B_{c0} \left(\frac{d\psi}{dr_\psi} \right)^{-2} \left(\frac{\partial r}{\partial r_\psi} \Big|_{\psi_0} \right)^2 \\ &\times \left[(\hat{s}' - 2) \frac{\partial r}{\partial r_\psi} \Big|_{\psi_0} + 2 \left(1 - \frac{1}{r_{\psi 0}} \frac{d^2 r_0}{d\theta'^2} \right) \right] + O\left(\frac{m_c^{-2}}{r_\psi^2 B_0} \right) \end{aligned} \quad (8.36)$$

to lowest order in aspect ratio. Calculating the indefinite integral of (8.36) is straightforward and is explicitly given by (E.8). The second term of (8.8) is found to be

$$\frac{B_{c0}}{R_{c0}^3 B_p^3} \frac{\partial l_p}{\partial \theta'} \vec{\nabla} \psi \cdot \vec{\nabla} \theta' = -\frac{B_{c0}}{r_{\psi 0}} \left(\frac{d\psi}{dr_\psi} \right)^{-2} \left(\frac{\partial r}{\partial r_\psi} \Big|_{\psi_0} \right)^2 \frac{dr_0}{d\theta'} + O\left(\frac{m_c^{-2}}{r_\psi^2 B_0} \right). \quad (8.37)$$

by substituting (8.4), (8.27), (8.32), and (8.35). At this point, by specifying the free parameter

$$\begin{aligned} \frac{d\theta_\alpha}{d\psi} &= \left(\frac{B_{c0}}{R_{c0}B_p} \frac{\partial l_p}{\partial \theta} \right)_{\theta=\theta_\alpha}^{-1} \\ &\times \left[- \int_{\theta_0}^{\theta_\alpha} \Big|_{\psi} d\theta' \left(\frac{\partial A_\alpha}{\partial \psi} \right)_{\text{orthog}} + \left(\frac{B_{c0}}{R_{c0}^3 B_p^3} \frac{\partial l_p}{\partial \theta'} \vec{\nabla} \psi \cdot \vec{\nabla} \theta' \right)_{\theta'=\theta_\alpha} \right] \end{aligned} \quad (8.38)$$

(not to be confused with (7.25), the value of $d\theta_\alpha/d\psi$ used in the previous chapter), we can use the third term of (8.8) to eliminate all of the terms in $\partial\alpha/\partial\psi$ that do not depend on θ . Here θ_0 is defined such that $\int_{\theta_0}^{\theta_\alpha} \Big|_{\psi} d\theta' (\partial A_\alpha/\partial\psi)_{\text{orthog}}$ does not have a term that is constant in poloidal angle. Additionally, we choose $\theta_\alpha(\psi_0) = 0$ for simplicity. Given this choice, (8.8) becomes

$$\frac{\partial\alpha}{\partial\psi} = - \int_{\theta_0}^{\theta} \Big|_{\psi} d\theta' \left(\frac{\partial A_\alpha}{\partial \psi} \right)_{\text{orthog}} - \frac{B_{c0}}{r_{\psi 0}} \left(\frac{d\psi}{dr_\psi} \right)^{-2} \left(\frac{\partial r}{\partial r_\psi} \Big|_{\psi_0} \right)^2 \frac{dr_0}{d\theta} + O\left(\frac{m_c^{-2}}{r_\psi^2 B_0} \right). \quad (8.39)$$

Substituting (8.21), (8.30), (8.34), and (8.39) into (8.11) gives

$$\begin{aligned} v_{ds\alpha} &= \frac{B_{c0}}{R_{c0}\Omega_s} \left(\frac{d\psi}{dr_\psi} \right)^{-1} \left[\frac{dr_0}{dr_\psi} \cos(\theta) + \frac{1}{r_{\psi 0}} \frac{dr_0}{dr_\psi} \frac{dr_0}{d\theta} \sin(\theta) \right. \\ &\quad + \frac{1}{B_{c0}} \left(\frac{d\psi}{dr_\psi} \right)^2 \left(\sin(\theta) - \frac{1}{r_{\psi 0}} \frac{\partial r_0}{\partial \theta} \cos(\theta) \right) \left(\frac{dr_0}{dr_\psi} \right)^{-1} \int_{\theta_0}^{\theta} \Big|_{\psi} d\theta' \left(\frac{\partial A_\alpha}{\partial \psi} \right)_{\text{orthog}} \Big] \\ &\quad + O\left(\frac{m_c^{-2}}{r_\psi R_0 \Omega_s} \right). \end{aligned} \quad (8.40)$$

To lowest order, this is the usual result for circular flux surfaces,

$$v_{ds\alpha 0} = \frac{B_{c0}}{R_{c0}\Omega_s} \left(\frac{d\psi}{dr_\psi} \right)^{-1} (\cos(\theta) + \hat{s}'\theta \sin(\theta)).$$

To next order this is a complicated expression with the form of

$$\begin{aligned} v_{ds\alpha 1} &= D_1 \theta \sin(\theta) + (D_2 \sin(\theta) + D_3 \theta \cos(\theta)) (D_4 \sin(z_{ms}) + D_5 \sin(z_{ns})) \\ &\quad + (D_6 \cos(\theta) + D_7 \theta \sin(\theta)) (D_8 \cos(z_{ms}) + D_9 \cos(z_{ns})) + D_{10} \sin(\theta) \\ &\quad \times [\sin((n-m)\theta) \cos(n\theta_{tn} - m\theta_{tm}) + \cos((n-m)\theta) \sin(n\theta_{tn} - m\theta_{tm})]. \end{aligned} \quad (8.41)$$

where D_i are constants (the full expression is given in appendix E). Even after averaging over z the last term remains, which has a coefficient of

$$D_{10} = \frac{r_{\psi 0}}{(n-m)} \left(m^2 (\Delta_m - 1) \frac{d\Delta_n}{dr_\psi} + n^2 (\Delta_n - 1) \frac{d\Delta_m}{dr_\psi} \right). \quad (8.42)$$

As we will show shortly, this term, which does not disappear after averaging over z , in general breaks the up-down symmetry of the gyrokinetic equations to $O(m_c^{-1})$. We see that if we set $\Delta_m = 1$, $\Delta_n = 1$, or $n = m$ we produce mirror symmetric flux surfaces without an envelope and this symmetry-breaking term cancels. Also, we note that if $n\theta_{tn} = m\theta_{tm}$ the symmetry-breaking term also vanishes. This condition is only met when the envelope created by the beating of the two high-order shaping modes is up-down symmetric. Lastly, if we break our ordering of $n - m \sim 1$ and set $n = 2m$, not only does the symmetry breaking term drop by an order (due to the $n - m$ in the denominator), but it varies on the fast spatial scale and will average to zero. This corresponds to flux surface shapes that lack an envelope like an ellipse, which only has Fourier components that are multiples of two.

Appendix E gives the full explicit expressions for all six geometric coefficients to lowest order in aspect ratio. We find those that do not depend on $\vec{\nabla}\alpha$ (i.e. $v_{ds\psi}$ and $|\vec{\nabla}\psi|^2$) are up-down symmetric in θ to $O(m_c^{-1})$ after averaging over the fast spatial scale. However, the other three coefficients (i.e. $v_{ds\alpha}$, $\vec{\nabla}\psi \cdot \vec{\nabla}\alpha$, and $|\vec{\nabla}\alpha|^2$) lose their large-scale symmetry at $O(m_c^{-1})$. The symmetry breaking terms arise from the interaction between κ_p and B_p^{-2} in (8.10). Since $m_c \gg 1$ the second order derivatives in κ_p (see (7.3)) brings the effect of shaping from $O(m_c^{-2})$ to $O(1)$. This shaping can then beat with the $O(m_c^{-1})$ shaping in B_p^{-2} and break the symmetry of the geometric coefficients to $O(m_c^{-1})$. We note that κ_p is “normal” curvature (i.e. perpendicular to the flux surface), as opposed to “geodesic” curvature (i.e. within the flux surface) [69]. The importance of κ_p is surprising because it arises from the *poloidal* field, not the *toroidal* field. Usually the focus is on the “normal” curvature of the *toroidal* field because it generates the largest contribution to the total field line curvature that appears in the magnetic drifts.

Ultimately, this beating between κ_p and B_p^{-2} is the dominant mechanism that breaks the up-down symmetry of the geometric coefficients to lowest order in aspect ratio. It is a subtle effect because the beating takes place in the integral in $\partial\alpha/\partial\psi$ (see (8.8) and (8.10)), which is contained in $\vec{\nabla}\alpha$ (see (8.6)). However, it does not enter into the magnetic drift velocity itself. From studying these equations we can see that the beating between κ_p and B_p^{-2} alters the local magnetic shear (but without modifying the total magnetic shear). Therefore, in the perfect $m_c \gg 1$ limit, adding a small amount of the fast shaping modifies local field line pitch from one flux surface to the next (without changing the field line spacing). This perturbs the local cross-sectional shape (i.e. the shape in the plane perpendicular to the field line) of the turbulent

eddies as they wrap around the torus. Specifically, it tilts the eddy cross-sectional shape a small amount one way or the other, depending on the location along the field line. This perturbation to the eddy has a slowly varying envelope, which is then acted on by the unperturbed up-down symmetric magnetic drifts.

The interaction of κ_p and B_p^{-2} certainly can create an envelope that breaks the up-down symmetry of the geometric coefficients and generates momentum flux, but it is still unclear at what order. By expanding the gyrokinetic and quasineutrality equations order-by-order in $m_c^{-1} \ll 1$ we will connect the symmetry-breaking of the geometric coefficients to symmetry-breaking of the distribution function and non-zero momentum flux.

8.1.2.2 $O(m_c)$ gyrokinetic equation

Expanding (6.5) to lowest order in $m_c \gg 1$ gives

$$w_{||} \left(\hat{b} \cdot \vec{\nabla} \theta \right)_0 m \frac{\partial \tilde{h}_{s0}}{\partial z} \bigg|_{\theta, w_{||}, \mu} = 0. \quad (8.43)$$

We see from (E.11) that $\left(\hat{b} \cdot \vec{\nabla} \theta \right)_0$ is a constant, so integrating over z gives

$$\tilde{h}_{s0} = 0 \quad (8.44)$$

$$\bar{h}_{s0} = h_{s0}. \quad (8.45)$$

8.1.2.3 $O(1)$ quasineutrality equation

Expanding (6.15) to lowest order in $m_c \gg 1$ gives

$$\phi_0 = \left(\sum_s \frac{Z_s^2 e^2 n_s}{T_s} \right)^{-1} \sum_s \frac{2\pi Z_s e B_{c0}}{m_s} \int dw_{||} d\mu (J_0(k_{\perp} \rho_s))_0 h_{s0}. \quad (8.46)$$

Using (8.45) and (E.17) we see that

$$\tilde{\phi}_0 = 0 \quad (8.47)$$

$$\bar{\phi}_0 = \phi_0 = \left(\sum_s \frac{Z_s^2 e^2 n_s}{T_s} \right)^{-1} \sum_s \frac{2\pi Z_s e B_{c0}}{m_s} \int dw_{||} d\mu \overline{(J_0(k_{\perp} \rho_s))}_0 \bar{h}_{s0}. \quad (8.48)$$

8.1.2.4 $O(1)$ gyrokinetic equation

Expanding (6.5) to $O(1)$ gives

$$\begin{aligned}
& \frac{\partial h_{s0}}{\partial t} + w_{||} \left(\hat{b} \cdot \vec{\nabla} \theta \right)_0 \left(\frac{\partial h_{s0}}{\partial \theta} \Big|_{z, w_{||}, \mu} + m \frac{\partial \tilde{h}_{s1}}{\partial z} \Big|_{\theta, w_{||}, \mu} \right) \\
& + i \left(w_{||}^2 + \frac{B_{c0}}{m_s} \mu \right) (k_{\psi} v_{ds\psi 0} + k_{\alpha} v_{ds\alpha 0}) h_{s0} \\
& + \{ (J_0(k_{\perp} \rho_s))_0 \phi_0, h_{s0} \} - \frac{Z_s e F_{Ms}}{T_s} \frac{\partial}{\partial t} \left((J_0(k_{\perp} \rho_s))_0 \phi_0 \right) \\
& + i k_{\alpha} (J_0(k_{\perp} \rho_s))_0 \phi_0 F_{Ms} \left[\frac{1}{n_s} \frac{dn_s}{d\psi} + \left(\frac{m_s w^2}{2T_s} - \frac{3}{2} \right) \frac{1}{T_s} \frac{dT_s}{d\psi} \right] = 0.
\end{aligned} \tag{8.49}$$

Averaging over z after using (8.45), (8.48), and (E.11) through (E.17) gives

$$\begin{aligned}
& \frac{\partial \bar{h}_{s0}}{\partial t} + w_{||} \overline{\left(\hat{b} \cdot \vec{\nabla} \theta \right)_0} \frac{\partial \bar{h}_{s0}}{\partial \theta} \Big|_{z, w_{||}, \mu} + i \left(w_{||}^2 + \frac{B_{c0}}{m_s} \mu \right) (k_{\psi} \bar{v}_{ds\psi 0} + k_{\alpha} \bar{v}_{ds\alpha 0}) \bar{h}_{s0} \\
& + \left\{ \overline{(J_0(k_{\perp} \rho_s))_0} \bar{\phi}_0, \bar{h}_{s0} \right\} - \frac{Z_s e F_{Ms}}{T_s} \frac{\partial}{\partial t} \left(\overline{(J_0(k_{\perp} \rho_s))_0} \bar{\phi}_0 \right) \\
& + i k_{\alpha} \overline{(J_0(k_{\perp} \rho_s))_0} \bar{\phi}_0 F_{Ms} \left[\frac{1}{n_s} \frac{dn_s}{d\psi} + \left(\frac{m_s w^2}{2T_s} - \frac{3}{2} \right) \frac{1}{T_s} \frac{dT_s}{d\psi} \right] = 0,
\end{aligned} \tag{8.50}$$

which does not depend on z . From (E.11) through (E.17) we see that (8.48) and (8.50) are unchanged by the $(k_{\psi}, k_{\alpha}, \theta, w_{||}, \mu, t) \rightarrow (-k_{\psi}, k_{\alpha}, -\theta, -w_{||}, \mu, t)$ coordinate system transformation when $\bar{h}_{s0} \rightarrow -\bar{h}_{s0}$ and $\bar{\phi}_0 \rightarrow -\bar{\phi}_0$. This symmetry of the $O(1)$ gyrokinetic equations is important because, as discussed in section 6.2, it can be used to demonstrate that the momentum flux must be zero.

Subtracting (8.50) from (8.49) we find

$$m w_{||} \overline{\left(\hat{b} \cdot \vec{\nabla} \theta \right)_0} \frac{\partial \tilde{h}_{s1}}{\partial z} \Big|_{\theta, w_{||}, \mu} = 0. \tag{8.51}$$

Therefore, we know that

$$\tilde{h}_{s1} = 0 \tag{8.52}$$

$$\bar{h}_{s1} = h_{s1}. \tag{8.53}$$

8.1.2.5 $O(1)$ momentum transport

Expanding (8.2) to lowest order gives

$$\begin{aligned} \Pi_{\zeta s 0} &= \frac{i R_{c0} B_{c0}}{\oint d\theta \left(\hat{b} \cdot \vec{\nabla} \theta \right)_0^{-1}} \sum_{k_\psi, k_\alpha} k_\alpha \oint d\theta \left(\hat{b} \cdot \vec{\nabla} \theta \right)_0^{-1} \\ &\times \int dw_{||} d\mu w_{||} (J_0(k_\perp \rho_s))_0 \phi_0(k_\psi, k_\alpha) h_{s0}(-k_\psi, -k_\alpha). \end{aligned} \quad (8.54)$$

Using (8.45), (8.48), (E.11), and (E.17) we find that

$$\Pi_{\zeta s 0} = \frac{i R_{c0} B_{c0}}{2\pi} \sum_{k_\psi, k_\alpha} k_\alpha \oint d\theta \int dw_{||} d\mu w_{||} \overline{(J_0(k_\perp \rho_s))_0} \bar{\phi}_0 \bar{h}_{s0}. \quad (8.55)$$

Therefore by the $(k_\psi, k_\alpha, \theta, w_{||}, \mu, t) \rightarrow (-k_\psi, k_\alpha, -\theta, -w_{||}, \mu, t)$ symmetry outlined in section 6.2 we know that $\Pi_{\zeta s 0} = 0$ when averaged over a turbulent decorrelation time.

8.1.2.6 $O(m_c^{-1})$ quasineutrality equation

Equation (6.15), expanded to $O(m_c^{-1})$, is

$$\phi_1 = \left(\sum_s \frac{Z_s^2 e^2 n_s}{T_s} \right)^{-1} \sum_s \frac{2\pi Z_s e B_{c0}}{m_s} \int dw_{||} d\mu \left((J_0(k_\perp \rho_s))_1 h_{s0} + (J_0(k_\perp \rho_s))_0 h_{s1} \right). \quad (8.56)$$

Using (8.45), (8.53), and (E.17), then averaging over z gives

$$\bar{\phi}_1 = \left(\sum_s \frac{Z_s^2 e^2 n_s}{T_s} \right)^{-1} \sum_s \frac{2\pi Z_s e B_{c0}}{m_s} \int dw_{||} d\mu \left(\overline{(J_0(k_\perp \rho_s))_1} \bar{h}_{s0} + \overline{(J_0(k_\perp \rho_s))_0} \bar{h}_{s1} \right). \quad (8.57)$$

Note that $\tilde{\phi}_1 \neq 0$.

8.1.2.7 $O(m_c^{-1})$ gyrokinetic equation

Expanding (6.5) to $O(m_c^{-1})$, using (8.45), (8.48), (8.53), (8.52), and (E.11) through (E.17), gives

$$\begin{aligned}
& \frac{\partial \bar{h}_{s1}}{\partial t} + w_{||} \left(\hat{b} \cdot \vec{\nabla} \theta \right)_0 \left(\frac{\partial \bar{h}_{s1}}{\partial \theta} \Big|_{z, w_{||}, \mu} + m \frac{\partial \tilde{h}_{s2}}{\partial z} \Big|_{\theta, w_{||}, \mu} \right) \\
& + i \left(w_{||}^2 + \frac{B_{c0}}{m_s} \mu \right) (k_\psi \bar{v}_{ds\psi 0} + k_\alpha \bar{v}_{ds\alpha 0}) \bar{h}_{s1} + \left\{ \overline{(J_0(k_\perp \rho_s))}_0 \bar{\phi}_0, \bar{h}_{s1} \right\} \\
& + \left\{ \overline{(J_0(k_\perp \rho_s))}_0 \bar{\phi}_1, \bar{h}_{s0} \right\} - \frac{Z_s e F_{Ms}}{T_s} \frac{\partial}{\partial t} \left(\overline{(J_0(k_\perp \rho_s))}_0 \bar{\phi}_1 \right) \\
& + i k_\alpha \overline{(J_0(k_\perp \rho_s))}_0 \bar{\phi}_1 F_{Ms} \left[\frac{1}{n_s} \frac{dn_s}{d\psi} + \left(\frac{m_s w^2}{2T_s} - \frac{3}{2} \right) \frac{1}{T_s} \frac{dT_s}{d\psi} \right] \\
& = w_{||} \left(\hat{b} \cdot \vec{\nabla} \theta \right)_1 \frac{\partial \bar{h}_{s0}}{\partial \theta} \Big|_{z, w_{||}, \mu} - i \left(w_{||}^2 + \frac{B_{c0}}{m_s} \mu \right) (k_\psi \bar{v}_{ds\psi 1} + k_\alpha \bar{v}_{ds\alpha 1}) \bar{h}_{s0} \\
& - \left\{ \overline{(J_0(k_\perp \rho_s))}_1 \bar{\phi}_0, \bar{h}_{s0} \right\} + \frac{Z_s e F_{Ms}}{T_s} \frac{\partial}{\partial t} \left(\overline{(J_0(k_\perp \rho_s))}_1 \bar{\phi}_0 \right) \\
& - i k_\alpha \overline{(J_0(k_\perp \rho_s))}_1 \bar{\phi}_0 F_{Ms} \left[\frac{1}{n_s} \frac{dn_s}{d\psi} + \left(\frac{m_s w^2}{2T_s} - \frac{3}{2} \right) \frac{1}{T_s} \frac{dT_s}{d\psi} \right]. \tag{8.58}
\end{aligned}$$

Averaging over z we find that

$$\begin{aligned}
& \frac{\partial \bar{h}_{s1}}{\partial t} + w_{||} \hat{b} \cdot \vec{\nabla} \theta \frac{\partial \bar{h}_{s1}}{\partial \theta} \Big|_{z, w_{||}, \mu} + i \left(w_{||}^2 + \frac{B_{c0}}{m_s} \mu \right) (k_\psi \bar{v}_{ds\psi 0} + k_\alpha \bar{v}_{ds\alpha 0}) \bar{h}_{s1} \\
& + \left\{ \overline{(J_0(k_\perp \rho_s))}_0 \bar{\phi}_0, \bar{h}_{s1} \right\} + \left\{ \overline{(J_0(k_\perp \rho_s))}_0 \bar{\phi}_1, \bar{h}_{s0} \right\} - \frac{Z_s e F_{Ms}}{T_s} \frac{\partial}{\partial t} \left(\overline{(J_0(k_\perp \rho_s))}_0 \bar{\phi}_1 \right) \\
& + i k_\alpha \overline{(J_0(k_\perp \rho_s))}_0 \bar{\phi}_1 F_{Ms} \left[\frac{1}{n_s} \frac{dn_s}{d\psi} + \left(\frac{m_s w^2}{2T_s} - \frac{3}{2} \right) \frac{1}{T_s} \frac{dT_s}{d\psi} \right] \\
& = w_{||} \left(\hat{b} \cdot \vec{\nabla} \theta \right)_1 \frac{\partial \bar{h}_{s0}}{\partial \theta} \Big|_{z, w_{||}, \mu} - i \left(w_{||}^2 + \frac{B_{c0}}{m_s} \mu \right) (k_\psi \bar{v}_{ds\psi 1} + k_\alpha \bar{v}_{ds\alpha 1}) \bar{h}_{s0} \\
& - \left\{ \overline{(J_0(k_\perp \rho_s))}_1 \bar{\phi}_0, \bar{h}_{s0} \right\} + \frac{Z_s e F_{Ms}}{T_s} \frac{\partial}{\partial t} \left(\overline{(J_0(k_\perp \rho_s))}_1 \bar{\phi}_0 \right) \\
& - i k_\alpha \overline{(J_0(k_\perp \rho_s))}_1 \bar{\phi}_0 F_{Ms} \left[\frac{1}{n_s} \frac{dn_s}{d\psi} + \left(\frac{m_s w^2}{2T_s} - \frac{3}{2} \right) \frac{1}{T_s} \frac{dT_s}{d\psi} \right]. \tag{8.59}
\end{aligned}$$

From (E.21) and (E.23) through (E.26) we see that (8.57) and (8.59) are *not* symmetric in $(k_\psi, k_\alpha, \theta, w_{||}, \mu, t) \rightarrow (-k_\psi, k_\alpha, -\theta, -w_{||}, \mu, t)$ when $\bar{h}_{s0} \rightarrow -\bar{h}_{s0}$, $\bar{\phi}_0 \rightarrow -\bar{\phi}_0$, $\bar{h}_{s1} \rightarrow -\bar{h}_{s1}$, and $\bar{\phi}_1 \rightarrow -\bar{\phi}_1$. This is due to both the drift term $\bar{v}_{ds\alpha 1}$ as well as $(\vec{\nabla} \psi \cdot \vec{\nabla} \alpha)_1$ and $|\vec{\nabla} \alpha|_1^2$ in $\overline{(J_0(k_\perp \rho_s))}_1$ (which accounts for finite gyroradius effects).

8.1.2.8 $O(m_c^{-1})$ momentum transport

Expanding (8.2) to $O(m_c^{-1})$ and using (E.11) and (E.19) gives

$$\begin{aligned} \Pi_{\zeta s1} = \frac{iR_{c0}B_{c0}}{2\pi} \sum_{k_\psi, k_\alpha} k_\alpha \oint d\theta \int dw_{||} d\mu w_{||} \left[- \overline{(\hat{b} \cdot \vec{\nabla} \theta)}_0^{-1} (\hat{b} \cdot \vec{\nabla} \theta)_1 (J_0(k_\perp \rho_s))_0 \phi_0 h_{s0} \right. \\ \left. + (J_0(k_\perp \rho_s))_1 \phi_0 h_{s0} + (J_0(k_\perp \rho_s))_0 \phi_1 h_{s0} + (J_0(k_\perp \rho_s))_0 \phi_0 h_{s1} \right]. \end{aligned} \quad (8.60)$$

After applying (E.17), (E.19), (8.45), (8.48), and (8.53) we find

$$\begin{aligned} \Pi_{\zeta s1} = iR_{c0}B_{c0} \sum_{k_\psi, k_\alpha} k_\alpha \oint d\theta \int dw_{||} d\mu w_{||} \left[\overline{(J_0(k_\perp \rho_s))_1} \bar{\phi}_0 \bar{h}_{s0} \right. \\ \left. + \overline{(J_0(k_\perp \rho_s))_0} \bar{\phi}_1 \bar{h}_{s0} + \overline{(J_0(k_\perp \rho_s))_0} \bar{\phi}_0 \bar{h}_{s1} \right]. \end{aligned} \quad (8.61)$$

Since neither $\overline{(J_0(k_\perp \rho_s))_1}$, $\bar{\phi}_1$, nor \bar{h}_{s1} have a definite parity in $(k_\psi, k_\alpha, \theta, w_{||}, \mu, t) \rightarrow (-k_\psi, k_\alpha, -\theta, -w_{||}, \mu, t)$, we cannot constrain $\Pi_{\zeta s1}$ to be zero. This means that we expect the momentum flux to scale as $\Pi_{\zeta s} \sim m_c^{-1} \Pi_{gB}$. Since the energy flux Q_s is non-zero to lowest order in m_c (i.e. circular flux surfaces still have a non-zero energy flux), we can also say that $(v_{thi}/R_{c0}) \Pi_{\zeta s}/Q_s \sim m_c^{-1}$.

8.1.3 General shaping in the gyrokinetic model

Section 8.1.2 showed that the momentum flux scales as $O(m_c^{-1})$, given a specific geometry (circular with two high-order cylindrical harmonic shaping effects) and a specific shaping ordering ($\Delta_m - 1 \sim m_c^{-2}$). However, this is a concrete, analytically tractable example of a more general argument. Here we will bound the symmetry breaking of the geometric coefficients by systematically ordering all of the quantities that compose them. We will make no presumptions about the low mode number shaping (other than to assume up-down symmetry) nor will we order the size of the fast mode number shaping (other than to assume $\Delta_m - 1 \ll 1$). We note that the analysis of this section does not use an expansion in aspect ratio.

Table 8.1 gives a step-by-step summary of the results of the calculation. To begin, we must make some choices concerning the nature of the flux surface shape. The first two rows define the assumptions concerning the high-order flux surface shaping. We require that the high-order shaping must be periodic, that $\tilde{r}(\theta, z) \sim O((\Delta_m - 1)r_{\psi 0})$ on the flux surface of interest, and that $\partial r / \partial r_\psi \sim O(m_c(\Delta_m - 1))$ (which we discussed previously in arriving at (8.16)). This is all consistent with (5.8) and (5.9), which were used in the calculation of section 8.1.2.

Table 8.1: Scalings of the strength of fast plasma shaping effects for various geometric quantities, where Q_{low} is the geometric quantity in the absence of any large mode number shaping (i.e. $\Delta_m = 1$) and all quantities are evaluated at $r_\psi = r_{\psi 0}$.

Q	Reference	\tilde{Q}/Q_{low}	$(\bar{Q} - Q_{\text{low}})/Q_{\text{low}}$
r	(5.8)	$\Delta_m - 1$	0
$\partial r / \partial r_\psi$	(5.9), (8.16)	$m_c (\Delta_m - 1)$	0
R	(5.25)	$\Delta_m - 1$	0
Z	(5.26)	$\Delta_m - 1$	0
$\partial R / \partial r_\psi$	(5.25)	$m_c (\Delta_m - 1)$	0
$\partial Z / \partial r_\psi$	(5.26)	$m_c (\Delta_m - 1)$	0
$\partial R / \partial \theta$	(5.25)	$m_c (\Delta_m - 1)$	0
$\partial Z / \partial \theta$	(5.26)	$m_c (\Delta_m - 1)$	0
$\partial^2 R / \partial \theta^2$	(5.25)	$m_c^2 (\Delta_m - 1)$	0
$\partial^2 Z / \partial \theta^2$	(5.26)	$m_c^2 (\Delta_m - 1)$	0
$\vec{\nabla} r_\psi$	(8.4)	$m_c (\Delta_m - 1)$	$m_c^2 (\Delta_m - 1)^2$
$\vec{\nabla} \theta$	(5.8)	$\Delta_m - 1$	$(\Delta_m - 1)^2$
$\vec{\nabla} \zeta$	(5.25)	$\Delta_m - 1$	$(\Delta_m - 1)^2$
B_ζ	(D.1)	$\Delta_m - 1$	$(\Delta_m - 1)^2$
$\vec{\nabla} \psi$	(8.4)	$m_c (\Delta_m - 1)$	$m_c^2 (\Delta_m - 1)^2$
$ \vec{\nabla} \psi ^2$	(8.4)	$m_c (\Delta_m - 1)$	$m_c^2 (\Delta_m - 1)^2$
B_p	(8.3)	$m_c (\Delta_m - 1)$	$m_c^2 (\Delta_m - 1)^2$
B	(8.3), (D.1)	$m_c (\Delta_m - 1)$	$m_c^2 (\Delta_m - 1)^2$
$\hat{b} \cdot \vec{\nabla} \theta$	(5.8), (8.3)	$m_c (\Delta_m - 1)$	$m_c^2 (\Delta_m - 1)^2$
$\partial B / \partial \theta$	(8.3), (D.1)	$m_c^2 (\Delta_m - 1)$	$m_c^2 (\Delta_m - 1)^2$
$v_{ds\psi}$	(6.9)	$m_c^2 (\Delta_m - 1)$	$m_c^3 (\Delta_m - 1)^2$
$a_{s }$	(6.12)	$m_c^2 (\Delta_m - 1)$	$m_c^3 (\Delta_m - 1)^2$
$dl_p / d\theta$	(7.4)	$m_c (\Delta_m - 1)$	$m_c^2 (\Delta_m - 1)^2$
κ_p	(7.3)	$m_c^2 (\Delta_m - 1)$	$m_c^2 (\Delta_m - 1)^2$
A_α	(D.8)	$m_c (\Delta_m - 1)$	$m_c^2 (\Delta_m - 1)^2$
$\partial A_\alpha / \partial \psi$	(D.14)	$m_c^2 (\Delta_m - 1)$	$m_c^3 (\Delta_m - 1)^2$
$\int d\theta \partial A_\alpha / \partial \psi$	(D.7)	$m_c (\Delta_m - 1)$	$m_c^3 (\Delta_m - 1)^2$
$\vec{\nabla} \alpha$	(D.7)	$m_c (\Delta_m - 1)$	$m_c^3 (\Delta_m - 1)^2$
$\partial B / \partial r_\psi$	(D.6), (D.18)	$m_c^2 (\Delta_m - 1)$	$m_c^3 (\Delta_m - 1)^2$
$v_{ds\alpha}$	(6.10)	$m_c^2 (\Delta_m - 1)$	$m_c^3 (\Delta_m - 1)^2$
$\vec{\nabla} \psi \cdot \vec{\nabla} \alpha$	(8.4), (D.7)	$m_c (\Delta_m - 1)$	$m_c^3 (\Delta_m - 1)^2$
$ \vec{\nabla} \alpha ^2$	(D.7)	$m_c (\Delta_m - 1)$	$m_c^3 (\Delta_m - 1)^2$

Now, we can derive the orderings for increasingly complex quantities and eventually find the geometric coefficients. For example, we can use (5.25) and (5.26) to derive the order that shaping enters into R and Z . We also know that when we take a poloidal derivative of \bar{Q} , a z -independent quantity, it remains of the same order. However, when we take a poloidal derivative of \tilde{Q} , the z -dependent part of a quantity, it gains an additional factor of m . Therefore, the orderings of the z -dependent parts of $\partial R/\partial\theta$ and $\partial Z/\partial\theta$ are larger than the orderings of \tilde{R} and \tilde{Z} by a factor of m_c . Also, when we calculate quantities such as $\vec{\nabla}r_\psi$ (see (8.4)) we get beating between the different high-order shaping effects. Therefore, when we Taylor expand in $m_c \gg 1$ and $\Delta_m - 1 \ll 1$, the shaping in the numerator and denominators of $\vec{\nabla}r_\psi$ can interact to produce terms that vary on the slow scale. This means that, when we use (7.9) to average over z , these slow terms remain and can break the up-down symmetry. The quantities $\vec{\nabla}\theta$ and $\vec{\nabla}\zeta$ can be expressed as \hat{e}_θ/r and \hat{e}_ζ/R respectively, so their scalings can be found by directly Taylor expanding (5.8) and (5.25).

As discussed at the end of section 8.1.2.1, the poloidal curvature, κ_p , turns out to produce the most important symmetry-breaking term. In (7.3) we see the two poloidal derivatives that bring the effect of shaping up to $O(m_c^2(\Delta_m - 1))$. However because of the relationship between $R(r_{\psi 0}, \theta)$ and $Z(r_{\psi 0}, \theta)$ (given by (5.25) and (5.26)), the beating between $\partial^2 R/\partial\theta^2$ and $\partial Z/\partial\theta$ as well as $\partial^2 Z/\partial\theta^2$ and $\partial R/\partial\theta$ cancels to $O(m_c^3(\Delta_m - 1)^2)$ as shown in (8.28). Nevertheless, the poloidal curvature can still beat against the $O(m_c(\Delta_m - 1))$ shaping of B_p^{-2} in (8.10). This means that $\partial A_\alpha/\partial\psi$ (i.e. the integrand in $\vec{\nabla}\alpha$) contains $O(m_c^3(\Delta_m - 1)^2)$ terms from the fast shaping that are independent of z and break the up-down symmetry. When we take the integral to calculate $\vec{\nabla}\alpha$ the z -dependent terms lose a factor of m_c , but the $O(m_c^3(\Delta_m - 1)^2)$ z -independent terms are not altered. Hence, the symmetry of the three geometric coefficients that contain $\vec{\nabla}\alpha$ is broken to $O(m_c^3(\Delta_m - 1)^2)$.

We note that table 8.1 only establishes an upper bound on the scaling of geometric quantities. When considering a specific geometry, it is always possible for terms to vanish or become small, giving zero to the expected order. For example, unless the flux surfaces have low order shaping, the z -dependent portion of $\partial l_p/\partial\theta$ will scale as $\Delta_m - 1$, rather than $m_c(\Delta_m - 1)$. Similarly if the tokamak has a large aspect ratio or if the flux surfaces lack low order shaping the symmetry-breaking in $v_{ds\psi}$ and $a_{s||}$ turns out to be $O(m_c^2(\Delta_m - 1))$, not $O(m_c^3(\Delta_m - 1))$. Another example can be seen from the simple geometry discussed in section 8.1.2. If we create mirror symmetric flux surfaces without an envelope by setting $\Delta_m = 1$, $\Delta_n = 1$, or $n = m$ all of the symmetry-breaking terms in the geometric coefficients cancel (see (8.41) and (8.42))

and the momentum transport is zero at all orders in the expansion. Additionally, from (8.41) we see that if $n\theta_{tn} = m\theta_{tm}$ the symmetry-breaking terms also cancel. This condition is only met when the envelope created by the beating of the two high-order shaping modes is up-down symmetric.

We have just shown that, in general, the up-down symmetry breaking in the geometric coefficients can be no larger than $O(m_c^3(\Delta_m - 1)^2)$. If we give $\Delta_m - 1$ a definite ordering in m , then we can expand the gyrokinetic equations (see (6.5), (6.15), and (6.21)) as we did in the previous section. Keeping all terms of $O(m_c^4(\Delta_m - 1)^2)$ or larger leaves us with a completely up-down symmetric system of equations. From the expansion in section 8.1.2 we know that these up-down symmetric equations determine the momentum flux to $O(m_c^4(\Delta_m - 1)^2)$. Hence, we know that Π_{ζ_s} can scale no stronger than $m_c^3(\Delta_m - 1)^2$.

However, there is one case that requires special treatment. Thus far we have only assumed that $\Delta_m - 1 \ll 1$, which means we are free to use the ordering $\Delta_m - 1 \sim m_c^{-1}$. This ordering requires convex regions in the flux surface shape (see section 8.1.2), but it does not necessarily introduce x-points into the plasma (see appendix A). When we adopt this ordering we see that the symmetry of the geometric coefficients is broken to $O(m_c)$, which causes problems when we try to repeat the order-by-order expansion performed in section 8.1.2. Naively, as $\vec{\nabla}\psi \cdot \vec{\nabla}\alpha$ and $|\vec{\nabla}\alpha|^2$ become very large, we would expect the nonlinear and drive terms of the gyrokinetic equation to vanish (because $J_0(k_\perp \rho_s) \rightarrow 0$), meaning unstable solutions appear impossible. A more careful, sophisticated treatment of the Bessel functions (and the gyrokinetic equation as a whole) is beyond the scope of this thesis. Regardless, we have established that the momentum flux must scale as $O(1)$ at the very least, because we know that the symmetry of the $O(1)$ gyrokinetic equation is broken. The same argument applies for $\Delta_m - 1 \gtrsim m_c^{-3/2}$.

In summary, we expect that high mode number flux surface shaping will beat together to create slowly varying envelopes that generate intrinsic momentum transport that scales as

$$\frac{v_{thi}}{R_{c0}} \frac{\Pi_{\zeta_s}}{Q_s} \sim m_c^3 (\Delta_m - 1)^2 \quad (8.62)$$

when $\Delta_m - 1 \lesssim m_c^{-3/2}$. We note that dividing by the energy flux to get the momentum transport figure of merit derived in section 6.1 does not change the scalings because the $O(1)$ energy flux (i.e. that of flux surfaces without high mode number shaping) is non-zero. Equation (8.62) is consistent with section 8.1.2, where we used a $\Delta_m - 1 \sim m_c^{-2}$

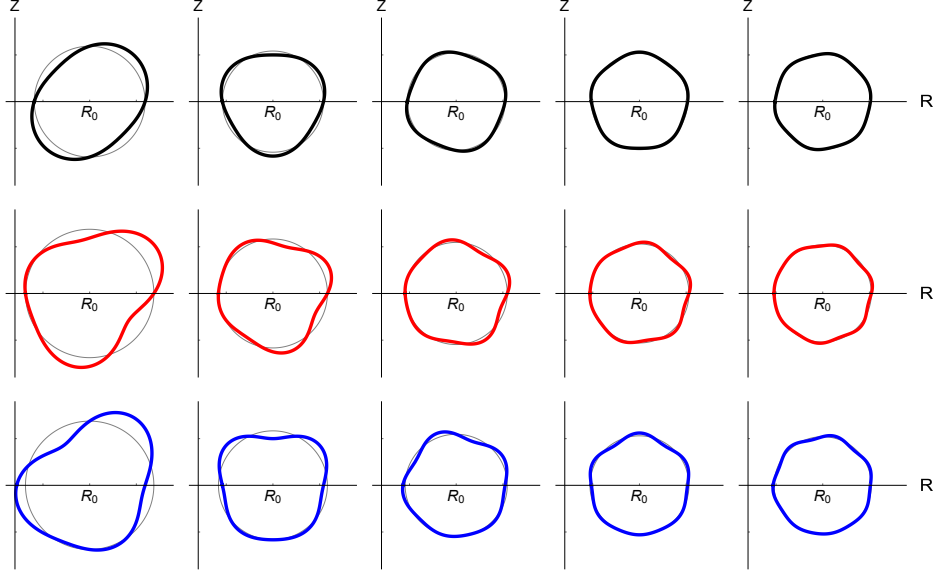


Figure 8.1: The $m_c = 2$ through $m_c = 6$ flux surface geometries in the mirror symmetric (top row), non-mirror symmetric with up-down symmetric envelope (middle row) and non-mirror symmetric with up-down asymmetric envelope (bottom row) scans, where circular flux surfaces are shown for comparison (grey).

ordering with a particular geometry specification to derive that $(v_{thi}/R_{c0}) \Pi_{\zeta s}/Q_s \sim m_c^{-1}$.

8.2 Numerical results

In this section we will present numerical results to test the analytic conclusions of sections 8.1.2 and 8.1.3 and compare with the results of chapter 7. We use GS2 to calculate the nonlinear turbulent fluxes generated by a given geometry and investigate the influence of the shape of the flux surface of interest by scanning m_c , a characteristic poloidal shaping mode number. We will compare the results of these numerical scans to the analytic scalings with $m_c \gg 1$ for mirror symmetric geometries (see section 7.3), non-mirror symmetric geometries with an up-down symmetric envelope, and non-mirror symmetric geometries with an up-down asymmetric envelope (see sections 8.1.2 and 8.1.3).

All simulations are electrostatic and collisionless with deuterium ions and kinetic electrons. Unless specified, all parameters are fixed at Cyclone base case values (see (7.37)). Since the non-mirror symmetric geometries have strong flux surface shaping these simulations needed to be run using $a/L_{Ts} = 3.0$ to ensure that the turbulence was driven unstable. To estimate the impact of this on our results, a single mirror

symmetric case was run at $a/L_{Ts} = 3.0$, in addition to the run with $a/L_{Ts} = 2.3$. This change in the temperature gradient was found to alter the ratio of the momentum to energy flux by less than a 5%. All simulations used at least 48 poloidal grid points, 127 radial wavenumber grid points, 22 poloidal wavenumber grid points, 12 energy grid points, and 10 untrapped pitch angle grid points (i.e. values of $\lambda \equiv w_{\perp}^2 / (w^2 B)$).

The geometry for the three scans is shown in figure 8.1 and is specified by (5.8), (5.9), (5.11) and (5.12) from the constant current Miller local equilibrium. The mirror symmetric scan has only one mode, $m = m_c$, while the two non-mirror symmetric scans have a second mode at $n = m_c + 1$. In section 8.1.2 we ordered $\Delta_m - 1 \sim m_c^{-2}$, so we will set the strength of the shaping such that $m_c^2 (\Delta_m - 1) = 1.5$ and $m_c^2 (\Delta_n - 1) = 1.5$ (if needed) is constant in the scan. For the mirror symmetric simulations we chose the tilt angle to be $\theta_{tm} = \pi / (2m_c)$, the angle halfway between the neighbouring up-down symmetric configurations (at $\theta_{tm} = 0$ and $\theta_{tm} = \pi/m_c$). For the non-mirror symmetric cases we must also set $\theta_{tn} = (m_c/n) \theta_{tm}$ (such that the envelope is up-down symmetric) or $\theta_{tn} = 0$ (such that the envelope is up-down asymmetric and halfway between neighbouring configurations with up-down symmetric envelopes). According to the symmetry breaking term in (8.41), a flux surface with only two shaping modes has an up-down symmetric envelope if and only if

$$\theta_{tn} = \frac{m_c}{n} \left(\theta_{tm} + Y_1 \frac{\pi}{m_c} \right) \quad (8.63)$$

for some integer Y_1 .

In general, from the argument in section 8.1.3, we would predict the momentum flux in an up-down asymmetric geometry to scale as $(v_{thi}/R_{c0}) \Pi_{\zeta s}/Q_s \sim m_c^{-1}$. Indeed, we expect this to be the case for the non-mirror symmetric scan with an up-down asymmetric envelope, as we confirmed in section 8.1.2. However, section 7.3 shows the mirror symmetric scan is a special case where the momentum flux almost entirely cancels, giving the scaling $(v_{thi}/R_{c0}) \Pi_{\zeta s}/Q_s \sim \exp(-\beta m_c^{\gamma})$ for constant β and γ . Similarly, sections 8.1.2 and 8.1.3 show that configurations with an up-down symmetric envelope, even if they are non-mirror symmetric, see the same cancellation. Hence, they also have exponentially small momentum transport. We note that reference [41] contrasted a mirror symmetric scan with a scan in non-mirror symmetric geometries, but did not consider the effect of the up-down symmetry of the envelope. All of the non-mirror symmetric simulations that were performed had an up-down symmetric envelope, so the scaling should be identical to the mirror symmetric scan (i.e. exponential). Here we add a third scan of non-mirror symmetric geometries with

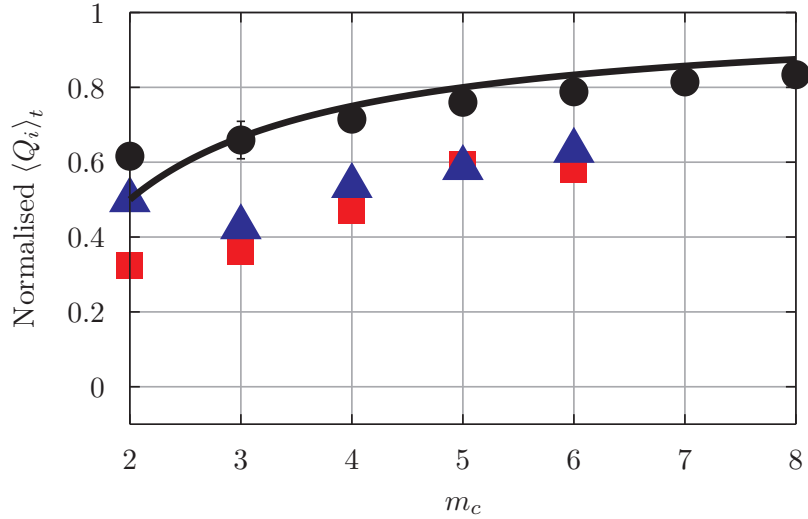


Figure 8.2: The radial ion energy flux from mirror symmetric flux surfaces (black, circles), non-mirror symmetric flux surfaces with an up-down symmetric envelope (red, squares), and non-mirror symmetric flux surfaces with an up-down asymmetric envelope (blue, triangles) normalised to the energy flux of a circular flux surface. Also shown is the m_c^{-1} scaling (black, solid) expected for all three geometry scans.

an up-down asymmetric envelope, which we expect to produce momentum transport that decays much more slowly with $m_c \gg 1$ (i.e. polynomially).

As with the momentum flux, we expect that the energy flux in non-mirror symmetric configurations with an up-down asymmetric envelope to converge to that of circular flux surfaces like m_c^{-1} . However, in the other two sets configurations we expect the energy flux to have the same m_c^{-1} scaling, as opposed to the exponential scaling expected for the momentum flux. This is because there are up-down symmetric fast shaping terms in the geometric coefficients (e.g. the first term in (E.21), (E.23), and (E.24)) that cause a change in energy transport, whereas they do not cause momentum transport.

Figure 8.2 shows the time-averaged ion energy flux calculated by GS2 for the three scans, which are all consistent with our theoretical expectations. In figure 8.3, we see the time-averaged ratio of the ion momentum and energy fluxes from the GS2 simulations. Again, we see behaviour that is consistent with our expectations from analytic theory. Clearly the non-mirror symmetric configurations with an up-down asymmetric envelope decay more slowly than the other two scans with $m_c \gg 1$. We note that section 7.3 only demonstrates that the momentum flux from mirror symmetric configurations cannot scale polynomially. It does not predict the scaling must be $\exp(-m_c)$, as opposed to $\exp(-m_c/2)$ or $m_c \exp(-m_c^2)$ for example. However, the

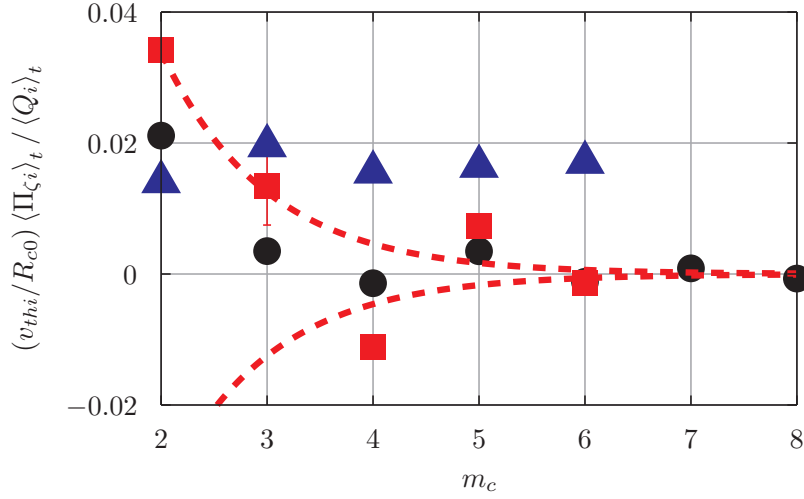


Figure 8.3: The momentum transport from mirror symmetric flux surfaces (black, circles), non-mirror symmetric flux surfaces with an up-down symmetric envelope (red, squares) and non-mirror symmetric flux surfaces with an up-down asymmetric envelope (blue, triangles). Also shown is an example exponential scaling (red, dotted) appropriate for the mirror symmetric and non-mirror symmetric with up-down asymmetric envelope scans.

trendline shown in figure 8.3, $\exp(-m_c)$, seems to fit the data fairly well. Additionally, figure 8.3 shows that the non-mirror symmetric configurations with an up-down symmetric envelope produce more rotation than the configurations with an up-down asymmetric envelope at $m_c = 2$. It seems reasonable to attribute this to a failure to fully satisfy the assumption that $m_c \gg 1$.

8.3 Interpretation

This chapter determined that the intrinsic momentum flux generated by fast shaping with a slowly varying up-down asymmetric envelope is polynomially small in the scale of the fast shaping. Chapter 7 concluded that the momentum flux in mirror symmetric equilibria is exponentially small in the scale of the shaping. In order to interpret the results of these analytic arguments we will distinguish between “geometric” effects and “shaping” effects. Geometric effects are those that give a poloidal dependence to the geometric coefficients, apart from the linear dependence built into α due to magnetic shear. Shaping effects are the subset of the geometric effects that are specified in the flux surface shape or its radial derivative (i.e. the $m \neq 0$ terms in (5.8) and (5.9)). Using this terminology we can view the tokamak as having an inherent $m = 1$ geometric effect due to toroidicity, as discussed in section 7.3. However, we can see it

is distinct from the $m = 1$ shaping effect (i.e. the Shafranov shift) by looking at the geometric coefficients to lowest order in aspect ratio. The $m = 1$ toroidal geometric effect only appears in the two magnetic drift coefficients (see (E.12) and (E.13)), while the $m = 1$ shaping effect affects all six (see (E.19) through (E.24)). This toroidal geometric effect is not present in non-toroidal magnetic geometries such as the screw pinch.

Section 6.2 shows that if the magnetic geometry does not include at least two geometric effects with different tilt angles the momentum flux must be small in $\rho_* \ll 1$. Hence, in a screw pinch (without toroidicity to define up-down symmetry) the only option to drive intrinsic rotation is non-mirror symmetric shaping. Conversely, in a tokamak we can use either non-mirror symmetric shaping or an up-down asymmetric shaping effect with the toroidal geometric effect. The possibility of ignoring toroidicity entirely and using two modes with different tilt angles to drive momentum transport provides motivation to explore non-mirror symmetric configurations. This would be advantageous if, for some reason, toroidicity turns out to be very ineffective at driving rotation.

Sections 8.1.2 and 8.1.3 reveal another way to generate rotation. Namely, to beat two shaping effects together to make an slowly varying envelope that breaks up-down symmetry. This generates momentum flux that is polynomially small (for purely concave flux surfaces) in either mode number of the original shaping effects. Therefore, using a combination of low order shaping effects (e.g. elongation, triangularity) to create an up-down asymmetric envelope to drive rotation appears optimal. This reinforces the conclusions of chapter 3, which found that low order shaping modes were advantageous from MHD considerations. Specifically, we found that low order modes better penetrate to the magnetic axis from the plasma edge. Hence, they can make the inner flux surfaces of a device more asymmetric. Lastly, from the tilting symmetry presented in chapter 7 we learned that the momentum flux generated by two geometrical effects is exponentially small in the difference in the spatial scales of the poloidal variation they create.

Hence, the analytic arguments of chapters 3, 7, and 8 indicate that using low order, neighbouring shaping effects (e.g. elongation, triangularity) to break up-down asymmetry is best for creating rotation [18, 70]. Chapter 7 and the transport properties of screw pinches establish a distinction between mirror and non-mirror symmetric configurations and suggest that non-mirror symmetric configurations may be able to generate higher levels of rotation. We will explore these strategies at length in chapters 9 and 10.

Chapter 9

Non-mirror symmetry: Shafranov shift and tilted elongation

Much of this chapter appears in reference [22].

Chapters 3, 7, and 8 indicate that a non-mirror symmetric geometry with an up-down asymmetric envelope created by low order shaping effects is optimal for maximising intrinsic rotation. In this context, there are two options. The first is to introduce up-down asymmetric elongation using external poloidal field coils and then rely on the Shafranov shift (i.e. the shift in the magnetic axis due to toroidicity) to break mirror symmetry. This appears optimal because it makes use of the lowest possible shaping modes (i.e. $m = 1$ and $m = 2$). However, this strategy has the drawbacks that the effect of the Shafranov shift is formally small in aspect ratio and the direction/magnitude of the shift is a consequence of the plasma β profile and the global MHD equilibrium. Hence it is not independently controlled by external coils. Additionally, including effects that are small in aspect ratio also introduces β' , which controls the effect of the pressure gradient on the magnetic equilibrium. We will see that β' tends to strongly decrease the momentum transport. The second option is to use external coils to introduce both elongation and triangularity (i.e. $m = 2$ and $m = 3$ shaping) into the flux surface shape and directly break mirror symmetry. Both modes are lowest order in aspect ratio and can be directly controlled by external shaping magnets, but this relies on higher order shaping modes than the first option.

Practically speaking, these two strategies are intertwined as the divertor geometry nearly always introduces some triangularity into the flux surfaces and the Shafranov shift exists regardless of the shape of flux surfaces. Nevertheless, for simplicity it is useful to distinguish them and examine each option independently. In this chapter we will explore the former: the influence of the Shafranov shift and the effect of the β

profile on the turbulent momentum flux in the core of tokamaks. In chapter 10 we will explore the latter: the effect breaking flux surface mirror symmetry by independently varying the tilt angles of elongation and triangularity.

In this chapter we will perform nonlinear gyrokinetic simulations of tilted elliptical flux surfaces with a Shafranov shift. Section 9.1 starts by summarising the input parameters used in the gyrokinetic simulations. Section 9.2 details the results of several numerical scans aimed at illuminating the effect of the Shafranov shift and the β profile on momentum transport. In section 9.3 we discuss the sensitivity of the momentum transport to changes in the magnetic equilibrium caused by altering the local gradient of β . Furthermore, in section 9.4 we consider the impact of changing the shape of the radial profile of β .

9.1 Input Parameters

As in chapters 7 and 8, we will use GS2 to calculate the turbulent transport in shaped variants of the Cyclone base case (specified by the parameters of (7.37)). Most of our simulations will model tilted elliptical flux surfaces, all of which have an elongation of $\kappa = 2$. The turbulent fluxes calculated by GS2 will be normalised to gyroBohm values given by (7.38) and (7.39).

We will use a modified version of GS2 to simulate local Miller equilibria with flux surfaces prescribed with Exact specification, given by (5.18), (5.19), and (5.27) through (5.31). In order to create a realistic Shafranov shift, we will take the results from section 5.2, which uses the location of the magnetic axis shown for the constant current case in figure 4.5(b). Additionally, since the size of the Shafranov shift is closely connected to the plasma pressure, we included the effect of β' on the magnetic equilibrium. To capture this GS2 requires a local value of

$$\beta' \equiv \frac{2\mu_0 a}{B_0^2} \frac{dp}{da_\psi} \quad (9.1)$$

because it constructs the poloidal magnetic field to be consistent with the Grad-Shafranov equation. We will find that the momentum transport is quite sensitive to β' , so it is an important parameter. In keeping with rough projections for ITER [15], we use a pressure profile that is linear in a_ψ . This allows us to estimate that

$$\beta' \approx -\frac{2\mu_0 p_{\text{axis}}}{B_0^2} \approx -0.06, \quad (9.2)$$

using an ITER-like value for p_{axis} . Since we are running electrostatic simulations the value of β itself has no effect.

We note that assuming a constant β' (i.e. dp/da_ψ) profile is formally inconsistent with the constant $dp/d\psi$ profile used in the MHD calculation of the Shafranov shift. Hence, using the results shown in figure 4.5 together with (9.2) is not formally valid. However, figure 4.6 shows that the magnitude and direction of the Shafranov shift is insensitive to large changes in the shape of the pressure profile at constant R_{0b} , a , κ_b , I_p , and $p_{\text{axis}}/\psi_{0b}$. This suggests that, since we have kept the proper parameters fixed, the pressure profile mismatch will not have much effect.

9.2 Parameter scan results

A total of four scans in θ_κ , the tilt angle of the flux surface of interest, were performed at

- (1) $\beta' = 0$ with no Shafranov shift,
- (2) $\beta' = 0$ with a modest Shafranov shift (approximately half the ITER-like Shafranov shift),
- (3) $\beta' = 0$ with an ITER-like Shafranov shift, and
- (4) an ITER-like $\beta' = -0.06$ with an ITER-like Shafranov shift.

These were done to directly determine the influence of the Shafranov shift and β' . The magnitude and direction of the local ITER-like Shafranov shift was kept consistent with (5.22) and (5.23). Additionally, a single simulation was performed with $\beta' = -0.06$ and no Shafranov shift in order to isolate the effect of β' .

Four scans in ρ_0 , the minor radial coordinate of the flux surface of interest, were performed at

- (1) $\beta' = 0$ with no Shafranov shift,
- (2) $\beta' = 0$ with an ITER-like Shafranov shift,
- (3) an ITER-like $\beta' = -0.06$ with no Shafranov shift, and

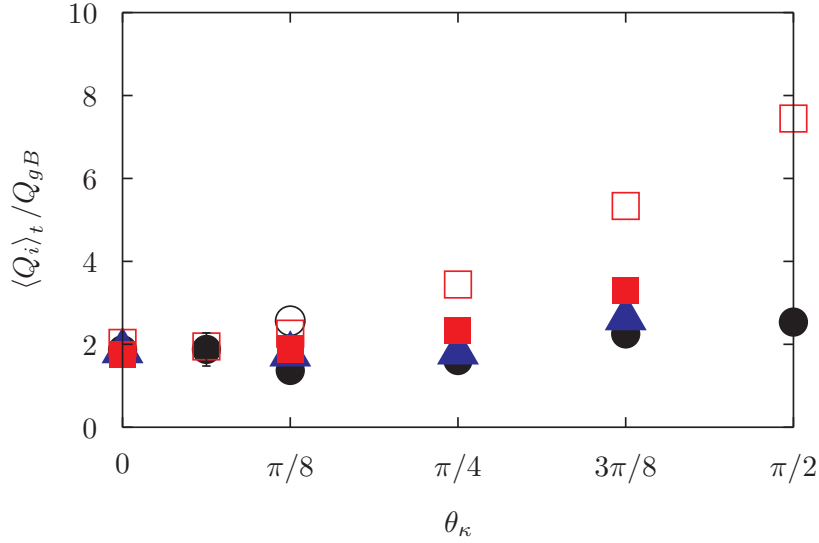


Figure 9.1: The ion energy flux for flux surfaces with no shift (black, circles), a modest shift (blue, triangles), and an ITER-like shift (red, squares) for $\beta' = 0$ (filled) and an ITER-like β' (empty).

- (4) an ITER-like $\beta' = -0.06$ with an ITER-like Shafranov shift.

All simulations had elliptical flux surfaces with $\theta_\kappa = \pi/8$. These scans were done in order to investigate the balance between the Shafranov shift, which we expect to enhance the momentum transport, and β' , which our GS2 simulations will reveal to reduce the momentum transport. For these scans we kept β' constant to be consistent with ITER (according to (9.2)) and again calculated the local Shafranov shift at each minor radius according to (5.22) and (5.23).

Lastly, a small scan was performed with circular flux surfaces in which θ_{axis} , the direction of the Shafranov shift, was varied. This is unphysical, but it was done to explicitly isolate the effect of a pure flux surface Shafranov shift.

9.2.1 Elliptical boundary tilt scans

For the tilted elliptical scans, the ion energy flux calculated by GS2 is shown in figure 9.1. In all simulations the electron energy flux was consistently smaller than the ion energy flux, typically by a factor of four. We see that the energy flux is fairly insensitive to the effects of both the Shafranov shift and β' in the domain of $\theta_\kappa \in [0, \pi/8]$. At more extreme tilt angles we see that β' dramatically increases the energy flux, as does the shift (albeit to a lesser extent).

The ratio of the momentum flux to the energy flux, which is an estimate of intrinsic rotation through (6.30), is shown in figure 9.2. As expected, we see that the presence

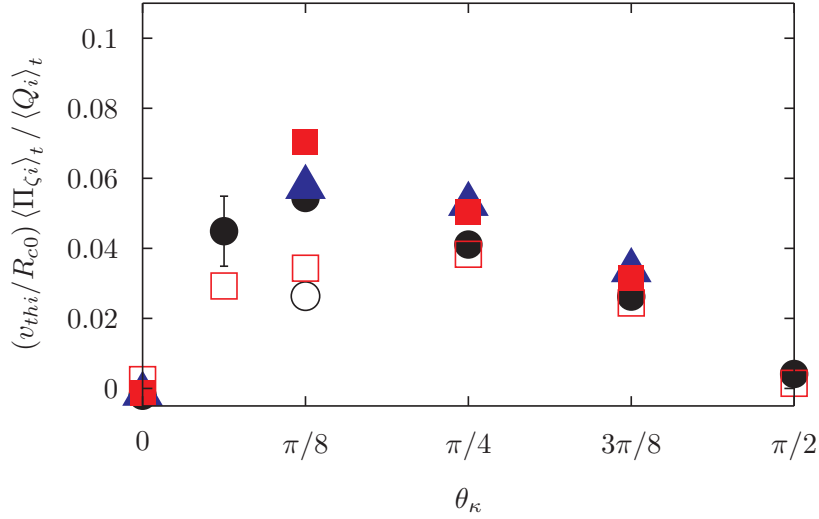


Figure 9.2: The momentum transport for flux surfaces with no shift (black, circles), a modest shift (blue, triangles), and an ITER-like shift (red, squares) for $\beta' = 0$ (filled) and an ITER-like β' (empty).

of an ITER-like Shafranov shift increases the momentum transport by approximately 30%. However, a non-zero β' significantly reduces the momentum transport. These two effects counteract one another and for ITER-like values at $\theta_{\kappa} = \pi/8$ and $\rho_0 = 0.54$ the shift is overshadowed by β' , leading to a net reduction in the momentum transport of about 30%.

9.2.2 Minor radial scans

These scans keep β' , $d \ln(T_s)/d\rho$, $d \ln(n_s)/d\rho$, q , and \hat{s} constant with minor radius. We chose to keep β' constant to be consistent with ITER (according to (9.2)). The others were kept fixed in order to avoid varying too many parameters in the scan. However, constant values for $d \ln(T_s)/d\rho$ and $d \ln(n_s)/d\rho$ are not an unreasonable approximation to many experiments, especially in the core of tokamaks [71].

The minor radial dependence of the momentum flux, shown in figure 9.3, is consistent with the previous scans. Comparing the two scans with $\beta' = 0$, we see that the difference in the momentum transport of the two scans increases with minor radius. This makes sense because the magnitude of the local shift increases linearly with minor radius according to (5.22) and (5.23).

Additionally, throughout this scan the magnitude of the Shafranov shift changes, while β' remains constant. Hence, we can compare the no shift, $\beta' = 0$ case to the ITER-like shift, ITER-like β' case to demonstrate the counteracting effects of the shift and β' on the momentum transport. Because the shift is weak at small

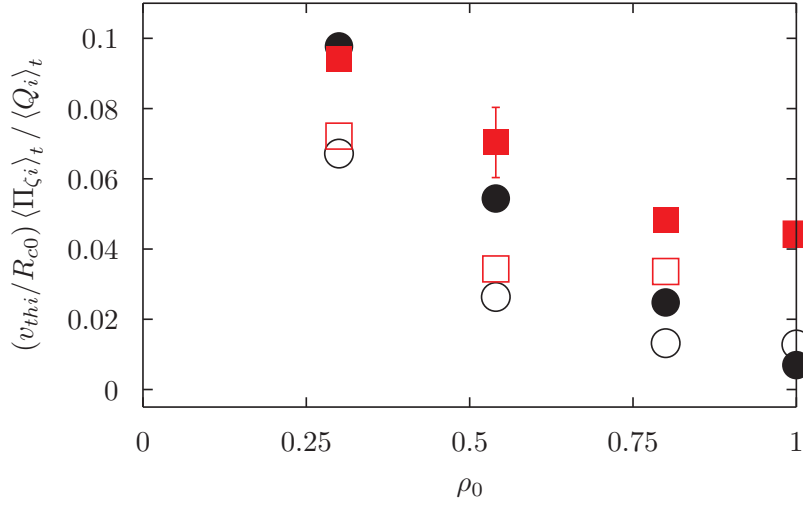


Figure 9.3: The radial dependence of the momentum transport for flux surfaces with no shift (black, circles) and a strong shift (red, squares) varied according to (5.22) and (5.23), for $\beta' = 0$ (filled) and an ITER-like β' (empty).

values of ρ_0 , the net effect of the shift and β' is to lower the momentum transport. However, at large values of ρ_0 the shift is stronger, but β' remains the same. Here the net effect of the shift and β' is to enhance the momentum transport. Note that at $\rho_0 = 1$ the momentum transport in the shifted configurations with and without β' are indistinguishable.

Lastly, the dominant trend in figure 9.3 is the roughly linear decrease of the momentum transport with minor radius. This is not currently understood as nearly all simulations of intrinsic rotation from up-down asymmetry were performed using $a_{\psi 0}/R_{c0} \approx 1/6$. However, the decreasing trend with increasing $a_{\psi 0}/R_{c0}$ is consistent with the results of several simulations performed at $a_{\psi 0}/R_{c0} \approx 1/12$ and $a_{\psi 0}/R_{c0} \approx 1/3$ in reference [18]. These results suggest that in this parameter range the momentum transport increases with the aspect ratio.

9.2.3 Circular flux surface scan

To completely isolate the effect of the Shafranov shift on momentum transport we also ran simulations with shifted circular flux surfaces as shown in figure 9.4. To create up-down asymmetry and drive momentum transport we varied the direction of the tilt by changing the parameter θ_{axis} with the magnitude of the shift fixed at a value $\sim 30\%$ larger than an ITER-like machine. Scanning θ_{axis} is unphysical because circular flux surfaces can only ever have a shift in the outboard radial direction, which

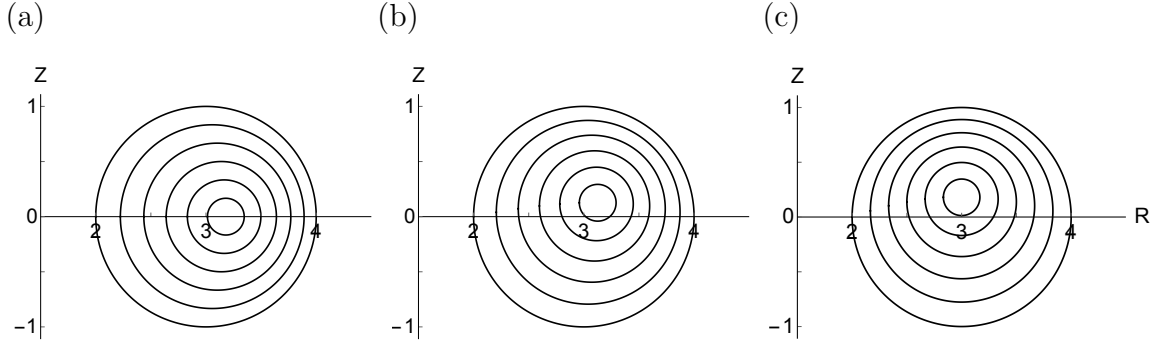


Figure 9.4: The magnetic geometry for circular flux surfaces with an ITER-like (a) horizontal shift, (b) diagonal shift, or (c) vertical shift.

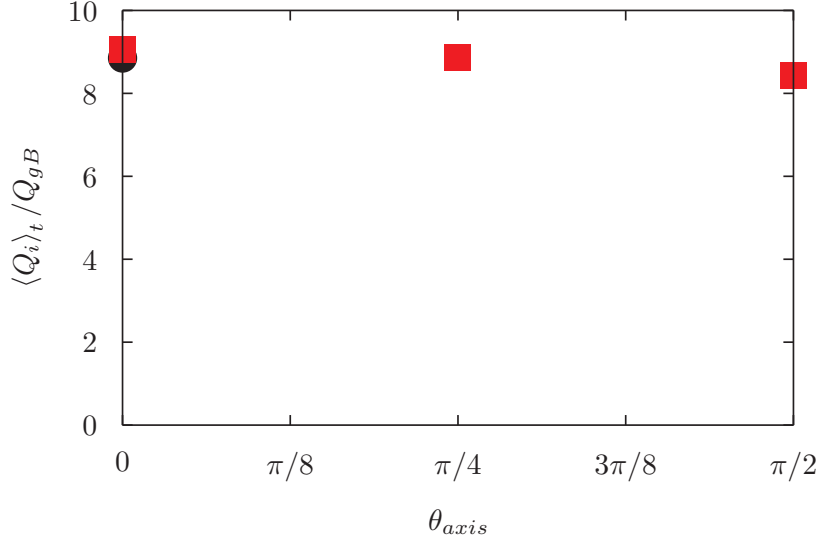


Figure 9.5: The energy flux for circular flux surfaces with no shift (black, circles) and an ITER-like shift (red, squares) as a function of the direction of the Shafranov shift, where all simulations have $\beta' = 0$.

corresponds to $\theta_{axis} = 0$. Though unphysical, this scan will help clarify the influence of the Shafranov shift.

Figure 9.5 shows that the presence and direction of the Shafranov shift has little effect on the energy flux from circular flux surfaces. This is akin to the tilted elliptical results in the range of $\theta_\kappa \in [0, \pi/8]$, but different from the tilted elliptical results in the range of $\theta_\kappa \in [\pi/8, \pi/2]$. A possible explanation for figure 9.5 is that the magnitude of the shift in the circular equilibria is similar to that in the $\theta_\kappa = \pi/16$ elliptical equilibria, but considerably less than the shift present in the elliptical equilibria with large tilt angles.

In figure 9.6, we see the effect of a strong Shafranov shift on momentum transport.

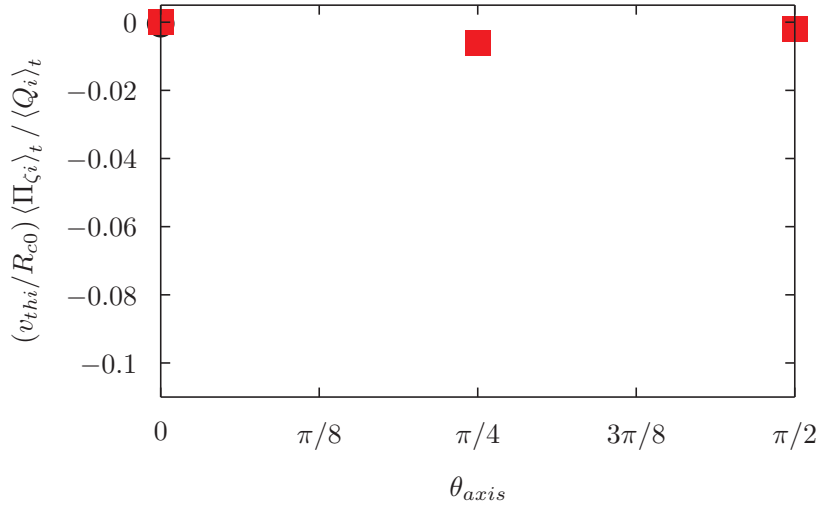


Figure 9.6: The momentum transport for circular flux surfaces with no shift (black, circles) and an ITER-like shift (red, squares) as a function of the direction of the Shafranov shift, where all simulations have $\beta' = 0$. Note that we have kept the range of the vertical axis the same as in figures 9.2 and 9.3 for ease of comparison.

It appears that a pure shift in circular flux surfaces (even when it is diagonal or vertical) drives minimal rotation compared to that generated by elliptical flux surfaces. This is somewhat surprising since the shift is an $m = 1$ shaping effect and, from the analysis in chapter 7, we expect the momentum flux to scale as $\exp(-\beta m^\gamma)$ in mirror symmetric configurations. However, there are two important caveats. Firstly, the exponential scaling is only true in the limit of $m \gg 1$, which is clearly not satisfied for $m = 1$. Secondly, the Shafranov shift has a relatively minor effect on the magnetic equilibrium compared with elongating the flux surfaces to $\kappa = 2$ (even when the shift is 30% stronger than that expected in ITER). This can be seen by looking at the geometric coefficients that appear in the gyrokinetic equation (see chapter 6). Since these coefficients are the only way the magnetic geometry enters the local gyrokinetic model, they must control the momentum transport. For example, in figure 9.7 we see that elongating an unshifted circular configuration changes the coefficient $|\vec{\nabla}\psi|^2$ by 300%, while introducing the Shafranov shift only makes a 50% difference. Hence, we believe that the Shafranov shift and elongation are comparably effective at transporting momentum, but that practical limits on the maximum value of β constrain the Shafranov shift to have a small effect on the magnetic equilibrium compared to externally applied plasma shaping.

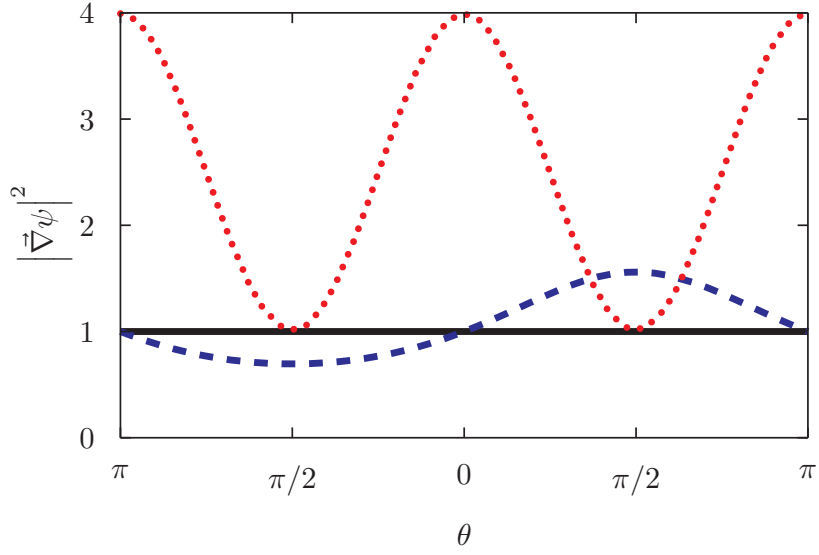


Figure 9.7: The geometric coefficient $\left|\vec{\nabla}\psi\right|^2$ for unshifted circular flux surfaces (black, solid), circular flux surfaces with a strong vertical shift (blue, dashed), and unshifted flux surfaces with a vertical elongation of $\kappa = 2$ (red, dotted) normalised to the unshifted circular value.

9.3 Effect of the value of β'

In section 9.2 we included the effect of the Shafranov shift in nonlinear, local gyrokinetic simulations and found that it enhanced momentum transport as expected. Since the magnitude of the shift depends on the plasma pressure, we also included a non-zero β' . We found that β' strongly reduced the momentum flux, often entirely cancelling the enhancement due to the Shafranov shift. Consequently, it is important to understand how β' alters the geometric coefficients of gyrokinetics.

In appendix F we discuss how β' enters into the analytic expressions for the geometric coefficients. We show that β' vanishes in the large aspect ratio limit (for the orderings of (2.4)), like the Shafranov shift. This means that for large aspect ratio tokamaks β' can be ignored and the results of reference [18] (which ignores β') apply. However, the Shafranov shift also vanishes in this limit, so it cannot be used to enhance the momentum transport.

Figure 9.8 uses the simulations from the minor radial scan to show the quantitative effect of β' on the geometric coefficient $v_{ds\alpha}$ (defined by (6.10)) with different values of w_{\parallel} and w_{\perp} . We chose $v_{ds\alpha}$ as chapter 8 indicates that it may be the most important geometric coefficient for understanding intrinsic rotation transport due to up-down asymmetry. We see that including a non-zero β' tends to reduce the up-down

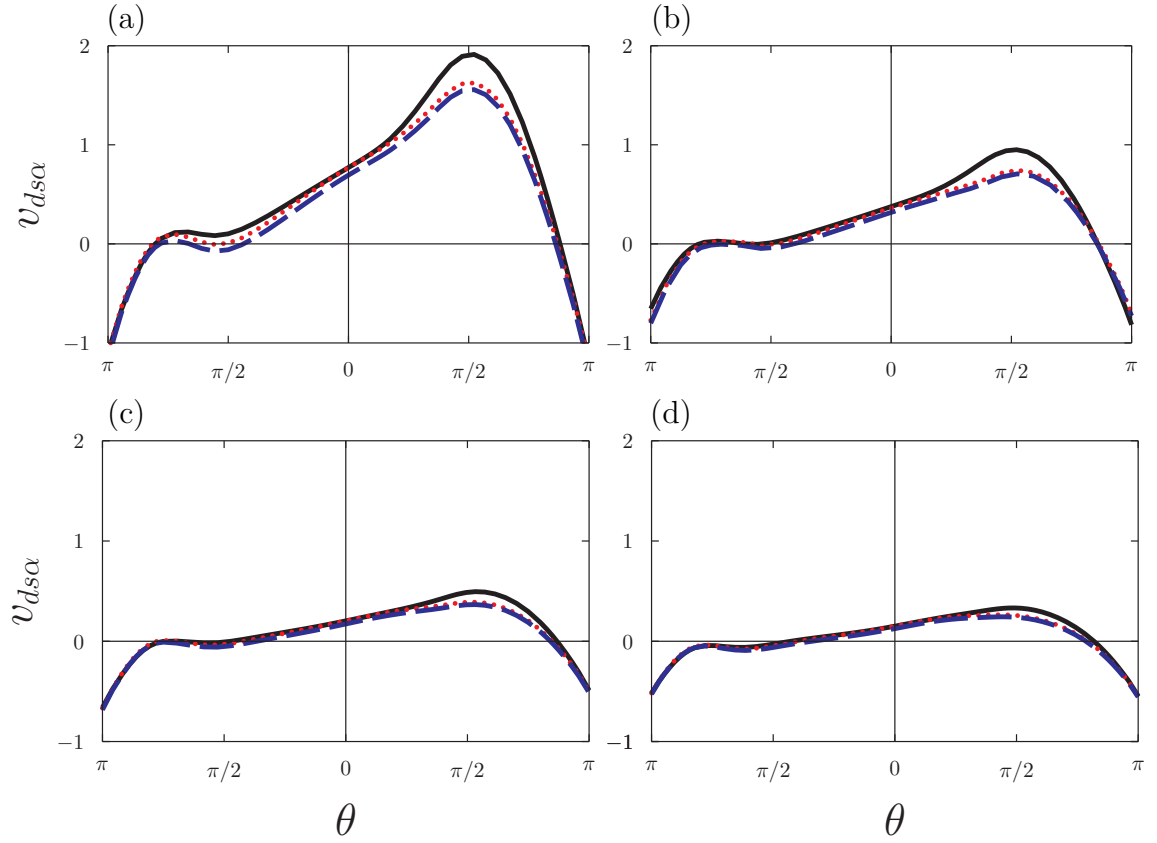


Figure 9.8: The geometric coefficient $v_{ds\alpha}$ in units of $v_{ths}^2/(a^2\Omega_s)$ without Shafranov shift at (a) $\rho_0 = 0.3$, (b) $\rho_0 = 0.54$, (c) $\rho_0 = 0.8$, and (d) $\rho_0 = 1$ for no β' , $w_{||}^2 = v_{ths}^2$, $w_{\perp}^2 = 0$ (black, solid); an ITER-like β' , $w_{||}^2 = v_{ths}^2$, $w_{\perp}^2 = 0$ (red, dotted); and an ITER-like β' , $w_{||}^2 = 0$, $w_{\perp}^2 = 2v_{ths}^2$ (blue, dashed).

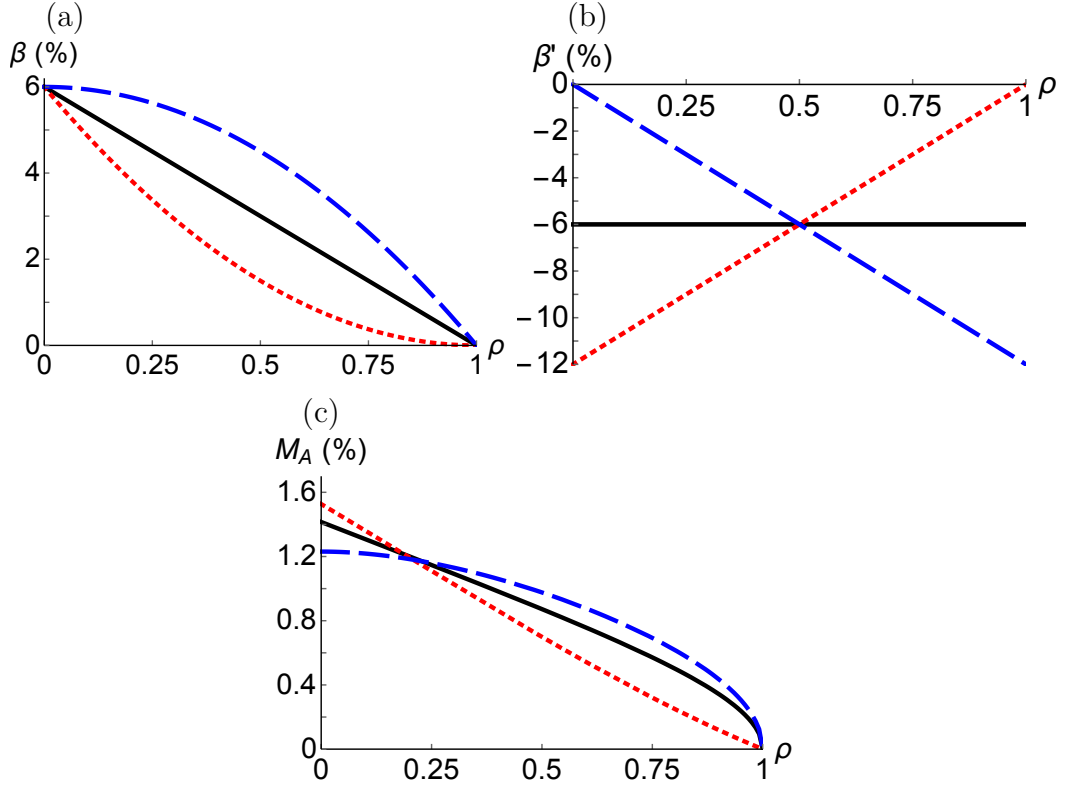


Figure 9.9: Example (a) β profiles, their corresponding (b) β' profile, and their (c) Alfvén Mach number profile, estimated using (6.30) for a constant β' (black, solid), linear peaked β' (red, dotted), and linear hollow β' (blue, dashed) profiles.

asymmetry of $v_{ds\alpha}$, which is consistent with the observed reduction in momentum transport.

9.4 Effect of the β profile

In order to estimate a realistic value for β' , we used the on-axis value of β predicted for ITER and assumed β was linear with minor radius a_ψ . This gave a reasonable order of magnitude estimate. However, since the momentum transport is strongly and adversely affected by β' it is worthwhile to discuss the implications of different radial profiles of β' . For example, we expect that in H-mode operation β' would be larger at the plasma edge and smaller in the core compared to L-mode. Unfortunately, from the estimate of rotation given by (6.30), we see that β' is necessary, even though including the effect of β' in the geometric coefficients reduces the momentum flux. Physically the necessity of β' is intuitive because the pressure gradient is the source of free energy that ultimately drives the momentum transport. Because of all these competing

dependencies on β and β' , both explicitly and through $(v_{thi}/R_{c0}) \langle \Pi_{\zeta i} \rangle_t / \langle Q_i \rangle_t$, it is difficult to determine the β profile that maximises rotation. In figure 9.9 we use (6.30) and the approximation

$$\frac{v_{thi}}{R_c} \frac{\langle \Pi_{\zeta i} \rangle_t}{\langle Q_i \rangle_t} \approx c_1 + c_2 \rho + c_3 \beta' + c_4 \rho \beta' \quad (9.3)$$

to estimate the rotation profile for different β profiles. Here the coefficients $c_1 = 0.11$, $c_2 = -0.06$, $c_3 = 0.34$, and $c_4 = -0.28$ are determined by a fit to the data in figure 9.3. We include the dependence on β' and ρ in the fit because the momentum transport is sensitive to both. Figure 9.9 shows that the shape of the β profile can have a significant effect on the rotation profile. We see that a more peaked pressure profile seems to lead to a more peaked rotation profile. It is interesting to note that the rotation profiles with the lowest on-axis Mach number have the broadest rotation profiles. This means that the β profile that maximises the *on-axis* Mach number is not necessarily optimal because broad rotation profiles are expected to be significantly more effective at stabilising MHD modes [6].

Chapter 10

Non-mirror symmetry: Tilted elongation and tilted triangularity

From our analytic scaling studies in chapters 7 and 8 we have identified two most promising types of non-mirror symmetry. In chapter 9 we explored the first: using the Shafranov shift to break the mirror symmetry of tilted elliptical flux surfaces. In this chapter we will examine the second: using externally applied elongation and triangularity with independent tilt angles to directly make the flux surface shapes non-mirror symmetric. We will compare these two-mode geometries (i.e. flux surfaces with both elongation and triangularity) with single-mode geometries (i.e. flux surfaces with only elongation or triangularity) to see if the momentum transport can be significantly increased.

To do this, we will use GS2 to calculate the nonlinear electrostatic fluxes for a two dimensional scan in θ_κ and θ_δ , the tilt angles of elongation and triangularity respectively. In keeping with previous simulations, we will use a shaped variant of the Cyclone base case (specified by the parameters of (7.37)) without collisions, except we must increase the temperature gradient of both species to $a/L_{Ts} = 3.0$ to ensure that the turbulence is unstable. The strength of elongation and triangularity is set at $\Delta_2 = 1.7$ and $\Delta_3 = 1.3$ respectively, which were values estimated from the shape of the ITER plasma [15]. We note that this elongation is significantly lower than the value of 2 used in chapter 9.

These unusual, highly-shaped flux surface shapes have quite detailed and sharp poloidal structure. Properly resolving this requires a fine poloidal grid, typically with 96 grid points. This means that these simulations are considerably more expensive than single-mode flux surfaces (which typically require between 32 and 64 grid points).

10.1 Exact shaping geometry scan

We performed the scan using the Exact geometry specified by (5.18) and (5.19) (with $\theta_{t2} = \theta_\kappa$ and $\theta_{t3} = \theta_\delta$) in order to produce figure 10.1. Note that the missing geometries are redundant as the up-down symmetry argument (see section 6.2) implies that an up-down reflection of the flux surface shape changes the sign of the momentum flux and does not effect the energy flux.

Figure 10.1(a) shows how the intrinsic rotation generated by the two-mode geometries compares with that generated by flux surfaces with only elongation or triangularity. We see that the maximum intrinsic rotation from the two-mode geometry (i.e. that from the $\theta_\kappa = \pi/4$, $\theta_\delta = \pi/6$ case) is over 60% larger than the maximum that can be generated with only elongation. Furthermore, the sum of the rotation generated by purely elongated flux surfaces and purely triangular flux surfaces falls short of the rotation generated by flux surfaces with both elongation and triangularity. This suggests that there is a nonlinear interaction between the different shaping effects.

One possible explanation is the breaking of flux surface mirror symmetry. This is the dominant mechanism in a screw pinch, where momentum transport is driven by the direct interaction of different shaping effects. However, this does not explain the size of the momentum flux in the $\theta_\kappa = \pi/4$, $\theta_\delta = \pi/12$ case, which is mirror symmetric. In fact, while the geometry with the largest momentum transport is non-mirror symmetric, on average the mirror and non-mirror symmetric configurations have roughly similar levels of turbulent transport. This indicates that the importance of non-mirror symmetry (e.g. the direct interaction of elongation and triangularity) for momentum transport is minimal in these low mode number configurations.

Another explanation is that the beating between elongation and triangularity creates an $m = 1$ mode (i.e. an envelope), which drives the extra rotation. However, the configuration with the highest rotation has an up-down symmetric $m = 1$ envelope, which we can see by substituting $\theta_{t2} = \theta_\kappa = \pi/4$ and $\theta_{t3} = \theta_\delta = \pi/6$ into (8.63). This suggests that the tilting symmetry argument, which predicts that non-mirror symmetric configurations with an up-down symmetric envelope should have exponentially small momentum transport in $m_c \gg 1$, is not applicable to these configurations. This behaviour is consistent with figure 8.3, which shows that configurations with an up-down asymmetric envelope have larger momentum transport than those with an up-down symmetric envelope at high m , but not at $m = 2$. To understand why the tilting symmetry argument breaks down for elongation and triangularity we

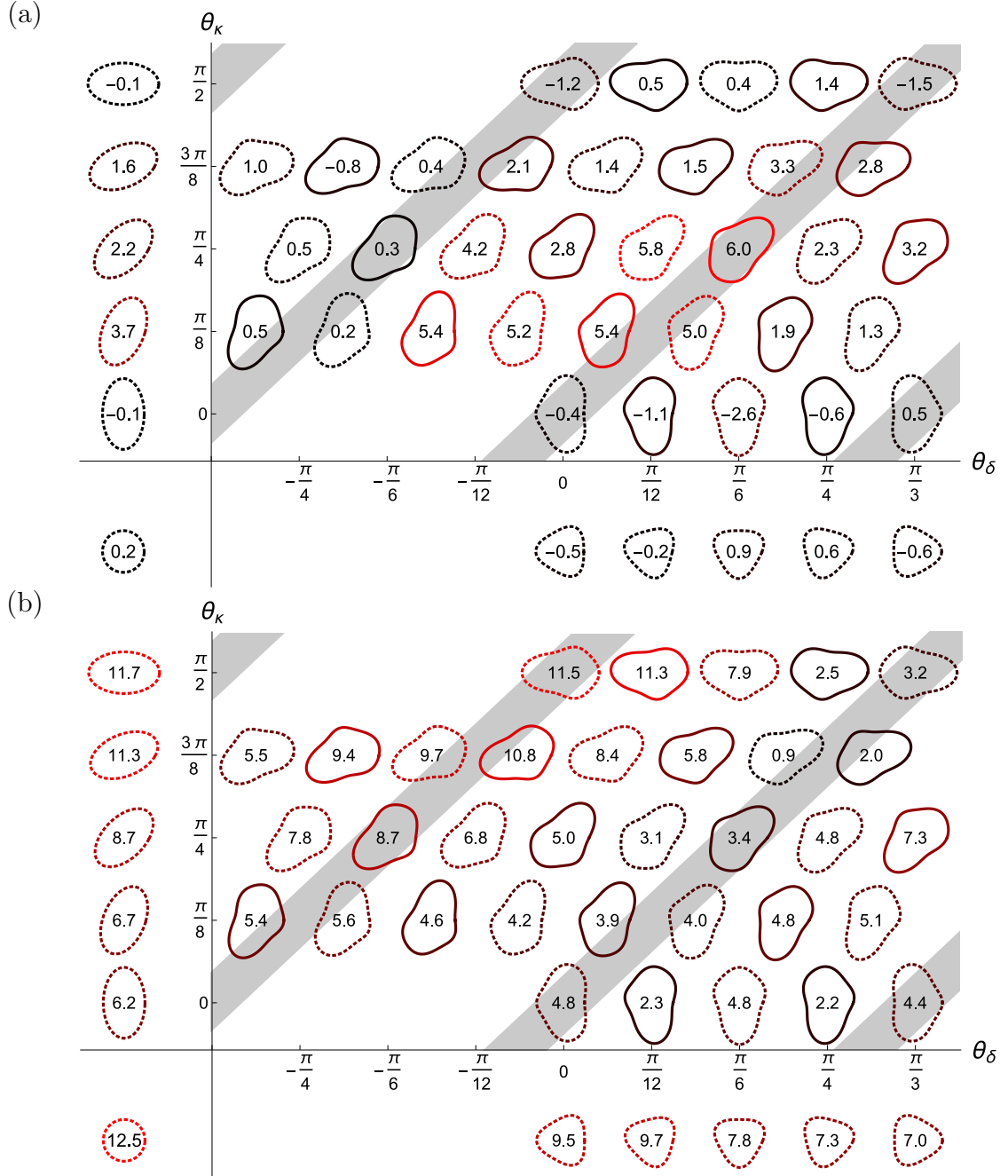


Figure 10.1: Values of (a) $100 \times (v_{thi}/R_{c0}) \langle \Pi_{\zeta i} \rangle_t / \langle Q_i \rangle_t$ and (b) $\langle Q_i \rangle_t / Q_{gB}$ (with errors of ± 0.5 and ± 0.3 respectively) are indicated by the numbers/colours for various non-mirror symmetric (solid lines) and mirror symmetric (dotted lines) flux surfaces created with elongation and triangularity (using the Exact geometry specification). The thick grey bands indicate geometries with up-down symmetric envelopes according to (8.63). Purely elongated flux surfaces are shown in quadrant II, a circular flux surface is shown in quadrant III, and purely triangular flux surfaces are shown in quadrant IV for comparison.

will study figure 7.3. We see that the poloidal distribution of momentum flux from circular flux surfaces tends to have a strong $m = 2$ Fourier mode due to the inherent toroidicity of the tokamak. Furthermore, shaping the flux surface with a mode m creates large Fourier components in the distribution of momentum flux at $m - 1$ and $m - 2$. These facts were used in chapter 7 to explain why the agreement in figure 7.4 breaks down for shaping modes with $m \leq 4$. Therefore, we expect triangularity to create an $m = 2$ Fourier mode in the momentum flux, which can beat against the inherent $m = 2$ component from toroidicity to produce an $m = 0$ component, which does not average to zero over the flux surface. This direct interaction between toroidicity and what we are considering “fast” shaping breaks the tilting symmetry. To put the issue simply, we relied on an expansion in $m_c \gg 1$ (or more precisely $m_c - 2 \gg 1$), which is not satisfied by elongation and triangularity (i.e. $m = 2$ and $m = 3$).

Instead, for these geometries it appears that the intrinsic rotation drive is dominated by the direct interaction of elongation and triangularity with toroidicity.

While it is true that in figure 10.1(a) the flux surfaces with two shaping modes generate significantly more rotation than the single-mode surfaces, it is not necessarily a fair comparison. The two-mode flux surfaces are more shaped, meaning they require more external coils/current and are less stable to axisymmetric modes. Looking at figure 9.2, we see that the maximum two-mode value (at $\Delta_2 = 1.7$ and $\Delta_3 = 1.3$) is only slightly above that produced by pure elongation with $\Delta_2 = 2$ (simulated in chapter 9). However, the two-mode flux surfaces seem preferable for reasons apart from momentum transport. Figure 10.1(b) shows that the highest performing two-mode geometries directly stabilise turbulence and increase the confinement time. In fact the turbulence is completely stabilised at the standard Cyclone base case temperature gradient of $a/L_{Ts} = 2.3$. Hence not only is the turbulence reduced, but the critical gradient is increased substantially (even compared to the elongated flux surfaces with $\Delta_2 = 2$). We note that, as in the Shafranov shift scans, the electron energy flux was consistently smaller than the ion energy flux, typically by a factor of four.

Chapter 11

Conclusions

The “optimal” flux surface geometry, as indicated by the analysis of this thesis, is shown in figure 11.1. It appears optimal because it generated the highest intrinsic rotation of any configuration simulated (see figure 10.1(a)) and has among the lowest energy flux (see figure 10.1(b)). These values could almost certainly be improved by going to stronger shaping, but we constrained our search to more practical geometries by using the magnitude of shaping from ITER. The boundary flux surface of the optimal geometry is specified by (5.18), (5.30), and (5.31) with $a = a_{\psi 0} = 1$, $R_{0b} = R_{c0} = 3$, $\kappa = \Delta_2 = 1.7$, $\delta \approx \Delta_3 = 1.3$, $\theta_\kappa = \theta_{t2} = \pi/4$, and $\theta_\delta = \theta_{t3} = \pi/6$. The MHD equilibrium was calculated assuming a constant current profile according to (2.21) and (2.33). This is because a constant profile reasonably approximates experiments, although figure 3.4 shows that a hollow current profile would increase the shaping of the inner flux surfaces.

The precise tilt angles of the optimal geometry indicate the mechanisms that transport momentum in flux surfaces with elongation and triangularity. The tilting symmetry presented in section 7.1 demonstrates that non-mirror symmetric geometries with an up-down symmetric envelope must have exponentially small momentum transport in the Fourier mode number of the fast shaping. This contrasts with the results of sections 8.1.2 and 8.1.3, which show that a polynomial scaling holds when the envelope is up-down asymmetric. However, the optimal geometry turns out have an exactly up-down symmetric envelope. This suggests that the beating of elongation and triangularity to produce an $m = 1$ envelope, which can then interact with toroidicity, is not particularly important. Additionally, while the optimal geometry is non-mirror symmetric, figure 10.1(a) shows several mirror symmetric configurations that generate fairly comparable momentum transport. This indicates that the momentum transported due to the direct interaction of elongation with triangularity (as would be dominant in a screw pinch) is fairly small in tokamaks. Hence, we believe

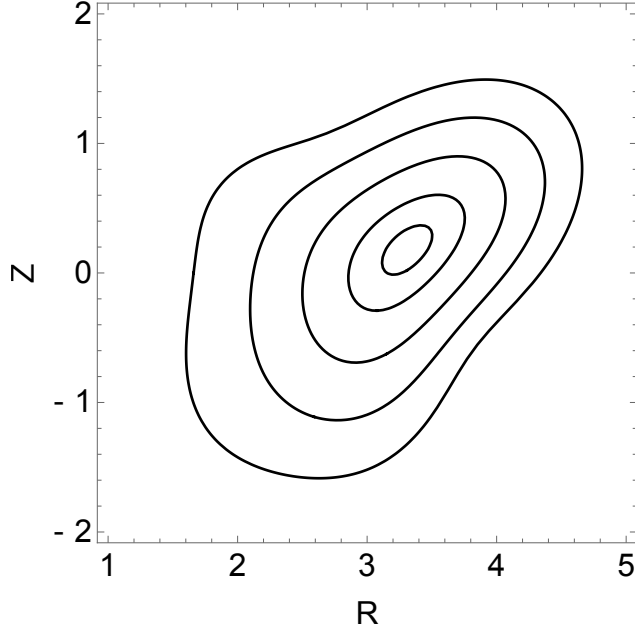


Figure 11.1: The “optimal” magnetic geometry, i.e. the flux surface equilibrium that is expected to maximise intrinsic toroidal rotation generated by up-down asymmetry.

that the momentum transport is dominated by the interactions of elongation and triangularity with toroidicity, but not through creating an $m = 1$ envelope.

The nonlinear gyrokinetic simulations shown in figure 10.1(a) indicate that, without the effect of plasma pressure, the optimal geometry will generate momentum transport with $(v_{thi}/R_{c0}) \langle \Pi_{\zeta i} \rangle_t / \langle Q_i \rangle_t \approx 0.06$. We note that the simulations from figure 10.1(a) were performed at a Cyclone base case value of $\rho_0 = 0.54$, rather than at the edge. However, figure 9.3 suggests that a mid-radius simulation without the effects of the Shafranov shift or β' is not a bad estimate for the value at the edge including the Shafranov shift and β' . Therefore, even though including a constant ITER-like dp/da_ψ can enhance momentum transport through the Shafranov shift (see section 9.2) or reduce it through the way it modifies the magnetic geometry within the flux surface (see section 9.3), we will assume these two effects roughly cancel with the effect of changing the value of ρ_0 .

Using (6.30), we can estimate an on-axis Alfvén Mach number of 1.5%, assuming $(v_{thi}/R_{c0}) \langle \Pi_{\zeta i} \rangle_t / \langle Q_i \rangle_t \approx 0.06$ is constant across the entire minor radius. This value of 1.5% is similar to figure 9.9(c), which uses a more sophisticated treatment of elongated configurations with a Shafranov shift. We note that both of these estimates ignores the momentum pinch, which may enhance the level of rotation by a much as a factor of three [62]. Conversely, we know that, unlike elongation (see figure 3.4(b)),

triangularity does not penetrate effectively to the core (see figure 3.4(e)). This causes the inner flux surfaces of figure 11.1 to be less strongly shaped than the outer surfaces, so we might expect a reduction in the momentum transport. However, looking more closely at (6.30), we see that the on-axis rotation is the minor radial integral of $(v_{thi}/R_{c0}) \langle \Pi_{\zeta i} \rangle_t / \langle Q_i \rangle_t$, weighted by the pressure gradient. Hence, a strategy to deal with the finite penetration of triangularity is to have a broad pressure profile with a steep gradient near the edge (i.e. H-mode). Not only will this make better use of the edge plasma shaping, but figure 9.9 indicates it will lead to a broader rotation profile (which is better for stabilising MHD modes). *Nevertheless, up-down asymmetry looks to be capable of generating rotation with an on-axis Alfvén Mach number of 1.5% in large devices, which is approximately what is needed to stabilise certain MHD modes and allow for violation of the Troyon limit.*

Part III

Appendices

Appendix A

Maximum achievable flux surface shaping

Much of this appendix appears in reference [41].

If we try to create flux surfaces with extreme shaping, we will eventually introduce x-points into the plasma, opening the flux surfaces. Since open field lines cannot confine fusion plasmas, this provides a fundamental limit on the strength of plasma shaping. To quantify this we will take (2.21) with a single shaping mode m from our analysis of the constant current profile and require that $\vec{\nabla}\psi_N = 0$. This gives us the condition that

$$N_{0,m} = \frac{\hat{j}_0 b_x^{2-m}}{2m}, \quad (\text{A.1})$$

where b_x is the radial location of all m of the x-points. Substituting this into (3.8) and making use of (3.2) gives

$$\Delta_x^{-2} + \frac{2}{m}\Delta_x^{-m} = 1 - \frac{2}{m}, \quad (\text{A.2})$$

where $\Delta_x \equiv b_x/a_x$ is the strongest flux surface shaping possible and a_x is the minimum distance of the separatrix from the magnetic axis. This can be solved exactly using numerical methods or approximated analytically as

$$\Delta_x - 1 = \frac{1.2785}{m} + O(m^{-2}), \quad (\text{A.3})$$

in the limit that $m \gg 1$. The numerical constant in (A.3) is the solution $x = 1.2785$ to

$$x - \exp(-x) = 1. \quad (\text{A.4})$$

Hence, we can conclude that, given a constant current profile, $\Delta_m - 1 \sim m^{-1}$ is the strongest possible scaling. Any scaling stronger than this will necessarily introduce x-points into the plasma.

Appendix B

Location of the magnetic axis for a tilted elliptical boundary and constant current profile

Much of this appendix appears in reference [22].

In order to find the location of the magnetic axis for a constant toroidal current profile we will start with (2.21). By requiring that $\psi_0(r_b(\theta), \theta) = \psi_{0b}$ be constant on the tilted elliptical boundary parameterized by (4.1), we find that

$$\psi_{0b} = \frac{\hat{j}_0}{2} \frac{a^2 \kappa_b^2}{\kappa_b^2 + 1} \quad (\text{B.1})$$

$$N_{0,2} = \frac{\hat{j}_0}{4} \frac{\kappa_b^2 - 1}{\kappa_b^2 + 1} \quad (\text{B.2})$$

as well as $\theta_{t02} = \theta_{\kappa b}$ (according to (4.3)). All other lowest order Fourier coefficients are zero.

Calculating the next order Fourier coefficients from the boundary condition (i.e. requiring that $\psi_1(r_b(\theta), \theta) = \psi_{1b}$ is constant) is algebraically intensive. We start with (2.33), the next order solution of the poloidal flux for a constant current profile. Note that while the current profile is assumed to be constant, we are allowing for a pressure gradient that is linear in ψ . First, we will postulate that the fifth, third, and first Fourier harmonics are the only ones required to match the boundary condition. All other next order Fourier coefficients are set to zero. Then we change poloidal angle to $\theta_s \equiv \theta + \theta_{\kappa b}$ in order to align the coordinate system with the minor and major axes of the elliptical boundary flux surface. Next we change from polar coordinates to Cartesian coordinates in the poloidal plane (i.e. $r = \sqrt{X^2 + Y^2}$ and

$\theta_s = \arctan(Y/X)$). This converts $\psi_1(r, \theta_s)$ into $\psi_1(X, Y)$, a fifth-order polynomial that contains products of X and Y . For the boundary condition we use

$$\left(\frac{X}{a}\right)^2 + \left(\frac{Y}{\kappa_b a}\right)^2 = 1, \quad (\text{B.3})$$

the traditional Cartesian formula for an ellipse, instead of (4.1). Solving (B.3) for $Y(X)$ and substituting it into $\psi_1(X, Y)$ allows us to eliminate all appearances of X^2 , X^4 , Y^2 , and Y^4 . We are left with a fifth-order polynomial that only has six terms, one proportional to each of X^5 , $Y^5(X)$, X^3 , $Y^3(X)$, X , and $Y(X)$. Since we have already made use of the boundary condition, we know that the whole polynomial must be constant. Requiring that the coefficients of the six terms be zero gives

$$C_{1,m} = A_{Cm} \cos(m\theta_{\kappa b}) - A_{Sm} \sin(m\theta_{\kappa b}) \quad (\text{B.4})$$

$$S_{1,m} = -A_{Sm} \cos(m\theta_{\kappa b}) - A_{Cm} \sin(m\theta_{\kappa b}), \quad (\text{B.5})$$

where

$$A_{C5} \equiv (\kappa_b^2 - 1) \frac{\hat{f}_{0p}\hat{j}_{0p}}{48R_{0b}} \frac{(\kappa_b^2 - 1)\hat{j}_0 - (7\kappa_b^2 + 5)N_{0,2}}{5\kappa_b^4 + 10\kappa_b^2 + 1} \cos(\theta_{\kappa b}) \quad (\text{B.6})$$

$$A_{S5} \equiv -(-\kappa_b^2 + 1) \frac{\hat{f}_{0p}\hat{j}_{0p}}{48R_{0b}} \frac{(-\kappa_b^2 + 1)\hat{j}_0 + (5\kappa_b^2 + 7)N_{0,2}}{\kappa_b^4 + 10\kappa_b^2 + 5} \sin(\theta_{\kappa b}) \quad (\text{B.7})$$

$$A_{C3} \equiv \frac{1}{4R_{0b}} \frac{1}{3\kappa_b^2 + 1} \left((\kappa_b^2 - 1) \left(\frac{\hat{j}_0}{4} + \hat{j}_{0p} + N_{0,2} \right) + \frac{1}{3} \frac{(-5\kappa_b^4 + 2\kappa_b^2 + 3)\hat{j}_0 + 4(5\kappa_b^4 + 4\kappa_b^2 + 3)N_{0,2}}{5\kappa_b^4 + 10\kappa_b^2 + 1} \kappa_b^2 a^2 \hat{f}_{0p}\hat{j}_{0p} \right) \cos(\theta_{\kappa b}) \quad (\text{B.8})$$

$$A_{S3} \equiv \frac{1}{4R_{0b}} \frac{1}{\kappa_b^2 + 3} \left((-\kappa_b^2 + 1) \left(\frac{\hat{j}_0}{4} + \hat{j}_{0p} - N_{0,2} \right) + \frac{1}{3} \frac{(3\kappa_b^4 + 2\kappa_b^2 - 5)\hat{j}_0 - 4(3\kappa_b^4 + 4\kappa_b^2 + 5)N_{0,2}}{\kappa_b^4 + 10\kappa_b^2 + 5} \kappa_b^2 a^2 \hat{f}_{0p}\hat{j}_{0p} \right) \sin(\theta_{\kappa b}) \quad (\text{B.9})$$

$$A_{C1} \equiv -\frac{1}{4R_{0b}} \frac{\kappa_b^2 a^2}{3\kappa_b^2 + 1} \left((\hat{j}_0 + 4\hat{j}_{0p} + 4N_{0,2}) - \frac{4}{3} \frac{2(\kappa_b^2 + 1)\hat{j}_0 + (\kappa_b^2 + 7)N_{0,2}}{5\kappa_b^4 + 10\kappa_b^2 + 1} \kappa_b^2 a^2 \hat{f}_{0p}\hat{j}_{0p} \right) \cos(\theta_{\kappa b}) \quad (\text{B.10})$$

$$A_{S1} \equiv \frac{1}{4R_{0b}} \frac{\kappa_b^2 a^2}{\kappa_b^2 + 3} \left((\hat{j}_0 + 4\hat{j}_{0p} - 4N_{0,2}) - \frac{4}{3} \frac{2(\kappa_b^2 + 1)\hat{j}_0 - (7\kappa_b^2 + 1)N_{0,2}}{\kappa_b^4 + 10\kappa_b^2 + 5} \kappa_b^2 a^2 \hat{f}_{0p}\hat{j}_{0p} \right) \sin(\theta_{\kappa b}) \quad (\text{B.11})$$

and $A_{Cm} = A_{Sm} = 0$ for all other m . These coefficients reduce to those found in section 2.1.2 of reference [70] when $\hat{f}_{0p} = 0$ as expected.

The above equations give the full analytic solution to the Grad-Shafranov equation to lowest and next order in aspect ratio for a constant toroidal current profile, linear (in ψ) pressure gradient, and tilted elliptical boundary. We want to substitute these solutions into (4.12) and solve for r_{axis} and θ_{axis} , the minor radial and poloidal locations of the magnetic axis. The simplest approach is to first expand (4.12) to lowest order in $\epsilon \ll 1$ and change to Cartesian coordinates to find

$$\vec{\nabla}\psi_0(R, Z)\Big|_{R=R_{\text{axis0}}, Z=Z_{\text{axis0}}} + \vec{\nabla}\psi_1(R, Z)\Big|_{R=R_{0b}, Z=Z_{0b}} = 0, \quad (\text{B.12})$$

where R_{axis0} and Z_{axis0} are the lowest order solutions for the major radial and axial locations of the magnetic axis respectively. The solution to this,

$$R_{\text{axis0}} - R_{0b} = \frac{1}{2} \frac{S_{0,2}S_{1,1} - \left(\frac{\hat{j}_0}{4} - C_{0,2}\right)C_{1,1}}{\left(\frac{\hat{j}_0}{4}\right)^2 - C_{0,2}^2 - S_{0,2}^2} \quad (\text{B.13})$$

$$Z_{\text{axis0}} - Z_{0b} = \frac{1}{2} \frac{S_{0,2}C_{1,1} - \left(\frac{\hat{j}_0}{4} + C_{0,2}\right)S_{1,1}}{\left(\frac{\hat{j}_0}{4}\right)^2 - C_{0,2}^2 - S_{0,2}^2}, \quad (\text{B.14})$$

is easy to find and gives the location of the magnetic axis to first order in $\epsilon \ll 1$. However, this turns out to be a fairly poor approximation and does not produce close agreement with the numerical results from ECOM. However, if we solve (4.12) exactly (even though ψ is not calculated exactly) we get a much better approximation that matches ECOM. The crucial step to solving (4.12) exactly is to assume that the lowest order solution for the location of the magnetic axis in (B.13) and (B.14) has the exactly correct tilt angle, i.e.

$$\theta_{\text{axis}} = \theta_{\text{axis0}} = \arctan\left(\frac{Z_{\text{axis0}} - Z_{0b}}{R_{\text{axis0}} - R_{0b}}\right). \quad (\text{B.15})$$

We can see that this is indeed true by substituting (B.15) into (4.12), which produces a quartic equation of the form

$$d_4 r_{\text{axis}}^4 + d_2 r_{\text{axis}}^2 + d_1 r_{\text{axis}} + d_0 = 0 \quad (\text{B.16})$$

with coefficients

$$d_4 \equiv -\frac{5\hat{f}_{0p}\hat{j}_0}{8R_{0b}} \left[\frac{\hat{j}_0 \cos(\theta_{\text{axis0}})}{6} + \frac{C_{0,2} \cos(\theta_{\text{axis0}}) + S_{0,2} \sin(\theta_{\text{axis0}})}{3} \right. \\ \left. + \frac{C_{0,2} \cos(3\theta_{\text{axis0}}) + S_{0,2} \sin(3\theta_{\text{axis0}})}{2} \right] + 5(C_{1,5} \cos(5\theta_{\text{axis0}}) + S_{1,5} \sin(5\theta_{\text{axis0}})) \quad (\text{B.17})$$

$$d_2 \equiv \frac{3}{4R_{0b}} \left[\left(\frac{\hat{j}_0 + 4\hat{j}_{0p}}{4} + C_{0,2} \right) \cos(\theta_{\text{axis0}}) + S_{0,2} \sin(\theta_{\text{axis0}}) \right] \\ + 3(C_{1,3} \cos(3\theta_{\text{axis0}}) + S_{1,3} \sin(3\theta_{\text{axis0}})) \quad (\text{B.18})$$

$$d_1 \equiv 2 \left(\frac{\hat{j}_0}{4} + C_{0,2} \cos(2\theta_{\text{axis0}}) + S_{0,2} \sin(2\theta_{\text{axis0}}) \right) \quad (\text{B.19})$$

$$d_0 \equiv C_{11} \cos(\theta_{\text{axis0}}) + S_{1,1} \sin(\theta_{\text{axis0}}). \quad (\text{B.20})$$

The exact location of the magnetic axis is given by solution of this quartic and (B.15). Quartics have a very complicated analytic solution, so in practice it is simpler to solve computationally. However, for the special case of $\hat{f}_{0p} = 0$ we see that $d_4 = 0$ and the quartic reduces to a quadratic solved by

$$r_{\text{axis}} = \frac{-d_1 + \sqrt{d_1^2 - 4d_2d_0}}{2d_2}. \quad (\text{B.21})$$

Appendix C

Electromagnetic turbulent fluxes and energy exchange

Much of this appendix appears in reference [43].

From references [20, 49, 53] among others we see that the electromagnetic fluxes of particles, momentum, and energy as well as the energy exchange between species are the only turbulent quantities needed to evolve the transport equations for particles, momentum, and energy. Furthermore, it is convenient to calculate these fluxes in a frame rotating with the bulk plasma, using the velocity variable $\vec{w} \equiv \vec{v} - R\Omega_\zeta \hat{e}_\zeta$. To do so we will follow the procedure outlined in section II.D and appendix E of reference [20].

The complete electromagnetic turbulent flux of particles in a tokamak can be defined as

$$\Gamma_s \equiv \langle \gamma_s \rangle_\psi \equiv - \left\langle R \left\langle \left\langle \int d^3w \underline{h}_s \hat{e}_\zeta \cdot \left(\delta \vec{E} + \vec{w} \times \delta \vec{B} \right) \right\rangle_{\Delta\psi} \right\rangle_{\Delta t} \right\rangle_\psi, \quad (\text{C.1})$$

where γ_s is the poloidally-dependent particle flux (defined by (7.40) in the electrostatic limit), $\delta \vec{E} = -\vec{\nabla}_\perp \underline{\phi}$ is the turbulent electric field, $\delta \vec{B} = \underline{B}_\parallel \hat{b} + \vec{\nabla} \underline{A}_\parallel \times \hat{b}$ is the turbulent magnetic field, and the (\dots) indicates that the quantity has not been Fourier analysed.

After considerable manipulation we find the flux of particles to be

$$\begin{aligned} \Gamma_s = & \frac{4\pi^2 i}{m_s V'} \left\langle \sum_{k_\psi, k_\alpha} k_\alpha \oint d\theta J B \int dw_{||} d\mu h_s(-k_\psi, -k_\alpha) \right. \\ & \times \left[\phi(k_\psi, k_\alpha) J_0(k_\perp \rho_s) \right. \\ & - A_{||}(k_\psi, k_\alpha) w_{||} J_0(k_\perp \rho_s) \\ & \left. \left. + B_{||}(k_\psi, k_\alpha) \frac{1}{\Omega_s} \frac{\mu B}{m_s} \frac{2J_1(k_\perp \rho_s)}{k_\perp \rho_s} \right] \right\rangle_{\Delta t}. \end{aligned} \quad (C.2)$$

The complete electromagnetic turbulent flux of toroidal angular momentum in a tokamak can be defined as

$$\Pi_\zeta \equiv \sum_s \Pi_{\zeta s} + \Pi_{\zeta B}, \quad (C.3)$$

where

$$\Pi_{\zeta s} \equiv \langle \pi_{\zeta s} \rangle_\psi \quad (C.4)$$

$$\equiv - \left\langle R \left\langle \left\langle \int d^3 w h_s m_s R (\vec{w} \cdot \hat{e}_\zeta + R \Omega_\zeta) \hat{e}_\zeta \cdot (\delta \vec{E} + \vec{w} \times \delta \vec{B}) \right\rangle_{\Delta\psi} \right\rangle_{\Delta t} \right\rangle_\psi \quad (C.5)$$

is the contribution from particles,

$$\Pi_{\zeta B} \equiv - \left\langle R \left\langle \left\langle \hat{e}_\zeta \cdot \vec{\sigma} \cdot \vec{\nabla} \psi \right\rangle_{\Delta\psi} \right\rangle_{\Delta t} \right\rangle_\psi \quad (C.6)$$

is the momentum transported by the electromagnetic fields, π_s is the poloidally-dependent angular momentum flux (defined by (7.41) in the electrostatic limit),

$$\vec{\sigma} \equiv \frac{1}{\mu_0} \vec{B} \vec{B} - \frac{1}{2\mu_0} B^2 \vec{I} \quad (C.7)$$

is the Maxwell stress tensor, and \vec{I} is the identity matrix. After considerable manipulation we find the angular momentum transported by particles to be

$$\begin{aligned} \Pi_{\zeta s} = & \frac{4\pi^2 i}{V'} \left\langle \sum_{k_\psi, k_\alpha} k_\alpha \oint d\theta J B \int dw_{||} d\mu h_s(-k_\psi, -k_\alpha) \right. \\ & \times \left\{ \phi(k_\psi, k_\alpha) \left[\left(\frac{I}{B} w_{||} + R^2 \Omega_\zeta \right) J_0(k_\perp \rho_s) + \frac{i}{\Omega_s} \frac{k^\psi}{B} \frac{\mu B}{m_s} \frac{2J_1(k_\perp \rho_s)}{k_\perp \rho_s} \right] \right. \\ & - A_{||}(k_\psi, k_\alpha) \left[\left(\frac{I}{B} w_{||} + R^2 \Omega_\zeta \right) w_{||} J_0(k_\perp \rho_s) + \left(i \frac{w_{||}}{\Omega_s} \frac{k^\psi}{B} + \frac{I}{B} \right) \frac{\mu B}{m_s} \frac{2J_1(k_\perp \rho_s)}{k_\perp \rho_s} \right] \\ & \left. \left. + B_{||}(k_\psi, k_\alpha) \frac{1}{\Omega_s} \left[\left(\frac{I}{B} w_{||} + R^2 \Omega_\zeta \right) \frac{\mu B}{m_s} \frac{2J_1(k_\perp \rho_s)}{k_\perp \rho_s} + \frac{i}{2\Omega_s} \frac{k^\psi}{B} \frac{\mu^2 B^2}{m_s^2} G(k_\perp \rho_s) \right] \right\} \right\rangle_{\Delta t} \end{aligned} \quad (C.8)$$

and the transport by the fluctuating fields to be

$$\begin{aligned} \Pi_{\zeta B} = \frac{2\pi i}{\mu_0 V'} \left\langle \sum_{k_\psi, k_\alpha} k_\alpha \oint d\theta J A_{||} (k_\psi, k_\alpha) \right. \\ \left. \times \left[-ik^\psi A_{||} (-k_\psi, -k_\alpha) + IB_{||} (-k_\psi, -k_\alpha) \right] \right\rangle_{\Delta t}, \end{aligned} \quad (\text{C.9})$$

where $k^\psi \equiv \vec{k}_\perp \cdot \vec{\nabla} \psi = k_\psi \left| \vec{\nabla} \psi \right|^2 + k_\alpha \vec{\nabla} \psi \cdot \vec{\nabla} \alpha$ and $G(x) \equiv 8(2J_1(x) - xJ_0(x))/x^3$. Note that, when summing over all species, (6.17) can be used to show that the $B_{||}$ term in (C.9) cancels the fourth $A_{||}$ term in (C.8).

The complete electromagnetic turbulent flux of energy carried by particles can be defined as

$$\begin{aligned} Q_s \equiv \langle q_s \rangle_\psi \equiv - \left\langle R \left\langle \left\langle \int d^3 w \underline{h}_s \left(\frac{m_s}{2} w^2 + Z_s e \Phi_0 - \frac{m_s}{2} R^2 \Omega_\zeta^2 \right) \right. \right. \right. \\ \left. \left. \left. \hat{e}_\zeta \cdot \left(\delta \vec{E} + \vec{w} \times \delta \vec{B} \right) \right\rangle_{\Delta \psi} \right\rangle_{\Delta t} \right\rangle_\psi, \end{aligned} \quad (\text{C.10})$$

where q_s is the poloidally-dependent energy flux (defined by (7.42) in the electrostatic limit). After considerable manipulation we find the energy transported by particles to be

$$\begin{aligned} Q_s = \frac{4\pi^2 i}{V'} \left\langle \sum_{k_\psi, k_\alpha} k_\alpha \oint d\theta J B \int dw_{||} d\mu \, h_s (-k_\psi, -k_\alpha) \left(\frac{w^2}{2} + \frac{Z_s e \Phi_0}{m_s} - \frac{m_s}{2} R^2 \Omega_\zeta^2 \right) \right. \\ \times [\phi(k_\psi, k_\alpha) (J_0(k_\perp \rho_s)) \\ - A_{||}(k_\psi, k_\alpha) (w_{||} J_0(k_\perp \rho_s)) \\ \left. + B_{||}(k_\psi, k_\alpha) \frac{1}{\Omega_s} \left(\frac{\mu B 2J_1(k_\perp \rho_s)}{m_s k_\perp \rho_s} \right) \right] \right\rangle_{\Delta t}. \end{aligned} \quad (\text{C.11})$$

The complete electromagnetic turbulent energy exchange between species can be written as

$$P_{Qs} \equiv \langle p_{Qs} \rangle_\psi \equiv \left\langle \left\langle \left\langle \int d^3 w Z_s e \underline{h}_s \frac{\partial \underline{\chi}}{\partial t} \right\rangle_{\Delta \psi} \right\rangle_{\Delta t} \right\rangle_\psi, \quad (\text{C.12})$$

where $\underline{\chi} \equiv \phi - \vec{w} \cdot \vec{A}$ is the generalised potential and p_{Qs} is the poloidally-dependent turbulent energy exchange (defined by (7.43) in the electrostatic limit). After con-

siderable manipulation we find the energy exchange to be

$$\begin{aligned}
P_{Qs} = & \frac{4\pi^2}{V'} \left\langle \sum_{k_\psi, k_\alpha} \oint d\theta J \Omega_s \int dw_{||} d\mu h_s(-k_\psi, -k_\alpha) \right. \\
& \times \left[\frac{\partial}{\partial t} (\phi(k_\psi, k_\alpha)) J_0(k_\perp \rho_s) \right. \\
& - \frac{\partial}{\partial t} (A_{||}(k_\psi, k_\alpha)) w_{||} J_0(k_\perp \rho_s) \\
& \left. + \frac{\partial}{\partial t} (B_{||}(k_\psi, k_\alpha)) \frac{1}{\Omega_s} \frac{\mu B}{m_s} \frac{2J_1(k_\perp \rho_s)}{k_\perp \rho_s} \right] \Bigg\rangle_{\Delta t}.
\end{aligned} \tag{C.13}$$

Appendix D

Calculation of the geometric coefficients within Miller local equilibrium

Much of this appendix appears in reference [41].

In this appendix we will calculate the ten geometric coefficients (i.e. $\hat{b} \cdot \vec{\nabla} \theta$, B , $v_{ds\psi}$, $v_{ds\alpha}$, $a_{s||}$, $|\vec{\nabla} \psi|^2$, $\vec{\nabla} \psi \cdot \vec{\nabla} \alpha$, $|\vec{\nabla} \alpha|^2$, R , and $\partial R / \partial \psi|_\theta$) that appear in the electromagnetic gyrokinetic equations with rotation. Here we will use the normal cylindrical poloidal angle θ , but the expressions are general to an arbitrary poloidal angle. In order to calculate these coefficients for the local equilibrium specification (given in chapter 5) we must work within the local Miller geometry model. This means that we begin knowing the shape of the flux surface of interest (i.e. $R(\theta)$ and $Z(\theta)$), how it changes with minor radius (i.e. $\partial R / \partial r_\psi|_\theta$ and $\partial Z / \partial r_\psi|_\theta$), and several flux functions (e.g. the toroidal magnetic field flux function, the safety factor, the magnetic shear, and the pseudo-density (see (6.2)) evaluated on the flux surface of interest. With only this information we can calculate the toroidal and poloidal magnetic fields using

$$\vec{B}_\zeta = \frac{I(\psi)}{R} \hat{e}_\zeta \quad (\text{D.1})$$

$$\vec{B}_p = \vec{\nabla} \zeta \times \vec{\nabla} r_\psi \frac{d\psi}{dr_\psi}, \quad (\text{D.2})$$

where $d\psi/dr_\psi$ can be calculated to be

$$\frac{d\psi}{dr_\psi} = \frac{I(\psi)}{2\pi q} \oint_0^{2\pi} \Big|_\psi d\theta \left(R^2 \vec{\nabla} r_\psi \cdot \left(\vec{\nabla} \theta \times \vec{\nabla} \zeta \right) \right)^{-1} \quad (\text{D.3})$$

from the definition of the safety factor (i.e. (7.1)) and the gradients of r_ψ , θ , and ζ can be found from (8.4). Using only this information we can calculate $\hat{b} \cdot \vec{\nabla} \theta$, B , $v_{ds\psi}$ (defined by (6.9)), $a_{s||}$ (defined by (6.12)), $|\vec{\nabla} \psi|^2$, R , and $\partial R / \partial \psi|_\theta$.

However calculating $v_{ds\alpha}$ (defined by (6.10)), $\vec{\nabla}\psi \cdot \vec{\nabla}\alpha$, and $|\vec{\nabla}\alpha|^2$ requires considerably more work as we must know $\vec{\nabla}\alpha$, $\partial B_\zeta/\partial\psi|_\theta$, and $\partial B_p/\partial\psi|_\theta$. Starting with $\partial B_p/\partial\psi|_\theta$, we see from (D.2) that it will depend on second order radial derivatives, which are not inputs to the Miller local equilibrium. The Miller model deals with this by calculating them through the Grad-Shafranov equation (i.e. (2.2)). We can rearrange (2.2) to get

$$\frac{R^2}{J} \frac{\partial}{\partial\psi} (JB_p^2) + \frac{R^2}{J} \frac{\partial}{\partial\theta} \left(\frac{J}{R^2} \vec{\nabla}\psi \cdot \vec{\nabla}\theta \right) = -\mu_0 R^2 \left. \frac{\partial p}{\partial\psi} \right|_R - I \frac{dI}{d\psi}, \quad (\text{D.4})$$

where the Jacobian is given by

$$J \equiv \left| \vec{\nabla}\psi \cdot (\vec{\nabla}\theta \times \vec{\nabla}\zeta) \right|^{-1} = (\vec{B}_p \cdot \vec{\nabla}\theta)^{-1} = \frac{1}{B_p} \left. \frac{\partial l_p}{\partial\theta} \right|_\psi \quad (\text{D.5})$$

and l_p is the arc length defined such that (7.4) holds. We note that when $\Omega_\zeta = 0$ the quantity $\partial p/\partial\psi|_R = dp/d\psi$ is an input to the calculation, otherwise it is determined by (6.2), (6.3), and (6.11). Simplifying further and using (8.4) we finally find that

$$\begin{aligned} \frac{\partial B_p}{\partial\psi} = & -\frac{\mu_0}{B_p} \left. \frac{\partial p}{\partial\psi} \right|_R - \frac{I}{R^2 B_p} \frac{dI}{d\psi} - B_p \left(\frac{\partial l_p}{\partial\theta} \right)^{-1} \frac{\partial}{\partial\psi} \left(\frac{\partial l_p}{\partial\theta} \right) \\ & + \left(\frac{\partial l_p}{\partial\theta} \right)^{-1} \frac{\partial}{\partial\theta} \left(B_p \left(\frac{\partial l_p}{\partial\theta} \right)^{-1} \frac{\partial \vec{r}}{\partial\psi} \cdot \frac{\partial \vec{r}}{\partial\theta} \right). \end{aligned} \quad (\text{D.6})$$

At this point we have yet to determine $dI/d\psi$, but will do so below.

Next we directly differentiate (6.4) to find

$$\vec{\nabla}\alpha = \left(- \int_{\theta_\alpha}^\theta \left. d\theta' \frac{\partial A_\alpha}{\partial\psi} + A_\alpha(\psi, \theta_\alpha) \frac{d\theta_\alpha}{d\psi} - \frac{d\Omega_\zeta}{d\psi} t \right) \vec{\nabla}\psi - A_\alpha(\psi, \theta) \vec{\nabla}\theta + \vec{\nabla}\zeta, \quad (\text{D.7})$$

where

$$A_\alpha(\psi, \theta) \equiv \frac{I(\psi)}{R^2 \vec{B} \cdot \vec{\nabla}\theta} \quad (\text{D.8})$$

is the integrand in the definition of α . All quantities in (D.7) are known except for the radial derivative of A_α . We can calculate it by using the product rule on (D.8) to find

$$\begin{aligned} \frac{\partial A_\alpha}{\partial\psi} = & A_\alpha \left[\left(1 + \frac{I^2}{R^2 B_p^2} \right) \frac{1}{I} \frac{dI}{d\psi} + \frac{\mu_0}{B_p^2} \left. \frac{\partial p}{\partial\psi} \right|_R - \frac{2}{R} \frac{\partial R}{\partial\psi} \right. \\ & \left. - \frac{1}{B_p} \left(\frac{\partial l_p}{\partial\theta} \right)^{-1} \frac{\partial}{\partial\theta} \left(B_p \left(\frac{\partial l_p}{\partial\theta} \right)^{-1} \frac{\partial \vec{r}}{\partial\psi} \cdot \frac{\partial \vec{r}}{\partial\theta} \right) + 2 \left(\frac{\partial l_p}{\partial\theta} \right)^{-1} \frac{\partial}{\partial\psi} \left(\frac{\partial l_p}{\partial\theta} \right) \right], \end{aligned} \quad (\text{D.9})$$

where we have made use of (D.5) and (D.6). While this form is acceptable for the purposes of this thesis, we will rearrange it into a form that is more physically illuminating. To do so we will write

$$\frac{\partial \vec{r}}{\partial \psi} = \frac{1}{RB_p} \left(\frac{\partial l_p}{\partial \theta} \right)^{-1} \frac{\partial \vec{r}}{\partial \theta} \times \hat{e}_\zeta + \left(\frac{\partial l_p}{\partial \theta} \right)^{-2} \left(\frac{\partial \vec{r}}{\partial \psi} \cdot \frac{\partial \vec{r}}{\partial \theta} \right) \frac{\partial \vec{r}}{\partial \theta} \quad (\text{D.10})$$

using only (7.4), (D.5), and vector identities such as $\partial \vec{r} / \partial \psi \cdot (\partial \vec{r} / \partial \theta \times \partial \vec{r} / \partial \zeta) = \left(\vec{\nabla} \psi \cdot \left(\vec{\nabla} \theta \times \vec{\nabla} \zeta \right) \right)^{-1}$. This allows us to see that

$$-\frac{2}{R} \frac{\partial R}{\partial \psi} = -\frac{2}{R} \frac{\partial \vec{r}}{\partial \psi} \cdot \vec{\nabla} R \quad (\text{D.11})$$

$$= -\frac{2}{R^2 B_p} \left(\frac{\partial l_p}{\partial \theta} \right)^{-1} \frac{\partial Z}{\partial \theta} + R^2 \frac{\partial}{\partial \theta} \left(\frac{1}{R^2} \right) \left(\frac{\partial l_p}{\partial \theta} \right)^{-2} \frac{\partial \vec{r}}{\partial \psi} \cdot \frac{\partial \vec{r}}{\partial \theta}. \quad (\text{D.12})$$

Combining this result with the second-to-last term in (D.9) and applying the product rule several times, we find

$$\begin{aligned} & -\frac{2}{R} \frac{\partial R}{\partial \psi} - \frac{1}{B_p} \left(\frac{\partial l_p}{\partial \theta} \right)^{-1} \frac{\partial}{\partial \theta} \left(B_p \left(\frac{\partial l_p}{\partial \theta} \right)^{-1} \frac{\partial \vec{r}}{\partial \psi} \cdot \frac{\partial \vec{r}}{\partial \theta} \right) \\ &= -\frac{2}{R^2 B_p} \left(\frac{\partial l_p}{\partial \theta} \right)^{-1} \frac{\partial Z}{\partial \theta} + R^2 B_p \left(\frac{\partial l_p}{\partial \theta} \right)^{-1} \frac{\partial}{\partial \theta} \left(\frac{1}{R^2 B_p} \left(\frac{\partial l_p}{\partial \theta} \right)^{-1} \frac{\partial \vec{r}}{\partial \psi} \cdot \frac{\partial \vec{r}}{\partial \theta} \right) \\ & \quad - 2 \left(\frac{\partial l_p}{\partial \theta} \right)^{-1} \frac{\partial}{\partial \theta} \left(\left(\frac{\partial l_p}{\partial \theta} \right)^{-1} \frac{\partial \vec{r}}{\partial \theta} \right) \cdot \frac{\partial \vec{r}}{\partial \psi} - 2 \left(\frac{\partial l_p}{\partial \theta} \right)^{-2} \frac{\partial}{\partial \theta} \left(\frac{\partial \vec{r}}{\partial \psi} \right) \cdot \frac{\partial \vec{r}}{\partial \theta}. \end{aligned} \quad (\text{D.13})$$

Using (7.4) we see that the last term of (D.13) exactly cancels the final term appearing in (D.9). This shows that we can rewrite (D.9) as

$$\begin{aligned} \frac{\partial A_\alpha}{\partial \psi} &= A_\alpha \left[\frac{1}{I} \frac{dI}{d\psi} + \frac{I}{R^2 B_p^2} \frac{dI}{d\psi} + \frac{\mu_0}{B_p^2} \frac{\partial p}{\partial \psi} \Big|_R - \frac{2}{R^2 B_p} \left(\frac{\partial l_p}{\partial \theta} \right)^{-1} \frac{\partial Z}{\partial \theta} \right. \\ & \quad \left. - 2 \left(\frac{\partial l_p}{\partial \theta} \right)^{-1} \frac{\partial}{\partial \theta} \left(\left(\frac{\partial l_p}{\partial \theta} \right)^{-1} \frac{\partial \vec{r}}{\partial \theta} \right) \cdot \frac{\partial \vec{r}}{\partial \psi} \right] + \frac{\partial}{\partial \theta} \left(\frac{I}{R^2 B_p} \left(\frac{\partial l_p}{\partial \theta} \right)^{-1} \frac{\partial \vec{r}}{\partial \psi} \cdot \frac{\partial \vec{r}}{\partial \theta} \right). \end{aligned} \quad (\text{D.14})$$

Lastly, substituting this into (D.7) and using (7.3) produces

$$\begin{aligned} \vec{\nabla} \alpha &= \left(- \int_{\theta_\alpha}^{\theta} d\theta' A_\alpha(\psi, \theta') \left[\frac{1}{I} \frac{dI}{d\psi} + \frac{I}{R^2 B_p^2} \frac{dI}{d\psi} + \frac{\mu_0}{B_p^2} \frac{\partial p}{\partial \psi} \Big|_R - \frac{2}{R^2 B_p} \left(\frac{\partial l_p}{\partial \theta'} \right)^{-1} \frac{\partial Z}{\partial \theta'} \right. \right. \\ & \quad \left. \left. + \frac{2\kappa_p}{RB_p} \right] + \left[\frac{A_\alpha(\psi, \theta')}{R^2 B_p^2} \vec{\nabla} \psi \cdot \vec{\nabla} \theta' \right]_{\theta'=\theta_\alpha}^{\theta'=\theta} + A_\alpha(\psi, \theta_\alpha) \frac{d\theta_\alpha}{d\psi} - \frac{d\Omega_\zeta t}{d\psi} \right) \vec{\nabla} \psi \\ & \quad - A_\alpha(\psi, \theta) \vec{\nabla} \theta + \vec{\nabla} \zeta. \end{aligned} \quad (\text{D.15})$$

The first term inside the integral represents the change in the field line pitch that results from changing the toroidal field flux function on neighbouring flux surfaces. The second term in the integral accounts for the modification to the flux surface equilibrium that results from a radial gradient in the toroidal flux function. As we will explore in appendix F, the third term expresses the effect the pressure gradient has on the equilibrium. Despite appearances, the fourth term corresponds to how the toroidal magnetic field weakens as the major radial location changes. The last term in the integral accounts for the flux expansion (and weakening of the poloidal magnetic field) that occurs at regions of large poloidal curvature (see (3.15)). The term immediately following the integral accounts for the particulars of how θ is defined, but we note this term vanishes if contours of constant θ are perpendicular to the flux surface of interest. The last term in the coefficient of $\vec{\nabla}\psi$ is a consequence of changing which field line is labelled $\alpha = 0$ from flux surface to flux surface. The final two terms of (D.15) reflect the nonuniform spacing of the field lines in the poloidal direction and the uniform spacing in the toroidal direction respectively.

Equation (D.15) allows us to calculate $\vec{\nabla}\psi \cdot \vec{\nabla}\alpha$, and $|\vec{\nabla}\alpha|^2$, but we must remember that we still lack an expression for $dI/d\psi$. This can be calculated by taking the radial gradient of the safety factor (i.e. (7.1)) in order to get the magnetic shear,

$$\frac{dq}{d\psi} = \frac{1}{2\pi} \oint_0^{2\pi} \bigg|_{\psi} d\theta \frac{\partial A_\alpha}{\partial \psi}. \quad (\text{D.16})$$

This turns out to be very closely related to $\vec{\nabla}\alpha$, so we can use (D.14) to find

$$\begin{aligned} \frac{dI}{d\psi} = I & \left(q + \frac{1}{2\pi} \oint_0^{2\pi} \bigg|_{\psi} d\theta A_\alpha(\psi, \theta) \frac{I^2}{R^2 B_p^2} \right)^{-1} \\ & \times \left(\frac{dq}{d\psi} - \frac{1}{2\pi} \oint_0^{2\pi} \bigg|_{\psi} d\theta A_\alpha(\psi, \theta) \left[\frac{\mu_0}{B_p^2} \frac{\partial p}{\partial \psi} \bigg|_R - \frac{2}{R^2 B_p} \left(\frac{\partial l_p}{\partial \theta} \right)^{-1} \frac{\partial Z}{\partial \theta} + \frac{2\kappa_p}{R B_p} \right] \right). \end{aligned} \quad (\text{D.17})$$

Lastly we can directly differentiate (D.1) to find

$$\frac{\partial B_\zeta}{\partial \psi} = \frac{1}{R} \frac{dI}{d\psi} - \frac{I}{R^2} \left(\frac{d\psi}{dr_\psi} \right)^{-1} \frac{\partial R}{\partial r_\psi}, \quad (\text{D.18})$$

where we remember that $\partial R/\partial r_\psi$ is an input to the Miller model. This fully determines $v_{ds\alpha}$, which is defined by (6.10).

The expressions in this section allow us to directly calculate all of the gyrokinetic geometric coefficients within the framework of the Miller local equilibrium model.

Appendix E

Non-mirror symmetric geometric coefficients

Much of this appendix appears in reference [41].

In this section we give the full gyrokinetic geometric coefficients to lowest and next order in $m_c \gg 1$ for the geometry investigated in section 8.1.2. These coefficients are accurate to lowest order in aspect ratio, given the orderings of (8.15) and (8.16). In deriving these coefficients the following quantities are useful as way points:

$$\frac{\partial R}{\partial \theta} = -r_{\psi 0} \left[\sin(\theta) - \frac{1}{2} \cos(\theta) \left(m(\Delta_m - 1) \sin(z_{ms}) + n(\Delta_n - 1) \sin(z_{ns}) \right) \right. \\ \left. - \frac{1}{2} \sin(\theta) \left((\Delta_m - 1) \cos(z_{ms}) + (\Delta_n - 1) \cos(z_{ns}) \right) \right] + O(m_c^{-3} r_{\psi}) \quad (\text{E.1})$$

$$\frac{\partial Z}{\partial \theta} = r_{\psi 0} \left[\cos(\theta) + \frac{1}{2} \sin(\theta) \left(m(\Delta_m - 1) \sin(z_{ms}) + n(\Delta_n - 1) \sin(z_{ns}) \right) \right. \\ \left. - \frac{1}{2} \cos(\theta) \left((\Delta_m - 1) \cos(z_{ms}) + (\Delta_n - 1) \cos(z_{ns}) \right) \right] + O(m_c^{-3} r_{\psi}) \quad (\text{E.2})$$

$$\vec{\nabla} r_{\psi} = \left[\cos(\theta) + \frac{r_{\psi 0}}{2} \cos(\theta) \left(\frac{d\Delta_m}{dr_{\psi}} \cos(z_{ms}) + \frac{d\Delta_n}{dr_{\psi}} \cos(z_{ns}) \right) \right. \\ \left. + \frac{1}{2} \sin(\theta) \left(m(\Delta_m - 1) \sin(z_{ms}) + n(\Delta_n - 1) \sin(z_{ns}) \right) \right] \hat{e}_R \\ + \left[\sin(\theta) + \frac{r_{\psi 0}}{2} \sin(\theta) \left(\frac{d\Delta_m}{dr_{\psi}} \cos(z_{ms}) + \frac{d\Delta_n}{dr_{\psi}} \cos(z_{ns}) \right) \right. \\ \left. - \frac{1}{2} \cos(\theta) \left(m(\Delta_m - 1) \sin(z_{ms}) + n(\Delta_n - 1) \sin(z_{ns}) \right) \right] \hat{e}_Z + O(m_c^{-2}) \quad (\text{E.3})$$

$$\vec{\nabla} \theta = \frac{1}{r_{\psi 0}} \left(-\sin(\theta) \hat{e}_R + \cos(\theta) \hat{e}_Z \right) + O\left(\frac{m_c^{-2}}{r_{\psi}}\right) \quad (\text{E.4})$$

$$\frac{\partial R}{\partial r_\psi} = \cos(\theta) - \frac{r_{\psi 0}}{2} \cos(\theta) \left(\frac{d\Delta_m}{dr_\psi} \cos(z_{ms}) + \frac{d\Delta_n}{dr_\psi} \cos(z_{ns}) \right) + O(m_c^{-2}) \quad (\text{E.5})$$

$$\frac{\partial Z}{\partial r_\psi} = \sin(\theta) - \frac{r_{\psi 0}}{2} \sin(\theta) \left(\frac{d\Delta_m}{dr_\psi} \cos(z_{ms}) + \frac{d\Delta_n}{dr_\psi} \cos(z_{ns}) \right) + O(m_c^{-2}) \quad (\text{E.6})$$

$$\begin{aligned} \left(\frac{\partial A_\alpha}{\partial \psi} \right)_{\text{orthog}} &= B_{c0} \left(\frac{d\psi}{dr_\psi} \right)^{-2} \left[\hat{s}' + \frac{r_{\psi 0}}{2} \left(m^2 (\Delta_m - 1) \frac{d\Delta_m}{dr_\psi} + n^2 (\Delta_n - 1) \frac{d\Delta_n}{dr_\psi} \right) \right. \\ &\quad - \left(m^2 (\Delta_m - 1) + (3\hat{s}' - 2) \frac{r_{\psi 0}}{2} \frac{d\Delta_m}{dr_\psi} \right) \cos(z_{ms}) \\ &\quad - \left(n^2 (\Delta_n - 1) + (3\hat{s}' - 2) \frac{r_{\psi 0}}{2} \frac{d\Delta_n}{dr_\psi} \right) \cos(z_{ns}) \\ &\quad + \frac{r_{\psi 0}}{2} \left(m^2 (\Delta_m - 1) \frac{d\Delta_m}{dr_\psi} \cos(2z_{ms}) + n^2 (\Delta_n - 1) \frac{d\Delta_n}{dr_\psi} \cos(2z_{ns}) \right) \\ &\quad + \frac{r_{\psi 0}}{2} \left(m^2 (\Delta_m - 1) \frac{d\Delta_n}{dr_\psi} + n^2 (\Delta_n - 1) \frac{d\Delta_m}{dr_\psi} \right) \\ &\quad \left. \times \left(\cos(z_{ms} + z_{ns}) + \cos(z_{ms} - z_{ns}) \right) \right] + O\left(\frac{m_c^{-2}}{r_\psi^2 B_0} \right) \end{aligned} \quad (\text{E.7})$$

$$\begin{aligned} \int_{\theta_0}^{\theta} \Big|_{\psi} d\theta' \left(\frac{\partial A_\alpha}{\partial \psi} \right)_{\text{orthog}} &= B_{c0} \left(\frac{d\psi}{dr_\psi} \right)^{-2} \left[\hat{s}' \theta \right. \\ &\quad + \frac{r_{\psi 0}}{2} \left(m^2 (\Delta_m - 1) \frac{d\Delta_m}{dr_\psi} + n^2 (\Delta_n - 1) \frac{d\Delta_n}{dr_\psi} \right) \theta \\ &\quad - \frac{1}{m} \left(m^2 (\Delta_m - 1) + (3\hat{s}' - 2) \frac{r_{\psi 0}}{2} \frac{d\Delta_m}{dr_\psi} \right) \sin(z_{ms}) \\ &\quad - \frac{1}{n} \left(n^2 (\Delta_n - 1) + (3\hat{s}' - 2) \frac{r_{\psi 0}}{2} \frac{d\Delta_n}{dr_\psi} \right) \sin(z_{ns}) \\ &\quad + \frac{r_{\psi 0}}{4} \left(m (\Delta_m - 1) \frac{d\Delta_m}{dr_\psi} \sin(2z_{ms}) + n (\Delta_n - 1) \frac{d\Delta_n}{dr_\psi} \sin(2z_{ns}) \right) \\ &\quad + \frac{r_{\psi 0}}{2} \left(m^2 (\Delta_m - 1) \frac{d\Delta_n}{dr_\psi} + n^2 (\Delta_n - 1) \frac{d\Delta_m}{dr_\psi} \right) \\ &\quad \times \left(\frac{1}{m+n} \sin(z_{ms} + z_{ns}) + \frac{1}{m-n} \sin(z_{ms} - z_{ns}) \right) \Big] \\ &\quad + O\left(\frac{m_c^{-2}}{r_\psi^2 B_0} \right). \end{aligned} \quad (\text{E.8})$$

Here z_{ms} and z_{ns} are defined by (8.19) and (8.20), while the constant θ_0 is defined such that $\int_{\theta_0}^{\theta_\alpha} \Big|_{\psi} d\theta' (\partial A_\alpha / \partial \psi)_{\text{orthog}}$ does not have a term that is independent of the

poloidal angle. Continuing the calculation we find

$$\begin{aligned}
\frac{\partial \alpha}{\partial \psi} = & -B_{c0} \left(\frac{d\psi}{dr_\psi} \right)^{-2} \left[\hat{s}' \theta + \frac{r_{\psi 0}}{2} \left(m^2 (\Delta_m - 1) \frac{d\Delta_m}{dr_\psi} + n^2 (\Delta_n - 1) \frac{d\Delta_n}{dr_\psi} \right) \theta \right. \\
& - \frac{1}{2} \left(m (\Delta_m - 1) \sin(z_{ms}) + n (\Delta_n - 1) \sin(z_{ns}) \right) \\
& + \frac{r_{\psi 0}}{2(n-m)} \left(m^2 (\Delta_m - 1) \frac{d\Delta_n}{dr_\psi} + n^2 (\Delta_n - 1) \frac{d\Delta_m}{dr_\psi} \right) \\
& \left. \times \sin((n-m)\theta + n\theta_{tn} - m\theta_{tm}) \right] + O\left(\frac{m_c^{-2}}{r_\psi^2 B_0}\right)
\end{aligned} \tag{E.9}$$

$$\begin{aligned}
\vec{\nabla} \alpha = & -B_{c0} \left(\frac{d\psi}{dr_\psi} \right)^{-1} \left\{ \right. \\
& \left[-\sin(\theta) + \hat{s}' \theta \cos(\theta) + \frac{r_{\psi 0}}{2} \left(m^2 (\Delta_m - 1) \frac{d\Delta_m}{dr_\psi} + n^2 (\Delta_n - 1) \frac{d\Delta_n}{dr_\psi} \right) \theta \cos(\theta) \right. \\
& - \frac{1}{2} \left(\cos(\theta) - \hat{s}' \theta \sin(\theta) \right) \left(m (\Delta_m - 1) \sin(z_{ms}) + n (\Delta_n - 1) \sin(z_{ns}) \right) \\
& + \frac{r_{\psi 0}}{2} \left(\sin(\theta) + \hat{s}' \theta \cos(\theta) \right) \left(\frac{d\Delta_m}{dr_\psi} \cos(z_{ms}) + \frac{d\Delta_n}{dr_\psi} \cos(z_{ns}) \right) \\
& + \frac{r_{\psi 0}}{2(n-m)} \left(m^2 (\Delta_m - 1) \frac{d\Delta_n}{dr_\psi} + n^2 (\Delta_n - 1) \frac{d\Delta_m}{dr_\psi} \right) \cos(\theta) \\
& \left. \times \sin((n-m)\theta + n\theta_{tn} - m\theta_{tm}) \right] \hat{e}_R \\
& + \left[\cos(\theta) + \hat{s}' \theta \sin(\theta) + \frac{r_{\psi 0}}{2} \left(m^2 (\Delta_m - 1) \frac{d\Delta_m}{dr_\psi} + n^2 (\Delta_n - 1) \frac{d\Delta_n}{dr_\psi} \right) \theta \sin(\theta) \right. \\
& - \frac{1}{2} \left(\sin(\theta) + \hat{s}' \theta \cos(\theta) \right) \left(m (\Delta_m - 1) \sin(z_{ms}) + n (\Delta_n - 1) \sin(z_{ns}) \right) \\
& - \frac{r_{\psi 0}}{2} \left(\cos(\theta) - \hat{s}' \theta \sin(\theta) \right) \left(\frac{d\Delta_m}{dr_\psi} \cos(z_{ms}) + \frac{d\Delta_n}{dr_\psi} \cos(z_{ns}) \right) \\
& + \frac{r_{\psi 0}}{2(n-m)} \left(m^2 (\Delta_m - 1) \frac{d\Delta_n}{dr_\psi} + n^2 (\Delta_n - 1) \frac{d\Delta_m}{dr_\psi} \right) \sin(\theta) \\
& \left. \times \sin((n-m)\theta + n\theta_{tn} - m\theta_{tm}) \right] \hat{e}_Z \left. \right\} + O\left(\frac{m_c^{-2}}{r_\psi}\right).
\end{aligned} \tag{E.10}$$

The $O(1)$ geometric coefficients are simply those of a circular tokamak and are

given by

$$\left(\hat{b} \cdot \vec{\nabla} \theta\right)_0 = \overline{\left(\hat{b} \cdot \vec{\nabla} \theta\right)}_0 = \frac{1}{r_{\psi 0} R_{c0} B_{c0}} \frac{d\psi}{dr_{\psi}} \quad (\text{E.11})$$

$$v_{ds\psi 0} = \bar{v}_{ds\psi 0} = -\frac{1}{R_{c0} \Omega_s} \frac{d\psi}{dr_{\psi}} \sin(\theta) \quad (\text{E.12})$$

$$v_{ds\alpha 0} = \bar{v}_{ds\alpha 0} = \frac{B_{c0}}{R_{c0} \Omega_s} \left(\frac{d\psi}{dr_{\psi}}\right)^{-1} (\cos(\theta) + \hat{s}' \theta \sin(\theta)) \quad (\text{E.13})$$

$$\left|\vec{\nabla} \psi\right|_0^2 = \overline{\left|\vec{\nabla} \psi\right|}_0^2 = \left(\frac{d\psi}{dr_{\psi}}\right)^2 \quad (\text{E.14})$$

$$\left(\vec{\nabla} \psi \cdot \vec{\nabla} \alpha\right)_0 = \overline{\left(\vec{\nabla} \psi \cdot \vec{\nabla} \alpha\right)}_0 = -B_{c0} \hat{s}' \theta \quad (\text{E.15})$$

$$\left|\vec{\nabla} \alpha\right|_0^2 = \overline{\left|\vec{\nabla} \alpha\right|}_0^2 = B_{c0}^2 \left(\frac{d\psi}{dr_{\psi}}\right)^{-2} (1 + \hat{s}'^2 \theta^2) \quad (\text{E.16})$$

$$(J_0(k_{\perp} \rho_s))_0 = \overline{(J_0(k_{\perp} \rho_s))}_0 = J_0(k_{\perp 0} \rho_s), \quad (\text{E.17})$$

where \hat{s}' is defined by (8.1) and

$$k_{\perp 0} \rho_s \equiv \sqrt{\frac{2m_s \mu}{Z_s^2 e^2 B_{c0}}} \sqrt{k_{\psi}^2 \left|\vec{\nabla} \psi\right|_0^2 + 2k_{\psi} k_{\alpha} \left(\vec{\nabla} \psi \cdot \vec{\nabla} \alpha\right)_0 + k_{\alpha}^2 \left|\vec{\nabla} \alpha\right|_0^2}. \quad (\text{E.18})$$

Note that all of the coefficients are independent of the short spatial scale coordinate, z .

To $O(m_c^{-1})$ the geometric coefficients are

$$\left(\hat{b} \cdot \vec{\nabla} \theta\right)_1 = \frac{1}{2R_{c0} B_{c0}} \frac{d\psi}{dr_{\psi}} \left(\frac{d\Delta_m}{dr_{\psi}} \cos(z_{ms}) + \frac{d\Delta_n}{dr_{\psi}} \cos(z_{ns})\right) \quad (\text{E.19})$$

$$\begin{aligned} v_{ds\psi 1} = & \frac{1}{2R_{c0} \Omega_s} \frac{d\psi}{dr_{\psi}} \left[\cos(\theta) \left(m(\Delta_m - 1) \sin(z_{ms}) + n(\Delta_n - 1) \sin(z_{ns}) \right) \right. \\ & \left. - r_{\psi 0} \sin(\theta) \left(\frac{d\Delta_m}{dr_{\psi}} \cos(z_{ms}) + \frac{d\Delta_n}{dr_{\psi}} \cos(z_{ns}) \right) \right] \quad (\text{E.20}) \end{aligned}$$

$$\begin{aligned}
v_{ds\alpha 1} &= \frac{B_{c0}}{2R_{c0}\Omega_s} \left(\frac{d\psi}{dr_\psi} \right)^{-1} \\
&\times \left[r_{\psi 0} \left(m^2 (\Delta_m - 1) \frac{d\Delta_m}{dr_\psi} + n^2 (\Delta_n - 1) \frac{d\Delta_n}{dr_\psi} \right) \theta \sin(\theta) \right. \\
&- \left(\sin(\theta) + \hat{s}'\theta \cos(\theta) \right) \left(m (\Delta_m - 1) \sin(z_{ms}) + n (\Delta_n - 1) \sin(z_{ns}) \right) \\
&- r_{\psi 0} \left(\cos(\theta) - \hat{s}'\theta \sin(\theta) \right) \left(\frac{d\Delta_m}{dr_\psi} \cos(z_{ms}) + \frac{d\Delta_n}{dr_\psi} \cos(z_{ns}) \right) \quad (E.21) \\
&+ \frac{r_{\psi 0}}{(n-m)} \left(m^2 (\Delta_m - 1) \frac{d\Delta_n}{dr_\psi} + n^2 (\Delta_n - 1) \frac{d\Delta_m}{dr_\psi} \right) \sin(\theta) \\
&\times \left(\sin((n-m)\theta) \cos(n\theta_{tn} - m\theta_{tm}) \right. \\
&\quad \left. + \cos((n-m)\theta) \sin(n\theta_{tn} - m\theta_{tm}) \right) \left. \right]
\end{aligned}$$

$$\left| \vec{\nabla} \psi \right|_1^2 = r_{\psi 0} \left(\frac{d\psi}{dr_\psi} \right)^2 \left(\frac{d\Delta_m}{dr_\psi} \cos(z_{ms}) + \frac{d\Delta_n}{dr_\psi} \cos(z_{ns}) \right) \quad (E.22)$$

$$\begin{aligned}
\left(\vec{\nabla} \psi \cdot \vec{\nabla} \alpha \right)_1 &= -B_{c0} \left[\frac{r_{\psi 0}}{2} \left(m^2 (\Delta_m - 1) \frac{d\Delta_m}{dr_\psi} + n^2 (\Delta_n - 1) \frac{d\Delta_n}{dr_\psi} \right) \theta \right. \\
&- \left(m (\Delta_m - 1) \sin(z_{ms}) + n (\Delta_n - 1) \sin(z_{ns}) \right) \\
&+ r_{\psi 0} \hat{s}'\theta \left(\frac{d\Delta_m}{dr_\psi} \cos(z_{ms}) + \frac{d\Delta_n}{dr_\psi} \cos(z_{ns}) \right) \quad (E.23) \\
&+ \frac{r_{\psi 0}}{2(n-m)} \left(m^2 (\Delta_m - 1) \frac{d\Delta_n}{dr_\psi} + n^2 (\Delta_n - 1) \frac{d\Delta_m}{dr_\psi} \right) \\
&\times \left(\sin((n-m)\theta) \cos(n\theta_{tn} - m\theta_{tm}) \right. \\
&\quad \left. + \cos((n-m)\theta) \sin(n\theta_{tn} - m\theta_{tm}) \right) \left. \right]
\end{aligned}$$

$$\begin{aligned}
\left| \vec{\nabla} \alpha \right|_1^2 &= B_{c0}^2 \left(\frac{d\psi}{dr_\psi} \right)^{-2} \left[r_{\psi 0} \left(m^2 (\Delta_m - 1) \frac{d\Delta_m}{dr_\psi} + n^2 (\Delta_n - 1) \frac{d\Delta_n}{dr_\psi} \right) \hat{s}'\theta^2 \right. \\
&- 2\hat{s}'\theta \left(m (\Delta_m - 1) \sin(z_{ms}) + n (\Delta_n - 1) \sin(z_{ns}) \right) \\
&- r_{\psi 0} (1 - \hat{s}'^2\theta^2) \left(\frac{d\Delta_m}{dr_\psi} \cos(z_{ms}) + \frac{d\Delta_n}{dr_\psi} \cos(z_{ns}) \right) \quad (E.24) \\
&+ \frac{r_{\psi 0}}{n-m} \left(m^2 (\Delta_m - 1) \frac{d\Delta_n}{dr_\psi} + n^2 (\Delta_n - 1) \frac{d\Delta_m}{dr_\psi} \right) \hat{s}'\theta \\
&\times \left(\sin((n-m)\theta) \cos(n\theta_{tn} - m\theta_{tm}) \right. \\
&\quad \left. + \cos((n-m)\theta) \sin(n\theta_{tn} - m\theta_{tm}) \right) \left. \right]
\end{aligned}$$

$$(J_0(k_{\perp}\rho_s))_1 = -k_{\perp 1}\rho_s J_1(k_{\perp 0}\rho_s), \quad (\text{E.25})$$

where

$$k_{\perp 1}\rho_s \equiv \frac{k_{\perp 0}\rho_s}{2} \frac{k_{\psi}^2 \left| \vec{\nabla} \psi \right|_1^2 + 2k_{\psi}k_{\alpha} \left(\vec{\nabla} \psi \cdot \vec{\nabla} \alpha \right)_1 + k_{\alpha}^2 \left| \vec{\nabla} \alpha \right|_1^2}{k_{\psi}^2 \left| \vec{\nabla} \psi \right|_0^2 + 2k_{\psi}k_{\alpha} \left(\vec{\nabla} \psi \cdot \vec{\nabla} \alpha \right)_0 + k_{\alpha}^2 \left| \vec{\nabla} \alpha \right|_0^2}. \quad (\text{E.26})$$

From the last terms in each of (E.21), (E.23), and (E.24) we see that (even after averaging over z) $v_{ds\alpha 1}$, $\left(\vec{\nabla} \psi \cdot \vec{\nabla} \alpha \right)_1$, and $\left| \vec{\nabla} \alpha \right|_1^2$ are all up-down asymmetric.

Appendix F

Dependence of the geometric coefficients on β'

Much of this appendix appears in reference [22].

In this appendix, we will study the sensitivity of the momentum flux to β' by investigating how the gyrokinetic equation changes with β' . The magnetic geometry only enters the local gyrokinetic model (in the absence of rotation) through eight geometric coefficients (i.e. $\hat{b} \cdot \vec{\nabla}\theta$, B , $v_{ds\psi}$, $v_{ds\alpha}$, $a_{s||}$, $|\vec{\nabla}\psi|^2$, $\vec{\nabla}\psi \cdot \vec{\nabla}\alpha$, and $|\vec{\nabla}\alpha|^2$), which are defined in chapter 6.

The calculation of the geometric coefficients in GS2 is done in the context of the Miller local equilibrium (see chapter 5 and appendix D). This must be done carefully as the Miller model takes the flux surface shape and its radial derivative as input, but all second order radial derivatives are calculated by ensuring the Grad-Shafranov equation is satisfied. It is through these second order radial derivatives (as well as the explicit dependence appearing in $v_{ds\alpha}$) that β' enters the geometric coefficients. Additionally, we note that we keep the safety factor, the magnetic shear, the background gradients, and the geometry fixed as we change β' . Therefore, while the Shafranov shift directly enters the flux surface geometry and affects all of the geometric coefficients, the effect of β' is limited to a few coefficients. The parameter β' , which is a normalised form of dp/da_ψ (see (9.1)), only enters into three coefficients: $v_{ds\alpha}$, $\vec{\nabla}\psi \cdot \vec{\nabla}\alpha$, and $|\vec{\nabla}\alpha|^2$. We will start with equations derived in appendix D and show precisely how β' enters into various quantities. Eventually we will find the three geometric coefficients and see that β' has an effect that is small in the inverse aspect ratio $\epsilon \ll 1$, when using the ohmically heated tokamak ordering (i.e. (2.4)).

First we combine (D.8) and (D.17) to get

$$\begin{aligned}
\underbrace{I \frac{dI}{d\psi}}_{B_0} = & \left(\underbrace{\frac{2\pi q}{I^3}}_{R_0^{-3} B_0^{-3}} + \underbrace{\oint_0^{2\pi} \Big|_{\psi} d\theta' \frac{1}{R^4 B_p^2 \vec{B} \cdot \vec{\nabla} \theta'}}_{\epsilon^{-2} R_0^{-3} B_0^{-3}} \right)^{-1} \left(\underbrace{\frac{2\pi}{I} \frac{dq}{d\psi}}_{\epsilon^{-2} R_0^{-3} B_0^{-2}} \right. \\
& \left. - \oint_0^{2\pi} \Big|_{\psi} d\theta' \underbrace{\frac{1}{R^2 \vec{B} \cdot \vec{\nabla} \theta'}}_{R_0^{-1} B_0^{-1}} \left[\underbrace{\frac{\mu_0}{B_p^2} \frac{dp}{d\psi}}_{\epsilon^{-2} R_0^{-2} B_0^{-1}} - \underbrace{\frac{2}{R^2 B_p} \left(\frac{\partial l_p}{\partial \theta'} \right)^{-1} \frac{\partial Z}{\partial \theta'}}_{\epsilon^{-1} R_0^{-2} B_0^{-1}} + \underbrace{\frac{2\kappa_p}{R B_p}}_{\epsilon^{-2} R_0^{-2} B_0^{-1}} \right] \right),
\end{aligned} \tag{F.1}$$

where the curly braces below the different terms give their ordering in $\epsilon \ll 1$. We see that introducing β' creates a lowest order modification to $I(dI/d\psi)$. Next, using (2.3), we can find that the right-hand side of the Grad-Shafranov equation can be written as

$$\begin{aligned}
\underbrace{\mu_0 j_{\zeta} R}_{B_0} = & - \left(\underbrace{\frac{2\pi q}{I^3}}_{R_0^{-3} B_0^{-3}} + \underbrace{\oint_0^{2\pi} \Big|_{\psi} d\theta' \frac{1}{R^4 B_p^2 \vec{B} \cdot \vec{\nabla} \theta'}}_{\epsilon^{-2} R_0^{-3} B_0^{-3}} \right)^{-1} \\
& \times \left[\underbrace{\mu_0 R^2 \frac{\partial p}{\partial \psi}}_{B_0} \left(\underbrace{\frac{2\pi q}{I^3}}_{R_0^{-3} B_0^{-3}} + \underbrace{\oint_0^{2\pi} \Big|_{\psi} d\theta' \frac{1}{R^4 B_p^2 \vec{B} \cdot \vec{\nabla} \theta'}}_{\epsilon^{-2} R_0^{-3} B_0^{-3}} - \underbrace{\frac{R_0^2}{R^2} \oint_0^{2\pi} \Big|_{\psi} d\theta' \frac{1}{R_0^2 R^2 B_p^2 \vec{B} \cdot \vec{\nabla} \theta'}}_{\epsilon^{-2} R_0^{-3} B_0^{-3}} \right) \right. \\
& \left. + \underbrace{\frac{2\pi}{I} \frac{dq}{d\psi}}_{\epsilon^{-2} R_0^{-3} B_0^{-2}} - \oint_0^{2\pi} \Big|_{\psi} d\theta' \underbrace{\frac{1}{R^2 \vec{B} \cdot \vec{\nabla} \theta'}}_{R_0^{-1} B_0^{-1}} \left(\underbrace{\frac{2\kappa_p}{R B_p}}_{\epsilon^{-2} R_0^{-2} B_0^{-1}} - \underbrace{\frac{2}{R^2 B_p} \left(\frac{\partial l_p}{\partial \theta'} \right)^{-1} \frac{\partial Z}{\partial \theta'}}_{\epsilon^{-1} R_0^{-2} B_0^{-1}} \right) \right],
\end{aligned} \tag{F.2}$$

which explicitly includes a term proportional to the pressure gradient (i.e. β'). However, to lowest order in aspect ratio the coefficient of this term is zero as it is composed of a safety factor term that is small and two integral terms that cancel with each other (because $R = R_0 + O(\epsilon R_0)$). All other quantities in (F.2) do not contain the pressure gradient and can be calculated directly from the flux surface geometry provided to the Miller model. Therefore, β' only introduces an $O(\epsilon B_0)$ modification to $\mu_0 j_{\zeta} R$.

We will see that the toroidal current density from the Grad-Shafranov equation (i.e. $\mu_0 j_{\zeta} R$) will appear in several places in the geometric coefficients. For example,

rearranging (D.6) gives the radial derivative of the poloidal field as

$$\underbrace{\frac{\partial B_p}{\partial \psi}}_{a^{-1}R_0^{-1}} = \underbrace{\frac{\mu_0 j_\zeta R}{R^2 B_p}}_{a^{-1}R_0^{-1}} - \underbrace{B_p \left(\frac{\partial l_p}{\partial \theta} \right)^{-1} \frac{\partial}{\partial \psi} \left(\frac{\partial l_p}{\partial \theta} \right)}_{a^{-1}R_0^{-1}} \quad (F.3)$$

$$+ \underbrace{\left(\frac{\partial l_p}{\partial \theta} \right)^{-1} \frac{\partial}{\partial \theta} \left(B_p \left(\frac{\partial l_p}{\partial \theta} \right)^{-1} \frac{\partial \vec{r}}{\partial \psi} \cdot \frac{\partial \vec{r}}{\partial \theta} \right)}_{a^{-1}R_0^{-1}}.$$

Although the toroidal current term appears as $O(a^{-1}R_0^{-1})$, the effect of β' on $\partial B_p/\partial \psi$ is small by an order (i.e. $O(\epsilon a^{-1}R_0^{-1})$) because β' does not enter $\mu_0 j_\zeta R$ to lowest order. To calculate the derivative of the toroidal field we can directly differentiate $B_\zeta = I/R$ to get (D.18). Ordering both terms we see that the effect of $dI/d\psi$ is small, so the effect of β' on $\partial B_\zeta/\partial \psi$ through (F.1) is small by one order, entering at $O(\epsilon a^{-1}R_0^{-1})$.

Using (D.8) and (D.15) gives

$$\underbrace{\vec{\nabla} \alpha}_{a^{-1}} = \left(- \int_{\theta_\alpha}^{\theta} \Big|_{\psi} d\theta' \underbrace{\frac{I}{R^2 \vec{B} \cdot \vec{\nabla} \theta'}}_1 \left[\underbrace{\frac{1}{I} \frac{dI}{d\psi}}_{\epsilon^2 a^{-2} B_0^{-1}} - \underbrace{\frac{\mu_0 j_\zeta R}{R^2 B_p^2}}_{a^{-2} B_0^{-1}} - \underbrace{\frac{2}{R^2 B_p} \left(\frac{\partial l_p}{\partial \theta'} \right)^{-1} \frac{\partial Z}{\partial \theta'}}_{\epsilon a^{-2} B_0^{-1}} + \underbrace{\frac{2\kappa_p}{R B_p}}_{a^{-2} B_0^{-1}} \right] \right.$$

$$+ \underbrace{\left[\frac{I \vec{\nabla} \psi \cdot \vec{\nabla} \theta'}{R^4 B_p^2 \vec{B} \cdot \vec{\nabla} \theta'} \right]_{\theta'=\theta_\alpha}^{\theta'=\theta}}_{a^{-2} B_0^{-1}} + \underbrace{\left(\frac{I}{R^2 \vec{B} \cdot \vec{\nabla} \theta'} \right)_{\theta'=\theta_\alpha} \frac{d\theta_\alpha}{d\psi}}_{a^{-2} B_0^{-1}} \underbrace{\vec{\nabla} \psi}_{a B_0} \quad (F.4)$$

$$- \underbrace{\frac{I}{R^2 \vec{B} \cdot \vec{\nabla} \theta}}_{a^{-1}} \vec{\nabla} \theta + \underbrace{\vec{\nabla} \zeta}_{\epsilon a^{-1}}.$$

By ordering the various terms we find that the $dI/d\psi$ term is small by two orders in $\epsilon \ll 1$. However, the $\mu_0 j_\zeta R$ term enters to lowest order, therefore the effect of β' on $\vec{\nabla} \alpha$ is only small by one order (i.e. $O(\epsilon a^{-1})$). The dependence of the coefficients $\vec{\nabla} \psi \cdot \vec{\nabla} \alpha$ and $|\vec{\nabla} \alpha|^2$ on $\vec{\nabla} \alpha$ is apparent. Hence β' does not enter $\vec{\nabla} \psi \cdot \vec{\nabla} \alpha$ and $|\vec{\nabla} \alpha|^2$ to lowest order in $\epsilon \ll 1$. Instead it enters to next order due to the quantity $\mu_0 j_\zeta R$, which is given by (F.2). The geometric coefficient $v_{ds\alpha}$ is more complicated. Substituting

(D.18) into (6.10) gives

$$\begin{aligned}
\underbrace{v_{ds\alpha}}_{a^{-1}R_0^{-1}v_{ths}^2\Omega_s^{-1}} &= - \underbrace{\frac{w_{||}^2}{\Omega_s}}_{v_{ths}^2\Omega_s^{-1}} \left(- \underbrace{\frac{\mu_0 j_\zeta R}{R^2 B}}_{\epsilon a^{-1}R_0^{-1}} - \underbrace{\frac{I^2}{R^3 B} \frac{\partial R}{\partial \psi}}_{a^{-1}R_0^{-1}} + \underbrace{\frac{B_p}{B} \frac{\partial B_p}{\partial \psi}}_{\epsilon a^{-1}R_0^{-1}} - \underbrace{\frac{\partial B}{\partial \theta} \frac{\hat{b} \cdot (\vec{\nabla} \theta \times \vec{\nabla} \alpha)}{B}}_{a^{-1}R_0^{-1}} \right) \\
&\quad - \underbrace{\frac{\mu B}{m_s \Omega_s}}_{v_{ths}^2\Omega_s^{-1}} \left(\underbrace{\frac{I}{R^2 B} \frac{dI}{d\psi}}_{\epsilon a^{-1}R_0^{-1}} - \underbrace{\frac{I^2}{R^3 B} \frac{\partial R}{\partial \psi}}_{a^{-1}R_0^{-1}} + \underbrace{\frac{B_p}{B} \frac{\partial B_p}{\partial \psi}}_{\epsilon a^{-1}R_0^{-1}} - \underbrace{\frac{\partial B}{\partial \theta} \frac{\hat{b} \cdot (\vec{\nabla} \theta \times \vec{\nabla} \alpha)}{B}}_{a^{-1}R_0^{-1}} \right). \tag{F.5}
\end{aligned}$$

We see that β' will enter into the $\mu_0 j_\zeta R$ term as well as both $\partial B_p / \partial \psi$ terms, but ordering these three terms reveals that the effect of β' is $O(\epsilon^2 a^{-1} R_0^{-1} v_{ths}^2 \Omega_s^{-1})$. The parameter β' has a much larger $O(\epsilon a^{-1} R_0^{-1} v_{ths}^2 \Omega_s^{-1})$ effect through the two $\vec{\nabla} \alpha$ terms as well as the $dI/d\psi$ term. Figure 9.8 illustrates the relative magnitudes of these two effects for several flux surface geometries. The difference between the dotted red line and the dashed blue line indicates the effect of the $dI/d\psi$ term, while the difference between the solid black line and the dotted red line indicates the effect of $\mu_0 j_\zeta R$ acting through $\vec{\nabla} \alpha$. We see that the effect of $\mu_0 j_\zeta R$ seems to dominate.

In conclusion, β' only enters into three of the geometric coefficients: $v_{ds\alpha}$, $\vec{\nabla} \psi \cdot \vec{\nabla} \alpha$, and $|\vec{\nabla} \alpha|^2$. Because β' has such a large effect on the momentum flux, this reinforces the idea from chapter 8 that $v_{ds\alpha}$ is a particularly important geometric coefficient for understanding intrinsic rotation transport due to up-down asymmetry. We also learned that the dominant effect of β' on $\vec{\nabla} \psi \cdot \vec{\nabla} \alpha$ and $|\vec{\nabla} \alpha|^2$ is through the quantity $\mu_0 j_\zeta R$ and is small in $\epsilon \ll 1$. The drift coefficient $v_{ds\alpha}$ also depends on β' to next order because of $\mu_0 j_\zeta R$. However, it has another separate dependence through the quantity $dI/d\psi$ that is formally the same size in $\epsilon \ll 1$, but it appears to be a weak effect (at least in the geometries of chapter 9). These dependences are the only way that the gyrokinetic model knows about β' . Hence they must be responsible for the significant reduction in the momentum transport.

References

- [1] L.H. Kantha and C.A. Clayson. *Numerical models of oceans and oceanic processes*. Academic press, 2000.
- [2] H.N. Pollack, S.J. Hurter, and J.R. Johnson. Heat flow from the earth's interior: analysis of the global data set. *Reviews of Geophysics*, 31(3):267, 1993.
- [3] Key world energy statistics. Technical report, International Energy Agency, 2015.
- [4] M. Keilhacker, A. Gibson, C. Gormezano, P.J. Lomas, P.R. Thomas, M.L. Watkins, P. Andrew, B. Balet, D. Borba, C.D. Challis, et al. High fusion performance from deuterium-tritium plasmas in JET. *Nucl. Fusion*, 39(2):209, 1999.
- [5] F. Troyon, R. Gruber, H. Saurenmann, S. Semenzato, and S. Succi. MHD-limits to plasma confinement. *Plasma Phys. Control. Fusion*, 26(1A):209, 1984.
- [6] Y. Liu, A. Bondeson, Y. Gribov, and A. Polevoi. Stabilization of resistive wall modes in ITER by active feedback and toroidal rotation. *Nucl. Fusion*, 44(2):232, 2004.
- [7] M. Okabayashi, J. Bialek, M.S. Chance, M.S. Chu, E.D. Fredrickson, A.M. Garofalo, M. Gryaznevich, R.E. Hatcher, T.H. Jensen, L.C. Johnson, et al. Active feedback stabilization of the resistive wall mode on the DIII-D device. *Phys. Plasmas*, 8(5):2071, 2001.
- [8] A.M. Garofalo, M.S. Chu, E.D. Fredrickson, M. Gryaznevich, T.H. Jensen, L.C. Johnson, R.J. La Haye, G.A. Navratil, M. Okabayashi, J.T. Scoville, et al. Resistive wall mode dynamics and active feedback control in DIII-D. *Nucl. Fusion*, 41(9):1171, 2001.
- [9] C.P. Ritz, H. Lin, T.L. Rhodes, and A.J. Wootton. Evidence for confinement improvement by velocity-shear suppression of edge turbulence. *Phys. Rev. Lett.*, 65(20):2543, 1990.

- [10] K.H. Burrell. Effects of $E \times B$ velocity shear and magnetic shear on turbulence and transport in magnetic confinement devices. *Phys. Plasmas*, 4(5):1499, 1997.
- [11] M. Barnes, F.I. Parra, E.G. Highcock, A.A. Schekochihin, S.C. Cowley, and C.M. Roach. Turbulent transport in tokamak plasmas with rotational shear. *Phys. Rev. Lett.*, 106(17):175004, 2011.
- [12] E.G. Highcock, M. Barnes, A.A. Schekochihin, F.I. Parra, C.M. Roach, and S.C. Cowley. Transport bifurcation in a rotating tokamak plasma. *Phys. Rev. Lett.*, 105(21):215003, 2010.
- [13] H. Reimerdes, T.C. Hender, S.A. Sabbagh, J.M. Bialek, M.S. Chu, A.M. Garofalo, M.P. Gryaznevich, D.F. Howell, G.L. Jackson, R.J. La Haye, et al. Cross-machine comparison of resonant field amplification and resistive wall mode stabilization by plasma rotation. *Phys. Plasmas*, 13(5):56107, 2006.
- [14] A.M. Garofalo, E.J. Strait, L.C. Johnson, R.J. La Haye, E.A. Lazarus, G.A. Navratil, M. Okabayashi, J.T. Scoville, T.S. Taylor, and A.D. Turnbull. Sustained stabilization of the resistive-wall mode by plasma rotation in the DIII-D tokamak. *Phys. Rev. Lett.*, 89(23):235001, 2002.
- [15] R. Aymar et al. Summary of the ITER final design report. *ITER document G A0 FDR*, 4:01, 2001.
- [16] F.I. Parra, M. Barnes, E.G. Highcock, A.A. Schekochihin, and S.C. Cowley. Momentum injection in tokamak plasmas and transitions to reduced transport. *Phys. Rev. Lett.*, 106(11):115004, 2011.
- [17] Y. Camenen, A. Bortolon, B.P. Duval, L. Federspiel, A.G. Peeters, F.J. Casson, W.A. Hornsby, A.N. Karpushov, F. Piras, O. Sauter, et al. Experimental evidence of momentum transport induced by an up-down asymmetric magnetic equilibrium in toroidal plasmas. *Phys. Rev. Lett.*, 105(13):135003, 2010.
- [18] J. Ball, F.I. Parra, M. Barnes, W. Dorland, G.W. Hammett, P. Rodrigues, and N.F. Loureiro. Intrinsic momentum transport in up-down asymmetric tokamaks. *Plasma Phys. Control. Fusion*, 56(9):095014, 2014.
- [19] A.G. Peeters, C. Angioni, et al. Linear gyrokinetic calculations of toroidal momentum transport in a tokamak due to the ion temperature gradient mode. *Phys. Plasmas*, 12(7):072515, 2005.

- [20] F.I. Parra, M. Barnes, and A.G. Peeters. Up-down symmetry of the turbulent transport of toroidal angular momentum in tokamaks. *Phys. Plasmas*, 18(6):062501, 2011.
- [21] H. Sugama, T.H. Watanabe, M. Nunami, and S. Nishimura. Momentum balance and radial electric fields in axisymmetric and nonaxisymmetric toroidal plasmas. *Plasma Phys. Control. Fusion*, 53(2):024004, 2011.
- [22] J. Ball, F.I. Parra, J. Lee, and A.J. Cerfon. Effect of the Shafranov shift and the gradient of β on intrinsic momentum transport in up-down asymmetric tokamaks. *arXiv preprint arXiv:1607.06387*, 2016.
- [23] J.P. Freidberg. *Ideal Magnetohydrodynamics*. Plenum Press, New York, NY, 1987.
- [24] H. Grad and H. Rubin. Hydromagnetic equilibria and force-free fields. *J. of Nucl. Energy (1954)*, 7(3):284, 1958.
- [25] A. Kuiroukidis and G.N. Throumoulopoulos. Symmetric and asymmetric equilibria with non-parallel flows. *Phys. Plasmas*, 19(2):022508, 2012.
- [26] J.P. Freidberg. *Ideal Magnetohydrodynamics*, chapter 6.4, page 126. Plenum Press, New York, NY, 1987.
- [27] J. Ball and F.I. Parra. Intuition for the radial penetration of flux surface shaping in tokamaks. *Plasma Phys. Control. Fusion*, 57(3):035006, 2015.
- [28] L.L. Lao, S.P. Hirshman, and R.M. Wieland. Variational moment solutions to the Grad–Shafranov equation. *Phys. Fluids*, 24(8):1431–1440, 1981.
- [29] A.J. Cerfon and J.P. Freidberg. “One size fits all” analytic solutions to the Grad–Shafranov equation. *Phys. Plasmas*, 17(3):032502, 2010.
- [30] C.V. Atanasiu, S. Günter, K. Lackner, and I.G. Miron. Analytical solutions to the Grad–Shafranov equation. *Phys. Plasmas*, 11(7):3510, 2004.
- [31] M. Romanelli and S. Sharapov. *Penetration of the Triangularity Shaping in High-Beta Tokamaks and Stability of the Internal Kink Mode*. JET Joint Undertaking, 2000.

- [32] L.L. Lao, H.E. St John, R.D. Stambaugh, A.G. Kellman, and W. Pfeiffer. Reconstruction of current profile parameters and plasma shapes in tokamaks. *Nucl. Fusion*, 25(11):1611, 1985.
- [33] P. Rodrigues, N.F. Loureiro, J. Ball, and F.I. Parra. Conditions for up-down asymmetry in the core of tokamak equilibria. *Nucl. Fusion*, 54(093003), 2014.
- [34] J.P.S. Bizarro. On the conditions for up-down asymmetry in the core of tokamak equilibria: a matter of simple geometry. *Nucl. Fusion*, 54(8):083015, 2014.
- [35] P. Rodrigues and J.P.S. Bizarro. On the toroidal current density flowing across a poloidal-magnetic-field null in an axisymmetric plasma. *Phys. Plasmas*, 20(4):040702, 2013.
- [36] F. Hofmann, S. Coda, P. Lavanchy, X. Llobet, Ph. Marmillod, Y. Martin, A. Martynov, J. Mlynar, J.-M. Moret, A. Pochelon, et al. Extension of the TCV operating space towards higher elongation and higher normalized current. *Nucl. Fusion*, 42(6):743, 2002.
- [37] M. Brix, N.C. Hawkes, A. Boboc, V. Drozdov, S.E. Sharapov, and JET-EFDA Contributors. Accuracy of EFIT equilibrium reconstruction with internal diagnostic information at JET. *Rev. Sci. Instrum.*, 79(10):10F325, 2008.
- [38] L.L. Lao, H.E. St John, Q. Peng, J.R. Ferron, E.J. Strait, T.S. Taylor, W.H. Meyer, C. Zhang, and K.I. You. MHD equilibrium reconstruction in the DIII-D tokamak. *Fusion Sci. Technol.*, 48(2):968, 2005.
- [39] J.P. Christiansen and J.B. Taylor. Determination of current distribution in a tokamak. *Nucl. Fusion*, 22(1):111, 1982.
- [40] J. Lee and A. Cerfon. ECOM: a fast and accurate solver for toroidal axisymmetric MHD equilibria. *Comput. Phys. Commun.*, 190:72, 2015.
- [41] J. Ball and F.I. Parra. Scaling of up-down asymmetric turbulent momentum flux with poloidal shaping mode number in tokamaks. *Plasma Phys. Control. Fusion*, 58(5):055016, 2016.
- [42] R.L. Miller, M.S. Chu, J.M. Greene, Y.R. Lin-Liu, and R.E. Waltz. Noncircular, finite aspect ratio, local equilibrium model. *Phys. Plasmas*, 5(4):973, 1998.

- [43] J. Ball, F.I. Parra, and M. Barnes. Poloidal tilting symmetry of high order tokamak flux surface shaping in gyrokinetics. *Plasma Phys. Control. Fusion*, 58(4):045023, 2016.
- [44] X.S. Lee, J.R. Myra, and P.J. Catto. General frequency gyrokinetics. *Phys. Fluids*, 26(1):223, 1983.
- [45] W.W. Lee. Gyrokinetic approach in particle simulation. *Phys. Fluids*, 26(2):556, 1983.
- [46] D.H.E. Dubin, J.A. Krommes, C. Oberman, and W.W. Lee. Nonlinear gyrokinetic equations. *Phys. Fluids*, 26(12):3524, 1983.
- [47] T.S. Hahm. Nonlinear gyrokinetic equations for tokamak microturbulence. *Phys. Fluids*, 31(9):2670, 1988.
- [48] H. Sugama, M. Okamoto, W. Horton, and M. Wakatani. Transport processes and entropy production in toroidal plasmas with gyrokinetic electromagnetic turbulence. *Phys. Plasmas*, 3(6):2379, 1996.
- [49] H. Sugama and W. Horton. Nonlinear electromagnetic gyrokinetic equation for plasmas with large mean flows. *Phys. Plasmas*, 5(7):2560, 1998.
- [50] A.J. Brizard and T.S. Hahm. Foundations of nonlinear gyrokinetic theory. *Rev. Mod. Phys.*, 79(2):421, 2007.
- [51] F.I. Parra and P.J. Catto. Limitations of gyrokinetics on transport time scales. *Plasma Phys. Control. Fusion*, 50(6):065014, 2008.
- [52] F.I. Parra and I. Calvo. Phase-space Lagrangian derivation of electrostatic gyrokinetics in general geometry. *Plasma Phys. Control. Fusion*, 53(4):045001, 2011.
- [53] I.G. Abel, G.G. Plunk, E. Wang, M.A. Barnes, S.C. Cowley, W. Dorland, and A.A. Schekochihin. Multiscale gyrokinetics for rotating tokamak plasmas: fluctuations, transport, and energy flows. *Rep. Prog. Phys.*, 76:116201, 2013.
- [54] G.R. McKee, C.C. Petty, R.E. Waltz, C. Fenzi, R.J. Fonck, J.E. Kinsey, T.C. Luce, K.H. Burrell, D.R. Baker, E.J. Doyle, et al. Non-dimensional scaling of turbulence characteristics and turbulent diffusivity. *Nucl. Fusion*, 41(9):1235, 2001.

- [55] F.L. Hinton and S.K. Wong. Neoclassical ion transport in rotating axisymmetric plasmas. *Phys. Fluids*, 28(10):3082, 1985.
- [56] J.W. Connor, S.C. Cowley, R.J. Hastie, and L.R. Pan. Toroidal rotation and momentum transport. *Plasma Phys. Control. Fusion*, 29(7):919, 1987.
- [57] P.J. Catto, I.B. Bernstein, and M. Tessarotto. Ion transport in toroidally rotating tokamak plasmas. *Phys. Fluids*, 30(9):2784, 1987.
- [58] E.K. Maschke and H. Perrin. Exact solutions of the stationary MHD equations for a rotating toroidal plasma. *Plasma Physics*, 22(6):579, 1980.
- [59] MA Beer, SC Cowley, and GW Hammett. Field-aligned coordinates for nonlinear simulations of tokamak turbulence. *Phys. Plasmas*, 2(7):2687, 1995.
- [60] W. Dorland, F. Jenko, M. Kotschenreuther, and B.N. Rogers. Electron temperature gradient turbulence. *Phys. Rev. Lett.*, 85(26):5579, 2000.
- [61] F.I. Parra, M. Barnes, I. Calvo, and P.J. Catto. Intrinsic rotation with gyrokinetic models. *Phys. Plasmas*, 19(5):056116, 2012.
- [62] A.G. Peeters, C. Angioni, and D. Strintzi. Toroidal momentum pinch velocity due to the coriolis drift effect on small scale instabilities in a toroidal plasma. *Phys. Rev. Lett.*, 98(26):265003, 2007.
- [63] J.P. Freidberg. *Plasma Physics and Fusion Energy*, chapter 14.2.1, page 452. Cambridge University Press, 2007.
- [64] H. Weisen, J.-M. Moret, S. Franke, I. Furno, Y. Martin, M. Anton, R. Behn, M.J. Dutch, B.P. Duval, F. Hofmann, et al. Effect of plasma shape on confinement and MHD behaviour in the TCV tokamak. *Nucl. Fusion*, 37(12):1741, 1997.
- [65] Y. Camenen, A. Pochelon, R. Behn, A. Bottino, A. Bortolon, S. Coda, A. Karpushov, O. Sauter, G. Zhuang, et al. Impact of plasma triangularity and collisionality on electron heat transport in TCV L-mode plasmas. *Nucl. Fusion*, 47(7):510, 2007.
- [66] S.P. Hakkarainen, R. Betti, J.P. Freidberg, and R. Gormley. Natural elongation and triangularity of tokamak equilibria. *Phys. Fluids B*, 2:1565, 1990.

- [67] R.C. Grimm, M.S. Chance, A.M.M. Todd, J. Manickam, M. Okabayashi, W.M. Tang, R.L. Dewar, H. Fishman, S.L. Mendelsohn, D.A. Monticello, et al. MHD stability properties of bean-shaped tokamaks. *Nucl. Fusion*, 25(7):805, 1985.
- [68] A.M. Dimits, G. Bateman, M.A. Beer, B.I. Cohen, W. Dorland, G.W. Hammett, C. Kim, J.E. Kinsey, M. Kotschenreuther, A.H. Kritiz, et al. Comparisons and physics basis of tokamak transport models and turbulence simulations. *Phys. Plasmas*, 7:969, 2000.
- [69] T. Rafiq and C.C. Hegna. Drift waves in helically symmetric stellarators. *Phys. Plasmas*, 12(11), 2005.
- [70] J. Ball. Nonlinear gyrokinetic simulations of intrinsic rotation in up-down asymmetric tokamaks. Master’s thesis, Massachusetts Institute of Technology, September 2013.
- [71] M. Barnes, I.G. Abel, W. Dorland, T. Görler, G.W. Hammett, and F. Jenko. Direct multiscale coupling of a transport code to gyrokinetic turbulence codes. *Phys. Plasmas*, 17(5):056109, 2010.